UNIVERSITAT DE BARCELONA

Regulation of hepatic metabolism by the autophagic protein TP53INP2

Petra Frager

ADVERTIMENT. La consulta d'aquesta tesi queda condicionada a l'acceptació de les següents condicions d'ús: La difusió d'aquesta tesi per mitjà del servei TDX (**www.tdx.cat**) i a través del Dipòsit Digital de la UB (**diposit.ub.edu**) ha estat autoritzada pels titulars dels drets de propietat intel·lectual únicament per a usos privats emmarcats en activitats d'investigació i docència. No s'autoritza la seva reproducció amb finalitats de lucre ni la seva difusió i posada a disposició des d'un lloc aliè al servei TDX ni al Dipòsit Digital de la UB. No s'autoritza la presentació del seu contingut en una finestra o marc aliè a TDX o al Dipòsit Digital de la UB (framing). Aquesta reserva de drets afecta tant al resum de presentació de la tesi com als seus continguts. En la utilització o cita de parts de la tesi és obligat indicar el nom de la persona autora.

ADVERTENCIA. La consulta de esta tesis queda condicionada a la aceptación de las siguientes condiciones de uso: La difusión de esta tesis por medio del servicio TDR (**www.tdx.cat**) y a través del Repositorio Digital de la UB (**diposit.ub.edu**) ha sido autorizada por los titulares de los derechos de propiedad intelectual únicamente para usos privados enmarcados en actividades de investigación y docencia. No se autoriza su reproducción con finalidades de lucro ni su difusión y puesta a disposición desde un sitio ajeno al servicio TDR o al Repositorio Digital de la UB. No se autoriza la presentación de su contenido en una ventana o marco ajeno a TDR o al Repositorio Digital de la UB (framing). Esta reserva de derechos afecta tanto al resumen de presentación de la tesis como a sus contenidos. En la utilización o cita de partes de la tesis es obligado indicar el nombre de la persona autora.

WARNING. On having consulted this thesis you're accepting the following use conditions: Spreading this thesis by the TDX (**www.tdx.cat**) service and by the UB Digital Repository (**diposit.ub.edu**) has been authorized by the titular of the intellectual property rights only for private uses placed in investigation and teaching activities. Reproduction with lucrative aims is not authorized nor its spreading and availability from a site foreign to the TDX service or to the UB Digital Repository. Introducing its content in a window or frame foreign to the TDX service or to the UB Digital Repository is not authorized (framing). Those rights affect to the presentation summary of the thesis as well as to its contents. In the using or citation of parts of the thesis it's obliged to indicate the name of the author.

Tesis doctoral

Regulation of hepatic metabolism by the autophagic protein TP53INP2

Petra Frager

Universidad de Barcelona

Barcelona, 2022

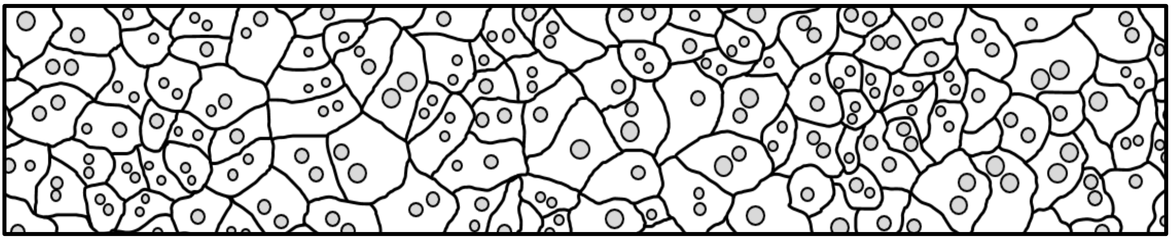

Universidad de Barcelona

Facultad de Biología

Departamento de Bioquímica y Biomedicina Molecular

Programa de Doctorado en Biomedicina

Regulation of hepatic metabolism by the autophagic protein TP53INP2

Petra Frager

Barcelona, 2022

Universidad de Barcelona

Facultad de Biología

Departamento de Bioquímica y Biomedicina Molecular

Institute for Research in Biomedicine (IRB Barcelona)

Programa de Doctorado en Biomedicina

Regulation of hepatic metabolism by the autophagic protein TP53INP2

Memoria presentada por **Petra Frager** para optar al
título de doctor por la Universidad de Barcelona.

Director y tutor	Doctoranda
Antonio Zorzano Olarte	Petra Frager

Barcelona, 2022

"Annahmen sind wie Seepocken an der Seite eines Bootes;
sie verlangsamen uns."
Christine Aschbacher, PhD; Robert B. Tucker

ACKNOWLEDGEMENTS

Eventually, my time in Barcelona comes to an end. It was a crazy time, doing a PhD and having a pandemic, it made these past five years special for sure. Somehow it made it feel longer, as it divided it into two eras, pre- and post-covid. But even though times where at time exhausting, I wouldn't have wanted to be anywhere else. I have met wonderful people along my way and here I would like to express my gratitude to them.

I cannot thank you enough Antonio, for giving me the chance to do my PhD in your group. I will always remember our interview, where I cut you short after 15 minutes because HR had scheduled another interview for me (with another PI, where I did not even intend to apply), only because I did not want to arrive late. I am forever grateful for your decision to still hire me after this short first impression. You have always been supportive and even in my most pessimistic times you managed to cheer me up with your infinite optimism. You managed to find the optimal balance between letting me do things independently and still guiding and supporting me in times I needed it. I couldn't have found a better mentor and supervisor. Thank you, Antonio!

To Saška, thank you for helping me through my PhD. You were always here for me and supported me trying to understand DOR, which is never easy. I am thankful, not only for your help on conducting this thesis, but also for being on my side during all the ups and downs during these 5 years. I had a wonderful time being in the lab with you and I will miss having you around. But Slovenia is not far from Austria, so there is no excuse for not visiting!

To JP, thank you for finally making me speak Spanish and for always helping me when I needed it. I loved our coffee breaks where you listened to the problems I had with my experiments and helped me figure out what to do. Thank you for your support and friendship!

Susana, I was so lucky to have you as a lab mate, but also as a neighbour and friend. Thank you for teaching me so many things and also for inviting me to your Halloween party, which was the start of a beautiful friendship. I am sorry to have accidentally germanized/austrianized you, but this just means we'll live close to each other again soon, so actually I am happy about it!

To my fellow PhD students: Nacho, Alba, Isa and Andrea, it was a pleasure to have had you in the lab and watch you finishing your projects. It gave me hope that I will get there too. To Jia, Katerina, Paula, Nico, Judith and Josep: All of you were amazing lab mates and before you know it, it will be you writing your thesis.

I would like to thank all the members of the Zorzano and Palacin lab, I think I will never work in a more diverse place. I loved being around all of you and I have to say there was not even one boring day in my life at the IRB. Special thanks to Jordi, for being the Kindergarten teacher of us all and for organizing everything, while whistling Georg Michael's Careless Whisper or making centrifuge sounds.

To the IRB oral party animals: Thank you for making this five years fun. All I wanted when I came here was to finish the PhD, but I left with friends for a lifetime. And we for sure set a record for most Bolera visits without ever actually bowling. Nevenka, I will miss our Spanish classes, coffees, beers, vermuts and you staying on my couch and saying sorry for no reason a million times. Cris, Michael, David, Fabian, Federica and Paloma, thank you for always being in the mood for Tuesday or Friday beers too. Without it, the PhD would have been much more exhausting. Whenever you come anywhere close to Austria, let me know and come for a visit!

An Claudia und Christian: Danke, dass ihr mich mal aus Kärnten „rausgeholt“ habt. Ohne euch wäre mir wahrscheinlich gar nicht eingefallen, dass man ja auch studieren kann, wenn man aus Reifnitz oder St. Jabob kommt.

An alle Fragers, Koraks, Grubers, Arnezeders, und meine ganze Familie: Danke, dass es euch gibt. Bald gibt es keine Entschuldigungen mehr fürs Fehlen bei Geburtstagen und sonstigen Feiern, also sehen wir uns zum Glück bald wieder öfter.

Lieber Django, was soll ich sagen. Ich kann gar nicht in Worte fassen, wie du mich während dieser Zeit unterstützt hast, trotzdem versuch ich es. Du bist mit mir nach Barcelona gekommen, und ohne dich wäre Barcelona wohl nie „zu Hause" geworden. Danke, dass du immer an mich glaubst, auch wenn ich es selbst gerade nicht tue.

An Irmi und Hubsi, ihr seid die besten Eltern der Welt. Hätte sich auch keiner gedacht, dass aus mir einmal eine Frau Doktor wird, aber ohne euch hätte das nie funktioniert. Danke für eure Unterstützung in schwierigen Zeiten, aber vor allem dafür, dass ihr mir zeigt, dass das Leben ja schön ist, wenn man gerade keinen PhD macht.

ABSTRACT

Decreased physical activity and increased consumption of energy-rich food are hallmark lifestyle modifications that developed and amplified over the course of only a few decades. These changes in our daily behavior are the culprits for the rise of various metabolic diseases, collectively regarded to as the metabolic syndrome, that has reached the magnitude of a global epidemic.

The hepatic manifestation of the metabolic syndrome is the non-alcoholic fatty liver disease (NAFLD), and it is estimated to affect every third adult person by 2030. Although considered relatively benign, NAFLD can progress to more severe liver diseases, up to the point of liver failure, through insufficiently understood processes. Different studies have shown a connection between autophagy and the development of steatosis. However, the different genetic models used in those studies report that steatosis can be ameliorated or enhanced by impaired autophagy and is dependent on the model as well as the experimental conditions.

In the present project we aimed to analyze the impact of liver-specific depletion of a positive regulator of autophagy termed TP53INP2 on liver metabolism and delineate its potential role in the development of steatosis.

We found that the hepatic expression of TP53INP2 in mice is modulated by nutrient deprivation as well as the presence of abundant nutrients. Mice specifically lacking TP53INP2 in the liver, show impaired hepatic free fatty acid oxidation and ketogenesis, evoked from a compromised transcriptional activity of the transcription factors PPARα and LXRα. We have observed that the hepatocyte-specific ablation of TP53INP2 enhances fasting- and dietary-induced steatosis and impacts cholesterol and bile acid metabolism upon consumption of diets rich in lipids and cholesterol. Furthermore, we have detected a role of TP53INP2 in the release of cholesterol from lysosomes, potentially involving the lysosome-associated membrane protein 1 (LAMP1).

Together, our data indicate that TP53INP2 is a key regulator of hepatic lipid metabolism through the modulation of PPARα and LXRα activity. We propose that such a modulation relies on the promotion of ligand availability, perhaps dependent of autophagy.

Table of Contents

1. Abbreviations 1

2. Introduction 5

    2.1. Metabolic syndrome – a man-made global epidemic 5

    2.2. Non-alcoholic fatty liver disease – the hepatic manifestation of the metabolic syndrome 6

        2.2.1. Risk factors and drivers of non-alcoholic fatty liver disease 7

        2.2.2. The limited treatment options for non-alcoholic liver disease .. 9

    2.3. Essential regulators of lipid homeostasis in liver 10

    2.4. Autophagy 12

        2.4.2. Lipophagy 18

    2.5. TP53INP2 – a positive regulator of autophagy 22

        2.5.1. TP53INP2 acts as a coactivator of the transcriptional activity of nuclear hormone receptors 25

        2.5.2. TP53INP2 promotes death receptor induced apoptosis 26

        2.5.3. TP53INP2 mediates ribosome biogenesis 26

        2.5.4. Tissue-specific physiological roles of TP53INP2 27

3. Objectives 33

4. Results 37

    4.1. Nutritional manipulation impacts hepatic expression of TP53INP2 . 37

        4.1.1. Evaluation of the impact of fasting on TP53INP2 expression 37

        4.1.2. High-fat diet treatment causes a transient upregulation of TP53INP2 expression in liver 38

4.1.3. TP53INP2 protein is depleted in a mouse model of non-alcoholic steatohepatitis 40

4.2. Evaluation of the metabolic impacts caused by TP53INP2 loss-of-function in liver 41

4.2.1. Validation of the hepatocyte-specific TP53INP2 knockout mouse model 41

4.2.2. Characterization of TP53INP2-LKO animals on standard diet 42

4.2.3. Characterization of TP53INP2-LKO animals on high-fat diet 62

4.2.4. Characterization of hepatic TP53INP2-depletion in animals subjected to a western diet 81

4.3. TP53INP2 protein reduces lysosomal free cholesterol accumulation upon Niemann-Pick C1 protein inhibition 89

5. Discussion 101

5.1. Hepatic TP53INP2 expression responds to nutritional manipulation 101

5.2. Evaluation of the impact of hepatic TP53INP2 loss-of-function in animals on standard diet.. 102

5.3. TP53INP2-depletion enhances HFD-induced hepatic steatosis and affects glucose and cholesterol metabolism... 109

5.4. Hepatocyte-specific TP53INP2-depletion impacts intracellular cholesterol trafficking 116

6. Conclusions 123

7. Material and Methods.. 127

7.1. Material 127

7.1.1. Buffers, solutions and gels 127

7.1.2. Reagents, equipment and kits 131

7.1.3. Research diets 133

7.1.4. Reagents, media, plasmids and vectors 134

7.1.5. Primers for genotyping and Real-time quantitative PCR 135

7.1.6. Primary and secondary antibodies 136

7.2. *In vivo* Methods 137

7.2.1. Generation of a liver-specific TP53INP2 knockout model ... 138

7.2.2. Validation of the model by genotyping 139

7.2.3. High-fat diet, Methionine and choline deficient diet, and Western diet treatment 141

7.2.4. Body composition measurement using Echo-MRI™ 142

7.2.5. Measurement of food intake and obtaining feces samples 142

7.2.6. Glucose tolerance test 143

7.2.7. Oral Lipid tolerance test 144

7.2.8. Very-Low Density Lipoprotein Secretion Assay 145

7.2.9. Blood sampling and plasma measurements 145

7.3. *Ex vivo* Methods 148

7.3.1. Histological analysis of liver samples 148

7.3.2. Extraction and analysis of hepatic lipids 148

7.4. *In vitro* Methods 149

7.4.1. Culture of MEFs, Huh7 and HEK293T cells 150

7.4.2. Isolation of primary hepatocytes 150

7.4.3. Counting cells using the Countess™ II cell counter 152

7.4.4. EBSS treatment of isolated primary hepatocytes 153

    - 7.4.5. Treatment of primary hepatocytes with LXRα and RXRα agonists 153
    - 7.4.6. Lentivirus production using HEK293T cells 154
    - 7.4.7. Lentiviral transduction of Huh7 cells to generate stable GFP- / TP53INP2-GFP overexpressing cells 155
    - 7.4.8. Luciferase assays performed in Huh7 cells 155
    - 7.4.9. Luciferase assays performed in mouse embryonic fibroblasts 157
    - 7.4.10. Assessment of autophagic flux in primary hepatocytes 158
    - 7.4.11. Isolation of human low-density lipoproteins and aggregation 159
    - 7.4.12. Evaluation of intracellular cholesterol localization in primary hepatocytes and mouse embryonic fibroblasts 160
    - 7.4.13. Treatment of mouse embryonic fibroblasts with LXRα agonist 161
  - 7.5. Molecular biology methodology 162
    - 7.5.1. Determination of relative gene expression by quantitative polymerase chain reaction 162
    - 7.5.2. Transcriptomics 166
    - 7.5.3. Protein analysis by Western Blot 166
  - 7.6. Statistics 173
- 8. References 177
- 9. List of Figures 195
- 10. List of Tables 202

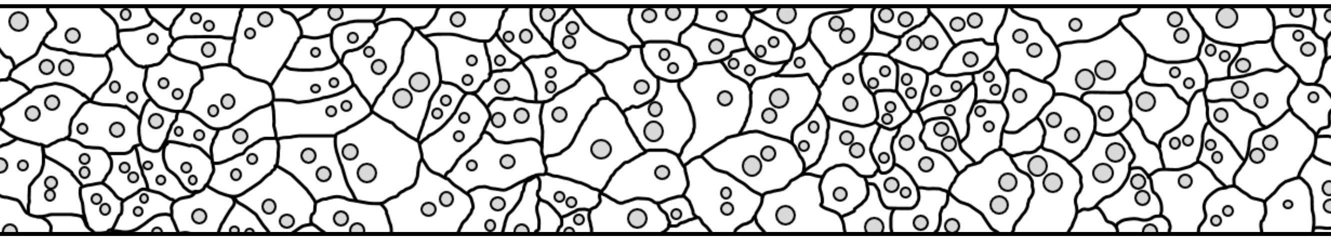

ABBREVIATIONS

1. ABBREVIATIONS

A

ABCA1	ATP-binding cassette transporter A1
ABCG	ATP-binding cassette sub-family G member
Acly	ATP-citrate lyase
Acox1	Acyl-CoA oxidase 1
agLDL	aggregated low-density lipoprotein
AIDS	Acquired immunodeficiency syndrome
ALT	Alanine aminotransferase
Ambra1	Activating molecule in Beclin1-regulated autophagy protein 1
AMPK	5' AMP-activated protein kinase
ApoA1	Apolipoprotein A1
ApoB	Apolipoprotein B
Asbt	Apical sodium-dependent bile acid transporter
AST	Aspartate aminotransferase
ATG	Autophagy related gene
ATGL	Adipose triglyceride lipase
ATP	Adenosine triphosphate
AUC	Area under the curve

B

BA	Bile acid
BafA1	Bafilomycin A1
BH3	Bcl-2 homology domain 3
Bif-1	Endophilin B1
BRCA1	Breast cancer type 1 susceptibility protein
Bsep	Bile salt export pump

1 | ABBREVIATIONS

C

C/EBP-α	CCAAT/enhancer-binding protein-α
C57BL/6J	Inbred mouse strain
ChIP	Chromatin immuno-precipitation
CHMP2A	Component charged MVB protein 2A
Chrebp	Carbohydrate-responsive element-binding protein
CMA	Chaperone mediated autophagy
COVID-19	Coronavirus disease 2019
CREB	cAMP response element-binding protein
CTRTC2	CREB-regulated transcription coactivator 2
CV	Central vein
Cyp2c55	Cytochrome P450 2C55
Cyp7a1	Cholesterol 7-alpha-hydroxylase

D

dDOR	Drosophila DOR
DMSO	Dimethyl sulfoxide
DNA	Deoxyribonucleic acid
DNL	*de novo* lipogenesis
DOR	Diabetes and obesity regulated gene

E

EBSS	Earle’s Balanced Salt Solution
EcR	Ecdysone receptor
EHBP1	EH domain-binding protein 1
EHD2	EH domain-containing protein 2
ELISA	Enzyme-linked immunosorbent assays
ER	Endoplasmic reticulum
ESCRT	Endosomal sorting complexes required for transport

F

F4/80	EGF-like module-containing mucin-like hormone receptor-like 1
FACS	Fluorescence-activated cell sorting
FasL	Fas ligand
FBS	Fetal bovine serum
FC	Free cholesterol
FIP200	Focal adhesion kinase interacting protein of 200kDa
FOXO1	Forkhead box O1
FXR	Farnesoid X receptor

G

G6PC	Catalytic subunit of G6Pase
GABARAP	Gamma-aminobutyric acid receptor-associated protein
GFP	Green fluorescent protein
GLUT-4	Glucose transporter type 4,
GR	Glucocorticoid receptor
GSEA	Gene set enrichment analysis
GSK3β	Glycogen synthase kinase 3β
GTT	Glucose tolerance test

H

H/E	Hematoxylin and eosin
HCC	Hepatocellular carcinoma
HDL	High-density lipoprotein
HFD	High-fat diet
HOMA-IR	Homeostasis model index of insulin resistance
HRP	Horseradish peroxidase
hsc70	Heat shock cognate protein of 70 kDa
HSL	Hormone sensitive lipase
hsp90	Heat shock protein of 90 kDa

I

IL-6	Interleukin-6
IR	Insulin resistance
IRS1/2	Insulin receptor substrate 1/2

K

KEGG	Kyoto Encyclopedia of Genes and Genomes
KO	Knockout

L

LAL	Lysosomal acid lipase
LAMP1	Lysosome-associated membrane protein 1
LAMP2A	Lysosomal membrane receptor protein 2
LD	Lipid droplet
LDL	Low-density lipoprotein
LDL-R	Low-density lipoprotein receptor
LIR	LC3 Interacting region
LKO	Liver-specific knockout
LRP1	Low-density lipoprotein (LDL) receptor-related protein 1
LXR	Liver X receptor
LXRE	Liver X Receptor Response Element

M

MAPK	Mitogen-activated protein kinase
MCD	Methionine and choline-deficient diet
MEF	Mouse embryonic fibroblast
MGL	Monoglyceride lipase
mRNA	Messenger ribonucleic acid
mTOR	Mammalian target of rapamycin
mTORC1	Mammalian target of rapamycin complex 1

N

NAFL	Non-alcoholic fatty liver
NAFLD	Non-alcoholic fatty liver disease
NASH	Non-alcoholic steatohepatitis
NBR1	Neighbor of BRCA1 gene 1
NEFA	Non-esterified free fatty acid
NES	Nuclear export signal
nLDL	native low-density lipoprotein
NLS	Nuclear Localization Signal
NMR	Nuclear Magnetic Resonance
NoLS	Nucleolar Localization Signal
Npc1/2	Niemann-Pick C1/2
NRBF2	Nuclear receptor binding factor 2
NRZ	NRZ tethering complex
ns	not significant
NSF	Soluble N-ethyl-maleimide-sensitive fusion protein
Ntcp	Na^+-dependent taurocholate cotransport peptide
Ntcp2	Apical-sodium-dependent BA transporter

O

OCT	Optimal cutting temperature
OLTT	Oral lipid tolerance test
ORO	Oil-Red-O
OSBP	Oxysterol-binding proteins

P

P-407	Poloxamer 407
p62	Ubiquitin-binding protein p62 (SQSTM1)
PAS	Periodic Acid-Schiff
PBS	Phosphate-Buffered Saline

PCR	Polymerase chain reaction
PE	Phosphatidylethanolamine
PGC1α	PPAR-gamma coactivator 1-alpha
PI3K	Phosphoinositide 3-kinase
PI3P	Phosphatidylinositol-3-phophate
PIC	POLR1/RNA polymerase preinitiation complex
PIK3C3	Phosphatidylinositol 3-kinase catalytic subunit type 3 (Vps34)
PIK3R4	Phosphoinositide 3-kinase regulatory subunit 4
PLIN	Perilipin
PML	Promyelocytic leukemia
POLR1	DNA-directed RNA polymerase I
PPAR	Peroxisome proliferator-activated receptors
PPRE	PPAR responsive element

R

RAB	Ras-related protein Rab
rDNA	ribosomal Deoxyribonucleic acid
RLU	Relative light units
RNA	Ribonucleic acid
RNASeq	RNA sequencing
ROS	Reactive oxygen species
RT	Room temperature
RT-qPCR	Real-time quantitative PCR
RXR	Retinoid X receptor

S

S1P	Site-1 protease
S2P	Site-2 protease
SEM	Standard error of the mean
SIRT1	NAD-dependent protein deacetylase sirtuin-1

SM	Skeletal muscle
SNAP29	Synaptosomal-associated protein 29
SNARE	Soluble NSF fusion protein attachment protein receptors
SOCS	Suppressor-of-cytokine-signaling
SQSTM1	Ubiquitin-binding protein p62 (SQSTM1)
SREBP	Sterol regulatory element binding protein
START	Steroidogenic acute regulatory protein (StAR)-related lipid transfer
STX17	Syntaxin-17

T

T1DM	Type 1 diabetes mellitus
T2DM	Type 2 diabetes mellitus
TFE3	Transcription factor E3
TFEB	Transcription factor EB
TG	Triglycerides
TIM	TRAF6 Interacting Motif
TMEM41B	Transmembrane protein 41B
TNFα	Tumor necrosis factor α
TORC2	CREB-regulated transcription coactivator 2
TP53INP1	Tumor protein p53-inducible nuclear protein 1
TP53INP2	Tumor protein p53-inducible nuclear protein 2
TRAF6	TNF receptor-associated factor 6
TRAIL	TNF-related apoptosis-inducing ligand
TRα1	Thyroid hormone receptor α

U

Ube2g2	Ubiquitin-conjugating enzyme E2 G2
UIM	Ubiquitin Interacting Motif
ULK1/2	Unc-51-like autophagy-activating kinase 1/2
UVRAG	UV radiation resistance-associated gene

V

VAMP	Vesicle-associated membrane protein
VDR	Vitamin D Receptor
VLDL	Very-low-density lipoproteins
VMP1	Vacuole membrane protein 1
Vps15	Phosphoinositide 3-kinase regulatory subunit 4
Vps34	Phosphatidylinositol 3-kinase catalytic subunit type 3
Vps37a	Vacuolar protein sorting-associated protein 37A
VPS4	Vacuolar protein sorting-associated protein 4

W

WAT	White adipose tissue
WD	Western diet
WIPI	WD repeat domain phosphoinositide-interacting protein family
WT	Wildtype

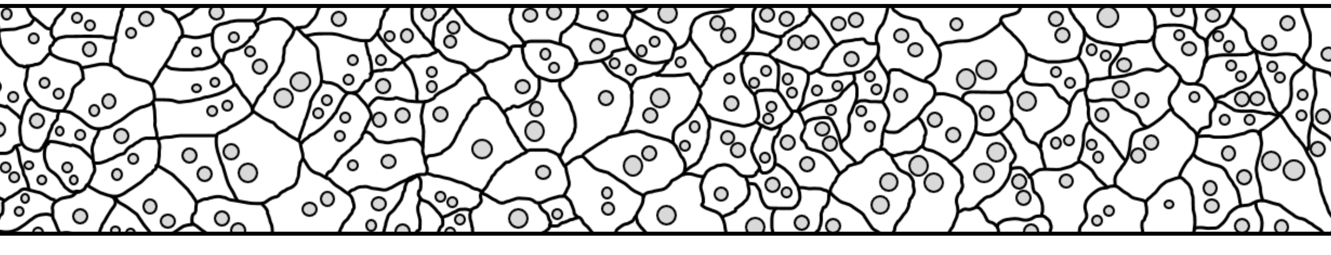

INTRODUCTION

2. INTRODUCTION

2.1. Metabolic syndrome – a man-made global epidemic

The metabolic syndrome is a generic term used to describe various medical conditions including abdominal obesity, insulin resistance, glucose intolerance, hypertension, dyslipidemia and non-alcoholic fatty liver disease (NAFLD) [1], and was first mentioned as Syndrome X in 1988 [2]. Although definitions and criteria of the metabolic syndrome vary amongst studies [1], the evidence is clear that the prevalence has reached concerning levels [1, 3]. Since then, research has shown that genetic predisposition is contributing to the metabolic syndrome and obesity [4, 5]. However, given the sharp increase during a relatively short period of time, genetics only account for a minor fraction of individuals suffering from metabolic syndrome [1]. A major contributor to the development of the metabolic syndrome is reduced physical activity, evoked by a diminished demand to be active during everyday life, explained by the increased time spent in a sedentary position in personal transportation, at the workplace and during leisure time activities such as watching television [1, 6, 7]. Another major cause for metabolic syndrome development is overnutrition and the consumption of sugary beverages, as well as a carbohydrate-rich or calorically dense diet [8-11]. The metabolic syndrome comprises cardiovascular risk factors contributing to morbidity and mortality [1]. Despite this increased risk, the metabolic syndrome is also associated with adverse effects in the course of other pathologies such as autoimmune diseases [12, 13], several types of cancer [14-17], and the Coronavirus disease 2019 (COVID-19) [18, 19]. Furthermore, the metabolic syndrome negatively impacts fertility, oocyte quality [20, 21], and sperm quality [22-24]. Given the prevalence of the metabolic syndrome, serious effort should be made to promote exercise and encourage healthier lifestyles, preventing the onset of the metabolic syndrome. This should be accompanied by further research to better understand the underlying pathological mechanisms of the metabolic syndrome to develop the best possible therapies [1].

2.2. Non-alcoholic fatty liver disease – the hepatic manifestation of the metabolic syndrome

The non-alcoholic fatty liver disease (NAFLD) is an ectopic accumulation of lipids, regarded as the hepatic manifestation of the metabolic syndrome [25, 26]. Its prevalence amongst the adult population is continuously increasing, estimated to reach 33% by 2030 [27]. NAFLD is characterized by steatosis in form of triglyceride and free cholesterol (FC) accumulation [28] and is considered to be relatively benign with a good long-term prognosis [29, 30]. Nonetheless, an estimated 10 - 30 % of individuals with simple steatosis progress to non-alcoholic steatohepatitis (NASH) [31], which is accompanied by hepatocyte injury, cell death and inflammation with or without fibrosis at varying degrees [32]. In course of several years, about 15 - 20 % of NASH livers develop cirrhosis [28, 33-35]. Cirrhosis has been shown to advance to hepatocellular carcinoma (HCC) with a risk of 1 - 2 % per year [36, 37], yet, about 20% of HCC cases occur in the absence of cirrhosis [38]. In 2021, HCC was the seventh most common type of cancer in the world and one of the leading causes for cancer-related deaths [39, 40]. Ultimately, end-stage-liver disease requires liver transplantation in patients suffering from NASH, cirrhosis and HCC [41, 42].

The transition of NAFLD to more severe pathologies, summarized in Figure 1, is very heterogenous and incompletely understood [42]. The pathogenic mechanisms include altered hepatocyte metabolism and autophagy, endoplasmic reticulum stress, systemic inflammation, insulin resistance, and diabetes [43-47].

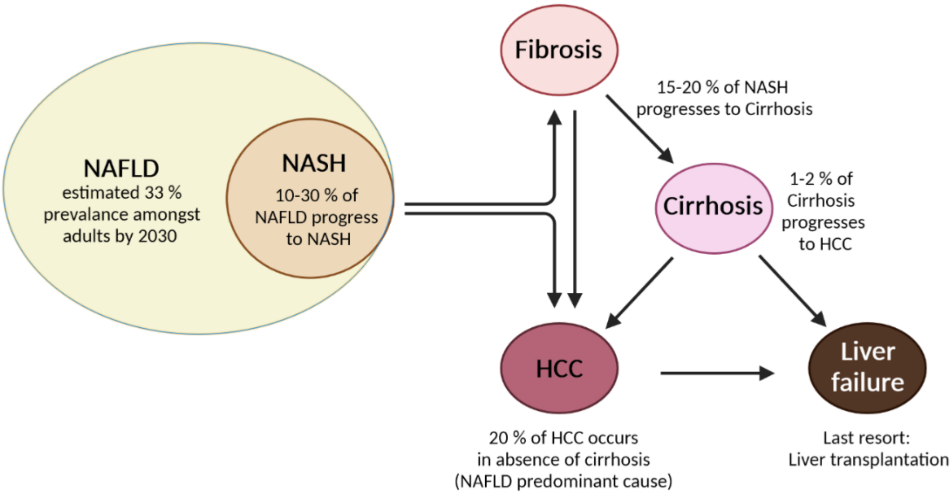
NAFLD
estimated 33 % prevalance amongst adults by 2030
NASH
10-30 % of NAFLD progress to NASH
Fibrosis
15-20 % of NASH progresses to Cirrhosis
Cirrhosis
1-2 % of Cirrhosis progresses to HCC
HCC
Liver failure
20 % of HCC occurs in absence of cirrhosis (NAFLD predominant cause)
Last resort: Liver transplantation

Figure 1. Progression of non-alcoholic fatty liver disease. Non-alcoholic fatty liver disease (NAFLD) progresses to non-alcoholic steatohepatitis (NASH) in 10 - 30 % of individuals and can be accompanied by various degrees of fibrosis. Up to 20 % of NASH livers develop cirrhosis in course of the disease. Cirrhosis increases the risk of hepatocellular carcinoma (HCC) development to 1-2% per year. About 20% of HCC occurs in the absence of cirrhosis, with NAFLD being the predominant cause in these cases. End-stage liver disease in form of cirrhosis and HCC requires liver transplantation in cases of liver failure (Adapted from Loomba et al., 2021).

2.2.1. Risk factors and drivers of non-alcoholic fatty liver disease

A well-known risk factor for NAFLD is obesity [48]. Typically, excess nutrients are stored in form of lipids within the adipose tissue. However, with chronic metabolic stress, the storage capacity of the adipose tissue can be overwhelmed which results in ectopic lipid accumulation, for instance within the liver [49]. Especially visceral (intra-abdominal) fat has been implicated in the initiation of a chronic inflammatory state by secretion of hormones, cytokines and free fatty acids that are directly transported to the liver via the portal vein [48]. Adiponectin, an adipokine secreted mostly from subcutaneous rather than visceral fat [48], has been implicated with an anti-steatotic effect in the liver [30, 50], and decreased serum levels have been observed in patients with steatosis and NASH [51, 52]. Furthermore, the adipose tissue secretes pro-inflammatory cytokines such as interleukin-6 (IL-6) and tumor necrosis factor α (TNFα), which was reported to be increased in plasma of patients with NASH and fibrosis [45, 53-55]. Ultimately, also the hepatic expression of TNFα and IL-6 mRNA is increased in NASH patients and further promotes inflammation [53, 56], which plays a key role in NAFLD pathogenesis and obesity related insulin resistance [30].

Insulin resistance (IR) is another crucial pathological factor in NAFLD development and is a condition with impaired capability of insulin to regulate glucose homeostasis [57, 58]. Insulin is a hormone secreted by beta-cells of the islets of Langerhans within the pancreas upon food intake [59, 60] and is directly transported to the liver through the portal vein [61]. Insulin receptors are located at the plasma membrane and insulin binding activates tyrosine kinases on the intracellular part of the transmembrane proteins. This initiates an intracellular signaling cascade that involves phosphorylation of cellular substrates such as the insulin receptor substrate 1 (IRS1) and IRS2. Phosphorylation of IRS subsequently activates downstream pathways. One of the pathways activated by insulin it the MAPK pathway, which is important for cell growth and mitogenesis. Another pathway activated by insulin is the PI3K-Akt pathway, that inhibits gluconeogenesis and facilitates protein and glycogen synthesis via activation of mammalian target of rapamycin (mTOR) and suppression of forkhead box O1 (FOXO1). Hepatic mTORC1 activation induces the expression of lipogenic genes and suppresses fatty acid oxidation and inhibits the expression of apolipoprotein B (ApoB) mRNA [30, 58], the predominant structural protein of very-low-density lipoproteins (VLDLs), crucial for VLDL secretion [62, 63]. Insulin mediated repression of FOXO1 attenuates gluconeogenesis in liver. PI3K-Akt signaling in muscle and adipose tissue increases glucose uptake by promoting glucose transporter 4 (GLUT-4) translocation to the plasma membrane [61]. In the adipose tissue, insulin signaling increases fatty acid and triglyceride synthesis while it suppresses lipolysis [64].

In an insulin resistant state, several parts of the insulin-signaling cascade may be disrupted by post-translational modifications due to the presence of inflammatory signals such as TNFα, or by the upregulation of the suppressor-of-cytokine-signaling (SOCS) pathway by IL-6, resulting in IRS1 and IRS2 degradation. These and other alterations ultimately lead to impaired insulin signaling in several tissues, causing harmful systemic effects. On the one hand, cellular glucose uptake in peripheral tissues is decreased and hepatic gluconeogenesis is not suppressed, resulting in elevated blood glucose levels [30]. On the other hand, the repression of lipolysis within the adipose tissue is blunted due to insulin resistance, resulting in an increased free fatty acid flux to the liver [65], where they are used as substrates for triglyceride synthesis which contributes to NAFLD development [58].

Lipotoxicity is another detrimental factor during NAFLD progression. Toxic lipid intermediates such as free fatty acids, free cholesterol, ceramides, phosphatidic acid, lysophosphatidic acid, and diacylglycerols accumulate in the liver and cause cell dysfunction and cell death [30, 66]. The accumulation of toxic intermediates is a major cause for oxidative stress, resulting in elevated levels of reactive oxygen species (ROS), which promote oxidative alterations in biomolecules, impairing their function and cell viability [66, 67].

Finally, it must be mentioned that there is overwhelming evidence that the above-mentioned risk factors obesity, inflammation, insulin resistance, lipotoxicity and oxidative stress act in concert and massively impact each other [29, 30, 68, 69].

2.2.2. The limited treatment options for non-alcoholic liver disease

The major recommendation for patients suffering from non-alcoholic liver disease (NAFLD) is weight loss [30]. However, since lifestyle changes are hard to maintain over a long period of time, a sustainable weight loss is not achieved by all patients [70]. Another intervention for patients with morbid obesity is bariatric surgery, which has been shown to improve the NAFLD pathophysiology [71, 72], but comes with the risk of post-surgery side effects such as acid reflux, vomiting, and increased incidence of hernias [73].

Currently, approved drugs for the treatment of NAFLD are not available. The development of disease-specific pharmacological treatments for NAFLD faces several difficulties, besides being an extremely time-consuming and expensive process [74, 75]. A major disadvantage in drug development is the heterogeneity of the progression from NAFLD to more advanced stages of liver disease between individuals, that makes it difficult to study the beneficial outcomes of a potential drug. Another drawback is that the golden standard of NAFLD diagnosis is the histological assessment of a biopsy, and this invasive procedure itself poses the risk of several adverse effects. This makes monitoring of drug effects difficult because follow-up biopsies are not often possible [58]. Thus, a better understanding of the progression of NAFLD and the identification of (blood)-based biomarkers for assessment of NAFLD development are needed [76].

2.3. Essential regulators of lipid homeostasis in liver

Lipid accumulation in the liver can result from increased hepatic uptake, increased *de novo* lipogenesis (DNL), or impaired lipid degradation through autophagy or oxidation [77, 78]. Transcriptional regulators of these processes maintain hepatic lipid homeostasis and prominent members include the peroxisome proliferator-activated receptors (PPARs), sterol regulatory element binding proteins (SREBPs), liver X receptors (LXRs), and the Farnesoid X receptor (FXR) [77, 79-82].

Peroxisome proliferator-activated receptors are nuclear receptors, forming a permissive heterodimer with retinoid X receptor α (RXRα), allowing the dimer to be activated by ligands of either protein [83]. PPARα is predominantly expressed in liver and is activated by long-chain fatty acids and eicosanoids. During fasting PPARα is activated and promotes mitochondrial and peroxisomal β-oxidation and ketogenesis [77, 84]. Hepatocyte-specific depletion of PPARα results in steatosis [85]. PPARγ is also expressed in liver and regulates hepatic inflammation in Kupffer and hepatic stellate cells. In hepatocytes, PPARγ activity enhances DNL and the uptake of fatty acids [86].

Sterol regulatory element-binding proteins (SREBPs) are involved in cholesterol and free fatty acid synthesis. The SREBP1 gene encodes for Srebp1a and Srebp1c from to distinct promoters, while the third member Srebp2 is transcribed from an additional gene (SREBP2). SREBPs reside in the endoplasmic reticulum membrane as inactive precursors, are cleaved through the action of the SREBP cleavage-activating protein (Scap) and incorporated into coat protein complex II (COPII)-coated vesicles, that pass through the Golgi. Within the Golgi, SREBPs are cleaved by two additional proteases, Site-1 protease (S1P) and S2P, causing the release of the transcriptionally active fragments that translocate to the nucleus. While Srebp1a and Srebp1c activate the transcription of genes required for DNL, Srebp2 enhances the expression of genes involved in cholesterol synthesis and uptake [87].

Liver X receptors (LXRs), LXRα and LXRβ, are transcription factors that form heterodimers with RXRα and regulate cholesterol, phospholipid and fatty acid homeostasis [42], as well as inflammation [88]. While LXRα is highly expressed in liver, LXRβ is ubiquitously expressed [89]. Oxysterols and demosterol (cholesterol derivatives and precursors) are endogenous ligands of LXRs [90]. Activation of LXRα in liver promotes bile acid synthesis, reverse cholesterol transport from peripheric tissues to the liver, and DNL through the activation of Srebp1c, while it represses genes involved in gluconeogenesis [91].

Farnesoid X receptors (FXRs) also form heterodimers with RXRα and are highly expressed within the liver and the intestine. FXRs regulate bile acid (BA) synthesis, export, and the entero-hepatic circulation of BAs, their endogenous ligands. Bile acids activate a negative feedback loop, repressing BA synthesis. FXR activation reduces hepatic lipid content through decreased bile-acid dependent intestinal absorption and by repression of lipogenic genes [82].

2.4. Autophagy

The catabolic process of autophagy facilitates the lysosomal degradation of intracellular components and the recycling of the nutrient products. There are three major types of autophagy described to date. Microautophagy involves the formation of invaginations at membranes of the lysosome and late endosome and direct engulfment of cytoplasmic content destined for lysosomal degradation (Figure 2A) [92].

Chaperone mediated autophagy (CMA) degrades only proteins containing a specific CMA-targeting motif (KFERQ). This motif is recognized and bound by cytosolic chaperones such as the heat shock cognate protein of 70 kDa (hsc70) and the heat shock protein of 90 kDa (hsp90). These chaperones form complexes facilitating the binding of the substrate to monomeric LAMP2A. Subsequent LAMP2A oligomerization allows the formation of a translocation complex mediating the translocation of the target protein. Lysosomal hsc70 facilitates the disassembly of the translocation complex and the target protein is finally degraded within the lysosome (Figure 2B) [93].

The most prevalent form of autophagy is macroautophagy (hereafter referred to as autophagy), which sequesters cellular components within double-membraned vesicles called autophagosomes, which fuse with the lysosome for degradation. Autophagy is a multistep mechanism involving a wide range of proteins, facilitating the different steps of the process. Autophagy is initiated and

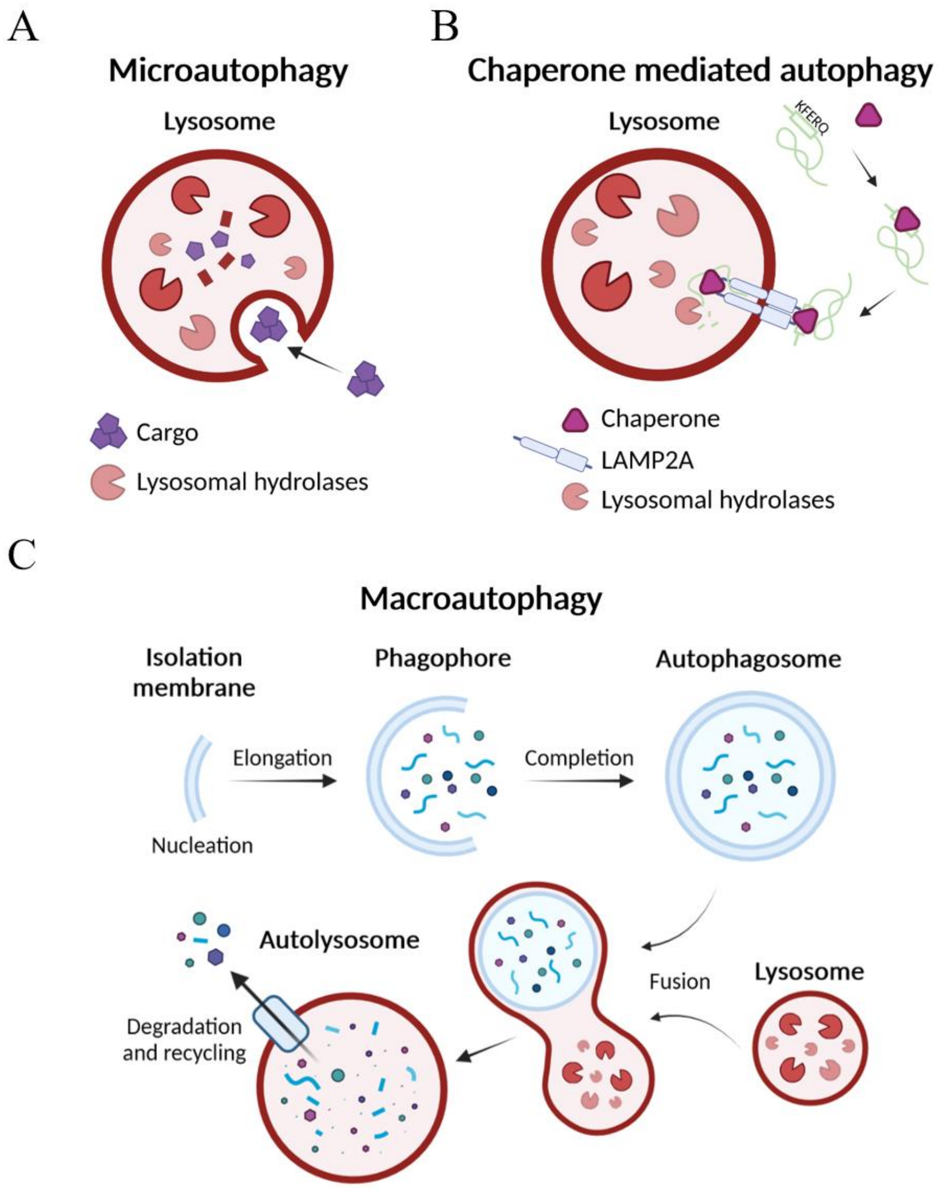
A
Microautophagy
Lysosome
Cargo
Lysosomal hydrolases
B
Chaperone mediated autophagy
Lysosome
KFERQ
Chaperone
LAMP2A
Lysosomal hydrolases
C
Macroautophagy
Isolation membrane
Phagophore
Autophagosome
Elongation
Completion
Nucleation
Autolysosome
Fusion
Lysosome
Degradation and recycling

Figure 2. Schematic models of the three major types of autophagy. (A) Microautophagy describes the direct engulfment of cargo through invaginations formed at membranes of the late endosomes and lysosomes. (B) Chaperone mediated autophagy (CMA) is the degradation of target proteins containing a motif consisting of five amino acids (KFERQ). This motif is recognized by chaperone protein complexes, which mediate the subsequential binding to the lysosomal membrane receptor protein (LAMP2A). Upon binding, LAMP2A oligomerizes, allowing the translocation of the target protein into the lysosomal lumen. The translocation complex (figure legend continues on the next page)

is disassembled by lysosomal chaperones and the target protein is degraded. (C) Macroautophagy (autophagy) is a multistep process involving nucleation (formation of the isolation membrane), its elongation to the phagophore, followed by completion to form the autophagosome. This double-membraned vesicles fuse with lysosomes for degradation of the autophagosome content by lysosomal acidic hydrolases. The degraded components are released from the lysosome for recycling.

nucleation gives rise to a double membrane structure, the isolation membrane. This membrane gets elongated and becomes the phagophore, which begins to gather cargo destined for degradation. The double-membraned autophagosome is completed, and fuses with the lysosome to allow the degradation of its content by acidic hydrolases (Figure 2C). The autophagic process is enabled by different ATG (autophagy related) proteins working in concert with additional proteins at every step during autophagy [92].

2.4.1.1. Initiation of autophagy and nucleation

Under nutrient-rich conditions, initiation of autophagy is repressed by active Mechanistic target of rapamycin kinase complex 1 (mTORC1) which inhibits ATG13 and Unc-51-like autophagy-activating kinase 1 (ULK1/ATG1) through phosphorylation, as well as ULK2. ATG13 and ULK1/2 are forming a protein complex, together with the Focal adhesion kinase interacting protein of 200kDa (FIP200/ATG17) and ATG101. This complex is referred to as the ULK complex (Figure 3A). Nutrient deprivation and rapamycin treatment causes the inactivation of mTORC1 and its dissociation from the ULK complex, allowing the autophosphorylation of ULK. Furthermore, AMP-activated protein kinase (AMPK) responds to decreasing ATP levels and activates ULK by phosphorylation. Together, this triggers the translocation of the complex to the sites of autophagosome formation [92, 94].

On the site of autophagosome formation, Beclin1 promotes the formation of a protein complex with Phosphatidylinositol-3-kinase catalytic subunit type 3 (Vps34/PIK3C3) and the phosphoinositide-3-kinase regulatory subunit 4

(Vps15/PIK3R4). This core-complex interacts with different cofactors including the activating molecule in Beclin1-regulated autophagy protein 1 (Ambra1), the nuclear receptor binding factor 2 (NRBF2), the UV radiation resistance associated gene (UVRAG) or ATG14L (Figure 3B). UVRAG and ATGL14L binding has been shown to be mutually exclusive. Beclin1 and ATG14L are phosphorylated and activated by ULK1. The Beclin1 containing complex facilitates the generation of phosphatidylinositol-3-phophate (PI3P) through its phosphatidylinositol-3-kinase activity. PI3P is enriched in the isolation membrane and facilitates the recruitment of further factors involved in phagophore formation [92, 95, 96]. The activity of the Beclin1-PI3K complex can be positively modulated by Endophilin B1 (Bif-1) [97] while the activity is impaired by inhibition of Beclin1 by Beclin2 or the RUN domain and cysteine-rich domain containing Beclin1-interacting protein (Rubicon) [98, 99].

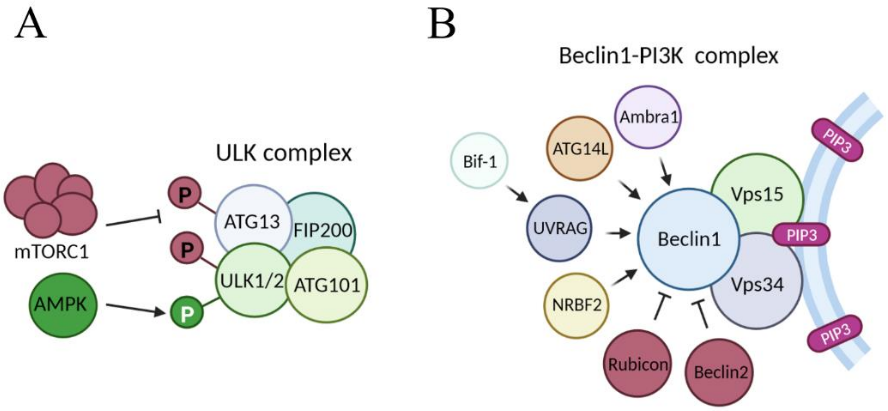

Figure 3. Schematic models of protein complexes involved in the initiation and nucleation of autophagy. (A) The ULK complex facilitates the initiation of autophagy and is regulated by mTORC1 and AMPK. (B) The Beclin1-PI3K complex is activated by the ULK complex and facilitates the nucleation steps of autophagy since the accumulation of phosphatidylinositol-3-phophate (PI3P) promotes autophagosome formation.

2.4.1.2. Elongation of the isolation membrane

The elongation of phagophores (Figure 4) involves the introduction of lipidated LC3 protein into the isolation membrane. First, the ATG4 protease

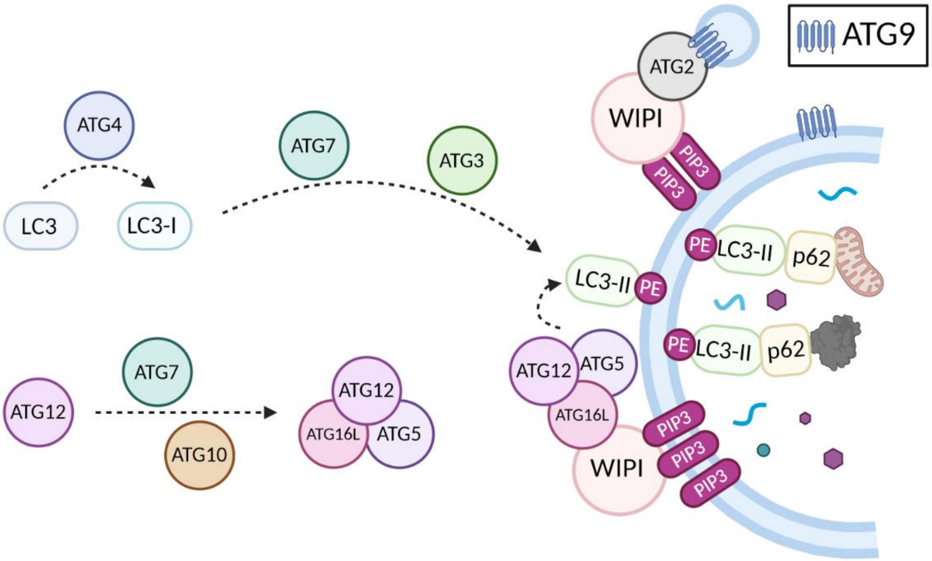

Figure 4. Schematic model of the elongation of the phagophore. LC3 is conjugated to phosphatidylethanolamine (PE) in a process involving ubiquitin-like conjugation enzymes. After cleavage by the protease ATG4, LC3-I is prepared for conjugation through ATG7 and ATG3. ATG12/5/16 complex formation is facilitated by ATG7 and ATG10. WIPI proteins are recruited by phosphatidylinositol-3-phophate (PI3P) within the phagophore membrane. The ATG12/5/16 complex binds to WIPI proteins and finally conjugates LC3-II to PE. Membrane bound LC3-II sequesters cargo destined for degradation through binding to cargo receptors such as p62, NRB1 and TP53INP2. The lipids required for the elongation of the phagophore membrane derive from ATG9 containing vesicles, which bind to the expanding initiation membrane in an WIPI/ATG2 dependent manner.

cleaves LC3 to its cytosolic form LC3-I [100]. Subsequently, ATG7 acts as an E1-like enzyme and ATG3 as an E2-like enzyme to prepare LC3-I to the conjugation to phosphatidylethanolamine (PE) by the ATG12/ATG5/ATG16L complex. The formation of this complex is essential for the elongation and is mediated by another ubiquitin-like conjugation system where ATG7 acts as an E1-like enzyme and ATG10 acts as an E2-like enzyme. The ATG12/ATG5/ATG16L complex subsequently acts as an E3-like enzyme to facilitate the conjugation of PE to ATG8 proteins such as LC3-I [92, 95]. Membranes enriched with PI3P through the activity of the Beclin1-PI3K complex, recruit proteins of the WD repeat domain phosphoinositide-interacting (WIPI) family, which is essential for the expansion of phagophores. WIPI proteins recruits ATG12/ATG5/ATG16L complexes, they associate with the exterior membrane of the phagophore and conjugate PE to LC3-II. In addition to the outer membrane, LC3-II is also found on the inner membrane of the phagophore, facilitating the recruitment of specific cargo to be sequestered into the developing autophagosome. This is facilitated through the binding to autophagy cargo receptors, such as Sequestosome 1 (SQSTM1/p62), neighbor of BRCA1 gene 1 (NBR1) as well as TP53INP2 [101-104].

The supply of lipids required for the elongation of the phagophore membrane is facilitated by ATG9, the only transmembrane ATG protein and is regulated by the ULK complex. ATG9 containing vesicles derive from the Golgi apparatus and the endoplasmic reticulum and become part of the isolation membrane and the outer autophagosomal membrane. In mammals, it is believed that WIPI proteins form a complex with ATG2 in order to bind ATG9 containing vesicles to facilitate phagophore elongation [105, 106].

2.4.1.3. Maturation of the autophagosome and fusion with the lysosome

The elongated phagophore finally is completed to become the mature autophagosome in a process involving the endosomal sorting complexes required for transport (ESCRT), consisting of the Vacuolar protein sorting-associated protein 37A (Vps37a), the Vacuolar protein sorting-associated protein 4 (VPS4), and the Component charged MVB protein 2A (CHMP2A) [107, 108]. Additionally, two transmembrane proteins are involved in this process, namely Transmembrane protein 41B (TMEM41B) and Vacuole membrane protein 1 (VMP1) [109-111], the latter is known as a direct binding partner of TP53INP2 [112].

Ultimately, autophagy culminates with the fusion of the mature autophagosome with the lysosome, forming the autolysosome . This allows the degradation of the cargo through lysosomal hydrolases. This step is mediated by a fusion machinery termed Soluble N-ethyl-maleimide-sensitive fusion protein (NSF) attachment protein receptors (SNARE), including the Vesicle-associated membrane protein 7 (VAMP7), VAMP8, the Synaptosomal-associated protein 29 (SNAP29), and Syntaxin-17 (STX17) [113, 114]. Furthermore, the efficient fusion of the autophagosome with the lysosome requires additional proteins such as the Lysosome-associated membrane protein 1 (LAMP1), LAMP2, and the Ras-related protein Rab-7 (RAB7) [95, 115-117].

2.4.2. Lipophagy

Autophagy can occur in a non-selective manner (bulk autophagy) or can be the very specific elimination of cellular components (selective autophagy) through receptor and adapter proteins [92]. Lipophagy has been described as a type of selective autophagy of lipid droplets (LDs) [118], however, the specific receptor proteins required for lipophagy have yet to be identified [95]. Lipophagy was first described in fasted livers but has been reported to take place in several cell types, under different metabolic states and has been reported to be impaired in non-alcoholic fatty liver disease patients [43, 118-120].

Current evidence suggests that all three types of autophagy, macro-, micro-, and chaperone mediated autophagy (CMA), are implicated in lipophagy. [118, 121, 122]. Additionally, cytosolic lipases are necessary for an efficient autophagic degradation of LDs [123] (Figure 5).

Although no lipids are degraded through CMA, it is involved in LD degradation. It has been shown that the LD surface proteins Perilipin 2 (PLIN2) and PLIN3 contain CMA-targeting motifs and are recognized by the chaperone protein hsc70, which delivers them to LAMP2A located on the surface of the lysosome. Subsequently, PLINs are unfolded, translocated into the lysosomal lumen and degraded. By covering the surface of LDs, PLINs prevent cytosolic lipases and proteins involved in phagophore formation from attaching to LDs, thus preventing their degradation. On the other hand, nutrient deprivation induces CMA-mediated PLIN2 degradation, permitting efficient LD degradation [121].

In response to lipolytic stimuli, cytosolic lipases such as Adipose triglyceride lipase (ATGL), Hormone sensitive lipase (HSL) and Monoglyceride lipase (MGL) associate with LDs and hydrolyze triacylglycerol (TG) to free fatty acids and glycerol [124]. ATGL, the lipase catalyzing the initial step of TG hydrolysis, was found to preferentially target large LDs, resulting in smaller sized LDs, which are the preferential substrates for lipophagy [125]. Moreover, ATGL and HSL possess multiple LIR motifs and have been shown to directly bind LC3. However, these lipases are not subjected to autophagic degradation, instead it has been shown that LC3 interaction is essential for ATGL/HSL activity and localization at the LD [78]. Interestingly, ATGL has been reported to induce Sirtuin 1 (SIRT1) activity. SIRT1 subsequently upregulates the expression of autophagic genes, including LC3, and promotes PPARα and PGC1α signaling, thus ATGL positively regulates autophagy/lipophagy, mitochondrial biogenesis and FA oxidation in an SIRT1-dependent manner [123].

Macrolipophagy was first observed in immortalized human hepatocytes and describes the selective uptake of LDs by autophagosomes. This process involves the recruitment of macroautophagy machinery proteins to the surface of triglyceride- or sterol ester-enriched LDs. Subsequently, an isolation membrane is formed, dependent on the joint action of LC3 and ATG7, followed by the engulfment of small LDs or fractions large lipid droplets. The LD containing autophagosome finally fuses with the lysosome, allowing the degradation of lipids by lysosomal lipases such as the lysosomal acid lipase (LAL) [118, 126] (Figure 5).

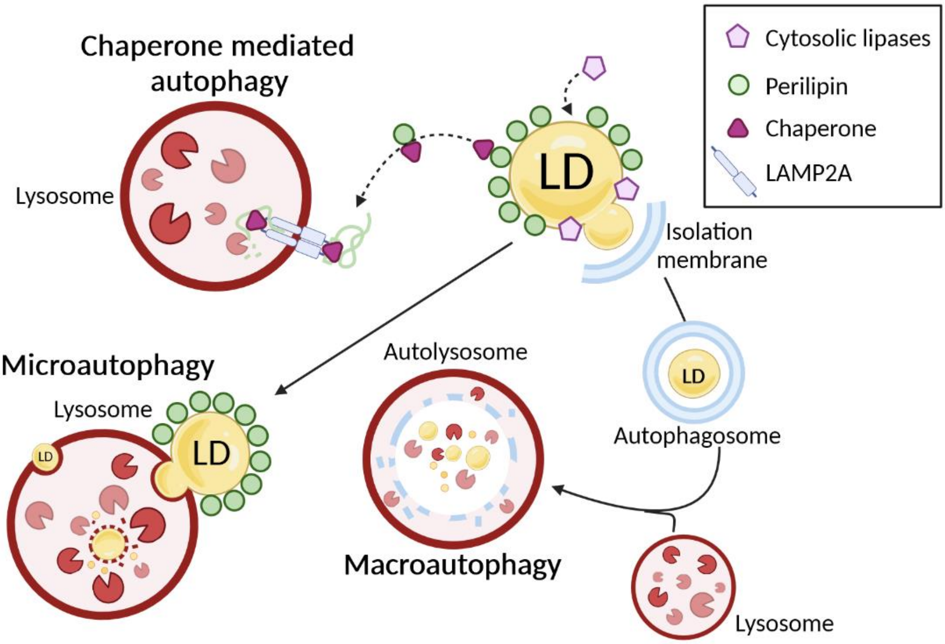
Chaperone mediated autophagy
Lysosome
Cytosolic lipases
Perilipin
Chaperone
LAMP2A
LD
Isolation membrane
Microautophagy
Lysosome
LD
LD
Autolysosome
LD
Autophagosome
Macroautophagy
Lysosome

Figure 5. Schematic model of processes involved in lipophagy. Lipid droplet (LD) resident surface proteins Perilipin 2 (PLIN2) and PLIN3 contain a CMA targeting-motif and are subjected to chaperone mediated autophagy. Removal of PLINs from the surface of LDs allows efficient TG hydrolysis through cytosolic lipases (ATGL, HSL, MGL) and the formation of isolation membranes and autophagosomes through components of the macroautophagy machinery. Small GTPases Rab7 and Rab10 promote the engulfment of small LDs or fractions of large LDs. LD containing autophagosomes subsequently fuse with lysosomes. Finally, LDs are degraded in the autolysosome. Microlipophagy is independent of the macroautophagic machinery and involves direct engulfment of small LDs or parts of large LDs.

Macrolipophagy has been reported to be regulated by various mechanisms. Two members of the Rab family of small GTPases (Rab7 and Rab10) are located on LDs upon nutrient deprivation and depletion of either protein causes the accumulation of LDs [127, 128]. The small GTPase Rab7, known for mediating autophagosomal maturation [115, 129], has been shown to facilitate the association of LDs with lysosomes and multivesicular bodies [127]. Rab 10 has been reported to form a complex with the membrane trafficking proteins EH domain-binding protein 1 (EHBP1) and EH domain-containing protein 2 (Ehd2). This complex mediates the elongation of autophagic membranes and complete engulfment of the LDs within autophagosomes[128]. Rab18 is another small GTPase located on the surface of LDs. In contrast to Rab7 and Rab10, Rab18 is involved in LD growth by tethering LDs to the endoplasmic reticulum in an SNARE and NRZ dependent manner [130]. Rab32 on the other hand, has been shown to negatively regulate ATGL expression, and represses lipolysis, however the mechanism is not known [131].

Additionally, lipophagy has been reported to be regulated by various transcription factors. The transcription factor EB (TFEB) is induced upon starvation and promotes autophagy by induction of LAL expression and LC3 expression [132]. Additionally, TFEB promotes PPARα and PPAR-gamma coactivator 1-alpha (PGC1α) activity [133]. The cAMP response element-binding protein (CREB) is induced my fasting, binds its coactivator CREB-regulated transcription coactivator 2 (CTRTC2/TORC2) and promotes lipophagy. In the fed-state, FXR is activated, disrupts the CREB/CTRTC2 complex and trans-represses its activity. FXR agonists were shown to inhibit lipophagy even in the fasted state [134]. Besides, activity of FXR is also reduced by PPARα activation [135]. Furthermore, overexpression of the transcription factor E3 (TFE3) was reported to result in reduced cellular lipid content and to prevent lipid accumulation in an lipophagy dependent manner through the activation of PGC1α [136]. Nutrient deprivation and metformin treatment activates forkhead homeobox type protein O1 (FoxO1) and promotes lipophagy, however this effect was only studied in adipocytes and the effects on other tissues were not assessed [137]. However, liver-specific FOXO1/3/4 triple knockout mice show enhanced lipid accumulation and an impaired autophagic flux, confirming the positive influence of Forkhead Box O Transcription Factors on lipophagy [138].

Furthermore, ubiquitination has been shown to be involved in lipophagy. The monotopic membrane protein Ancient ubiquitous protein 1 (AUP1) is found on endoplasmic reticulum and LD membranes. AUP1 on the LD surface gets ubiquitinated by the Ubiquitin-conjugating enzyme E2 G2 (Ube2g2), which induces the redistribution of LDs into clusters [139, 140]. Interestingly, a recent study of lipophagy in macrophages showed that cells, loaded with aggregated LDLs (agLDLs), showed enhanced autophagy, and recruitment of LC3, p62 and ubiquitin to the surface of LDs. LC3 on LDs was found in unconjugated and conjugated form, supporting the *in situ* lipidation of LC3-I to form LC3-II. Both single LDs and LD clusters were found in agLDL treated macrophages, directly interacted with lysosomes and increased in number upon autophagy inhibition. These results confirmed microlipophagy as an additional mechanism to degrade single LDs and LD clusters. An interesting study showed, that lipophagy can be activated upon overexpression of p62 containing a LD-binding domain from PLIN3, as p62 binds LC3 through its LIR-motif and gets recognized as an autophagic cargo. Overexpression of this fusion protein (forced lipophagy) in mouse embryos promoted LD clustering, suggesting that p62 on the LD surface is involved in LD clustering [141].

In contrast to macrolipophagy, microlipophagy is relatively poorly understood, as it was only recently demonstrated in 2020 by Schulze et al. [122, 142]. Microlipophagy is described as direct lysosomal engulfment and degradation of (multiple) small LDs or fractions of large LDs, through transient interactions between LDs and lysosomes (Figure 5). This process is independent of macroautophagy and has been shown to occur in hepatocytes. Furthermore, it has been shown that ATGL ablation blunts the uptake of lipids into lysosomes, due to its effect of decreasing the size of LDs. The activity of ATGL facilitates LD engulfment, since mammalian LDs are often larger than lysosomes [122, 143].

2.5. TP53INP2 – a positive regulator of autophagy

Tumor protein p53-inducible nuclear protein 2 (TP53INP2) was first identified in the laboratory of Dr. Antonio Zorzano by a screening of differentially expressed genes in the *gastrocnemius* muscle of healthy Wistar rats and obese Zucker rats, as well as Zucker diabetic rats. In both cases, the mRNA expression of TP53INP2 was significantly reduced compared to controls, thus leading to its initial name DOR (diabetes and obesity regulated gene) [Daniel Bach Gonzáles, PhD thesis, 2001][144]. Analysis of mRNA isolated from skeletal muscle biopsies (*vastus lateralis*) of control, type 2 diabetes mellitus (T2DM) and obese non-diabetic patients confirmed the reduction of TP53INP2 expression under these conditions in humans, but not in type 1 diabetes mellitus (T1DM) patients. Interestingly, the expression of TP53INP2 in skeletal muscle increased in response to insulin T1DM patients, but not in obese and T2DM patients [Daniel Bach Gonzáles, PhD thesis, 2001].

The human TP53INP2 gene is 9 kb long, located on chromosome 20q11.2, consists of 5 exons [145] and encodes for a protein containing 220 amino acid residues. It shares 84% identity with murine TP53INP2 protein, consisting of 221 amino acid residues. Tumor protein p53-inducible nuclear protein 1 (TP53INP1/SIP) is the only known human homologous protein of TP53INP2 originated from gene duplication [146] and shares only 36% identity with TP53INP2 [144].

Analysis of the murine TP53INP2 protein (Figure 6), revealed two well conserved regions of 15 and 45 amino acid residues, respectively. Although relatively short, region 1 contains a LC3 Interacting Region (LIR), allowing the binding to ATG8 protein family members such as LC3 and GABARAP [146], which is overlapping with a Nuclear Export Signal (NES), important for the nucleocytoplasmic shuttling. The second conserved region of TP53INP2 contains an Ubiquitin Interacting Motif (UIM) and a region forming an alpha-helix, the only known secondary structure, while the rest of the protein is considered disordered [144, 146-148]. Closer to the N-terminal part of TP53INP2 lies a Nuclear Localization Signal (NLS) [Caroline Mauvezin, PhD thesis, 2011], within a Nucleolar Localization Signal (NoLS) [149]. Furthermore, the N-terminal part contains a TRAF6 Interacting motif (TIM) [148].

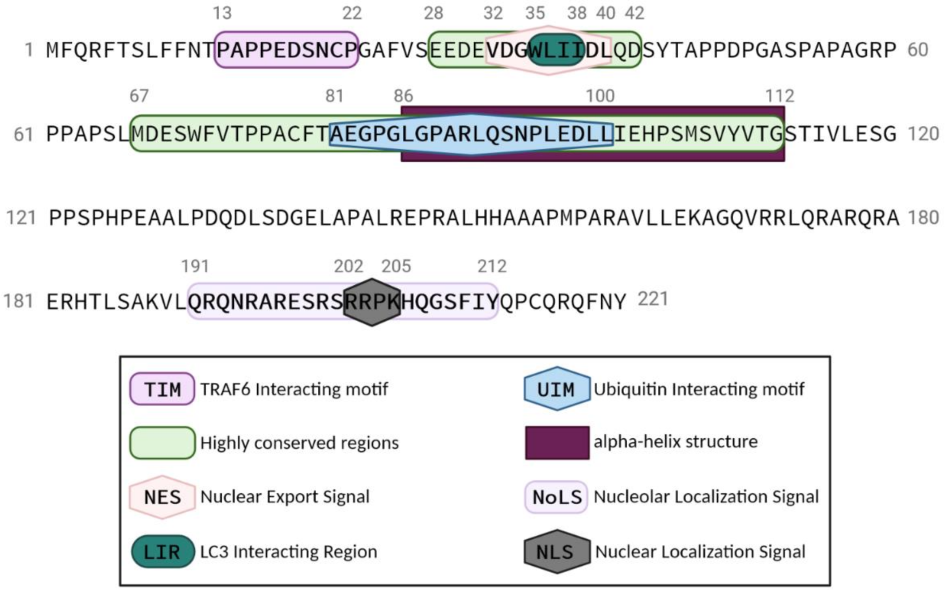
13 22 28 32 35 38 40 42
1 MFQRFTSLFFNTPAPPEDSNCPGAFVSEEDEVDGWLIIDLQDSYTAPPDPGASPAPAGRP 60
67 81 86 100 112
61 PPAPSLMDESWFVTPPACFTAEGPGLGPARLQSNPLEDLLIEHPSMSVYVTGSTIVLESG 120
121 PPSPHPEAALPDQDLSDGELAPALREPRALHHAAAPMPARAVLLEKAGQVRRLQRARQRA 180
191 202 205 212
181 ERHTLSAKVLQRQNRARESRSRRPKHQGSFIYQPCQRQFNY 221
TIM TRAF6 Interacting motif
UIM Ubiquitin Interacting motif
Highly conserved regions
alpha-helix structure
NES Nuclear Export Signal
NoLS Nucleolar Localization Signal
LIR LC3 Interacting Region
NLS Nuclear Localization Signal

Figure 6. Sequence of murine TP53INP2 protein including highlighted known motifs. [Figure adapted from Caroline Mauvezin, PhD thesis, 2011].

One of the best understood physiological roles of TP53INP2 is its function as a positive regulator of autophagy. Several studies have demonstrated direct interactions between TP53INP2 and autophagic proteins such as Vacuole membrane protein 1 (VMP1), and members of the ATG8 family including Gamma-aminobutyric acid receptor-associated protein (GABARAP), Gabarap-like 1 (GABARAPL1), GABARAPL2 (GATE-16), as well as the Microtubule-associated proteins 1A/1B light chain 3A (LC3A), LC3B and LC3C. These interactions have been shown to promote the formation of autophagosomes [112, 146, 150]. TP53INP2 protein was found to translocate between the nucleus and the cytosol under basal conditions, with the majority of TP53INP2 protein residing in the nucleus, localized in promyelocytic leukemia (PML) nuclear bodies. Upon induction of autophagy, for instance by rapamycin treatment or amino-acid starvation, TP53INP2 translocates to the cytoplasm [112, 144, 147, 150]. Furthermore, it has been reported that under nutrient-rich conditions, LC3 is located in the nucleus and cytosol in an acetylated form. Nutrient deprivation induces deacetylation of LC3 by the nuclear deacetylase SIRT1, allowing the interaction of LC3 with TP53INP2, in order to be transported to the cytoplasm [151]. In the cytoplasm, LC3 and other ATG8 protein members are conjugated to phosphatidylethanolamine (PE) in a process involving ATG7 and other ATG proteins. This allows their incorporation into double membrane structures and association with the autophagosomal membrane [152, 153]. Cytosolic TP53INP2 was found to act as a scaffold, facilitating the interaction of LC3 and ATG7, promoting autophagosome biogenesis [154]. Furthermore, TP53INP2 was reported to bind ubiquitin [155] and subsequently, a ubiquitin interacting motif (UIM) was detected in the sequence of TP53INP2 [148]. This UIM motif enables TP53INP2 to facilitate the degradation of ubiquitinated substrates by autophagy [104, 155].

2.5.1. TP53INP2 acts as a coactivator of the transcriptional activity of nuclear hormone receptors

Several studies have shown the availability of TP53INP2 to enhance the transcriptional activity of nuclear hormone receptors [144, 146, 156]. TP53INP2 was found to directly interact with thyroid hormone receptor α (TRα1) and enhance its transcriptional activity [144]. Assays performed in HeLa and HEK293 cells, performed to analyze the co-activation of different nuclear receptors, have shown that TP53INP2 coactivates the transcription of Peroxisome proliferator-activated receptor gamma (PPARγ), glucocorticoid receptor (GR), vitamin D receptor (VDR) and TRα1 upon their respective overexpression and simultaneous treatment with their ligand. The transcriptional activation of mentioned nuclear hormone receptors was specific, since TP53INP2 failed to induce the reporter activity of the transcription factors p53 and c-Myc, excluding a role of TP53INP2 as a general enhancer of transcription factors [146]. The ability of TP53INP2 to enhance transcriptional activation was also described for its homologue dDOR in *drosophila melanogaster*, which is able to bind and coactivate the ecdysone receptor (EcR) [156].

2.5.2. TP53INP2 promotes death receptor induced apoptosis

Programmed cell death, or apoptosis, is a process involved in development and is important for tissue homeostasis and maintaining of cell numbers, but can also be activated as a response to stress [157]. Apoptosis can be triggered by intrinsic defects, such as mutations, or through the extrinsic (receptor) pathway, for instance induced by anticancer chemotherapy [158]. TP53INP2 has been found to positively regulate death receptor-induced apoptosis. When death receptor signaling is stimulated by death ligands such as TRAIL or FasL, caspase-8 is activated, and cell death is executed by subsequent cleavage of caspase-3 or Bcl-2 homology domain 3 (BH3) protein, depending on the cell type. Caspase-8 is only fully activated upon its polyubiquitination by E3 ubiquitin ligases such as cullin-3 or TRAF6. TP53INP2 was found to bind to TRAF6 to via its N-terminal TRAF6 Interacting Motif (TIM). On the other hand, TP53INP2 is able to bind already ubiquitinated caspase-8 by its Ubiquitin Interacting motif (UIM) but was also found to bind non-ubiquitinated caspase-8. By acting as a scaffold, TP53INP2 brings caspase-8 into proximity of its E3 ubiquitin ligase, thereby promoting polyubiquitination and full activation of caspase-8. Thus, TP53INP2 expression could potentially be utilized as a biomarker to predict efficiency or TRAIL cancer treatment [148].

2.5.3. TP53INP2 mediates ribosome biogenesis

The C-terminus of TP53INP2 contains a nucleolar localization signal (NoLS), in addition to its nuclear localization signal (NLS). It was shown that nucleolar localization of TP53INP2 is essential to preserve ribosomal DNA (rDNA) promoter activity and rDNA transcription. Chromatin immuno-precipitation (ChIP) assays were used to confirm direct interactions of TP53INP2 with promoter-, coding-, and untranscribed regions of rDNA. Additionally, it was found that nucleolar TP53INP2 directly interacts with and is required for the efficient assembly of the POLR1/RNA polymerase preinitiation complex (PIC) at the rDNA promoter, thus mediates the biogenesis or ribosomes [149].

2.5.4. Tissue-specific physiological roles of TP53INP2

TP53INP2 mRNA is expressed in several tissues of mice at variable levels, with the highest expression in the skeletal muscle (Figure 7) [David Sala Cano, PhD thesis, 2013]. Skeletal muscle specific loss- and gain-of-function models of TP53INP2 allowed the identification of its function as a regulator of muscle mass. While the overexpression of TP53INP2 significantly reduced muscle mass in mice, the ablation of TP53INP2 resulted in muscle hypertrophy. When diabetes was induced by streptozotocin injections, TP53INP2-transgenic mice showed enhanced muscle loss compared to controls, while muscle-specific TP53INP2-ablation ameliorated the loss of muscle weight. Simultaneous injection of chloroquine, an autophagy inhibitor, allowed the observation that the enhanced loss in muscle mass upon TP53INP2 overexpression is autophagy-dependent [155].

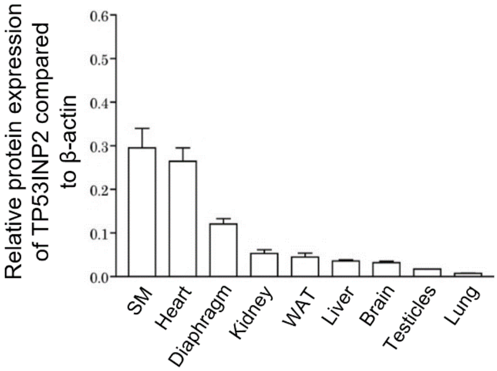

Figure 7. Relative mRNA expression of TP53INP2 in various mouse tissues. (SM = skeletal muscle, gastrocnemius; WAT = white adipose tissue). Data represent mean ± SEM (n = 3). [Figure from David Sala Cano, PhD thesis, 2013]

TP53INP2 expression was found to be reduced in the adipose tissue of obese subjects. In the same study, an inducible global TP53INP2 knockout model was generated, which demonstrated the expansion of subcutaneous white adipose tissue depots and obesity upon TP53INP2-depletion. The complex mechanism of induced adipogenesis upon TP53INP2 ablation was shown to involve enhanced levels of the transcriptional regulator β-catenin, known for the inhibition of adipogenesis by preventing peroxisome proliferator-activated receptor-γ (PPAR-γ) and CCAAT/enhancer-binding protein-α (C/EBP-α) activation [159]. Proteasomal degradation of β-catenin depends on its phosphorylation by glycogen synthase kinase 3β (GSK3β) [160, 161]. TP53INP2 was shown to sequester GSK3β into late endosomes in an autophagy dependent matter, resulting in enhanced β-catenin levels. On the other hand, TP53INP2-ablation reduced β-catenin levels which enabled enhanced adipogenesis [159]. This shows that even in tissues with relative low expression of TP53INP2 (Figure 7), its ablation can induce severe effects.

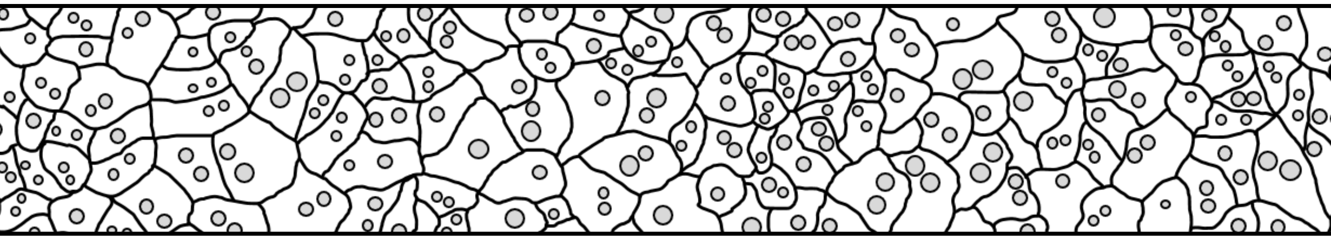

OBJECTIVES

3. OBJECTIVES

The TP53INP2 protein is known as a positive regulator of autophagy and is expressed in several metabolically active tissues. Previous studies in tissue-specific loss-of-function and gain-of-function models show that TP53INP2 impacts metabolism. Skeletal muscle specific ablation of TP53INP2 resulted in muscle hypertrophy, while TP53INP2 overexpression decreased muscle mass, showing the relevance of TP53INP2 as a regulator of muscle mass in muscle. In addition, studies using an inducible model of a global TP53INP2 knockout showed that the ablation of TP53INP2 enhances adiposity. TP53INP2 has also been shown to be expressed in the liver, however its physiological role is unclear. The purpose of this PhD thesis was to unravel the role of TP53INP2 in liver metabolism. In order to achieve this aim, the following specific objectives have been pursued:

1. To evaluate the impact of nutrient ablation and abundance on hepatic TP53INP2 expression.
2. To characterize the metabolic impact of TP53INP2-ablation in liver under different conditions such as fasting, and in the presence of high amounts of dietary derived lipids in form of a high-fat diet and a western diet.
3. To explore mechanisms responsible for the metabolic alterations associated with the hepatocyte-specific TP53INP2-ablation.

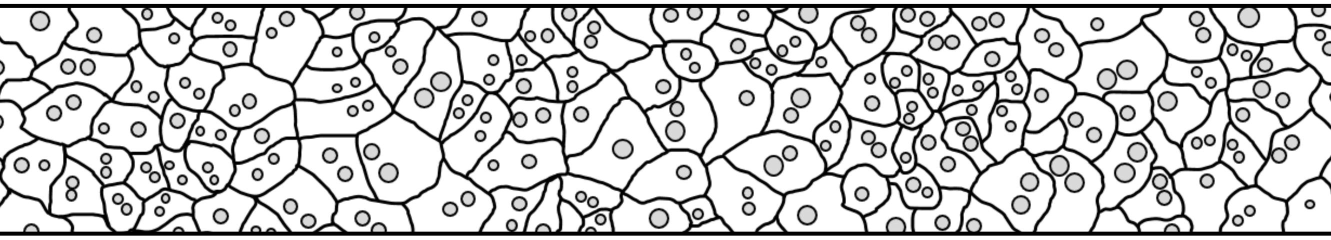

RESULTS

4. RESULTS

4.1. Nutritional manipulation impacts hepatic expression of TP53INP2

4.1.1. Evaluation of the impact of fasting on TP53INP2 expression

In order to evaluate if nutrient status affects TP53INP2 expression in liver, male loxP control animals (with an C57BL/6J genetic background) were subjected to an overnight fasting of 16 h. Fasted mice showed increased TP53INP2 mRNA levels in livers (Figure 8A). On the other hand, protein levels of TP53INP2 in 16 h fasted mice were diminished (Figure 8B). To determine if the effect of starvation can be reproduced in vitro, primary hepatocytes from different loxP control animals were isolated and cultured overnight (16 h) with complete media containing fetal bovine serum (FBS), or with Earle's Balanced Salt Solution (EBSS). Starvation of hepatocytes with EBSS elevated TP53INP2 mRNA levels (Figure 8C). Primary hepatocytes also responded to starvation with decreased protein levels of TP53INP2 (Figure 8D).

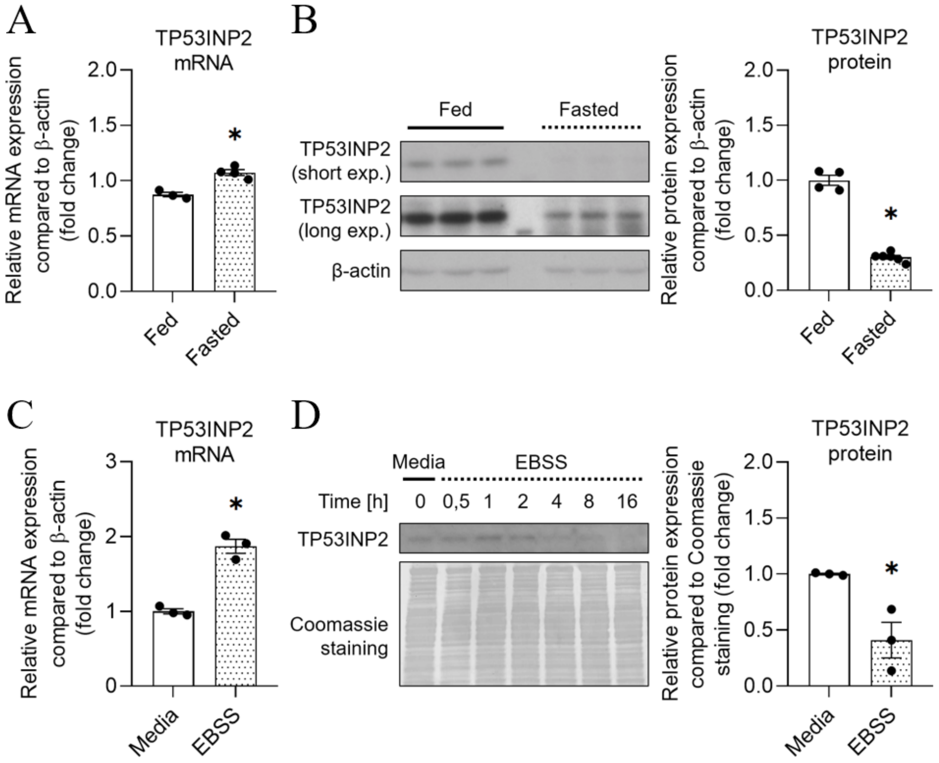

Figure 8. Overnight fasting upregulates mRNA and depletes protein levels of TP53INP2 in livers and isolated primary hepatocytes. (A) Hepatic TP53INP2 mRNA levels analyzed in livers of fed (*ad libitum*) and 16 h fasted loxP control mice with an C57BL/6J genetic background at the age of 24 weeks (n = 3 - 4). (B) Representative western blot and quantification of TP53INP2 protein levels in liver (n = 4 - 6). (C) TP53INP2 mRNA levels in isolated primary hepatocytes of loxP mice treated with culture media or EBSS starvation buffer overnight for 16 h. (n = 3). (D) Representative western blot of TP53INP2 protein levels in primary hepatocytes and quantification of protein levels in cells cultured in media or 16 h of EBSS buffer (n = 3). Data represent mean ± SEM. P-values < 0.05 were considered significant (*****).

4.1.2. High-fat diet treatment causes a transient upregulation of TP53INP2 expression in liver

To analyze the expression of hepatic TP53INP2 in the presence of abundant nutrients, male loxP control mice were subjected to a high-fat diet (HFD; D12492i, Research Diets) for periods of 8 or 16 weeks. A short HFD treatment of 8 weeks caused an upregulation of TP53INP2 mRNA (Figure 9A) and protein levels (Figure 9D) in livers. This upregulation was reversed by prolonging the HFD treatment to 16 weeks, as TP53INP2 mRNA returned to basal levels (Figure 9B). The decline in TP53INP2 mRNA by prolonged HFD treatment was not due to the higher age of the animals, as levels did not decline with aging (Figure 9C).

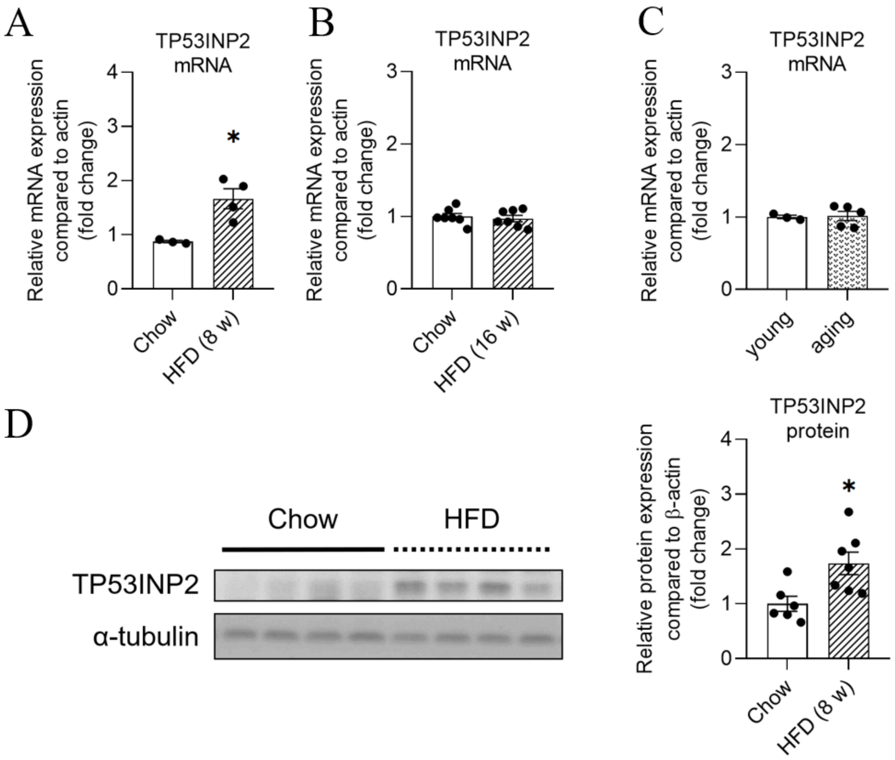

Figure 9. High-fat diet treatment transiently alters hepatic TP53INP2 levels. (A) TP53INP2 mRNA levels in livers of 16-week-old loxP control animals on standard chow diet or after 8 weeks of HFD treatment (n = 3 - 4). (B) Hepatic TP53INP2 mRNA levels in 24-week-old loxP animals on chow diet or subjected to 16 weeks of HFD (n = 7). (C) Gene expression of TP53INP2 mRNA levels of young (24-week-old) and old (2-year-old) loxP animals on chow diet (n = 3 - 5). (D) Representative western blot and quantification of hepatic TP53INP2 protein levels in loxP animals on chow diet and after an 8-week HFD-treatment (n = 6 - 7). Data represent mean ± SEM. P values < 0.05 were considered significant (*).

4.1.3. TP53INP2 protein is depleted in a mouse model of non-alcoholic steatohepatitis

In order to evaluate hepatic levels of TP53INP2 in a model of non-alcoholic steatohepatitis (NASH), C57BL6/J mice were subjected to a methionine and choline-deficient diet (MCD; A06071305, Research diets) for a period of three weeks. The diet was supplemented with 45 kcal% fat and the drinking water with 0.1 % L-methionine in order to prevent weight loss. This treatment elevated liver triglycerides and provoked inflammation and fibrosis of livers [162]. Hepatic levels of TP53INP2 protein were reduced under NASH conditions (Figure 10).

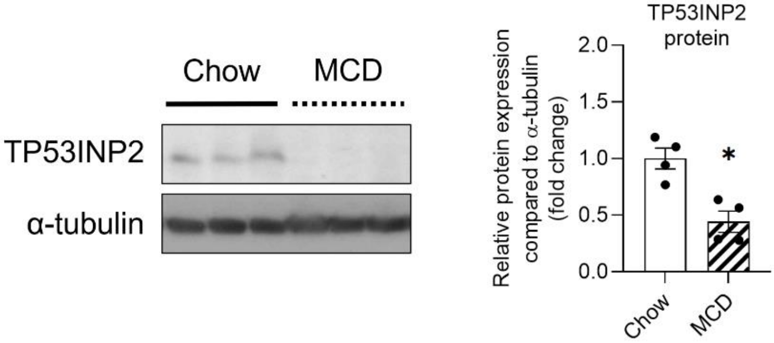

Figure 10. Hepatic TP53INP2 protein levels are depleted in a mouse model of non-alcoholic steatohepatitis. Representative western blot and quantification of TP53INP2 protein levels in mouse livers of 11-week-old C57BL6/J mice on chow diet or after 3 weeks of MCD diet (n = 4). Data represent mean ± SEM. A p-value < 0.05 was considered significant (*).

4.2. Evaluation of the metabolic impacts caused by TP53INP2 loss-of-function in liver

4.2.1. Validation of the hepatocyte-specific TP53INP2 knockout mouse model

The generation of the liver-specific TP53INP2 knockout (LKO) mouse model was performed by Dr. Saška Ivanova [148] by crossing homozygous TP53INP2$^{loxP/loxP}$ mice (loxP) [155] with a mouse strain expressing Cre recombinase specifically in hepatocytes under the albumin promoter. LKO mice showed significantly reduced TP53INP2 mRNA (Figure 11A) and protein levels (Figure 11BC) in livers, while TP53INP2 expression in other tissues was not affected (Figure 11D). Male mice were used as experimental animals and fed with standard diet (Chow, RM1, Special Diet Services), unless stated otherwise.

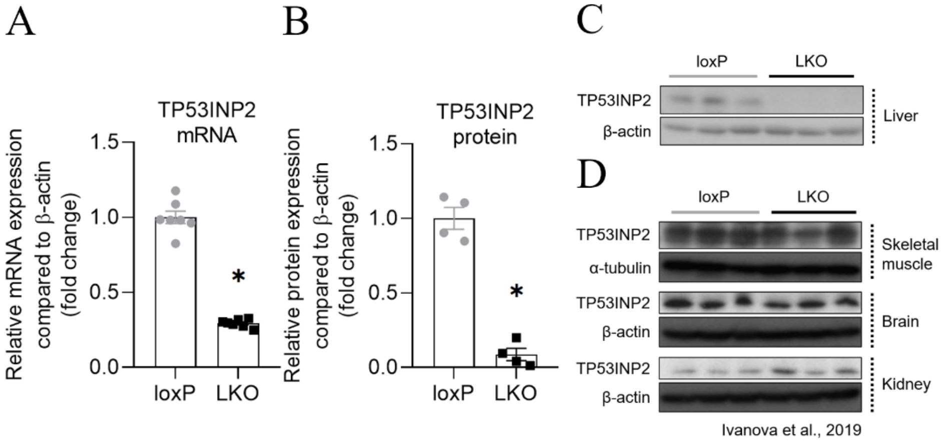

Ivanova et al., 2019

Figure 11. Liver-specific knockout of TP53INP2 markedly reduced TP53INP2 levels in livers. (A) Quantification of hepatic TP53INP2 mRNA levels in loxP and LKO mice (n = 7). (B) Quantification of TP53INP2 protein levels in livers of loxP and LKO mice (n = 4). (C) Representative western blot of hepatic TP53INP2 protein of loxP and LKO animals. (D) Representative western blots of TP53INP2 protein levels in non-hepatic tissues [148]. Data represent mean ± SEM. P-values < 0.05 were considered significant (*).

4.2.2. Characterization of TP53INP2-LKO animals on standard diet

4.2.2.1. Adult TP53INP2-LKO mice show normal body weight but accumulate less fat mass during aging.

Male adult TP53INP2-LKO and control mice were analyzed at 24 weeks of age and showed no differences in body weight (Figure 12A) or fat and lean mass distribution analyzed using EchoMRI (Figure 12B). Liver weight (Figure 12C) as well as the weight of non-hepatic tissues (Figure 12D) were similar in both genotypes.

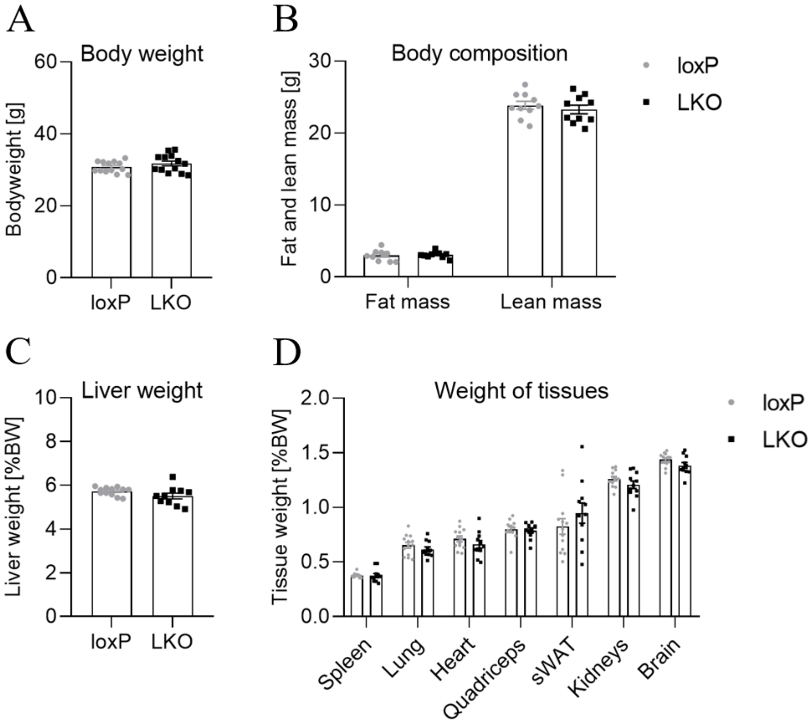

Figure 12. Body weight, body composition and weight of tissues are similar in control and TP53INP2-LKO mice in young adult mice. (A) Body weight of 24-week-old adult loxP and TP53INP2-LKO mice (n =9 - 13). (B) Body composition divided into fat and lean mass analyzed by EchoMRI (n = 10). (C) Liver weight of 24-week-old loxP and TP53INP2-LKO animals (n =10 - 12). (D) Weight of various non-hepatic tissues of control and LKO animals on standard-diet (n = 11 - 13). Data represent mean ± SEM. There was no statistical significance between genotypes.

To evaluate if TP53INP2 protein affects body weight during aging, we analyzed one-year-old animals. While loxP animals showed a significant increase in body weight during aging, the body weight of 12-month-old TP53INP2-LKO animals stayed similar to 4-month-old mice (Figure 13A). EchoMRI analysis of mice revealed that TP53INP2-depletion prevented fat mass accumulation during aging (Figure 13B). The liver weight was not affected in one-year-old TP53INP2-LKO mice (Figure 13C).

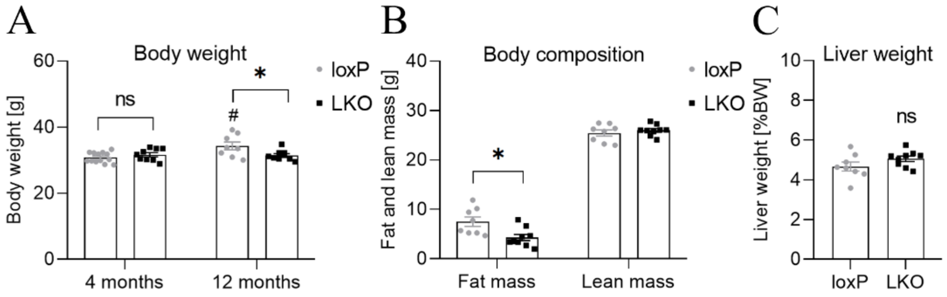

Figure 13. Twelve-month-old TP53INP2-LKO mice show lower body weight compared to control mice due to less fat accumulation. (A) Bodyweight of young (4 months) and older (12 months) male mice (n = 9 - 13). (B) Fat and lean mass distribution of one-year-old mice analyzed by EchoMRI (n = 8 - 9). (C) Liver weight of one-year-old animals (n = 8 - 9). Data represent mean ± SEM. P-values < 0.05 were considered significant (*****) for loxP vs. LKO and (#) for 4 months vs. 12 months.

The hepatic lipid content of 12-month-old animals was evaluated and was increased compared to 4-month-old animals. An aging period of one year elevated the triglyceride (Figure 14A) and cholesterol (Figure 14B) content of livers compared to 4-month-old adult mice, without differences between the genotypes.

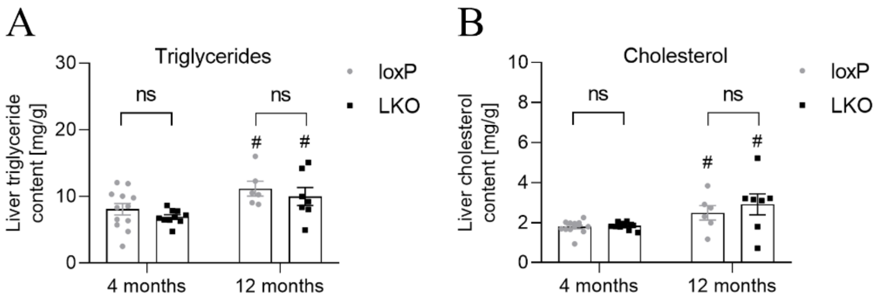

Figure 14. Aging causes a similar increase of hepatic triglyceride and cholesterol content in loxP and TP53INP2-LKO mice. Hepatic triglyceride (A) and cholesterol (B) levels of young (4 months) and older (12 months) mice (n = 6 - 13). Data represent mean ± SEM. P-values < 0.05 were considered significant (#) for 4 months vs. 12 months. There was no statistical significance between genotypes.

To evaluate potential liver damage, we analyzed the levels of alanine aminotransferase (ALT) and aspartate aminotransferase (AST), two enzymes that indicate liver injury when their plasma levels increase [163]. Although 12-month-old TP53INP2-LKO animals showed higher ALT levels than controls (Figure 15A), levels were significantly lower compared to younger animals, suggesting that livers were not damaged. This was corroborated by normal levels of AST in young and older mice (Figure 15B).

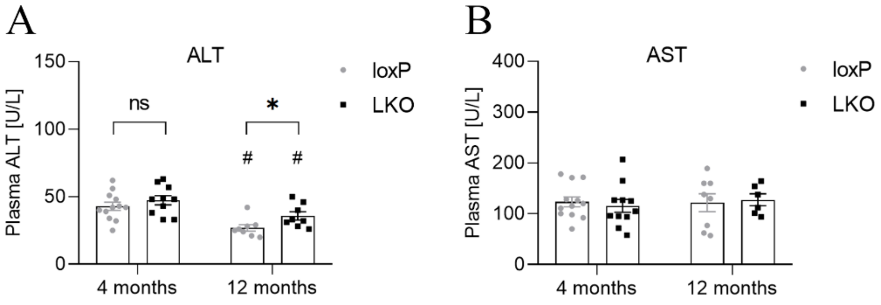

Figure 15. One-year-old TP53INP2-LKO mice show higher alanine aminotransferase levels than controls. Plasma alanine aminotransferase (A) and aspartate aminotransferase (B) levels of young (4 months) and older (12 months) animals (n = 8 - 12). Data represent mean ± SEM. P-values < 0.05 were considered significant (*) for loxP vs. LKO and (#) for 4 months vs. 12 months.

4.2.2.2. TP53INP2-depletion impairs autophagy in livers

Since the ablation of TP53INP2 protein impairs autophagy in skeletal muscle [155] and white adipose tissue [159], we analyzed if this is also the case in livers. Autophagy markers were analyzed in livers of 48 h fasted animals (Figure 16), where autophagy is strongly activated [164]. Although fasting decreased hepatic TP53INP2 levels (Figure 8), TP53INP2 protein was still expressed in loxP control mice (Figure 16B). While p62 protein levels were similar in loxP and LKO livers, there was an accumulation of LC3-I, the free mature form of LC3 protein [164]. LC3-II is the lipidated form of LC3, after the conjugation to phosphatidylethanolamine, a post-translational modification essential for efficient autophagy [165]. Reduced levels of LC3-II (Figure 16C) in TP53INP2-depleted livers showed impaired capability for LC3 lipidation.

Additionally, we analyzed the autophagic flux in isolated primary hepatocytes by treating them with a potent inhibitor of autophagy. Bafilomycin A1 (BafA1) prevents the fusion of autophagosomes and lysosomes and suppresses the acidification of the autolysosome [166]. Protein levels of autophagic markers were analyzed in BafA1 and vehicle treated primary hepatocytes (Figure 17). We found that TP53INP2-depleted hepatocytes accumulated less LC3-II protein upon autophagy inhibition, suggesting an impaired autophagic flux. There was also a tendency to accumulate less p62 protein.

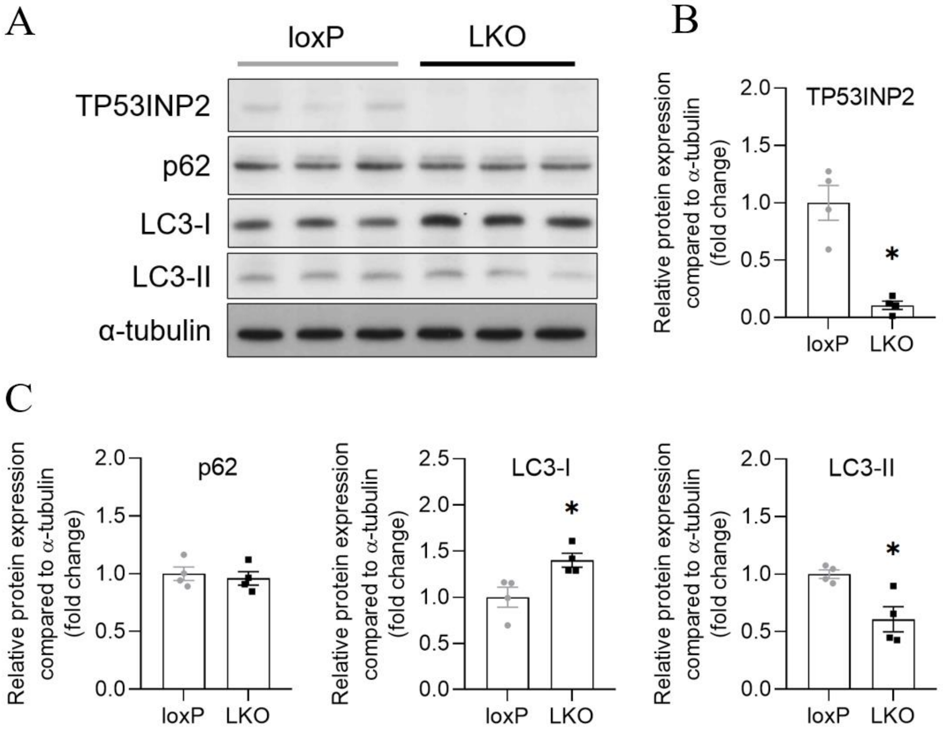

Figure 16. TP53INP2-depleted livers show impaired lipidation of LC3 protein when autophagy is activated by fasting. (A) Representative western blot of fasted livers (B) Quantification of TP53INP2 levels in fasted livers (n = 4). (C) Quantification of autophagic marker proteins p62 and LC3 in fasted livers (n = 4). Data represent mean ± SEM. P-values < 0.05 were considered significant (*****) for loxP vs. LKO.

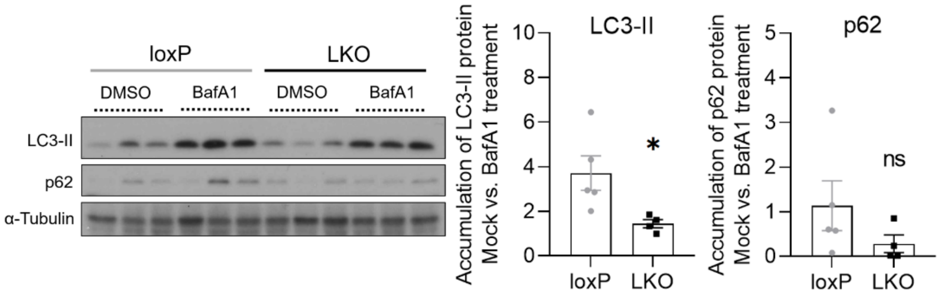

Figure 17. Primary hepatocytes isolated from TP53INP2-LKO animals show an impaired autophagic flux. Representative western blot and quantification of the accumulation of the autophagic marker proteins LC3 II and p62 upon Bafilomycin A1 (BafA1) treatment in isolated primary hepatocytes (n = 4 - 5). Data represent mean ± SEM. P-values < 0.05 were considered significant (*) for loxP vs. LKO.

4.2.2.3. TP53INP2-LKO animals show impaired lipid oxidation and ketogenesis upon fasting

In order to evaluate the impact of nutrient deprivation in TP53INP2-depletion animals were subjected to fasting. The body weight was reduced in all animals after an overnight fast of 16 h (Figure 18A), and the weight loss was similar in both genotypes (Figure 18B).

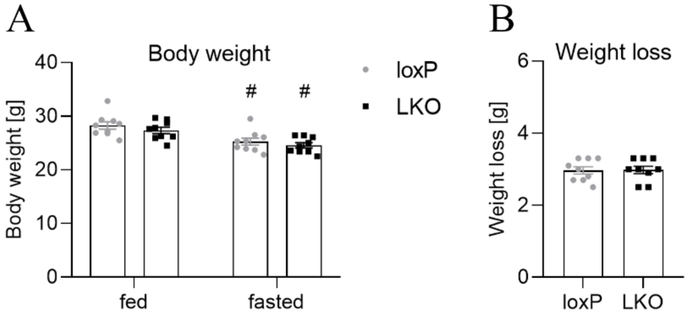

Figure 18. Overnight fasting provokes a similar weight loss in control and TP53INP2-LKO animals. (A) Body weight of fed and overnight fasted animals (n = 9). (B) Weight loss induced by an overnight fast of 16 hours (n = 9). Data represent mean ± SEM. P-values < 0.05 were considered significant (#) for fed vs. fasted. There was no statistical significance between genotypes.

Blood glucose levels in overnight fasted TP53INP2-LKO mice were similar to control animals (Figure 19A) at 4 months of age. To evaluate the handling of glucose during aging, a glucose tolerance test (GTT) was performed in one-year-old animals. Blood glucose levels followed the same trend after peritoneal injection of glucose in both genotypes (Figure 19B).

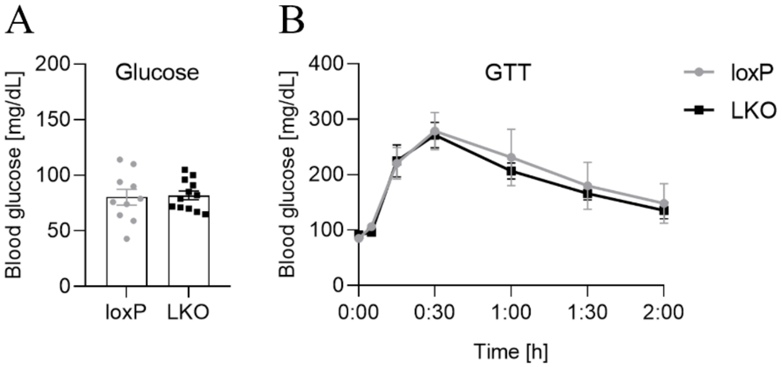

Figure 19. TP53INP2-LKO animals show normal glucose handling. (A) Fasting blood glucose levels of 4-month-old animals (n = 10 - 12). (B) Blood glucose levels during a glucose tolerance test (GTT) performed in one-year-old animals after an overnight fast (n = 5). Blood samples were collected at baseline and after peritoneal injection of a 2 g / kg bodyweight glucose bolus. Data represent mean ± SEM. There was no statistical significance between genotypes.

To evaluate postprandial metabolism in TP53INP2-LKO animals, food intake was synchronized. One hour into the light cycle, diet was removed for a short period of two hours, followed by a re-feeding of the animals. After an hour, blood samples (fed conditions) were collected by tail vein, and diet was removed to initiate a short fasting. After four hours, fasted blood samples were collected. We found slightly elevated blood glucose levels (Figure 20A) after the short fasting period. Additionally, TP53INP2-LKO animals failed to reduce plasma triglyceride (Figure 20B) levels after 4 hours of fasting. Furthermore, non-esterified free fatty acids (NEFAs) levels were increased in TP53INP2-LKO animals (Figure 20C) after a four hour fast, suggesting impaired hepatic β-oxidation [167]. Plasma cholesterol levels were not impacted by a short fast (Figure 20D).

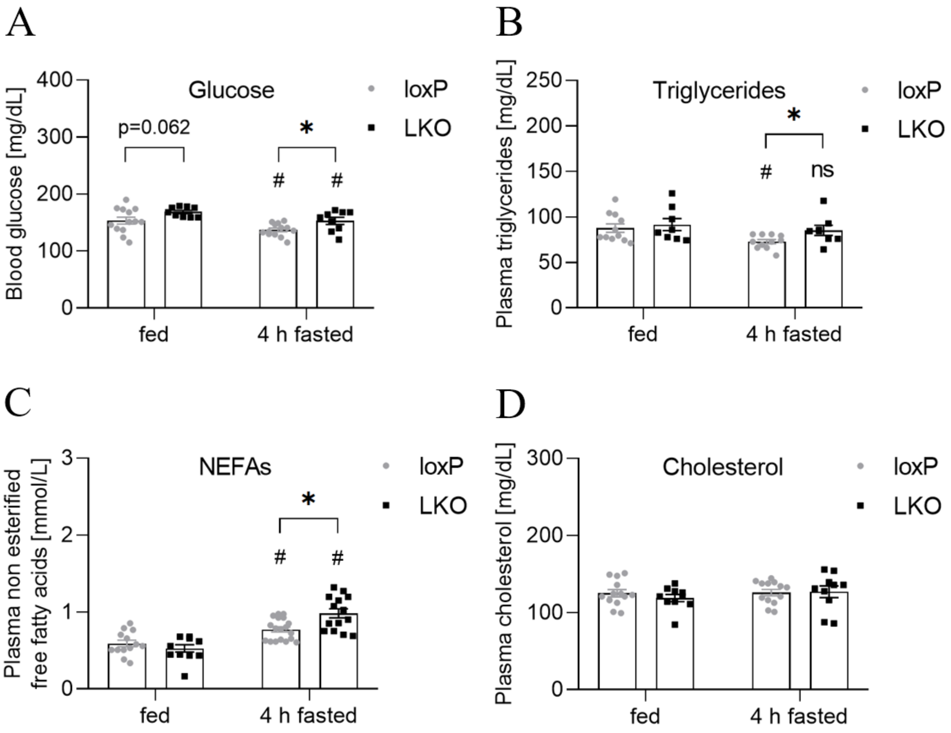

Figure 20. A short fast reveals impaired lipid oxidation in TP53INP2-LKO animals. (A) Blood glucose levels of fed and 4 h fasted animals (n = 9 - 13). Plasma (B) triglyceride, (C) non-esterified free fatty acids (NEFAs) and (D) cholesterol levels of fed and 4 h fasted animals (n = 8 - 18). Data represent mean ± SEM. P-values < 0.05 were considered significant (*****) for loxP vs. LKO and (#) for fed vs. 4 h fasted.

Plasma triglyceride (Figure 21A) and NEFA levels (Figure 21B) normalized to control levels after overnight fasting of 16 hours and cholesterol levels did not change (Figure 21C). TP53INP2-LKO animals showed reduced plasma β-hydroxybutyrate levels upon overnight fasting (Figure 21D), corroborating the reduced capability of β-oxidation in TP53INP2-depleted livers to provide substrates for ketogenesis [167].

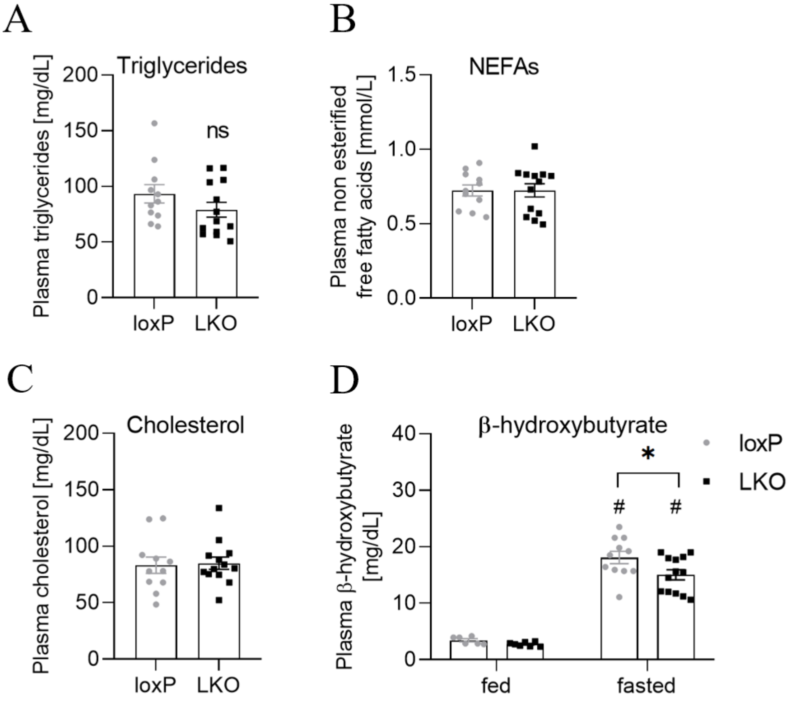

Figure 21. TP53INP2-depleted livers generate less ketone bodies upon overnight fasting. Plasma (A) triglyceride, (B) non-esterified free fatty acids (NEFAs), (C) cholesterol and (D) β-hydroxybutyrate levels of overnight fasted animals (n = 6 - 13). Data represent mean ± SEM. P-values < 0.05 were considered significant (*****) for loxP vs. LKO and (#) for fed vs. fasted.

Liver morphology of fed and overnight fasted mice was assessed by hematoxylin and eosin (H/E) staining of liver tissues and histological evaluation by microscopy (Figure 22). TP53INP2-depleted livers showed normal morphology under fed conditions, while fasted livers displayed a higher accumulation of small unstained vacuoles, resulting from the extraction of neutral lipids by solvents during sample preparation. These vacuoles also appeared in fasted control mice, although to a much lower degree. Indeed, we found elevated triglyceride (Figure 23A) and cholesterol levels (Figure 23B) in TP53INP2-depleted fasted livers.

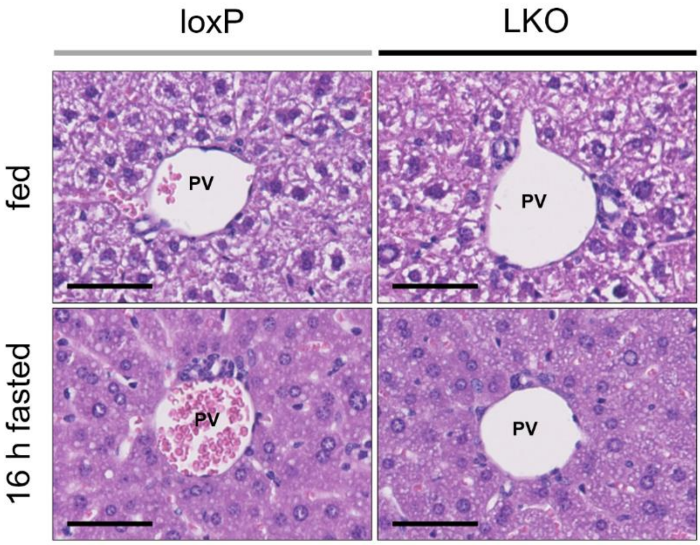

Figure 22. Fasted TP53INP2-LKO animals accumulate more lipids upon overnight fasting. Representative H/E staining of periportal regions in livers of loxP (left) and TP53INP2-LKO (right) animals. Fed animals (top) of both genotypes have normal liver morphology. TP53INP2-depleted livers show enhanced lipid accumulation (visible as white voids within the tissue) upon overnight fasting compared to controls (bottom). (PV) Portal vein; Scale bar: 50 µm.

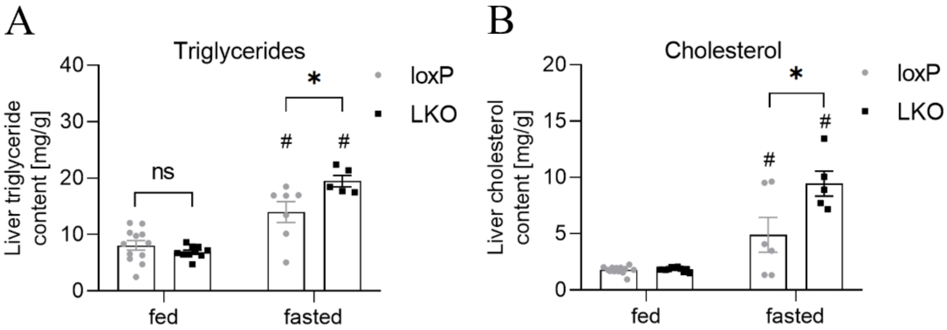

Figure 23. TP53INP2-depleted livers show enhanced accumulation of triglycerides and cholesterol upon overnight fasting. Hepatic (A) triglyceride and (B) cholesterol content in livers of fed and fasted animals (n = 5 - 13). Data represent mean ± SEM. P-values < 0.05 were considered significant (*****) for loxP vs. LKO and (#) for fed vs. fasted.

4.2.2.4. Transcriptomic analysis reveals impaired PPARα and LXRα transcriptional activity in TP53INP2-depleted livers

In order to better understand cellular processes in TP53INP2-depleted livers, we performed a transcriptomic analysis in livers of loxP and TP53INP2-LKO animals. RNAseq analysis revealed a total of 235 unique genes differentially expressed (pval < 0.01), out of them 87 genes were upregulated, and 148 genes were downregulated (Figure 24AB).

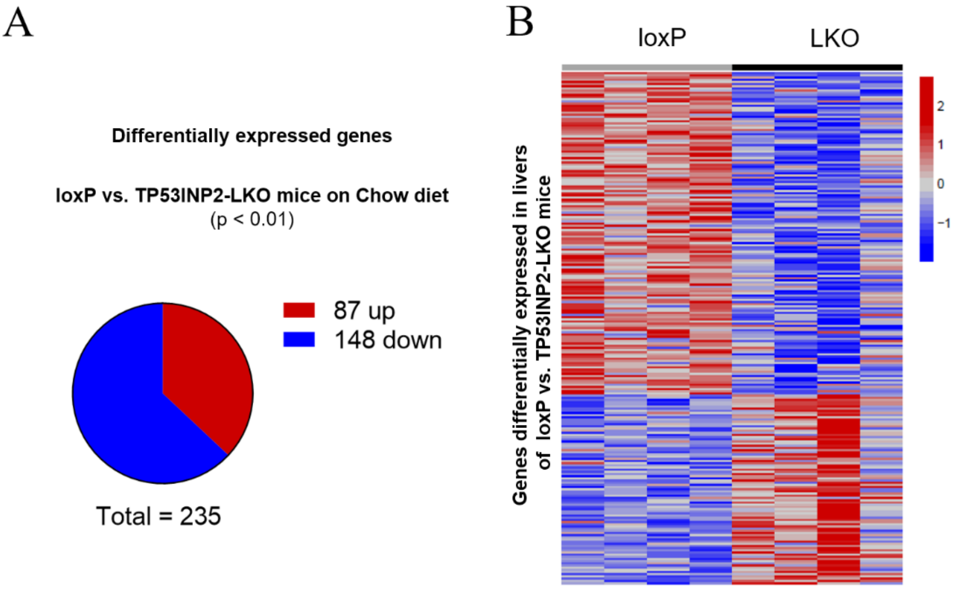

Figure 24. TP53INP2-depletion results in 235 differentially expressed genes in livers of loxP and TP53INP2-LKO animals. (A) Representation of up- and downregulated genes in TP53INP2-depleted livers. (B) Heatmap of differentially expressed genes analyzed by RNASeq (n = 4). P values < 0.01 were considered significant for loxP vs. LKO.

Interestingly, gene set enrichment analysis (GSEA) showed a downregulation of the peroxisome hallmark gene set in TP53INP2-depleted livers (Figure 25A). Furthermore, the fatty acid metabolism (Figure 25B), biosynthesis of unsaturated fatty acids (Figure 25C), and PPAR signaling pathways (Figure 25D) of the KEGG database showed significant downregulation.

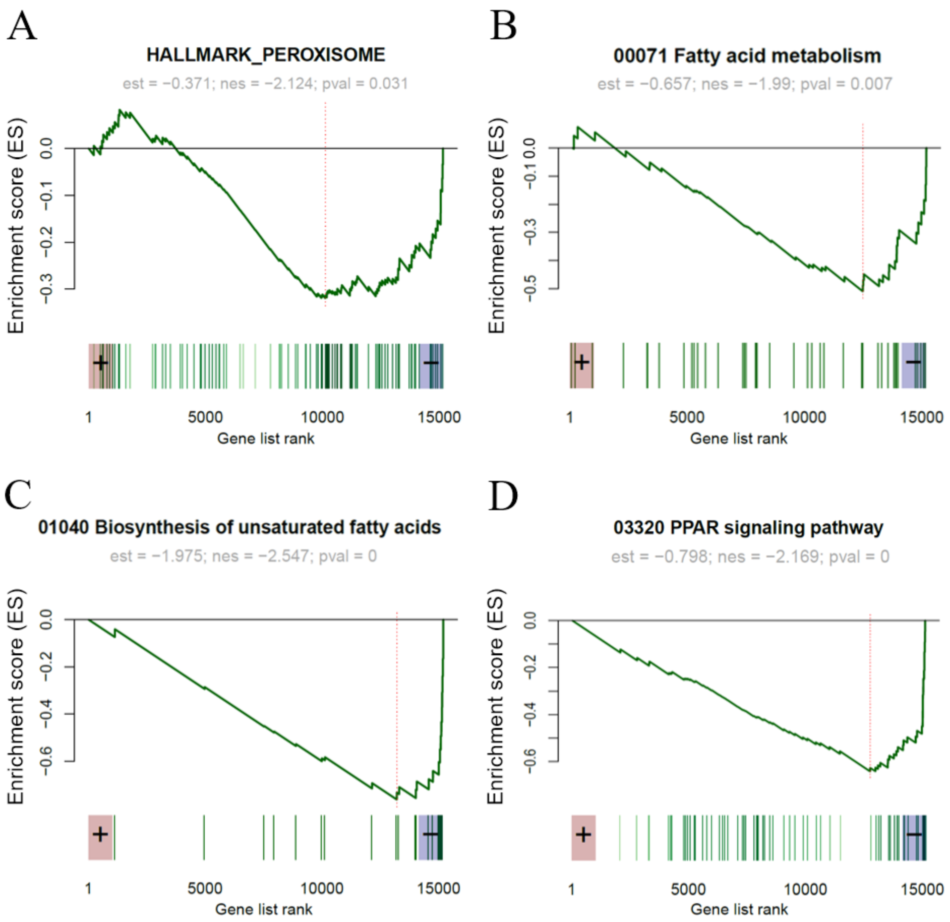

Figure 25. PPAR signaling and fatty acid metabolism pathways are downregulated in TP53INP2-depleted livers. Gene set enrichment analysis of the RNASeq experiment in control and TP53INP2-depleted livers (A) Downregulation of the peroxisome hallmark gene set in TP53INP2-depleted livers. Downregulation of the fatty acid metabolism (A), biosynthesis of unsaturated fatty acids (B) and PPAR signaling (D) KEGG pathways. P values < 0.05 were considered significant for loxP vs. LKO.

Additionally, genes found to be downregulated in TP53INP2-deficient livers were analyzed using the EnrichR GSEA tool. The ChEA 2016 gene set library contains results from transcription factor ChIP-seq studies. Out of the 148 downregulated genes, 58 genes overlapped with the LXR and RXR data sets and 52 with that of PPARα (Figure 26).

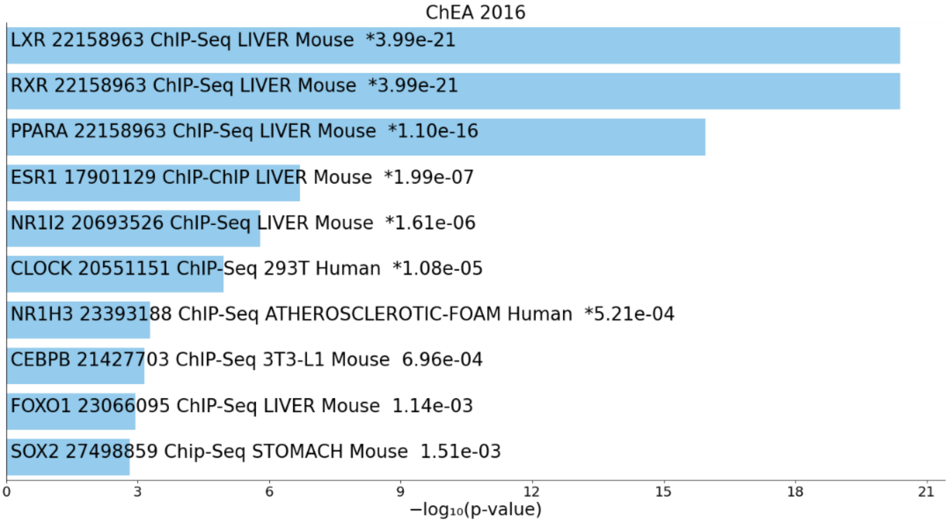

Figure 26. EnrichR Gene set enrichment analysis associated downregulated genes in TP53INP2-depleted livers with the transcription factors LXR, RXR and PPARα. Analysis of 148 downregulated genes in TP53INP2-livers using the ChEA 2016 gene set library containing results from transcription factor ChIP-seq studies. Downregulated genes overlapped most significantly with the data sets of LXR, RXR and PPARα.

In order to validate impaired PPARα and LXRα activity in TP53INP2-depleted livers, we measured the expression of their target genes by RT-qPCR. In case of PPARα-target genes, we found a significant downregulation of Cyp2c55, a member of the cytochrome P450 superfamily [168] and G6PC, the catalytic subunit of G6Pase involved in gluconeogenesis [169]. We also observed a trend for downregulated ATP-citrate lyase (Acly) involved in lipogenesis [170] and the peroxisomal acyl-CoA oxidase 1 (Acox1) involved in long-chain fatty acid oxidation [171] (Figure 27A).

Analysis of LXRα target genes showed a tendency for downregulation of ATP-binding cassette sub-family G member (ABCG)5 and a significant downregulation of ABCG8, it's heterodimeric partner involved in sterol transport across membranes [172, 173]. We found a tendency of reduced mRNA of cholesterol 7-alpha-hydroxylase (Cyp7a1) that plays a role in cholesterol homeostasis [174]. Sterol regulatory element-binding protein 1 (Srebp1c), important for cholesterol homeostasis, is another LXRα target gene that was significantly downregulated in TP53INP2-depleted livers [175].

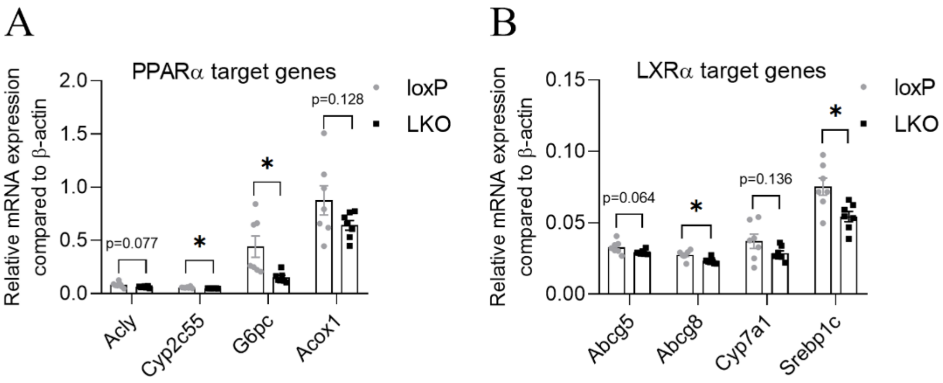

Figure 27. TP53INP2-depleted livers show impaired transcription of PPARα and LXRα target genes. (A) Relative mRNA levels of PPARα target genes (Acly, Cyp2c55, G6pc and Acox1) in control and TP53INP2-depleted livers (n = 7). (B) Relative mRNA expression of LXRα target genes (Abcg5, Abcg8, Cyp7a1 and Srebp1c) in loxP and TP53INP2-LKO livers (n = 7). Data represent mean ± SEM. P values < 0.05 were considered significant (*****) for loxP vs. LKO.

Since TP53INP2-LKO animals showed impaired hepatic PPARα and LXRα activity, we evaluated how isolated primary hepatocytes respond to agonist treatment under *in vitro* conditions. We treated hepatocytes, isolated from loxP and TP53INP2-LKO mice with the LXRα agonist GW3965 and additionally with an RXRα agonist (LG268), known to further increase transcriptional activity [176] and measured mRNA levels of LXRα target genes.

We found enhanced mRNA levels of ATP-binding cassette transporter A1 (Abca1), a transmembrane transporter for free cholesterol [177], in TP53INP2-depleted hepatocytes upon GW3965 treatment and levels were further increased by additional LG268 treatment (Figure 28A). Srebp1c, another LXRα-target, was higher expressed in TP53INP2-LKO hepatocytes upon GW3965 treatment. Surprisingly, basal levels were similar in isolated primary hepatocytes (Figure 28B), although Srepb1c expression was significantly reduced in livers (Figure 27B). Interestingly additional RXRα treatment failed to further increase

Srebp1c expression, instead they returned to basal levels. We also measured the expression of Abcg8, another gene we found to be downregulated in TP53INP2-depleted livers (Figure 27B). We did not find a decrease of Abcg8 mRNA in TP53INP2-LKO primary hepatocytes, and they responded to agonist treatment in a similar manner as control cells (Figure 28C). This experiment showed that LXRα activity within the same cells differs between *in vivo* and *in vitro* conditions.

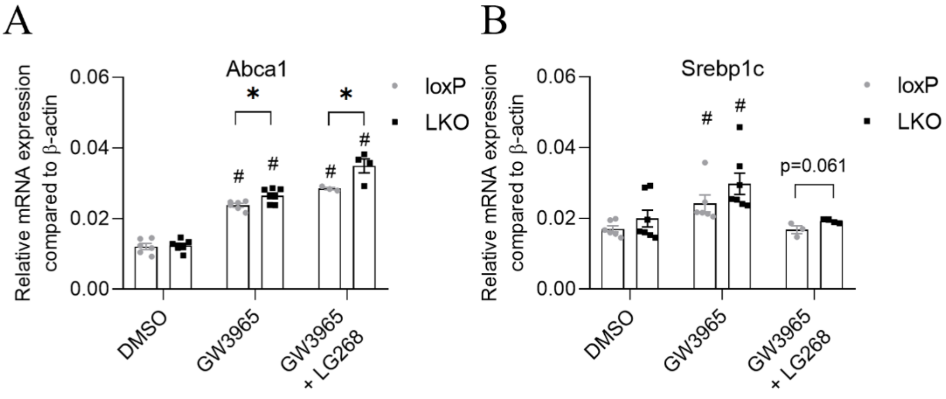

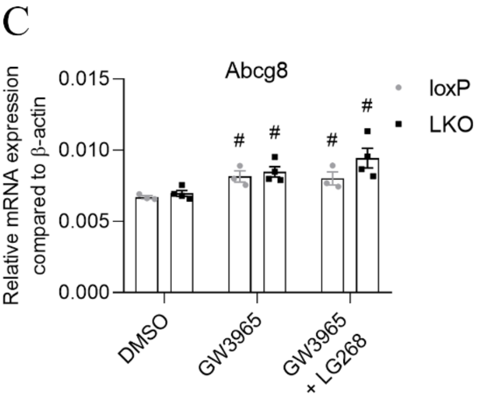

Figure 28. LXRα and RXRα agonist treatment results in enhanced expression of Abca1 in TP53INP2-depleteted hepatocytes. Relative mRNA expression of (A) Abca1 (n = 3 - 7), (B) Srebp1c (n = 3 - 7) and (C) Abcg8 (n = 3 - 4) measured in isolated primary hepatocytes treated with DMSO vehicle, GW3965 (1 μM) or GW3965 and LG268 (1 μM each). Data represent mean ± SEM. P values < 0.05 were considered significant (*****) for loxP vs. LKO and (#) for DMSO vs. agonist treatment.

To further investigate the transcriptional activity upon TP53INP2 ablation, luciferase assays were performed. Since the luciferase assay protocol takes two days between transfection and measurement, and primary hepatocytes dedifferentiate relatively quickly (data not shown), we decided to perform the assays in wild-type and TP53INP2 knockout mouse embryonic fibroblasts (MEFs).

To evaluate PPARα transcriptional activity, cells were co-transfected with luciferase linked to an upstream PPAR responsive element (PPRE), human PPARα and Renilla luciferase for normalization of transfection efficiency. Transcriptional activity was evaluated by measuring relative light units (RLU) using a luminometer, in cell homogenates after the addition of luciferase substrate to samples. Activity was evaluated in cells treated with a vehicle or upon treatment with the synthetic agonist WY-14643 [178]. In addition to PPARα luciferase assays, we also analyzed the transcriptional activity of LXRα. Experiments were performed as described for PPARα, except using a luciferase with an upstream Liver X Receptor Response Element (LXRE), overexpression of human LXRα and utilization of a synthetic LXRα-agonist (GW3965) [179].

TP53INP2-depleted MEFs showed higher PPARα activity, both in vehicle and agonist treated conditions. However, agonist treatment (WY-14643) in PPARα-overexpressing MEF cells failed to induce transcriptional activity compared to vehicle treated cells (Figure 29A), likely due to cytotoxic effects of high PPARα activity, as seen in other cell types [180]. LXRα activity showed do be increased as well by TP53INP2-depletion, in vehicle (DMSO) and agonist (GW3965) treated conditions (Figure 29B).

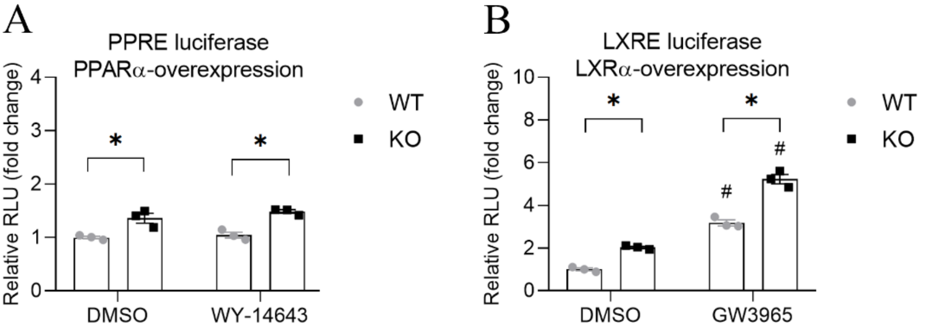

Figure 29. TP53INP2-KO MEF cells show enhanced transcriptional activity of PPARα and LXRα. (A) PPRE luciferase assay in wild-type and knockout MEFs overexpressing human PPARα. Cells were treated with DMSO or 100 μM WY-14643 (n = 3). (B) LXRE luciferase assay in human LXRα-overexpressing WT- and KO-MEFs, treated with DMSO or 1 μM GW3965 (n = 3). Data represent mean ± SEM. P-values < 0.05 were considered significant (*) for WT vs. KO and (#) for DMSO vs. agonist treatment.

To verify the results of the luciferase assays, protein expression of the LXRα target ATP-binding cassette transporter A1 (Abca1) was evaluated in control and TP53INP2-depleted cells. Abca1 is a plasma membrane protein exporting cholesterol and phospholipids from cells [181]. We found increased levels of Abca1 protein in basal (DMSO) and agonist (GW3965) treated TP53INP2-depleted MEF cells (Figure 30).

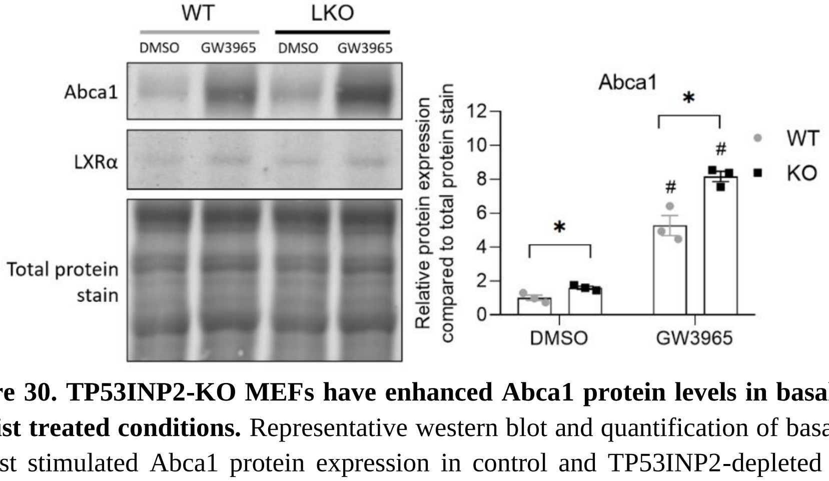

Figure 30. TP53INP2-KO MEFs have enhanced Abca1 protein levels in basal and agonist treated conditions. Representative western blot and quantification of basal and agonist stimulated Abca1 protein expression in control and TP53INP2-depleted MEF cells (n = 3). Data represent mean ± SEM. P-values < 0.05 were considered significant (*) for WT vs. KO and (#) for DMSO vs. agonist treatment.

To strengthen the relationship between TP53INP2 levels and PPARα and LXRα transcriptional activity, (human) TP53INP2-GFP overexpressing and GFP overexpressing control cells were generated for luciferase experiments. We used the Huh7 hepatocellular carcinoma cell line that has very low endogenous expression of TP53INP2. The GFP-tag was introduced at the C-terminal domain of TP53INP2, and the fusion protein showed normal cellular localization within nucleus and cytosol (data not shown). Lentiviral transduction, followed by selection for conveyed Puromycin-resistance and Fluorescence-activated cell sorting (FACS) for GFP-positive cells resulted in stable overexpression of GFP or TP53INP2-GFP in Huh7 cells (Figure 31A). Cell sorting of GFP-positive cells revealed a higher expression of GFP compared to TP53INP2-GFP of approximately two orders of magnitude (Figure 31B), likely due to pro-apoptotic effects of high cellular TP53INP2 levels [148].

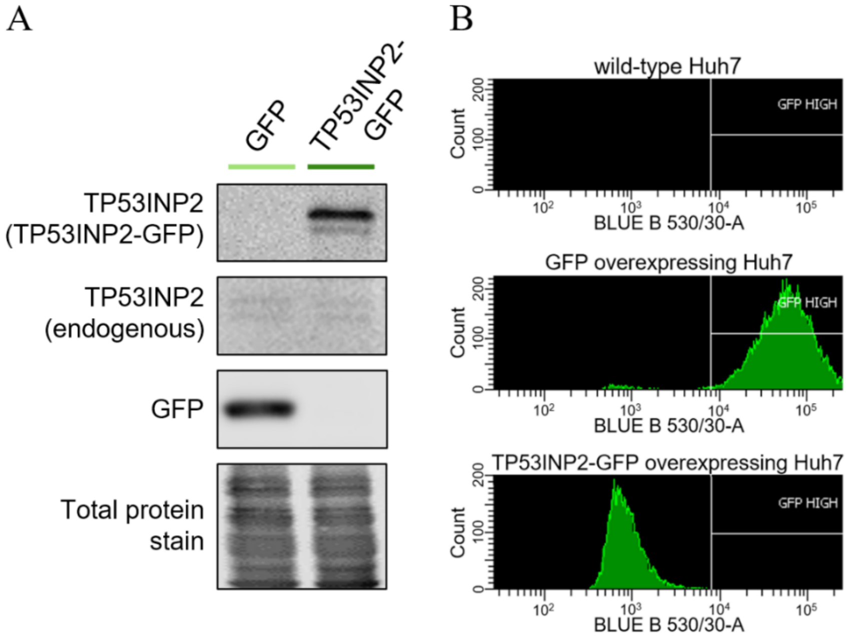

Figure 31. Validation of GFP or TP53INP2-GFP overexpression in the Huh7 hepatocellular carcinoma cell line. (A) Representative western blot of stable overexpressing GFP or TP53INP2-GFP. (B) Fluorescence (BLUE B 530/30-A) of wild-type, GFP or TP53INP2-GFP overexpressing Huh7 cells analyzed by Fluorescence-activated cell sorting (FACS).

We further investigated transcriptional activity in GFP or TP53INP2-GFP overexpressing cells by luciferase assays. We found impaired PPARα signaling in TP53INP2-GFP overexpressing cells, both in vehicle (DMSO) and agonist (WY-14643) treated cells (Figure 32). Agonist treatment at endogenous PPARα levels, as well as PPARα overexpression significantly increased PPARα activity. However, simultaneous PPARα overexpression and WY-14643 treatment resulted in impaired transcriptional activity compared to vehicle treated cells, likely due to aforementioned cytotoxic effects of high PPARα activity [180].

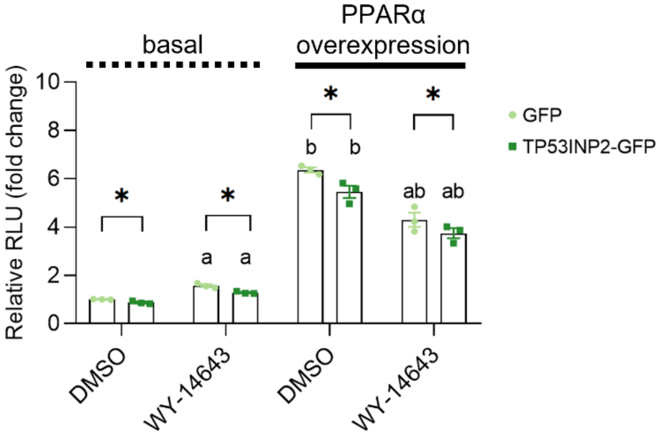

Figure 32. TP53INP2-GFP overexpressing Huh7 cells show impaired PPARα transcriptional activity. PPRE luciferase assay in stable GFP or TP53INP2-GFP overexpressing Huh7 cells, treated with a DSMO vehicle or with a PPARα agonist (100 µM WY-14643), under basal conditions and upon simultaneous PPARα overexpression (n = 3). Data represent mean ± SEM. P-values < 0.05 were considered significant (*) for GFP vs. TP53INP2-GFP, (a) for DMSO vs. WY-14643 treatment and (b) for basal vs. PPARα overexpression.

In the case of LXRE luciferase assays, we found that agonist (GW3965) treatment did not increase the transcriptional activity of LXRα in basal conditions, suggesting Huh7 cells have no endogenous LXRα expression. Overexpression of LXRα increased the transcriptional activity, especially in GW3965 treated cells, but to a lower extent in TP53INP2-overexpressing cells (Figure 33).

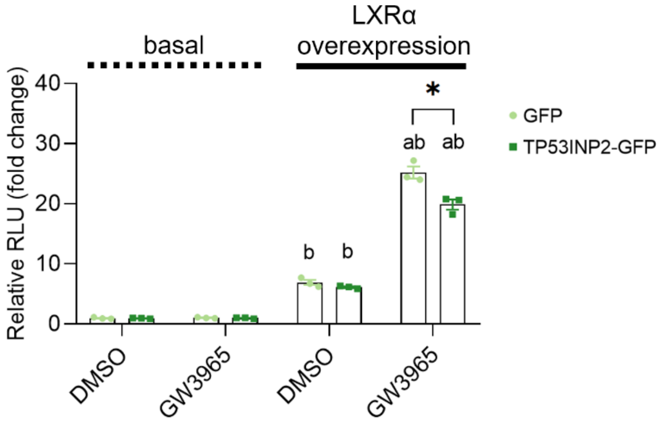

Figure 33. Agonist treated TP53INP2-GFP overexpressing Huh7 cells show impaired LXRα transcriptional activity upon LXRα-overexpression. LXRE luciferase assay in vehicle (DMSO) and agonist (1 µM GW3965) treated Huh7 cells overexpressing GFP or TP53INP2-GFP under basal conditions and upon LXRα overexpression (n = 3). Data represent mean ± SEM. P-values < 0.05 were considered significant (*) for GFP vs. TP53INP2 GFP, (a) for DMSO vs. GW3965 treatment and (b) for basal vs. LXRα overexpression.

These results confirm the negative impact of TP53INP2 protein on PPARα and LXRα signaling under *in vitro* conditions, and further studies will be needed to elucidate the different effects of TP53INP2 protein under *in vitro* and *in vivo* situations.

4.2.3. Characterization of TP53INP2-LKO animals on high-fat diet

In order to evaluate potential differences in metabolism upon nutrient abundance and non-alcoholic fatty liver (NAFLD) conditions, mice were subjected to a high-fat diet (HFD; D12492i, Research Diets), beginning at 8 weeks of age. HFD-treatment was performed for either 8 or 16 weeks, with age-matched control groups on chow diet (Figure 34).

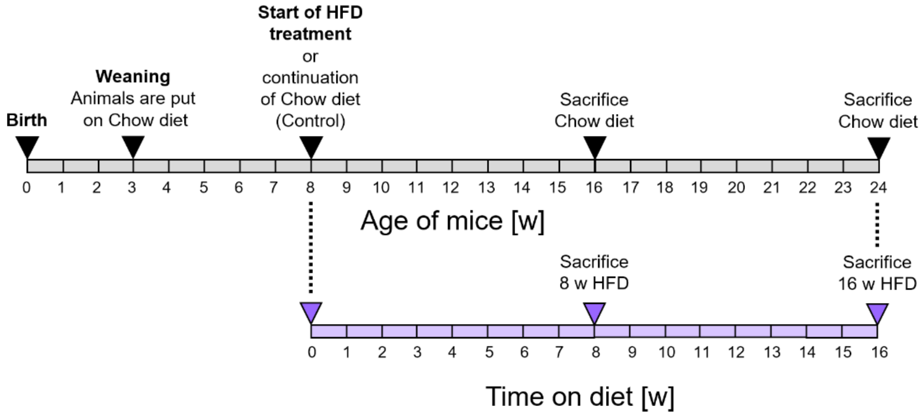
Birth
Weaning
Animals are put on Chow diet
Start of HFD treatment
or
continuation of Chow diet (Control)
Sacrifice Chow diet
Sacrifice Chow diet
0 1 2 3 4 5 6 7 8 9 10 11 12 13 14 15 16 17 18 19 20 21 22 23 24
Age of mice [w]
Sacrifice 8 w HFD
Sacrifice 16 w HFD
0 1 2 3 4 5 6 7 8 9 10 11 12 13 14 15 16
Time on diet [w]

Figure 34. Timeline of high-fat diet experiments. At the age of 8 weeks, animals were continuously fed with chow diet (control groups) or subjected to a HFD treatment. HFD animals and controls were sacrificed at 16 weeks of age or 24 weeks of age.

4.2.3.1. High-fat diet treatment enhances liver weight and increases the abundance of macrophages in in TP53INP2-LKO animals

HFD treated animals gained significantly more body weight than control animals, without differences between the genotypes (Figure 35A). A 16-week-long HFD treatment caused a significant increase in liver weight in TP53INP2-depleted animals compared to loxP animals (Figure 35B). Food intake and daily fecal excretion on chow and HFD were determined by single-housing animals at the age of 12 weeks (4 weeks after the initiation of HFD treatment). Animals on

HFD showed a reduction of food intake and fecal excretion, without significant differences between genotypes (Figure 35CD).

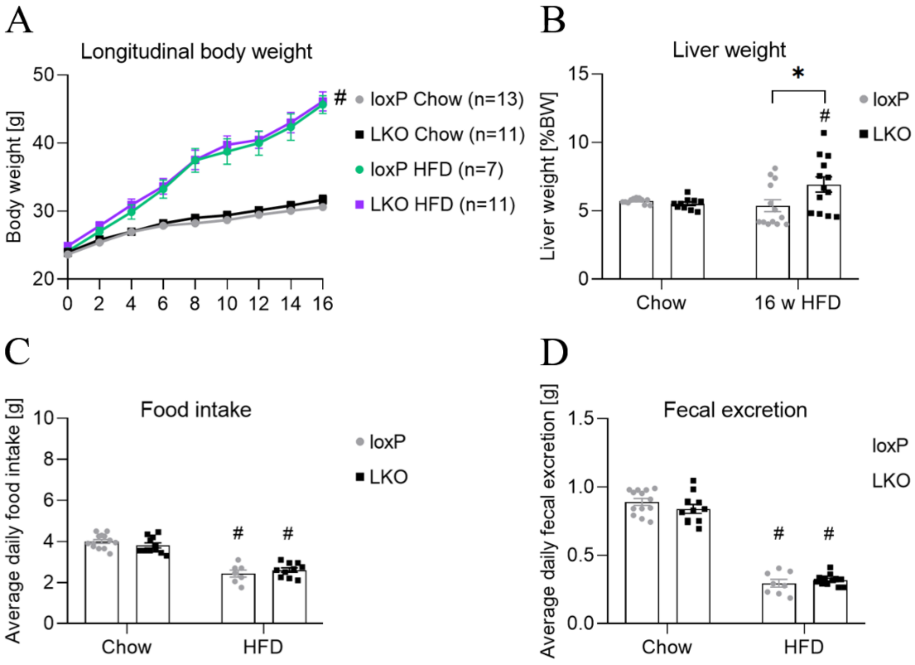

Figure 35. High-fat diet treatment of 16 weeks causes increased liver weight in TP53INP2-depleted animals. (A) Longitudinal body weight measurements in chow and HFD treated animals (n = 7 - 13). (B) Liver weight of 24-week-old animals on chow or HFD (n = 10 - 13). (C) Food intake and (D) fecal excretion on chow and HFD fed animals, determined at 12 weeks of age (n = 7 - 13). Data represent mean ± SEM. P-values < 0.05 were considered significant (*) for loxP vs. LKO and (#) for chow vs. HFD treatment.

Morphology of livers of chow and 16-week HFD treated animals was evaluated by histology. Liver tissue was stained with hematoxylin and eosin (H/E), Sirius Red and Masson's trichrome, to detect extracellular collagen [162, 182], or Periodic Acid-Schiff (PAS) staining to detect glycogen accumulation [183]. Liver morphology of H/E-stained livers was consistent in loxP and TP53INP2-LKO mice on chow diet. HFD-treatment caused unstained vacuoles in the liver tissue, resulting from extracted neutral lipids, which were more prominent in TP53INP2-depleted livers (Figure 36A). There were no detectable differences in collagen (Figure 36BC) and glycogen depositions (Figure 36D) between loxP and TP53INP2-LKO mice.

Furthermore, livers of control and 16-weeks HFD-treated animals were stained with an antibody against F4/80, a monocyte and macrophage specific marker [184]. The F4/80-positive area of immunohistochemistry images was analyzed to evaluate liver inflammation. Besides parenchymal hepatocytes, livers contain various non-parenchymal cells such as endothelial cells, fat storing stellate cells and resident macrophages called Kupffer cells [185]. Therefore, also livers of animals fed a standard diet showed positive staining for F4/80 (Figure 37A). HFD-treatment increased the F4/80-positive area in livers of TP53INP2-depleted animals compared to chow diet, but not in control animals (Figure 37BC), suggesting a potentially beneficial role of TP53INP2 on inflammation in livers under high-fat conditions.

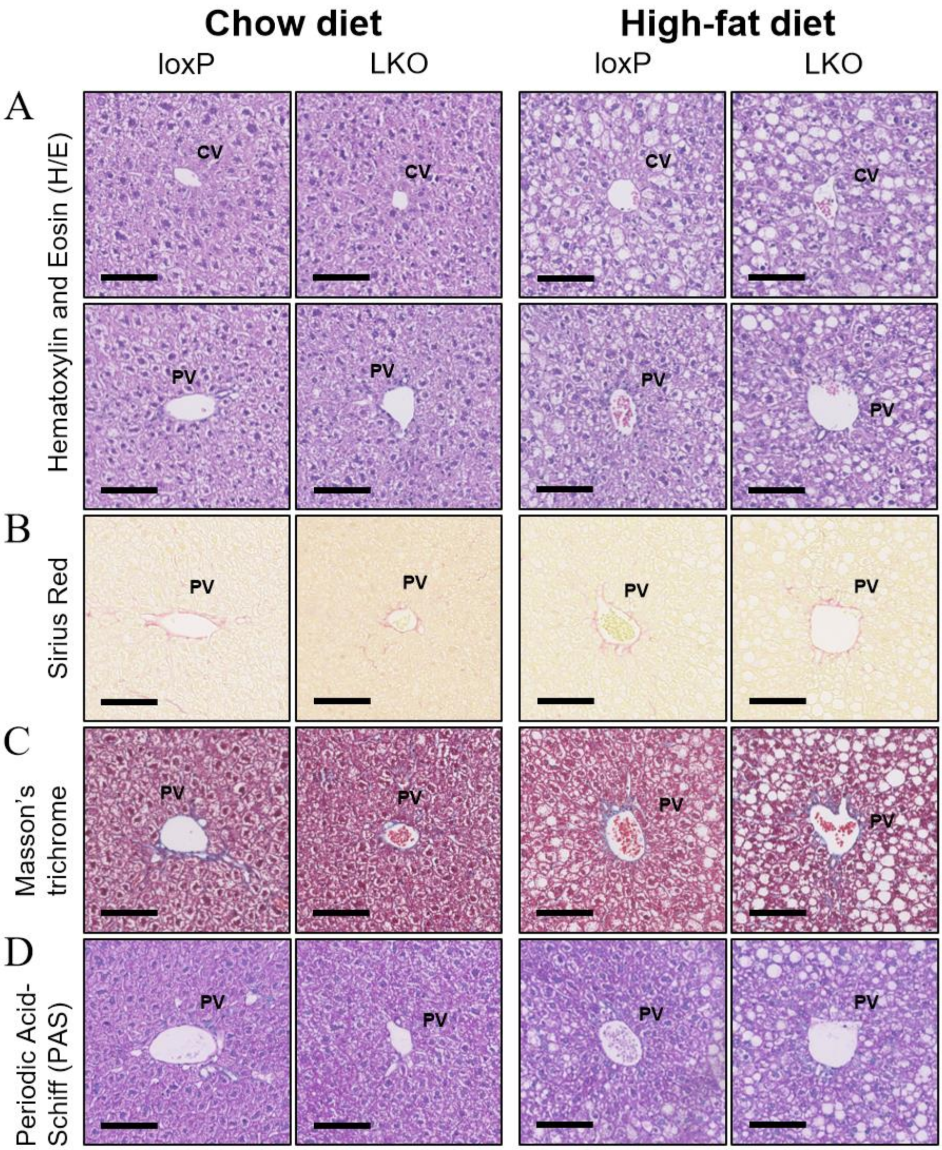
Chow diet
High-fat diet
loxP
LKO
loxP
LKO
A
Hematoxylin and Eosin (H/E)
CV
PV
B
Sirius Red
C
Masson's trichrome
D
Periodic Acid-Schiff (PAS)

Figure 36. Morphological studies of livers of chow and 16-weeks high-fat diet fed animals. Representative images of liver tissues from loxP and TP53INP2-LKO animals on chow (left panel) or after 16 weeks of high-fat diet treatment (right panel). (A) Hematoxylin and eosin (H/E) stained pericentral regions (first row) and periportal regions (second row). (B) Sirius Red, (C) Masson's trichrome and (D) Periodic Acid-Schiff (PAS) staining of periportal regions of loxP and TP53INP2-LKO animals (CV) Central vein; (PV) Portal vein; Scale bar: 100 μm.

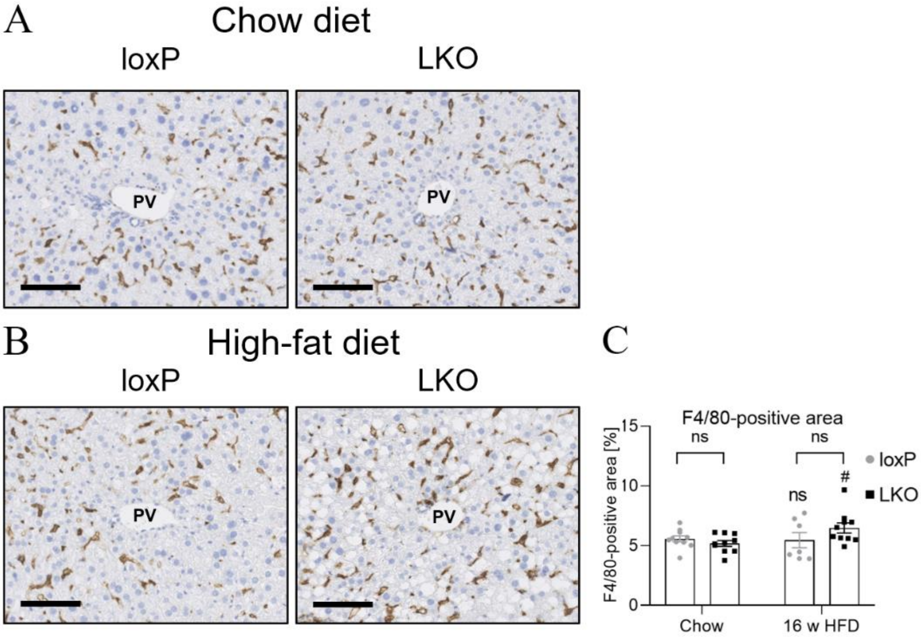
A
Chow diet
loxP
LKO
PV
PV
B
High-fat diet
loxP
LKO
PV
PV
C
F4/80-positive area
F4/80-positive area [%]
15
10
5
0
ns
ns
ns
#
● loxP
■ LKO
Chow
16 w HFD

Figure 37. High-fat diet treatment of 16 weeks increases F4/80-positive area in TP53INP2-depleted livers. Representative images of F4/80-stained periportal regions in liver tissues from chow (A) and 16-week long HFD (B) fed animals. (PV) Portal vein; Scale bar: 100 µm. (C) Quantification of F4/80-positive area in livers of chow and HFD treated animals (n = 7 – 10). Data represent mean ± SEM. P-values < 0.05 were considered significant (#) for chow vs. 16 w HFD treatment.

To further analyze liver damage, plasma alanine aminotransferase (ALT) and aspartate aminotransferase (AST) levels were measured in plasma of control and HFD (16 weeks) treated animals. HFD treatment significantly increased ALT levels in plasma of all animals, without differences between genotypes (Figure 38A). While plasma AST levels remained at the same level in loxP animals upon HFD treatment, TP53INP2-LKO animals showed a tendency for elevated AST levels compared to loxP animals (Figure 38B).

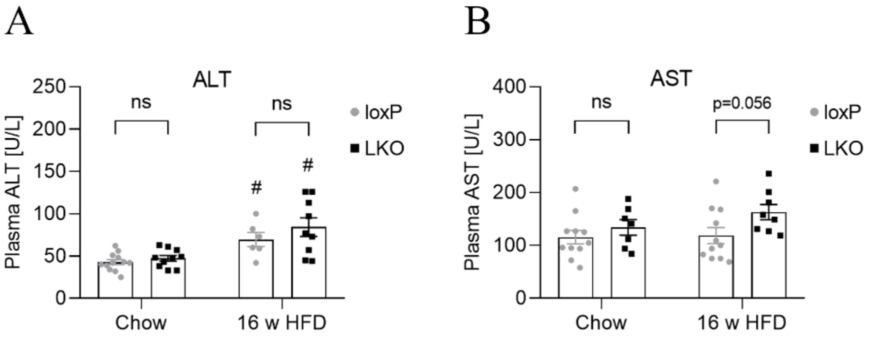

Figure 38. Plasma alanine aminotransferase and aspartate aminotransferase levels are similar in loxP and TP53INP2-LKO animals upon high-fat diet treatment. (A) Plasma alanine aminotransferase (ALT) and (B) aspartate aminotransferase (AST) levels of animals on chow diet or subjected to16 weeks of HFD (n = 6 - 12). Data represent mean ± SEM. P values < 0.05 were considered significant (#) for chow vs. 16 w HFD treatment.

The liver plays a major role in plasma protein synthesis, especially albumin, fibrinogen and globulins [186]. Albumin is the most abundant plasma protein [187] and its secretion is a parameter of normal liver function. Plasma albumin levels are retained within narrow limits [188]. Albumin binds to a wide range of ligands including fatty acids, prostaglandins and lipopolysaccharides, increasing their solubility and facilitating their transportation and detoxification [187]. Hypoalbuminemia has been found in cachectic patients suffering from cancer, AIDS and inflammatory disorders and contributes to morbidity [189]. There is also evidence, that fasting and dietary composition (protein, glucose and fat-content) [190, 191], as well as insulin levels [192] influence albumin concentrations.

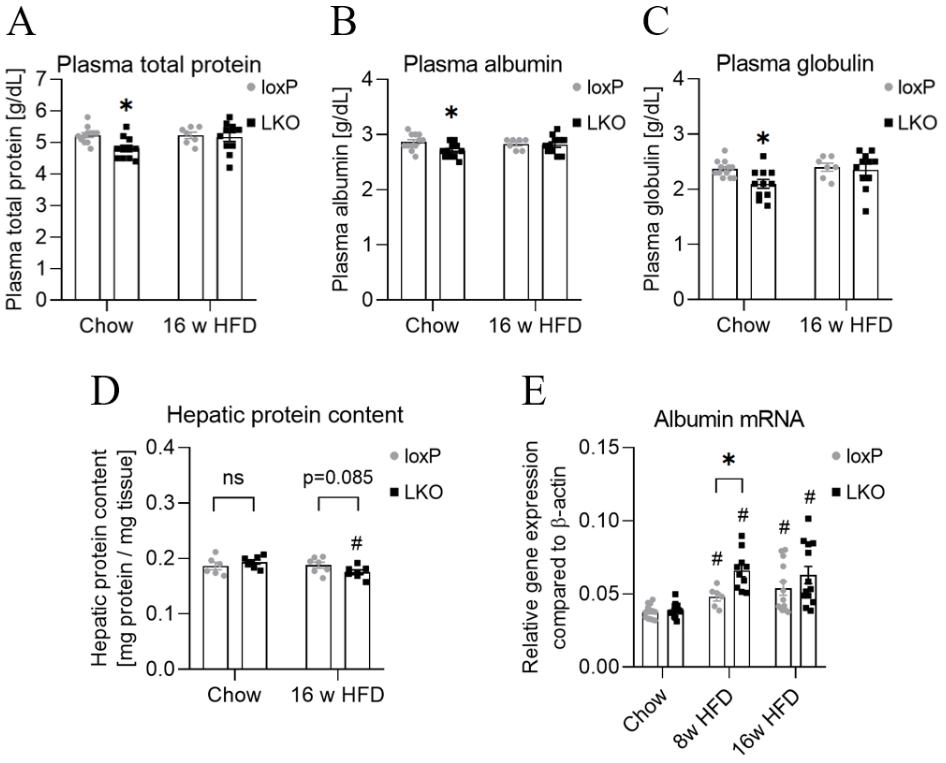

Figure 39. TP53INP2-LKO animals show reduced plasma protein concentrations on standard diet, abrogated by high-fat diet treatment. Animals were 24 weeks old with the exception of 8-week HFD treated animals, which were 16 weeks old. Plasma (A) total protein, (B) albumin, and (C) globulin levels in chow and 16 weeks high-fat diet (HFD) treated animals (n = 7 - 12). (D) Hepatic protein content of animals treated with chow or 16 weeks of HFD (n = 6 - 7). (E) Albumin mRNA expression measured in livers of animals on chow diet or after 8 or 16 weeks of HFD treatment. (n = 6 - 13). Data represent mean ± SEM. P-values < 0.05 were considered significant (*****) for loxP vs. LKO and (#) for chow vs. HFD treatment.

We analyzed the plasma protein profile in loxP and TP53INP2-LKO animals on standard and HFD and found decreased plasma levels of total protein, albumin and globulin in TP53INP2-LKO animals on standard diet and this decrease was abrogated by a 16-week HFD treatment (Figure 39ABC). Decreased protein secretion in TP53INP2-depleted livers on standard diet did not impact liver protein content. A HFD treatment of 16 weeks moderately decreased hepatic protein content compared to controls on chow diet in TP53INP2-LKO animals, while protein levels in livers of loxP animals remained constant (Figure 39D). Decreased albumin secretion of TP53INP2-depleted livers on chow diet were not caused by decreased mRNA expression of albumin, as levels were similar to control animals. However, TP53INP2-LKO animals increased albumin mRNA expression in course of a HFD treatment (Figure 39E).

4.2.3.2. Liver specific TP53INP2-depletion impairs glucose metabolism in mice subjected to a high-fat diet treatment

To analyze the impact of a high-fat diet (HFD) treatment on glucose metabolism in TP53INP2-LKO animals, we performed a glucose tolerance test (GTT) during week 8 the HFD treatment. Overnight (16 h) fasted animals showed elevated blood glucose levels (Figure 40A) and a tendency for increased fasting plasma insulin (Figure 40B). The homeostasis model index of insulin resistance (HOMA-IR) is a widely used measure of insulin resistance [193]. HOMA-IR values are calculated for each individual, by taking fasted blood glucose and fasting insulin levels into account. This analysis showed that hepatic TP53INP2-depletion causes increased insulin resistance upon a HFD treatment, as seen in the elevated HOMA-IR values (Figure 40C).

To further investigate the glucose metabolism of TP53INP2-LKO animals on HFD, above mentioned overnight fasted animals were subjected to a glucose tolerance test. Mice received an intraperitoneally injected bolus of glucose, and blood glucose and plasma insulin levels were determined for a period of two hours. Blood glucose levels rise to similar levels in loxP and TP53INP2-LKO animals, however the levels decline much faster in control animals (Figure 41A), suggesting impaired blood glucose clearance by TP53INP2-depleted livers. HFD-treated TP53INP2-LKO animals have enhanced plasma insulin levels 5 min after glucose bolus injection but adjust to plasma insulin levels of loxP control animals afterwards (Figure 41B).

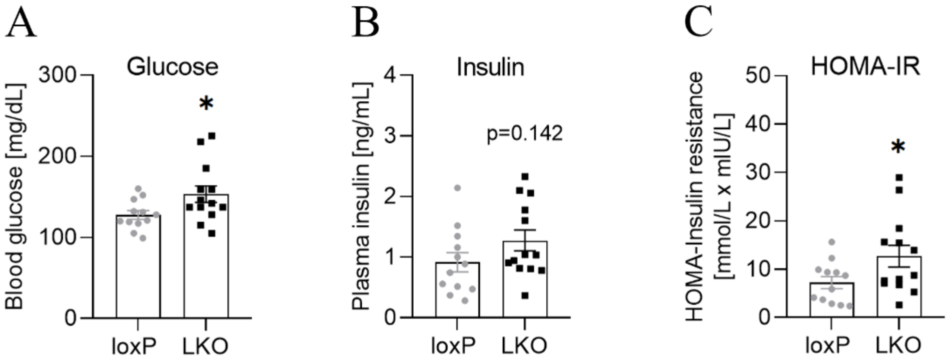

Figure 40. High-fat diet treatment of 7 weeks causes insulin resistance in TP53INP2-LKO animals. (A) Blood glucose levels after an overnight fast of loxP and TP53INP2-LKO animals measured at week 7 of a HFD treatment (n = 12 - 13). (B) Plasma insulin levels of overnight fasted loxP and LKO animals after 7 weeks of HFD treatment (n = 12 - 13). (C) Homeostatic Model Assessment of Insulin Resistance (HOMA-IR) calculated for overnight fasted control and TP53INP2-LKO animals after a 7-week HFD treatment. (n = 12 - 13). Data represent mean ± SEM. A P values < 0.05 were considered significant (*) for loxP vs. LKO.

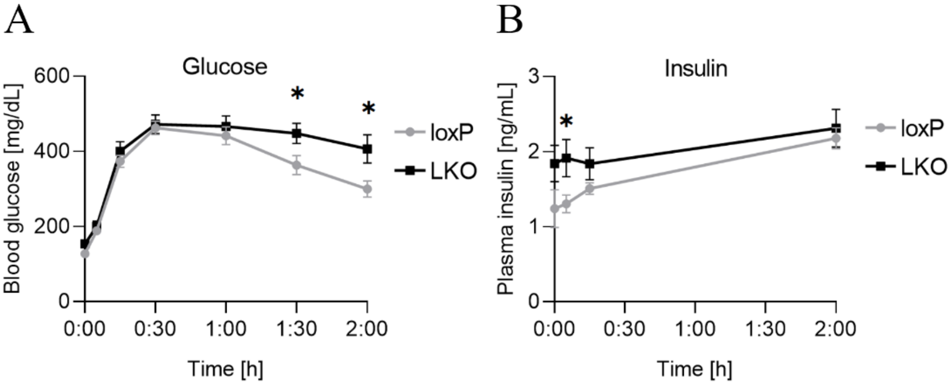

Figure 41. TP53INP2-LKO animals subjected to high-fat diet show impaired glucose handling during a glucose tolerance test. Glucose tolerance test (GTT) was performed in loxP and TP53INP2-LKO animals at week 7 of a high-fat diet treatment in overnight fasted animals. Blood samples were collected before and after peritoneal injection of a glucose bolus of 2 g / kg bodyweight at the indicated times. (A) Blood glucose levels during a GTT (n = 13). (B) Plasma insulin levels during a GTT (n = 5 - 6). Data represent mean ± SEM. P-values < 0.05 were considered significant (*) for loxP vs. LKO.

We further analyzed the plasma of fasted HFD-treated animals and noticed that while fasting plasma triglyceride levels are similar (Figure 42A), β-hydroxybutyrate levels are lower in HFD-treated fasted TP53INP2-LKO animals (Figure 42B), as observed in chow fed animals (Figure 21D). Additionally, we found lower plasma cholesterol levels in fasted TP53INP2-LKO animals after 7 weeks of HFD treatment (Figure 42C).

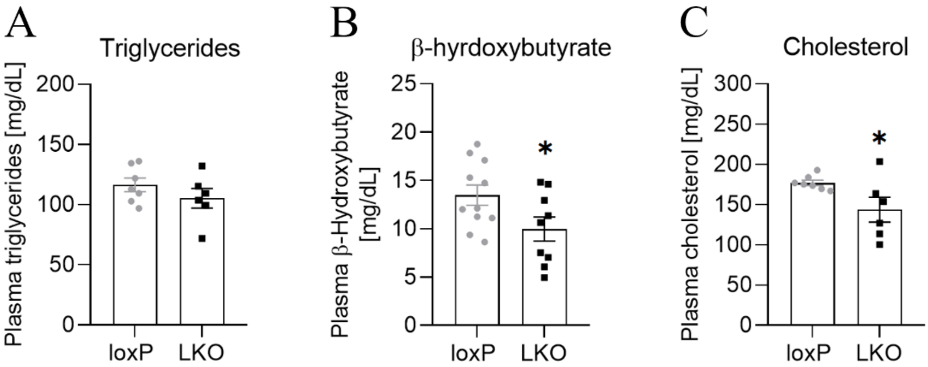

Figure 42. Overnight fasted TP53INP2-LKO animals subjected to 7 weeks of high-fat diet show decreased plasma ketone bodies and cholesterol levels. LoxP and TP53INP2-LKO animals were overnight fasted after a 7-week high-fat diet treatment. (A) Triglyceride (n = 6 - 7), (B) β-hydroxybutyrate (n = 9 - 11), and (C) cholesterol levels (n = 6 - 7), measured in plasma of overnight fasted loxP and TP53INP2-LKO animals. Data represent mean ± SEM. P-values < 0.05 were considered significant (*) for loxP vs. LKO.

4.2.3.3. Prolonged high-fat diet treatment causes enhanced accumulation of triglycerides in TP53INP2-depleted livers

Next, we analyzed plasma and hepatic triglyceride in control animals on a standard diet (24-week-old) and compared them with animals treated with a high-fat diet (HFD) for either 8 weeks (16-week-old animals) or for 16 weeks (24-week-old mice). We found that after a 16-week long period of HFD treatment, TP53INP2-LKO animals have lower levels of plasma triglycerides than controls (Figure 43A). This is accompanied by higher hepatic triglycerides, starting with a tendency at 8 weeks of HFD treatment, and reaching significance after 16 weeks of HFD consumption (Figure 43B). This enhanced accumulation of triglycerides was confirmed by increased Oil-Red-O (ORO) staining in TP53INP2-depleted livers (Figure 44AB).

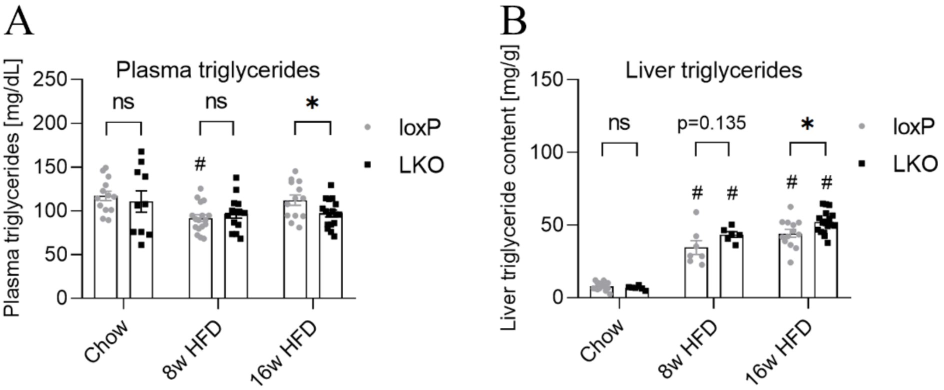

Figure 43. High-fat diet treatment of 16 weeks causes reduced plasma but elevated liver triglyceride levels in TP53INP2-LKO animals. Plasma and liver triglyceride levels were determined in chow fed and 16-week high-fat diet (HFD) treated animals at 24 weeks of age, and at 16 weeks of age in case of an 8-week HFD treatment. (A) Triglyceride levels in plasma of loxP and TP53INP2-LKO animals on chow diet or after 8 or 16 weeks of a HFD treatment (n =10 - 17). (B) Hepatic triglyceride content measured in control and TP53INP2-depleted livers of animals on chow diet or subjected to 8 or 16 weeks of a HFD treatment (n = 6 - 17). Data represent mean ± SEM. P-values < 0.05 were considered significant (*) for loxP vs. LKO and (#) chow vs. HFD treatment.

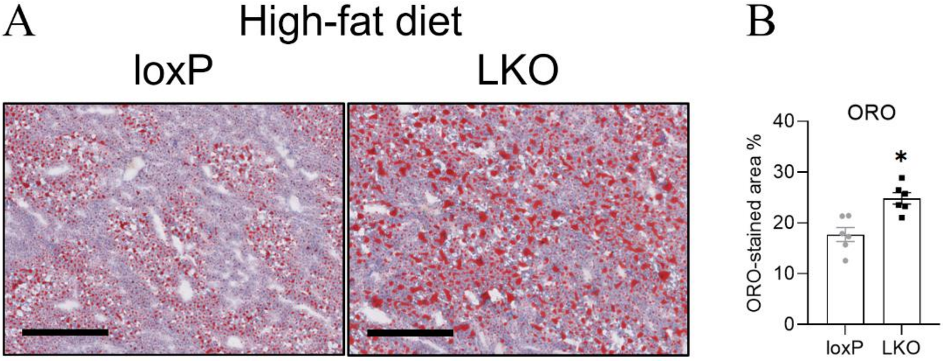

Figure 44. Livers of TP53INP2-LKO subjected to 16 weeks of HFD show increased Oil-Red-O staining. (A) Representative images and (B) quantification of Oil-Red-O (ORO) stained liver sections of 24-week-old loxP and TP53INP2-LKO animals after a 16-week period of HFD treatment (n = 6). Scalebar: 500 µm. Data represent mean ± SEM. A P-value < 0.05 was considered significant (*) for loxP vs. LKO.

To analyze, whether enhanced triglyceride accumulation in TP53INP2-depleted livers results from alterations in the metabolism of dietary derived lipids, we subjected mice to an oral lipid tolerance test (OLTT), performed 9 weeks after initiation of HFD treatment. Overnight fasted animals were given an oral gavage of Intralipid (Sigma), an emulsion of 20 % soybean oil at a dose of 10 µL / g bodyweight. Plasma triglyceride and NEFA-levels were monitored for a period of four hours after intralipid administration. Plasma triglyceride levels reached equal levels one hour after intralipid intake, suggesting similar intestinal absorption of lipids in loxP and TP53INP2-LKO animals. Plasma triglycerides declined uniformly in both genotypes (Figure 45A), implying similar capacity for postprandial clearance of lipids. This is corroborated by comparable values of the area under the curve (AUC) for plasma triglycerides during the OLTT in animals of both genotypes (Figure 45B). At the same time, plasma NEFA levels were observed, and we found a trend for lower NEFA levels in TP53INP2-LKO animals at one hour after the administration of intralipid: However, results of later measurements (Figure 45C), as well as the AUC for plasma NEFAs during the OLTT (Figure 45D) were similar for both genotypes.

Another well-known contributor to hepatic triglyceride accumulation is impaired secretion from the liver in form of very-low-density lipoproteins (VLDLs) [194]. To investigate this possibility, we analyzed VLDL-secretion by inhibiting lipases using Poloxamer 407 (P-407) in loxP and TP53INP2-LKO animals on standard diet and during week 12 of a HFD treatment. The consequential rise in plasma triglycerides represents hepatic VLDL-secretion [195]. Animals were fasted for four hours before P-407 administration (beginning one hour into the light cycle), to reduce the influence of diet-derived lipids on the analysis.

We found no differences in plasma triglycerides levels between genotypes after intraperitoneal injection of P-407, HFD-treated animals on the other hand had higher triglyceride levels than chow fed controls at 1 and 4 hours after the injection (Figure 46A). However, we calculated the hourly triglyceride secretion rate for the period between 1 - 4 h after P-407 treatment and found no statistical difference between genotypes or dietary intervention (Figure 46B). Plasma cholesterol levels also increased upon P-407 injection, as previously reported [196]. We found no significant differences in plasma cholesterol levels for different genotypes or diets (Figure 46C) or the calculated hourly cholesterol accumulation rate (Figure 46D).

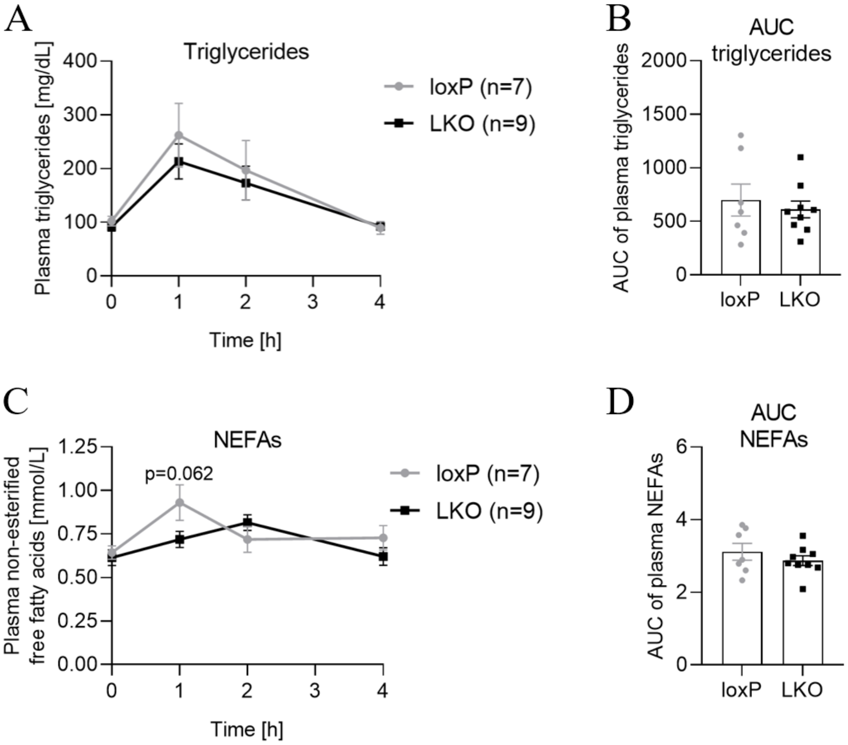

Figure 45. TP53INP2-LKO animals subjected to a HFD show normal lipid metabolism during an oral lipid tolerance test. An oral lipid tolerance test (OLTT) was performed in 17-week-old animals during week 10 of a high-fat diet treatment. Overnight fasted control and TP53INP2-LKO animals were given an oral gavage of intralipid, and (A) triglyceride and (C) non-esterified free fatty acid (NEFA) plasma levels were measured over a period of 4 hours. (B) Area under the curve (AUC) for plasma triglycerides during the OLTT (n = 7 - 9). (D) AUC of plasma NEFAs during the OLTT (n = 7 - 9). Data represent mean ± SEM. There was no statistical significance between genotypes.

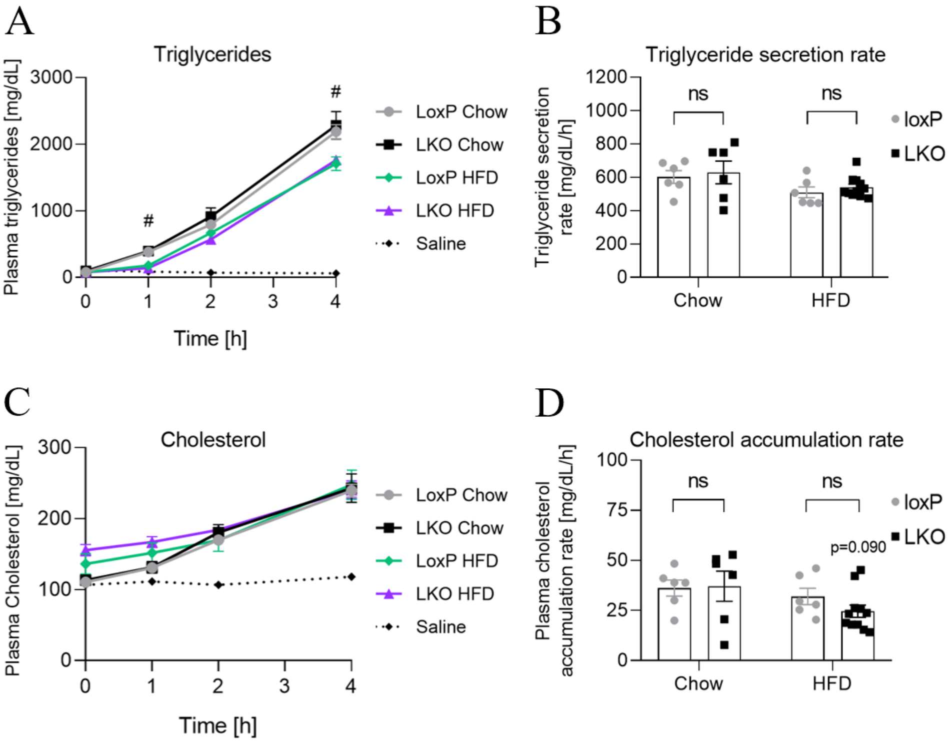

Figure 46. TP53INP2-LKO animals show normal very-low-density lipoprotein secretion compared to control animals. Very-low-density lipoprotein secretion assay was performed in 19-week-old animals on chow diet or during week 12 of a HFD treatment. Mice were subjected to a 4 hour fast, followed by the injection of 1 g / kg bodyweight Poloxamer 407 (P-407). (A) Plasma triglyceride levels at baseline and after injection of P-407 (n = 6 - 11). (B) Rate of triglyceride secretion was calculated for the increase over the period between 1 h - 4 h after P-407 injection (n = 6 - 11). (C) Plasma cholesterol levels at baseline and after P-407 injection (n = 6 - 11). (D) Rate of cholesterol accumulation was calculated for the increase in plasma cholesterol over the period between 1 - 4 h after P-407 injection (n = 6 - 11). Data represent mean ± SEM. There was no statistical significance between genotypes. P-values < 0.05 were considered significant (#) for chow vs. HFD.

Hepatic lipogenesis is partially regulated on transcriptional level, by transcription factors such as carbohydrate-responsive element-binding protein (Chrebp) and the sterol regulatory element-binding protein 1C (Srebp1c) or LXRα [197, 198]. We measured Chrebp, LXRα, and Srebp1c mRNA expression in livers of 16-week HFD treated animals in order to determine the role of

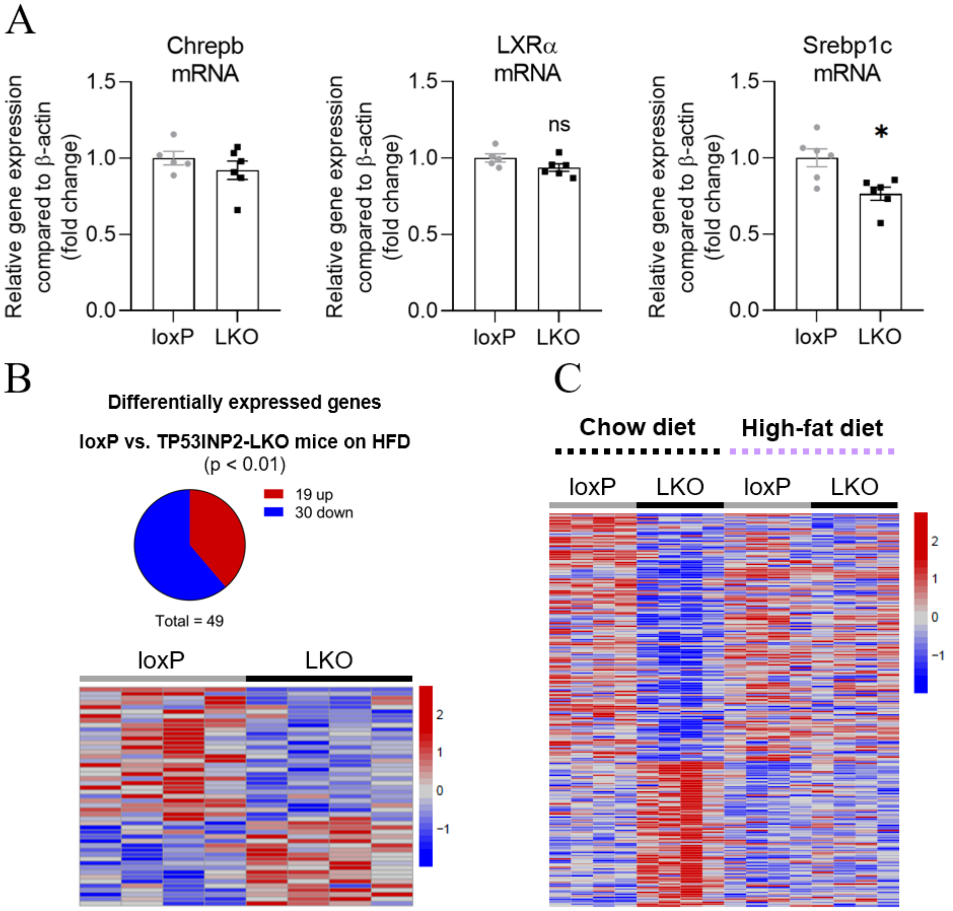

Figure 47. Elevated liver triglyceride content in TP53INP2-depleted livers on high-fat diet is not caused by enhanced lipogenesis. (A) Hepatic mRNA levels of key transcription factors involved in lipogenesis Chrebp, LXRα, and Srebp1c measured in livers of 24-week-old animals after 16 weeks of high-fat diet (n = 5 - 6). Data represent mean ± SEM. P-values < 0.05 were considered significant (*) for loxP vs. LKO. (B) Representation of up- and downregulated genes and heatmap of differentially expressed genes in livers of loxP and TP53INP2-LKO animals after 16 weeks of HFD treatment analyzed by RNASeq (n = 4). P-values < 0.01 were considered significant for loxP vs. LKO. (C) Heatmap of 235 genes differentially expressed between loxP and TP53INP2-depleted livers on Chow diet (P-values < 0.01 were considered significant) including the expression of these genes in livers of HFD-treated animals.

lipogenesis in the enhanced hepatic triglyceride accumulation of TP53INP2-LKO animals. We did not find changes in Chrebp and LXRα mRNA levels, and Srebp1c mRNA were reduced in TP53INP2-depleted livers (Figure 47A).

Furthermore, RNASeq analysis of loxP and TP53INP2-LKO animals subjected to 16 weeks of HFD showed only 49 differentially expressed genes between genotypes, suggesting that enhanced triglyceride accumulation in TP53INP2-depleted livers is not due to transcriptional changes. Moreover, comparison of RNAseq results of Chow and 16-week HFD treated animals showed that the differential expression of the 235 genes that used to be differentially expressed between loxP and TP53INP2-LKO on a standard diet is abrogated by the HFD treatment (Figure 47C).

4.2.3.4. TP53INP2-depleted livers show accelerated hepatic cholesterol accumulation when subjected to a high-fat diet, reversed by prolongation of the treatment

Plasma and hepatic cholesterol levels were measured in in control animals on a standard diet (24-week-old), animals treated with a high-fat diet (HFD) for either 8 weeks (16-week-old animals) or for 16 weeks (24-week-old mice). Levels of cholesterol in plasma increased in all animals upon HFD treatment, with a trend of being higher in TP53INP2-LKO animals after 16 weeks of HFD consumption (Figure 48A). Results of hepatic cholesterol content were more complex, as seen in Figure 48B. TP53INP2-LKO animals showed enhanced cholesterol accumulation after 8 weeks of HFD treatment compared to loxP control animals. LoxP animals reached similar levels only after prolongation of the HFD treatment to 16 weeks. At this timepoint, TP53INP2-LKO animals show decreased hepatic cholesterol levels, likely due to adaptations.

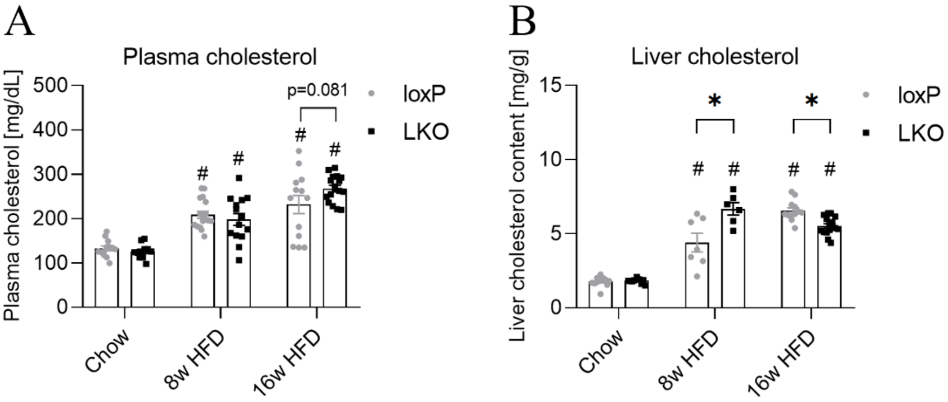

Figure 48. TP53INP2-LKO animals show enhanced hepatic cholesterol accumulation in course of a high-fat diet treatment, followed by decreased levels upon prolongation of the treatment. Plasma and liver cholesterol was measured in chow fed and 16-week high-fat diet (HFD) treated animals at 24 weeks of age, and at 16 weeks of age in case of an 8-week HFD treatment. (A) Plasma cholesterol levels of fed loxP and TP53INP2-LKO animals on chow diet or subjected to 8 or 16 weeks of HFD treatment (n = 11 - 17). (B) Hepatic cholesterol content measured in livers of animals subjected to standard chow diet or an 8 or 16-week long HFD treatment (n = 6 - 16). Data represent mean ± SEM. P-values < 0.05 were considered significant (*) for loxP vs. LKO and (#) for chow vs. HFD treatment.

Next, we evaluated the distribution of cholesterol in plasma. Plasma of loxP and TP53INP2-LKO animals treated with HFD for 16 weeks was depleted of ApoB containing lipoproteins by precipitation. High-density lipoproteins (HDLs) do not contain ApoB and remain in the supernatant, which was analyzed together with total plasma. Again, total cholesterol showed a tendency for being increased, this trend of higher cholesterol was also observed in the HDL-containing fraction, while cholesterol content in the calculated non-HDL fraction were similar (Figure 49A).

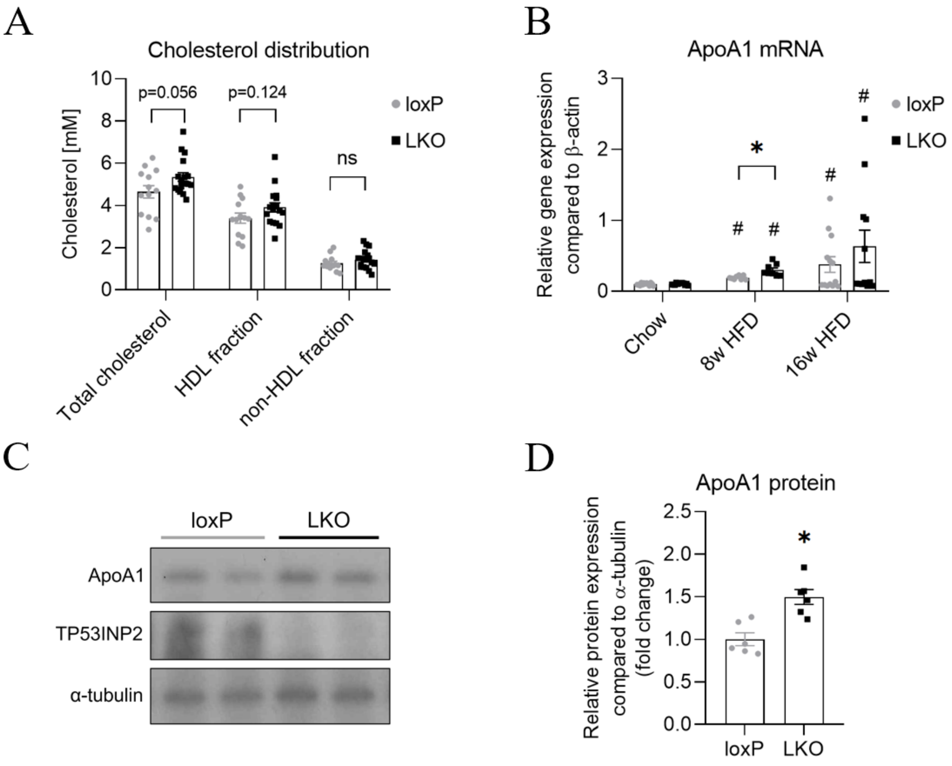

Figure 49. TP53INP2-depletion in livers of high-fat diet treated animals impacts high-density lipoprotein metabolism. Plasma cholesterol distribution and hepatic ApoA1 mRNA and ApoA1 protein levels were measured in chow fed and 16-week high-fat diet (HFD) treated animals at 24 weeks of age. Animals subjected to 8 weeks of HFD were 16 weeks old. (A) Plasma total cholesterol, and cholesterol distribution between high-density lipoprotein (HDL) and non-HDL fractions was measured in loxP and TP53INP2-LKO animals (n = 13 - 17). (A) Hepatic ApoA1 mRNA levels of loxP and LKO animals (n = 8 - 13). (C) Representative western blot and (D) quantification of hepatic ApoA1 protein levels in loxP and TP53INP2-LKO livers after a 16-week HFD treatment (n = 6). Data represent mean ± SEM. P-values < 0.05 were considered significant (*) for loxP vs. LKO and (#) for chow vs. HFD treatment.

ApoA1 serves as an important component for HDL structure, stability and function and accounts for up to 70% of the protein content of HDLs [199, 200]. The Liver, together with the small intestine, are the predominant sources of the ApoA1 apolipoprotein [201]. We analyzed hepatic ApoA1 mRNA expression in animals on chow and HFD. ApoA1 mRNA levels increased upon HFD treatment, and were significantly higher in TP53INP2-deleted livers compared to loxP controls, after 8 weeks of HFD consumption. Prolonged HFD treatment of 16 weeks resulted in enhanced ApoA1 mRNA levels compared to chow fed controls, but showed high standard deviations between individuals (Figure 49B). Protein levels of ApoA1, measured in animals subjected to 16 weeks of HFD, were significantly increased in TP53IN2-LKO animals (Figure 49CD).

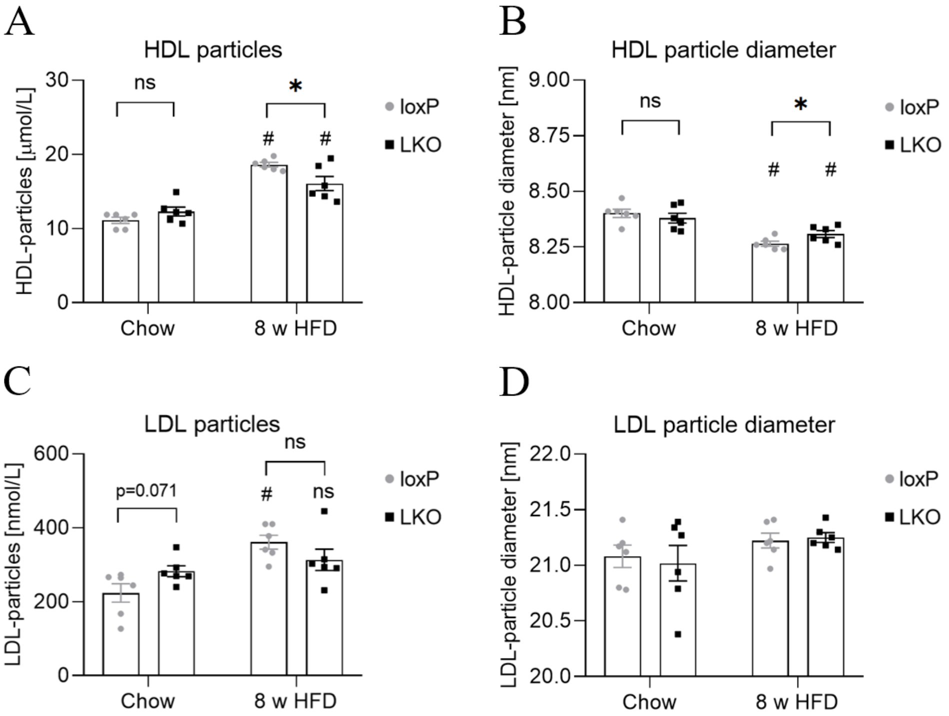

Figure 50. TP53INP2-depletion causes alterations in high-density lipoprotein particle number and diameter after 8 weeks of a high-fat diet treatment. Plasma of 16-week-old animals fed with chow diet or subjected to 8 weeks of high-fat diet (HFD) was analyzed with the Liposcale® test based on 2D diffusion-ordered Nuclear Magnetic Resonance (NMR) spectroscopy. (A) High-density lipoprotein (HDL) particle number and (B) HDL particle diameter measured in plasma of loxP and TP53INP2-LKO animals (n = 6). (B) Low-density lipoprotein (LDL) particle number and (B) LDL particle diameter assessed in plasma of control and TP53INP2-LKO animals (n = 6). Data represent mean ± SEM. P-values < 0.05 were considered significant (*) for loxP vs. LKO and (#) for chow vs. HFD treatment.

Besides aberrant lipid plasma concentrations, the size (diameter) and number of lipoprotein particles have been shown to be indicators of metabolic diseases [202, 203]. We analyzed lipoprotein particles in the plasma of 16-week-old loxP and TP53INP2-LKO animals fed with a chow diet or 8 weeks of HFD. The number of HDL particles was significantly increased by a HFD treatment, but to a lower extent in TP53INP2-LKO animals (Figure 50A). HDL particle diameter was significantly reduced in HFD treated animals compared to chow diet controls, and again, the difference was higher in loxP animals (Figure 50B), suggesting TP53INP2 impacts HDL particle number and diameter in high fat diet conditions. TP53INP2-LKO animals on standard diet show a tendency for enhanced low-density lipoprotein (LDL) particles in plasma. HFD treatment increased the number of LDL particles in plasma of loxP, but not in TP53INP2-LKO animals (Figure 50C). The diameter of LDL particles was not influenced by diet or genotype (Figure 50D).

4.2.4. Characterization of hepatic TP53INP2-depletion in animals subjected to a western diet

In order to further analyze the cholesterol metabolism of TP53INP2-depleted livers we treated loxP and TP53INP2-LKO animals with a diet containing high amounts of cholesterol (0.2 % w / w). Mice were subjected to a 16-week long western diet (WD; D12079Bi, Research Diets), beginning at 8 weeks of age (Figure 51).

A western diet treatment of 16 weeks resulted in increased body weight compared to animals fed a standard diet, without differences between loxP and TP53INP2-LKO mice (Figure 52A). Liver weight was not affected by a WD treatment (Figure 52B). Interestingly, hepatic TP53INP2 mRNA levels were significantly reduced in WD treated loxP animals (Figure 52C).

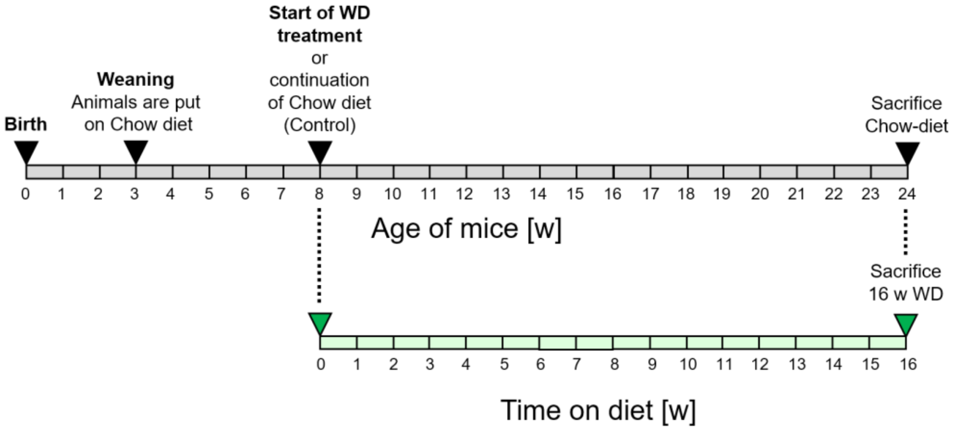
Start of WD treatment
or
continuation of Chow diet (Control)
Weaning
Animals are put on Chow diet
Birth
Sacrifice Chow-diet
0 1 2 3 4 5 6 7 8 9 10 11 12 13 14 15 16 17 18 19 20 21 22 23 24
Age of mice [w]
Sacrifice 16 w WD
0 1 2 3 4 5 6 7 8 9 10 11 12 13 14 15 16
Time on diet [w]

Figure 51. Timeline of western diet experiments. At the age of 8 weeks, animals were continuously fed with chow diet (control group) or subjected to a western diet (WD) treatment. Control and WD treated animals were sacrificed at 24 weeks of age.

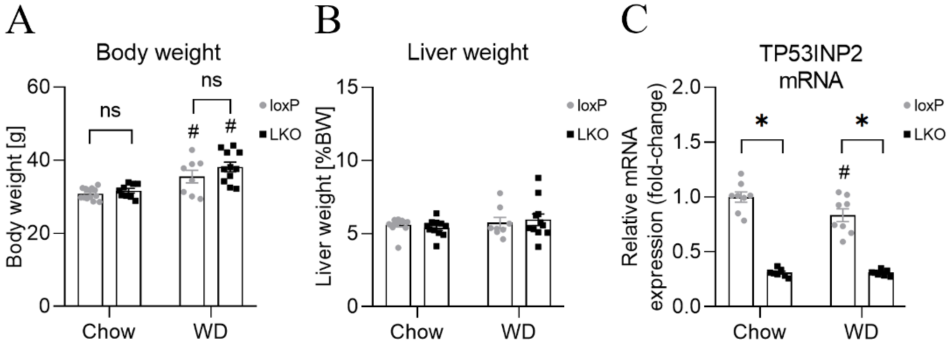

Figure 52. Western diet treatment causes no differences in body or liver weight between loxP and TP53INP2-LKO animals but results in a reduction of hepatic TP53INP2 expression. Animals were fed a standard chow diet or 16 weeks of western diet (WD) and were sacrificed at the age of 24 weeks. (A) Body weight of control and TP53INP2-LKO animals on chow and WD (n = 8 - 13). (B) Liver weight of loxP and LKO animals on chow and WD (n = 8 - 13). (C) Hepatic TP53INP2 mRNA expression measured in livers of loxP and LKO animals on chow and WD (n = 8). Data represent mean ± SEM. P-values < 0.05 were considered significant (*) for loxP vs. LKO and (#) for chow vs. WD treatment.

While plasma triglycerides were not influenced by the WD treatment (Figure 53A), liver triglyceride content increased significantly to similar levels in both genotypes (Figure 53B). Cholesterol levels in plasma and livers increased dramatically in response to WD treatment, without differences between the genotypes (Figure 53CD).

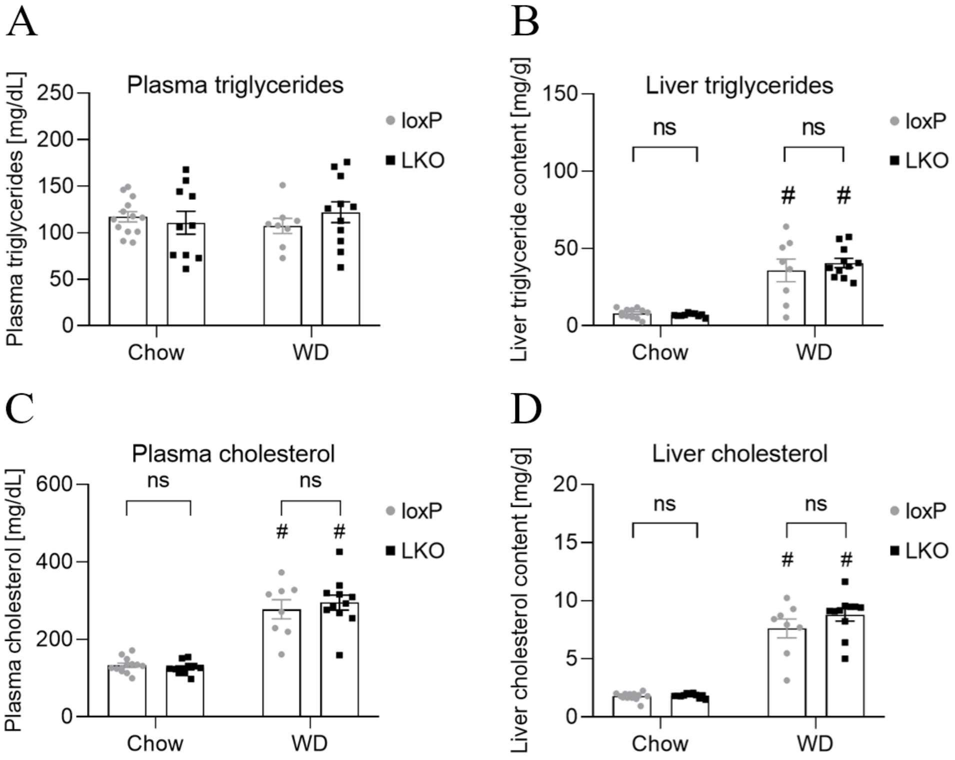

Figure 53. Elevated liver triglycerides and increased plasma and liver cholesterol levels caused by a western-diet treatment are not affected by hepatic TP53INP2-depletion. Animals were fed chow diet or 16 weeks of western diet (WD) and were sacrificed at the age of 24 weeks. (A) Plasma (n = 8 - 13) and (B) liver triglyceride levels (n = 8 - 12) of loxP and TP53INP2-LKO animals. (C) Plasma and (D) liver cholesterol levels of loxP and TP53INP2-LKO animals (n = 8 - 13). Data represent mean ± SEM. P-values < 0.05 were considered significant (*) for loxP vs. LKO and (#) for chow vs. WD treatment.

Morphological analysis of liver tissue from WD treated animals by H/E staining showed severe lipid accumulation in form of unstained vacuoles in pericentral and periportal regions in loxP and TP53INP2-LKO mice compared to animals on chow diet (Figure 54A). Livers of WD treated animals showed no signs of enhanced collagen deposition, determined by Sirius Red and Masson’s

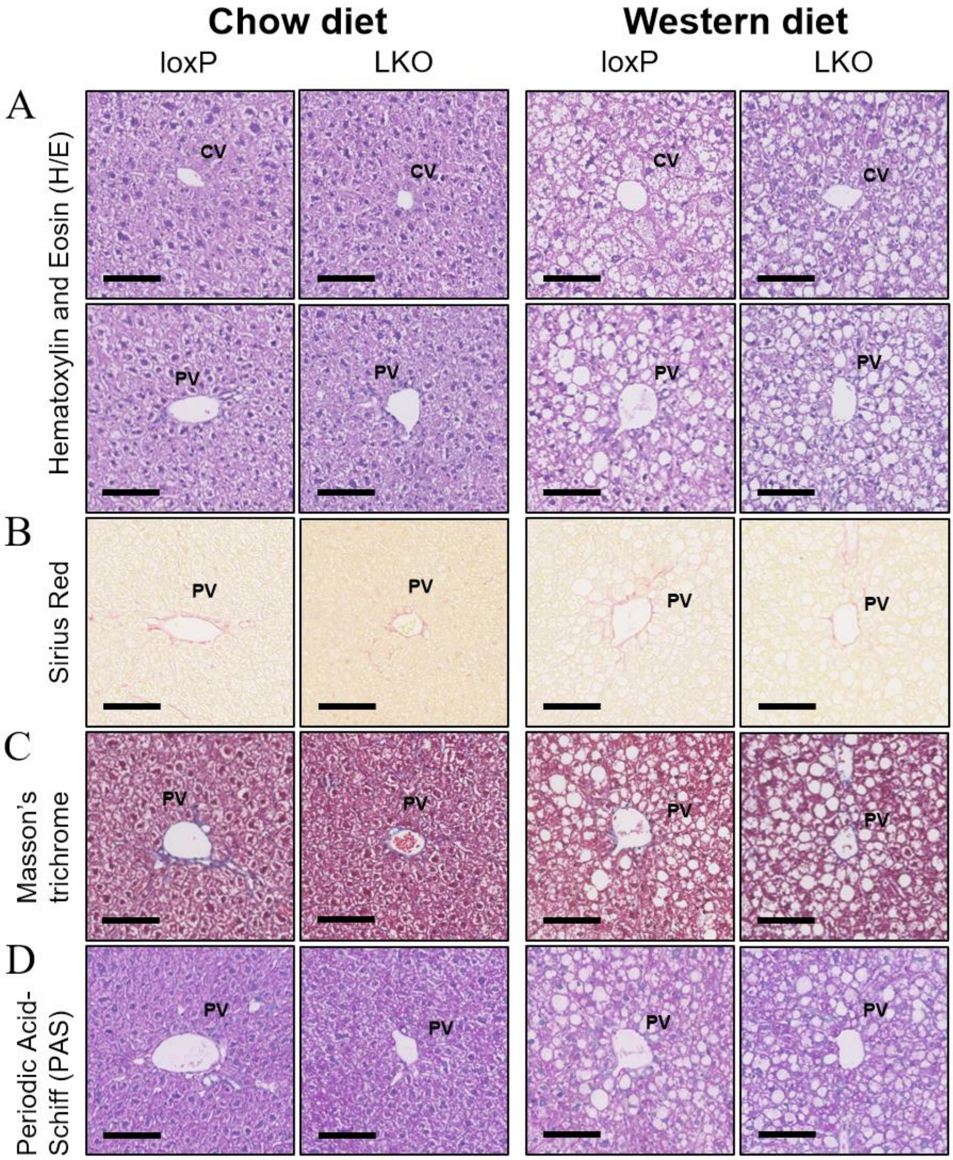
Chow diet
Western diet
loxP
LKO
loxP
LKO
A
Hematoxylin and Eosin (H/E)
CV
PV
B
Sirius Red
C
Masson's trichrome
D
Periodic Acid-Schiff (PAS)

Figure 54. Morphological analysis of livers of chow and 16-weeks western diet fed animals. Representative images of liver tissues from loxP and TP53INP2-LKO animals on chow diet (left panel) or after 16 weeks of western diet (right panel). (A) Hematoxylin and eosin (H/E) stained pericentral regions (first row) and periportal regions (second row). (B) Sirius Red, (C) Masson's trichrome and (D) Periodic Acid-Schiff (PAS) staining of periportal regions of loxP and TP53INP2-LKO animals (CV) Central vein; (PV) Portal vein; Scale bar: 100 µm.

trichrome staining (Figure 54BC). Glycogen levels were similar in all conditions, analyzed by PAS staining (Figure 54D).

The livers of WD fed animals were stained for the macrophage marker F4/80 and analyzed by immunohistochemistry. F4/80-staining of TP53INP2-depleted livers of animals treated with a WD was significantly increased compared to chow fed controls, a sign of increased numbers of Kupffer cells/ macrophages [204]. Western diet treatment did not increase the F4/80-stained area in loxP livers compared to chow fed controls (Figure 55ABC).

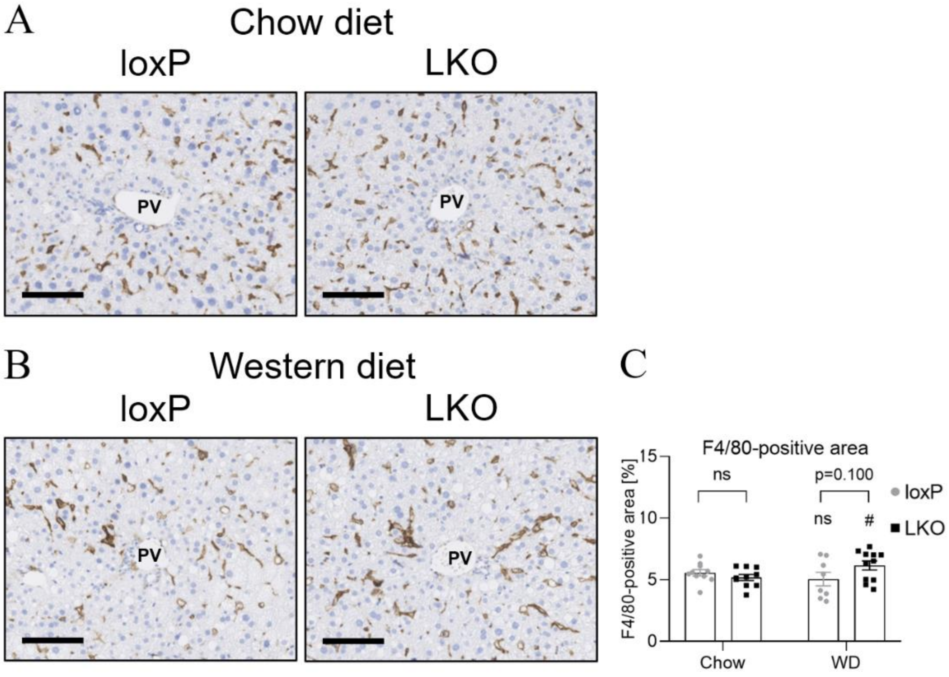

Figure 55. Western diet treatment of 16 weeks increases F4/80-positive area in TP53INP2-depleted livers. Representative images of F4/80 stained periportal regions in liver tissues from (A) chow and (B) 16-week long western diet (WD) fed animals at 24 weeks of age. (PV) Portal vein; Scale bar: 100 µm. (C) Quantification of F4/80-positive area in livers of chow and WD treated animals (n = 8 - 11). Data represent mean ± SEM. P-values < 0.05 were considered significant (#) for chow vs. WD treatment.

Liver damage parameters were analyzed in plasma of loxP and TP53INP2-LKO animals subjected to WD and compared to levels in chow fed animals. While plasma alanine aminotransferase (AST) levels were enhanced by a WD treatment in both genotypes, plasma aspartate aminotransferase (ALT) levels increased only significantly in loxP animals in response to WD (Figure 56AB).

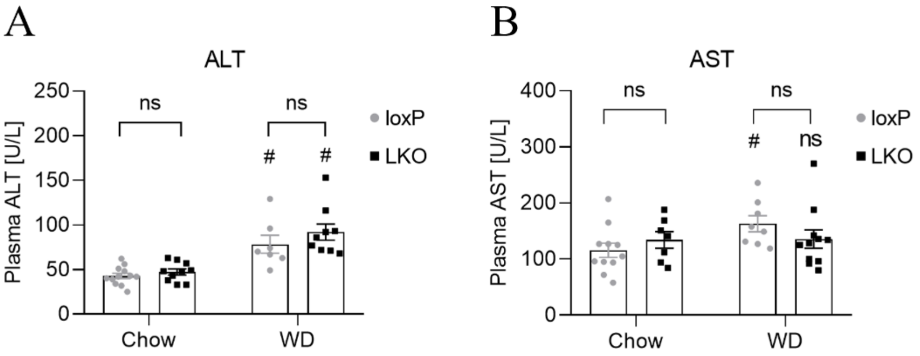

Figure 56. Western-diet elevates plasma alanine aminotransferase but not aspartate aminotransferase levels in TP53INP2-LKO animals. (A) Plasma alanine aminotransferase (ALT) and (B) aspartate aminotransferase (AST) levels of animals on chow diet or subjected to16 weeks of WD (n = 7 - 12). Data represent mean ± SEM. P-values < 0.05 were considered significant (#) for chow vs. WD treatment.

Cholesterol catabolism takes place in the liver and its end products are bile acids [205]. This pathway is essential for cholesterol homeostasis and prevents cholesterol accumulation. Most bile acids are synthesized via the neutral bile acid pathway, with cholesterol 7α-hydroxylase (Cyp7a1) being the rate-limiting enzyme [206]. Bile acids are amphipathic molecules, that form micelles together with phospholipids [207]. Conjugation of bile acids to amino acids increases their solubility, with the majority (~ 95 %) being conjugated to taurine in mice. Conjugated bile acids form sodium salts (bile salts) at a physiological pH. Bile salts are exported from hepatocytes via the bile salt export pump (Bsep) into bile canaliculi, eventually accumulating in the gall bladder in form of mixed micelles consisting of bile salts, phospholipids and cholesterol. These micelles are secreted into the intestinal tract and facilitate nutrient absorption. The majority of bile acids is reabsorbed in the terminal ileum, taken up by enterocytes through the apical-sodium-dependent BA transporter (Asbt/Ntcp2). Subsequently, bile acids are secreted into portal blood and transported to the liver, where they are taken up by hepatocytes via the Na^+-dependent taurocholate cotransport peptide (Ntcp) [206]. The enterohepatic circulation and synthesis of bile acids are regulated by the transcription factor FXRα, with bile acids acting as its endogenous ligands [208]. Hepatic FXRα signaling negatively regulates the expression of Cyp7a1 [209] and Ntcp [210], while it upregulates the expression of Bsep [211]. In the ileum, FXRα reduces the expression of Asbt/Ntcp2 [212].

We analyzed the levels of total bile acids in plasma of animals subjected to 16 weeks of WD treatment. WD-treated loxP animals had significantly increased plasma bile acid concentrations compared to TP53INP2-LKO animals (Figure 57A). Additionally, we analyzed the bile acid content in feces. These measurements were performed in 12-week-old single housed animals on chow diet, or after four weeks of the initiation of the WD treatment. LoxP animals had increased fecal total bile acid levels when treated with WD and levels were significantly higher than those of WD-treated TP53INP2-LKO animals (Figure 57B).

Given the differences in bile acid concentrations in plasma and feces of WD-treated loxP and TP53INP2-LKO animals, we measured the mRNA expression of FXRα and different target genes in livers and the ileum of those animals. Although TP53INP2-LKO animals had lower bile acid levels, we found a moderate increase in Fxrα mRNA compared to loxP animals. The mRNA expression of Fxrα target genes Cyp7a1, Ntcp and Bsep was similar in both genotypes (Figure 57C). The expression of Fxrα and Ntcp2 in the terminal ileum of WD-treated loxP and TP53INP2-LKO animals did not differ (Figure 57D).

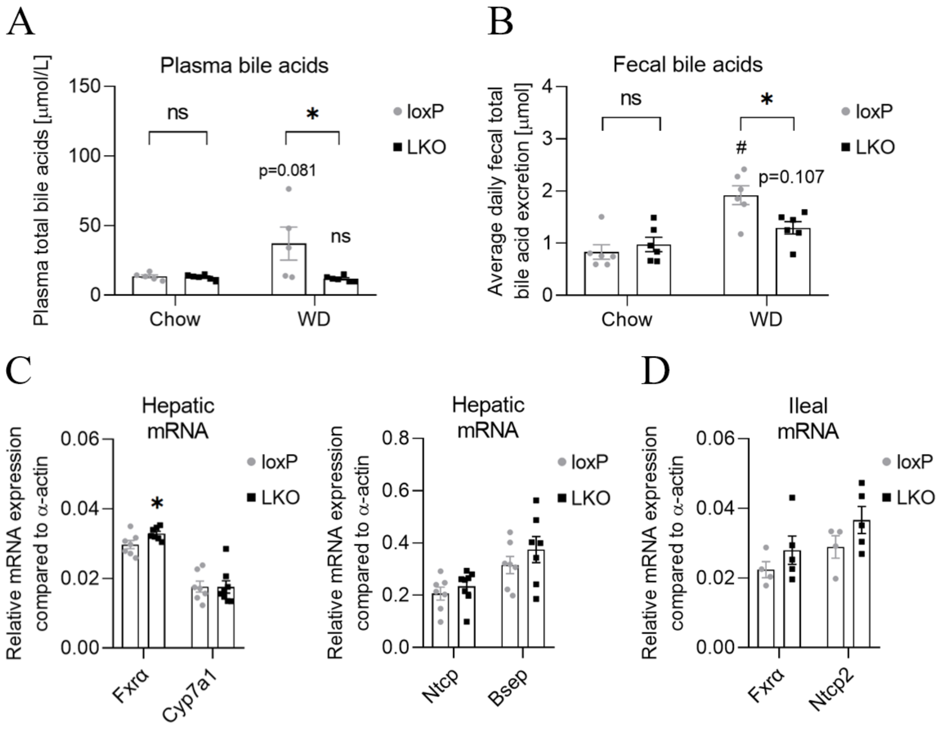

Figure 57. TP53INP2-depletion prevents increased plasma and fecal bile acid levels caused by western diet treatment. (A) Plasma bile acid levels measured in plasma of 24-week-old loxP and TP53INP2-LKO animals on chow diet or subjected to a 16-week western diet (WD) treatment (n = 5 - 6). (B) Fecal bile acid levels of 12-week-old single housed animals, determined in feces from mice on chow diet or at week five of a WD treatment (n = 6). (C) Hepatic mRNA expression of Fxrα, Cyp7a1, Ntcp and Bsep quantified in livers of 24-week-old loxP and TP53INP2-LKO animals subjected to a 16-week WD treatment (n = 7 - 8). (D) Expression of Fxrα and Ntcp2 mRNA in the ileum of 24-week-old loxP and TP53INP2-LKO mice subjected to a 16-week WD treatment (n = 4 - 5). Data represent mean ± SEM. P-values < 0.05 were considered significant (*) for loxP vs. LKO and (#) for chow vs. WD treatment.

4.3. TP53INP2 protein reduces lysosomal free cholesterol accumulation upon Niemann-Pick C1 protein inhibition

Since high-fat diet treatment impacted the cholesterol content in TP53INP2-depleted hepatocytes, we set out to investigate intracellular cholesterol trafficking in loxP and TP53INP2-LKO hepatocytes. We stained free cholesterol with Filipin III, a fluorescent polyene antibiotic produced by *Streptomycetes*, found to bind cholesterol with great affinity [213], frequently used to stain free cholesterol (FC) [214, 215].

Under physiological conditions, the majority of cellular cholesterol resides in the plasma membrane, followed by decreasing amounts in lysosomal, Golgi and endoplasmic reticulum membranes [216, 217]. Intracellular cholesterol transport can be facilitated by proteins such as various members of the steroidogenic acute regulatory protein (StAR)-related lipid transfer (START) domain family [218] or members of the Oxysterol-binding proteins (OSBPs) [219]. De novo synthesized cholesterol is transported from the endoplasmic reticulum to the plasma membrane in a vesicular, ATP-dependent manner [220], exogenous cholesterol is taken up by endocytosis, transported into lysosomes and redistributed as free cholesterol [221]. Free cholesterol is exported from late endosomes and lysosomes via the coordinated action of Niemann–Pick C 1 (Npc1) and Npc2 proteins [222]. U18666A blocks intracellular cholesterol trafficking by inhibiting Niemann-Pick C1 (NPC1) mediated release of FC from the lysosome [223].

Isolated primary hepatocytes from loxP and TP53INP2-LKO animals were treated with 1 μM U18666A or a DMSO vehicle for 24 h. Free cholesterol (FC) was stained in fixed cells using the Cholesterol Cell-Based Detection Assay Kit (Cayman, 1009779). We found no difference in Filipin III stained FC levels in basal conditions between loxP and TP53INP2-LKO hepatocytes (Figure

58AB). However, upon U18666A treatment, TP53INP2-depleted hepatocytes accumulated significantly more FC (Figure 58AC).

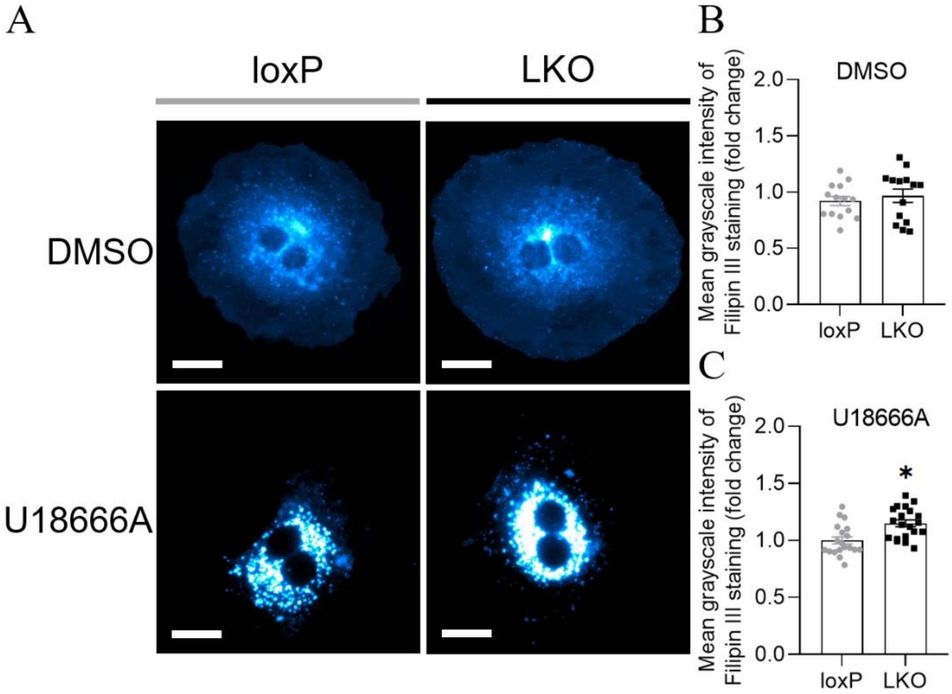
A
B
loxP
LKO
DMSO
U18666A
Mean grayscale intensity of Filipin III staining (fold change)
2.0
1.5
1.0
0.5
0.0
DMSO
loxP
LKO
C
U18666A
*

Figure 58. Niemann-Pick C1 protein inhibition by U18666A treatment causes increased free cholesterol accumulation in TP53INP2-depleted hepatocytes. (A) Representative images of Filipin III stained free cholesterol in loxP and TP53INP2-LKO isolated primary hepatocytes treated for 24 h with a vehicle (DMSO) or 1 µM U18666A. Scalebar: 25 µm. (B) Quantification of Filipin III intensity in vehicle treated primary hepatocytes from loxP and TP53INP2-LKO animals (n = 14 hepatocytes of three different animals per genotype). (C) Quantification of Filipin III intensity in 1 µM U18666A treated primary hepatocytes from loxP and TP53INP2-LKO animals (n = 19 - 20 hepatocytes of three different animals per genotype). Data represent mean ± SEM. P-values < 0.05 were considered significant (*) for loxP vs. LKO.

These results were not hepatocyte specific, as we obtained similar results in TP53INP2-KO mouse embryonic fibroblasts (MEFs), as seen in Figure 59. While hepatocytes showed no differences in FC levels in basal conditions (Figure 58B), free cholesterol levels in TP53INP2-KO MEFs were reduced (Figure

59AB). Yet, U18666A facilitated inhibition of Npc1 protein in MEFs resulted in increased lysosomal FC accumulation in TP53INP2-KO cells.

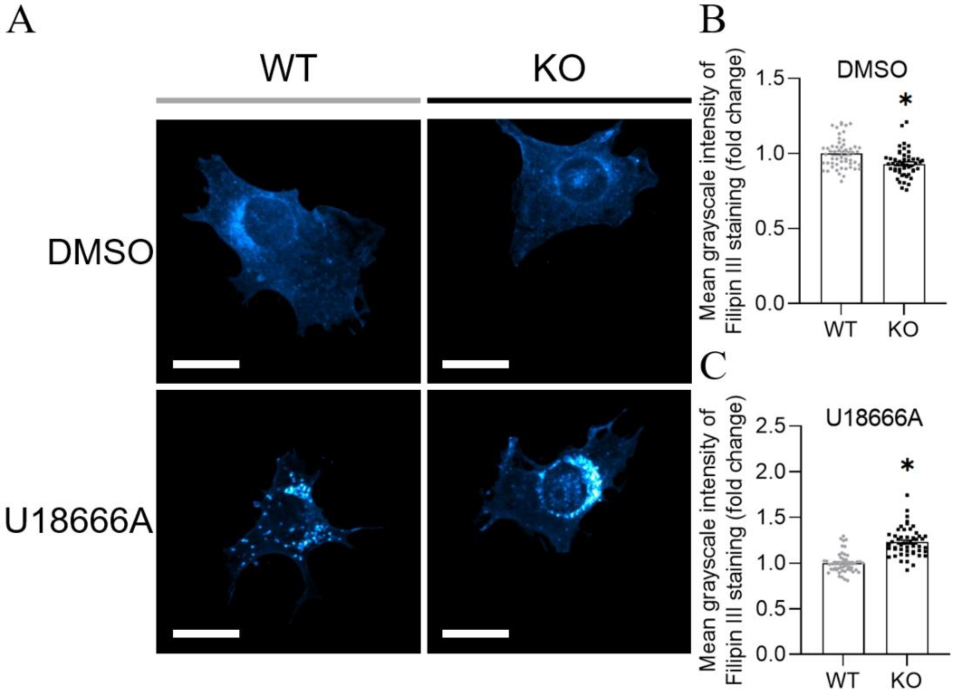
A
WT
KO
DMSO
U18666A
B
DMSO
Mean grayscale intensity of Filipin III staining (fold change)
1.5
1.0
0.5
0.0
*
WT
KO
C
U18666A
Mean grayscale intensity of Filipin III staining (fold change)
2.5
2.0
1.5
1.0
0.5
0.0
*
WT
KO

Figure 59. TP53INP2-KO mouse embryonic fibroblasts have lower basal levels of free cholesterol but accumulate more upon Niemann-Pick C1 protein inhibition by U18666A treatment. (A) Representative images of Filipin III stained free cholesterol in WT and TP53INP2-KO mouse embryonic fibroblasts (MEFs) treated for 24 h with a vehicle (DMSO) or 1 µM U18666A. Scalebar: 25 µm. (B) Quantification of Filipin III intensity in vehicle treated WT and KO MEFs (n = 49 – 55 cells from three individual experiments). (C) Quantification of Filipin III intensity in 1 µM U18666A treated WT and KO MEFs (n = 49 - 51 cells from three individual experiments). Data represent mean ± SEM. P-values < 0.05 were considered significant (*) for WT vs. KO.

Mouse embryonic fibroblasts were loaded with cholesterol by a 24 h incubation with native human low-density lipoprotein (LDL), as well as aggregated human LDL. While native LDL is internalized into cell via the LDL-Receptor (LDL-R) protein [224], aggregated LDL has been shown to be internalized via Low-density lipoprotein (LDL) receptor-related protein 1 (LRP1) causing massive intracellular cholesteryl ester accumulation in human macrophages and vascular smooth muscle cells [225, 226].

We stained FC with Filipin III in wild-type and TP53INP2-LKO MEFs treated for 24h with either 100 μM native or aggregated LDL in the presence of 1 μM U18666A. We found enhanced FC accumulation upon U18666A treatment in TP53INP2-depleted cells, in both conditions (Figure 60ABC).

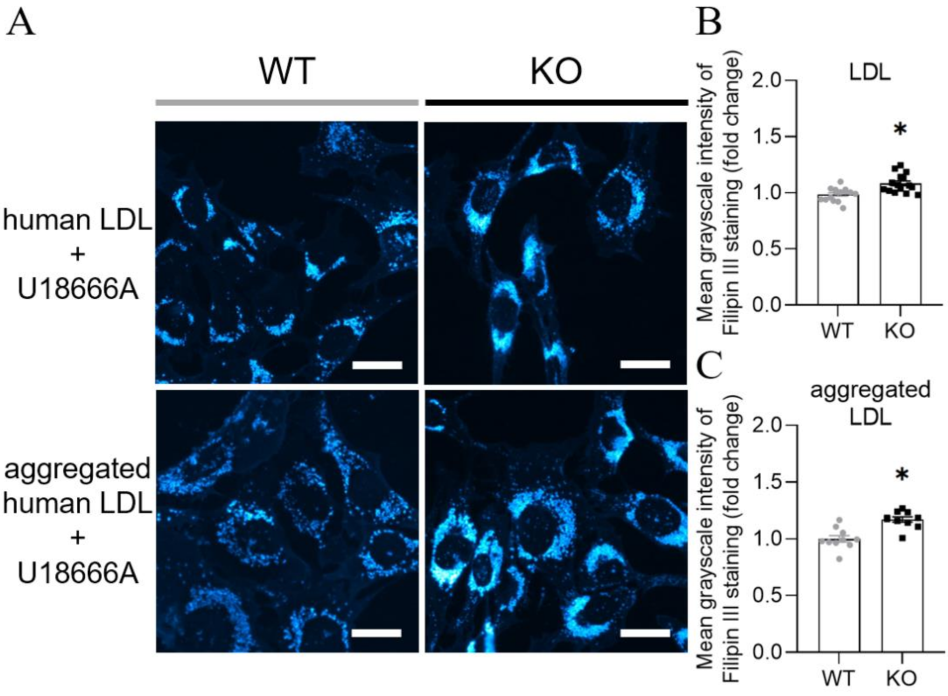
A
WT
KO
human LDL + U18666A
aggregated human LDL + U18666A
B
LDL
Mean grayscale intensity of Filipin III staining (fold change)
2.0
1.5
1.0
0.5
0.0
*
WT
KO
C
aggregated LDL
Mean grayscale intensity of Filipin III staining (fold change)
2.0
1.5
1.0
0.5
0.0
*
WT
KO

Figure 60. Niemann-Pick C1 protein inhibition by U18666A results in higher free cholesterol levels in TP53INP2-KO mouse embryonic fibroblasts in the presence of (aggregated) low-density lipoprotein. (A) Representative images of Filipin III stained free cholesterol in WT and TP53INP2-KO mouse embryonic fibroblasts (MEFs) treated for 24 h with 1 μM U18666A and 100 μg / mL native human low-density lipoprotein (LDL) or aggregated human LDL. Scalebar: 25 μm. (B) Quantification of Filipin III intensity in WT and KO MEFs treated for 24 h with U18666A and native human LDL (n = 15 cells from three individual experiments). (C) Quantification of Filipin III intensity in 24 h U18666A and aggregated human LDL treated WT and KO MEFs (n = 10 cells from three individual experiments). Data represent mean ± SEM. P-values < 0.05 were considered significant (*) for WT vs. KO.

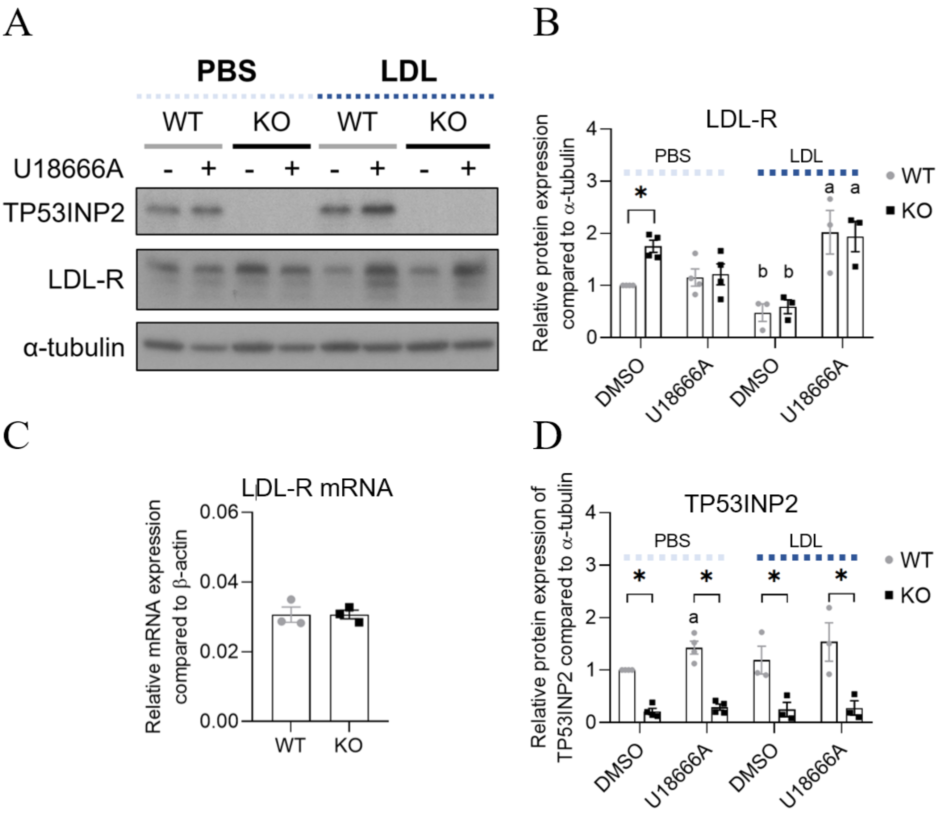

Figure 61. TP53INP2-KO mouse embryonic fibroblasts show enhanced protein levels of LDL-Receptor under basal conditions. Wild-type and TP53INP2-KO Mouse embryonic fibroblasts (MEFs) were treated for 24 h with 1 μM U18666A and 100 μg / mL human low-density lipoprotein (LDL). Quantification of (A) LDL-Receptor (LDL-R) protein and (B) TP53INP2 protein levels in WT and KO MEFs (n = 3 - 4). (C) Representative western blot of TP53INP2 and LDL-R protein levels in WT and KO MEFs. (D) LDL-R mRNA levels in WT and KO MEFs in basal conditions (n = 3). Data represent mean ± SEM. P-values < 0.05 were considered significant (*) for WT vs. KO, (a) for DMSO vs. U18666A treatment and (b) for PBS vs. LDL.

Given the increased FC accumulation in TP53INP2-depleted cells upon U18666A treatment we analyzed the protein levels of LDL-R in MEF cells. We found enhanced levels of LDL-R protein in TP53INP2-KO MEFs in vehicle treated cells. These differences were lost by U18666A and/or LDL treatment. LDL-treatment significantly reduced LDL-R protein levels in WT and KO cells, this reduction was abrogated by simultaneous U18666A treatment (Figure

61AB). These enhanced basal protein levels of LDL-R protein where not due to higher expression LDL-R mRNA, as levels were similar under these conditions in WT and TP53INP2-KO (Figure 61C). Furthermore, we found that TP53INP2 protein levels in WT-MEFs were moderately increased by U18666A treatment (Figure 61AD).

We analyzed LDL-R protein levels in livers of loxP and TP53INP2-LKO animals, and no difference was observed between the genotypes (Figure 62).

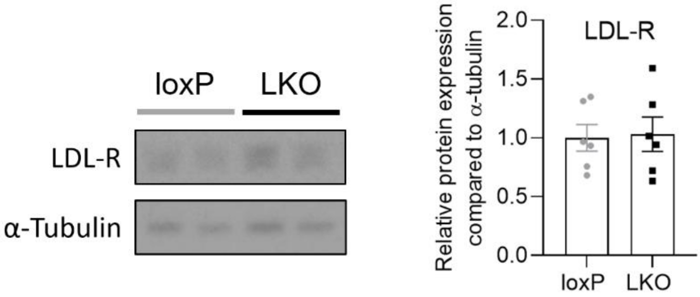

Figure 62. LDL-Receptor protein levels are similar to controls in TP53INP2-depleted livers. Representative western blot and quantification of LDL-Receptor (LDL-R) protein levels in livers of 24-week-old loxP and TP53INP2-LKO animals on standard diet (n = 6). There was no statistical difference between genotypes.

To analyze if autophagy is impaired by high cellular cholesterol content, we analyzed the autophagic flux in primary hepatocytes after an overnight (16 h) treatment with native LDLs and in PBS treated control cells.

TP53INP2-LKO hepatocytes demonstrated impaired LC3-II protein accumulation upon BafA1 treatment and a tendency to accumulate less p62 protein under basal conditions (Figure 63 ACD), as previously observed (Figure 17). LDL-treatment in TP53INP2-LKO hepatocytes did not further reduce the autophagic flux (Figure 63BCD). Overnight LDL-treatment significantly reduced LC3-II protein accumulation in loxP hepatocytes (Figure 63ABC) , accompanied with a trend for reduced p62 protein accumulation compared to control cells (Figure 63ABD). The differences in the autophagic flux between loxP and

TP53INP2-depleted hepatocytes were abolished by an LDL-treatment (Figure 63).

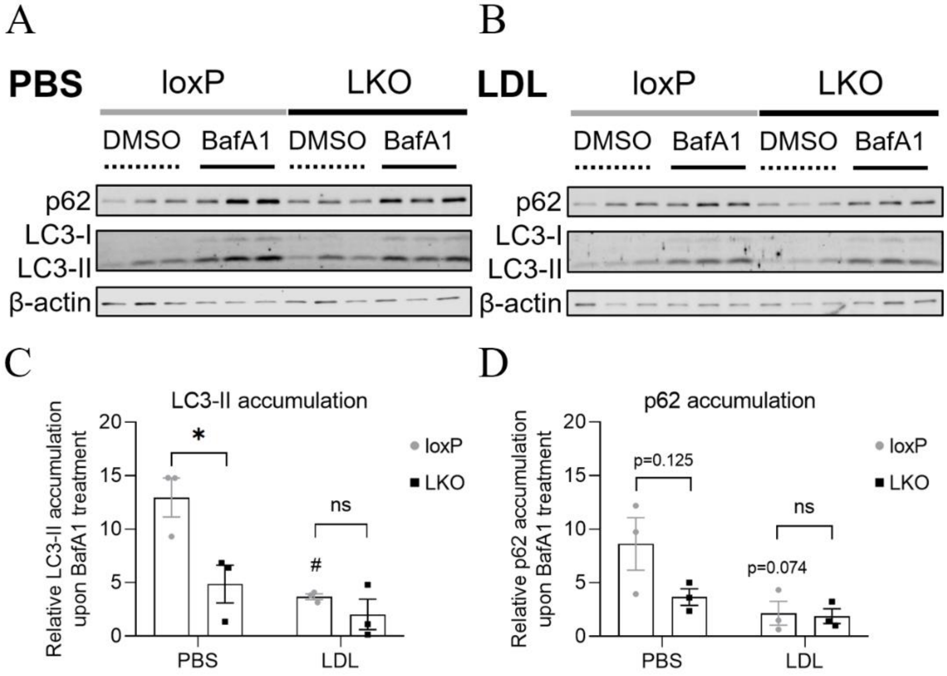

Figure 63. Cholesterol loading of primary hepatocytes by low-density lipoprotein treatment reduces autophagic flux in loxP cells to the level of TP53INP2-LKO hepatocytes. Primary hepatocytes were treated overnight (16 h) with 100 µg / mL human low-density lipoprotein (LDL) or a PBS vehicle. For the last 4 h of the treatment, 200 nM Bafilomycin A1 (BafA1) or a DMSO vehicle was added. Representative western blot of p62 and LC3 protein accumulation upon BafA1 treatment in (A) PBS vehicle or (B) LDL treated primary hepatocytes from loxP and TP53INP2-LKO animals. Quantification of (C) LC3-II and (D) p62 protein accumulation in BafA1 treated primary hepatocytes after an overnight treatment with PBS or LDL (n = 3). Data represent mean ± SEM. P-values < 0.05 were considered significant (*) for loxP vs. LKO and (#) for PBS vs. LDL.

Given the fact that the autophagic flux is reduced to similar levels in LDL-treated control and TP53INP2-depleted cells, but we still found increased FC accumulation under these conditions upon U18666A treatment, we analyzed additional contributors to lysosomal FC accumulation.

Lysosome-associated membrane protein 1 (LAMP1) is a lysosomal transmembrane protein located in the lysosomal membrane [227]. Overexpression of LAMP1 protein has been shown to rescue U18666A-induced FC accumulation [228]. Furthermore, LAMP1 is able to bind cholesterol, as well as NPC1 and NPC2 proteins [229].

We measured the expression of LAMP1 protein levels in WT and TP53INP2-KO MEFs and found enhanced basal levels in KO cells. While a 24 h treatment of U18666A significantly enhanced LAMP1 protein levels in WT cells, there was no further increase in TP53INP2-depleted cells (Figure 64).

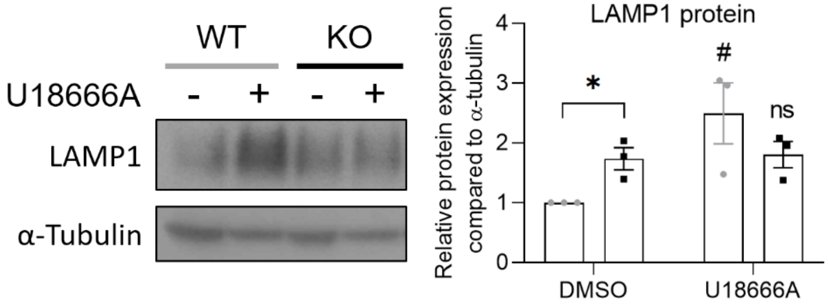

Figure 64. TP53INP2-KO mouse embryonic fibroblasts have enhanced basal protein levels of LAMP1 compared to controls but don't accumulate LAMP1 upon U18666A treatment. Representative western blot and quantification of LAMP1 protein levels in WT and TP53INP2-KO mouse embryonic fibroblasts under basal conditions (DMSO treated) or upon 24 h of 1 µM U18666A treatment (n = 3). Data represent mean ± SEM. P-values < 0.05 were considered significant (*) for WT vs. KO and (#) for DMSO vs. U18666A.

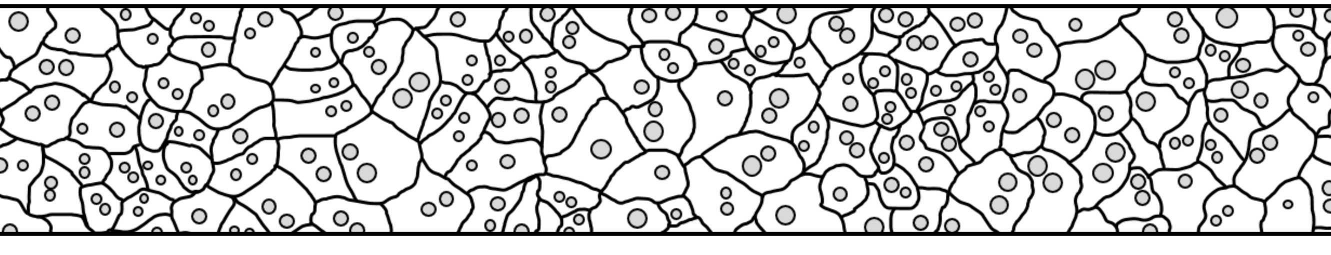

DISCUSSION

5. DISCUSSION

5.1. Hepatic TP53INP2 expression responds to nutritional manipulation

In this study, we have evaluated the hepatic expression of the autophagic protein TP53INP2 under various conditions. We found that TP53INP2 levels are significantly reduced in livers of overnight fasted animals, as well as in primary hepatocytes, treated for 16 h with the starvation buffer EBSS. However, under the same conditions, mRNA levels were enhanced. This can be explained by the fact, that TP53INP2 protein has been found to be degraded by the autophagic process [230], which is strongly induced by fasting conditions. Therefore, it is likely that there is continuous or even induced translation of the protein in hepatocytes, since it can also be detected in fasted livers via western blot, but its degradation through autophagy results in diminished protein levels.

Additionally, we found that TP53INP2 expression is enhanced on mRNA and protein level in livers of animals treated with high-fat diet (HFD) for a period of 8 weeks. This suggests, that TP53INP2 could be beneficial for hepatocytes in the presence of abundant nutrients. Interestingly, prolonging the HFD treatment to a period of 16 weeks blunted the upregulation of TP53INP2 mRNA, and similar mRNA levels found in livers of young and two-year-old animals showed that this was not due to the age difference between 8-week and 16-week HFD treated animals. Instead, the reduced hepatic expression compared to 8-week HFD treated animals could be due to the advanced steatotic conditions. This assumption goes in line with the reduced hepatic TP53INP2 protein expression that we found in the model of non-alcoholic steatohepatitis (NASH), where mice were fed with a methionine and choline-deficient diet for a period of three weeks to induce lipid accumulation, inflammation, and fibrosis. In this case, reduced protein levels of TP53INP2 are not likely to result from autophagic degradation, as MCD-treatment has been found to impair hepatic autophagy [231] and the mice

5.2. Evaluation of the impact of hepatic TP53INP2 loss-of-function in animals on standard diet

TP53INP2 is a protein found to be a positive regulator of autophagy [150]. In this study we have performed an evaluation of the impact of liver-specific TP53INP2-ablation in animals on standard diet. The Cre/lox system was utilized to generate mice lacking hepatic TP53INP2 protein. Upon successful generation and validation of the liver-specific knockout, 24-week-old adult animals were analyzed. We observed similar body weight and body composition of control loxP and TP53INP2-LKO animals. We did not find differences in the weight of the liver or other non-hepatic tissues. This is interesting, as the loss of hepatic autophagy in other mice models is detrimental for livers. Reports show that the hepatocyte-specific depletion of the autophagy-regulated protein (ATG) 5, as well as ATG7, both essential for the autophagic process, causes hepatomegaly and tumor formation in the liver [232-234]. Hepatomegaly without tumor formation was also reported for the liver-specific knockout focal adhesion kinase interacting protein of 200 kD (FIP200), which is required for autophagosome formation [235, 236]. The liver-specific knockout of Class III PI3K (PIK3C / Vps34), a regulator of autophagy, resulted in hepatomegaly [237]. Hepatomegaly was also observed in the liver-specific double knockout model of unc-51 like autophagy activating kinase 1 and 2 (Ulk1/2), two autophagy activating kinases [238, 239]. These models have in common that autophagy is essentially completely abolished, explaining the hepatomegaly phenotype. In the case of liver-specific TP53INP2-LKO animals, autophagy is still occurring, but less efficiently. This is likely the cause for the absence of hepatomegaly in this model.

LoxP control animals showed an increase in bodyweight during aging, as previously reported for C57BL/6J mice [240, 241], while TP53INP2-LKO animals did not. This difference in body weight was due to reduced fat mass of TP53INP2-LKO animals, suggesting an aberrant systemic lipid metabolism. Although the total fat mass in LKO animals was decreased, livers accumulated similar amounts of triglycerides and cholesterol in both genotypes during a one-year period of aging. We observed no apparent liver damage in one-year old animals at the sacrifice,. This was corroborated by the observation that plasma alanine aminotransferase (ALT) and plasma aspartate aminotransferase (AST) levels were not increased. In fact, plasma ALT levels were reduced in one-year old animals compared to 4-month-old mice, especially in loxP control animals. Decreased plasma ALT levels during aging have been previously reported for male C57BL/6J mice [242].

Next we analyzed the effect of hepatic TP53INP2-ablation on liver autophagy. We analyzed the protein levels of autophagic markers in livers of fasted animals and observed similar levels of p62, but differences in LC3 levels. Precisely, we detected an accumulation of the free mature form of LC3 (LC3-I), while levels of the lipidated form (LC3-II) were diminished. This suggests and impaired conjugation of phosphatidylethanolamine to LC3, which is essential for autophagy, as LC3-II levels correlate with the number of autophagosomes [165, 243]. Since LC3-II itself is subjected to autophagosomal degradation, it is central to measure LC-II levels in the presence and absence of autophagy inhibitors to estimate the efficiency of the autophagic flux [243]. We evaluated the autophagic flux in loxP and TP53INP2-depleted primary hepatocytes using Bafilomycin A1 (BafA1). We observed that TP53INP2-ablation causes a reduced autophagic flux, as we found less LC3-II accumulation in TP53INP2-LKO hepatocytes upon Baf1A treatment.

Given the defects in autophagy in livers of TP53INP2-LKO animals, we analyzed the effects of TP53INP2-ablation in fasted animals, as autophagy is activated by food deprivation [164]. We observed that an overnight fast of 16 h caused a significant weight loss of similar extent in all animals, regardless of the genotype. Hepatic TP53INP2-depletion did not impact glucose homeostasis in overnight fasted animals on a standard chow diet, as blood glucose levels were similar in 4-month-old animals. The results of a glucose tolerance test (GTT), performed in overnight fasted 1-year-old animals, showed a similar capacity to lower blood glucose levels after injection of a glucose bolus in loxP and TP53INP2-LKO animals, indicating that glucose metabolism in overnight fasted animals is not impacted by hepatic TP53INP2-ablation, neither in animals of advanced age.

However, when mice were fasted for a shorter period of 4 h, after food intake was synchronized, loxP animals showed lower blood glucose levels than TP53INP2-LKO animals. Additionally, a 4 h fast decreased plasma triglyceride levels in loxP animals, but not in TP53INP2-LKO animals. On the other hand, we observed that plasma non-esterified free fatty acids (NEFAs) levels increased significantly upon a short 4 h fast in all animals, but to a higher extent in TP53INP2-LKO animals, which could be the result of impaired oxidation of free fatty acids, which depends on PPARα activity [244].

The differences in blood glucose, plasma triglyceride and NEFA levels were abrogated, when mice were fasted for a longer period of 16 h. However, we found significantly lower plasma β-hydroxybutyrate levels in TP53INP2-LKO animals, corroborating the impaired capacity for fatty acid oxidation, since fatty acids are the main substrates for ketogenesis [245].

The observation that the differences in blood glucose, plasma triglyceride and NEFA levels after 4 h of fasting were abrogated by prolonging the fasting period suggests that loxP animals initially show a superior capacity to adapt to fasting conditions compared to TP53INP2-LKO mice.

Hematoxylin and Eosin (H/E) staining of liver tissues showed normal morphology of loxP and TP53INP2-LKO livers under fed conditions. In fasted conditions we found small unstained vacuoles, derived from extracted lipids during sample preparation. We observed that these vacuoles were more abundant in fasted TP53INP2-depleted livers. Hepatic lipids were extracted and measured in fed and fasted loxP and TP53INP2-LKO animals, to verify the enhanced lipid accumulation. All animals showed increased hepatic triglyceride and cholesterol content, as previously described and referred to as fasting-induced hepatic steatosis [246], however the levels were significantly higher in TP53INP2-depleted livers.

There is conflicting data about the role of autophagy in the development of steatosis. While hepatocyte-specific depletion of ATG7 is reported to enhance hepatic steatosis under fed and fasted conditions [118], others report that hepatic ATG7-depletion protects against fasting induced steatosis [247, 248]. Hepatocyte-specific knockout of autophagy-related gene 3 (ATG3) on the other hand was reported to ameliorate diet-induced steatosis, although in an autophagy independent manner [249]. Another study showed that liver-specific FIP200 knockout prevents fasting-induced hepatic steatosis [235]. Liver-specific depletion of Vps34 on the other hand resulted in steatosis under fed conditions [237]. This shows that distinct genetic models of impaired autophagy affect hepatic lipid metabolism differently.

Hepatic transcription was analyzed in livers of fed loxP and TP53INP2-LKO animals by performing RNASeq. Samples were processed by the Functional Genomics Core Facility of the IRB Barcelona and sequencing was performed at the CNAG sequencing unit of the Centre for Genomic Regulation. Obtained data was analyzed by the Biostatistics and Bioinformatic Core Facility of the IRB Barcelona and revealed the differential expression of 235 genes between the genotypes. Precisely, the expression of 87 genes was upregulated, while the expression of 148 genes was reduced in TP53INP2-LKO livers.

Gene set enrichment analysis (GSEA) showed a marked reduction of genes of the peroxisome hallmark gene set. Furthermore, the expression of genes belonging to the KEGG database pathways fatty acid metabolism, biosynthesis of unsaturated fatty acids, and PPAR signaling was significantly reduced.

Using the EnrichR GSEA tool, we analyzed the genes found to be downregulated in TP53INP2-LKO livers, to obtain information about transcription factors potentially contributing to the reduced expression. Results showed an overlap of 58 genes with LXR and RXR data sets, and of 52 genes with the PPARα data set of the ChEA 2016 gene set library suggesting impaired LXR and PPARα signaling in TP53INP2-depleted livers.

Impaired PPARα activity would explain the impaired fatty acid oxidation and ketogenesis, and the advanced fasting induced hepatic steatosis, as the same phenotype was observed in liver-specific PPARα animals [85]. Furthermore, we analyzed the expression of PPARα target genes in liver and found reduced mRNA levels of Cyp2c55, belonging to the cytochrome P450 superfamily [168] and the catalytic subunit of G6Pase (G6PC) [169]. In addition, we found a tendency for reduced expression of the lipogenic gene ATP-citrate lyase (Acly) [170] and the peroxisomal acyl-CoA oxidase 1 (Acox1) essential for long-chain fatty acid oxidation [171]. These results corroborate impaired PPARα transcriptional activity in livers of TP53INP2-LKO animals.

We also analyzed the expression of LXRα-target genes, as LXRα is highly expressed in the liver and important for triglyceride and cholesterol homeostasis, while LXRβ is ubiquitously expressed [91]. We observed a reduction of hepatic mRNA levels of the ATP-binding cassette sub-family G member (ABCG)8 and a tendency of reduced levels of its heterodimeric partner ABCG5, which together transport sterols across membranes [172, 173].

TP53INP2-depleted livers showed a tendency for reduced mRNA levels of the rate-limiting enzyme of the neutral pathway of bile acid synthesis, cholesterol 7-alpha-hydroxylase (Cyp7a1) [91], and reduced levels of sterol regulatory element-binding protein 1 (Srebp1c) mRNA, which plays an important role in cholesterol metabolism [175]. Together, our data suggests that TP53INP2-depletion impairs PPARα and LXRα transcriptional activity in livers.

Next, we set out to evaluate the transcriptional activity of LXRα *in vitro* using primary hepatocytes obtained from loxP and TP53INP2-LKO animals. LXRα forms a permissive heterodimer with the retinoid X receptor (RXRα), allowing the dimer to be activated by ligands of either partner [91]. We treated hepatocytes with a DMSO vehicle, a synthetic agonist for either LXRα (GW3965) alone or in combination with the synthetic RXRα agonist LG268.

Interestingly, under *in vitro* conditions, we found an enhanced mRNA expression of the LXRα target gene ATP-binding cassette transporter A1 (Abca1) upon LXRα- and LXRα/RXRα-agonist treatment in TP53INP2-depleted hepatocytes. The expression of Srebp1c, previously found to be reduced in TP53INP2-depleted livers, was similar in primary hepatocytes from either genotype under basal conditions. While LXRα agonist treatment alone increased Srebp1c mRNA levels, additional treatment with RXRα agonist reduced Sreb1c mRNA no basal levels. The expression of Abcg8, another LXRα target gene previously found to be expressed at lower levels in TP53INP2-depleted livers, was similar in isolated hepatocytes of either genotype. Agonist treatment increased Abcg8 levels, without differences between loxP or TP53INP2-LKO hepatocytes. The distinct results obtained from the same cells under *in vivo* and *in vitro* conditions suggest, that LXRα transcriptional activity is feasible, or can even be enhanced (in case of the Abca1 target gene) in TP53INP2-depleted cells. This suggests that the reduced activity of LXRα in livers could derive from the lack of availability of endogenous ligands.

Next, we performed luciferase assays to validate the enhanced transcriptional activity of TP53INP2-depleted cell in vitro. PPRE-luciferase and

LXRE-luciferase experiments were performed in mouse embryonic fibroblasts (MEFs) with simultaneous overexpression of human PPARα or LXRα, respectively. As expected, TP53INP2-KO MEFs showed enhanced levels of PPARα activity, in the absence or presence of the synthetic PPARα ligand WY-14643. Of note, WY-14643 treatment did not further increase PPARα transcriptional activity in cells when PPARα was overexpressed at the same time, likely due to cytotoxic effects that have been previously described [180]. We also observed higher transcriptional activity of LXRα in TP53INP2-LKO MEFs, in the presence of absence of the agonist GW3965. Furthermore, we analyzed the protein expression of Abca1 in WT and KO-MEFs in the presence and absence of GW3965. TP53INP2-KO MEFs showed enhanced protein levels of Abca1 under basal and agonist treated conditions.

To validate the relationship of TP53INP2 levels and PPARα/LXRα transcriptional activity, we also performed PPRE and LXRE luciferase experiments in TP53INP2-overexpressing cells. In order to do this, we generated stable GFP (control) and TP53INP2-GFP overexpressing Huh7 hepatocarcinoma cells via lentiviral transduction. Subsequently, cells were selected using puromycin, since the lentiviral transduction also conveyed a puromycin resistance. Additionally, GFP-positive cells were sorted by Fluorescence-activated cell sorting (FACS), which allowed us to detect that the expression of GFP compared to TP53INP2-GFP was significantly higher, possibly due to the pro-apoptotic effect of high TP53INP2-levels [148]. It is likely that cells expressing high levels of TP53INP2 already underwent apoptosis or proliferated less until the cells were finally sorted by FACS. However, both GFP and TP53INP2-GFP were overexpressed, and this was validated by western blot.

Finally, we used the generated GFP- or TP53INP2-GFP overexpressing Huh7 cells to perform PPRE- and LXRE-luciferase assays, with endogenous or overexpressed levels of PPARα or LXRα, respectively. We observed that overexpression of TP53INP2-GFP significantly impaired PPARα activity in all conditions, in the presence or absence of PPARα agonist WY-14643 and at endogenous and overexpressed levels of PPARα. WY-14643 treatment enhanced transcriptional activity at endogenous PPARα levels. Simultaneous PPARα overexpression and agonist treatment reduced the activity compared to vehicle treated cells. This observation of WY-14643 treatment was similar to the results we obtained in PPRE luciferase assays using MEF cells.

LXRα activity was low in Huh7 cells at endogenous levels, even upon agonist (GW3965) treatment, indicating that Huh7 cells have very limited LXRα expression. Overexpression of LXRα increased LXRα activity, but we found a reduced activity upon GW3965 treatment in TP53INP2-GFP overexpressing cells.

Together, our obtained results show that TP53INP2-ablation enhances, and TP53INP2 gain-of-function hinders the transcriptional activity of PPARα, as well as of LXRα, under *in vitro* conditions.

5.3. TP53INP2-depletion enhances HFD-induced hepatic steatosis and affects glucose and cholesterol metabolism

To analyze whether TP53INP2 plays a role in lipid metabolism, we subjected loxP and TP53INP2-LKO animals to a high-fat diet (HFD) treatment for either 8 or 16 weeks. HFD caused a significant weight gain in all animals compared to chow fed control animals, without differences between genotypes. TP53INP2-LKO showed enhanced liver weight after 16 weeks of HFD. Food intake and fecal excretion were reduced on the high-caloric HFD, but it was not influenced by the genotype. Morphological studies showed enhanced lipid accumulation under HFD conditions, and a non-alcoholic fatty liver disease (NAFLD) phenotype in animals, without enhanced glycogen deposition. The abundance of unstained vacuoles derived from extracted lipids was higher in the liver tissues of TP53INP2-LKO animals. Staining liver tissue with the macrophage marker F4/80 revealed that a 16-week HFD treatment increases the abundance of macrophages in TP53INP2-depleted livers compared to chow fed controls. The F4/80-stained area in HFD treated loxP animals did not increase compared to chow fed animals.

To further assess the condition of livers of animals subjected to HFD, we measured plasma parameters to evaluate liver damage and function. Plasma alanine aminotransferase (ALT) levels increased in loxP and TP53INP2-LKO mice after 16 weeks of HFD consumption. Although AST levels did not increase upon HFD treatment, there was a tendency of higher plasma levels in TP53INP2-LKO animals compared to loxP. Furthermore, plasma total protein, albumin and globulin levels were assessed, as the liver is the predominant origin of plasma proteins [186]. Interestingly, we found that chow fed TP53INP2-LKO animals show hypoproteinemia in form of decreased plasma levels of total protein, albumin and globulin, which was abrogated by a HFD treatment. Although secretion of plasma proteins was hampered in LKO animals on chow diet, hepatic protein content was similar in loxP and TP53INP2-depleted livers. While the HFD treatment raised plasma protein concentration to the levels of loxP animals, we found a moderate decrease in hepatic protein content. To evaluate if the impaired albumin secretion of TP53INP2-LKO animals on chow diet is a result of reduced transcription, we measured hepatic albumin mRNA levels. The hypoalbuminemia of chow-fed TP53INP2-LKO animals was not a result of reduced albumin mRNA transcription. Hepatic albumin mRNA levels increased upon HFD treatment and was significantly higher in TP53INP2-LKO animals after 8 weeks of HFD treatment, likely contributing to the adjusted plasma levels. Plasma albumin in regulating colloidal osmotic pressure, and acts as a carrier of bilirubin, long-chain fatty acids, divalent cations such as calcium and magnesium, bile acids and other metabolites, facilitating their distribution and clearance [250]. Reduced serum albumin levels correlate with mortality risk, even in seemingly healthy individuals [251]. Given the importance of plasma albumin it is of interest to further analyze the underlying cause of hypoalbuminemia in TP53INP2-LKO animals, which could be either impaired translation or secretion of the protein or an enhanced albumin catabolism.

Although TP53INP2-LKO animals showed normal glucose homeostasis on chow diet, we observed increased fasting blood glucose levels, and a tendency for elevated fasting plasma insulin after a HFD treatment of 7 weeks. These two parameters can be utilized to calculate a commonly used surrogate marker of insulin sensitivity termed homeostasis model index of insulin resistance (HOMA-IR). HFD-treated TP53INP2-LKO animals showed significantly enhanced HOMA-IR values compared to loxP control mice. A glucose tolerance test (GTT) performed in overnight fasted HFD-treated animals showed an impaired capability of TP53INP2-LKO animals to lower blood glucose concentration upon intraperitoneal injection of a glucose bolus. This was accompanied by enhanced insulin levels 5 min after the glucose bolus injection, corroborating the impaired glucose handling of HFD-fed TP53INP2-LKO animals.

We further analyzed the plasma obtained from fasted HFD-treated mice and observed similar fasting triglyceride levels between genotypes. However, we detected diminished plasma β-hydroxybutyrate levels, indicating that ketogenesis in TP53INP2-LKO animals is also impaired in HFD-fed animals. Furthermore, fasting plasma cholesterol levels were lower compared to loxP control animals.

To elucidate the influence of TP53INP2-depletion on triglyceride (TG) metabolism under HFD conditions, we performed several experiments. First, we measured plasma and hepatic triglyceride concentrations. We observed that 16-week HFD treated TP53INP2-LKO animals had lower plasma TG levels, while liver TG content was increased. Enhanced hepatic lipid accumulation in TP53INP2-depleted livers was also detected by Oil-Red-O staining of lipids in liver tissue of HFD-fed animals.

Given the advanced hepatic levels of triglycerides, we assessed if TP53INP2-depletion alters the metabolism of dietary derived lipids by performing an oral lipid tolerance test. HFD-treated overnight fasted animals were given an oral gavage of a soybean oil emulsion (Intralipid). Blood was collected before and hourly for a period of 4 hours after the administration of Intralipid. We did not detect differences in the handling of dietary derived lipids between genotypes, as the levels of TG and NEFA rose and declined in a similar manner, although we observed a tendency of lower NEFA levels in TP53INP2-LKO animals at one hour post-gavage.

Elevated hepatic triglycerides could be a result of impaired very-low-density lipoprotein (VLDL) secretion by the liver [194, 252]. To further address this possibility, we performed a VLDL-secretion assay using Poloxamer 407 (P-407). Chow and HFD-treated animals were fasted for four hours to decrease the influence of dietary derived lipids. After obtaining a basal blood sample, P-407 was injected intraperitoneally to inhibit lipases [195]. Subsequently, plasma TG and cholesterol levels were monitored for a period of 4 hours. Although plasma TG levels of HFD-fed animals were significantly higher at the timepoints 1 and 4 h post-injection, the calculated hourly secretion rate of triglycerides was not impacted by the diet or genotype of animals, suggesting the rate of VLDL secretion by livers was similar under all experimental conditions. Plasma levels of cholesterol did not differ significantly between chow and HFD treated animals of either genotype, however, the calculated hourly cholesterol accumulation in plasma upon P-407 injection showed a tendency to be lower in HFD-treated TP53INP2-LKO animals. Given these results, impaired VLDL secretion is not contributing to enhanced hepatic triglyceride content in TP53INP2-LKO animals on HFD.

Hepatic steatosis could be the result of enhanced lipogenesis. To validate if this is the case in HFD-treated TP53INP2-LKO animals, we measured the expression of transcription factors that are essential for de novo lipogenesis in the livers of animals subjected to 16 weeks of HFD. The mRNA levels of Carbohydrate-responsive element-binding protein (Chrebp), a transcription factor for glucose mediated lipogenesis, were equal in loxP and TP53INP2-LKO animals. Liver X Receptor α (LXRα) mRNA in HFD-fed animals did not depend on the genotype. The mRNA levels of Srebp1c, another important lipogenic transcription factor, were reduced in TP53INP2-LKO animals. Furthermore, RNAseq analysis performed with isolated RNA from mice after 16 weeks of HFD, showed only 49 differentially expressed genes between the genotypes, suggesting the phenotype of TP53INP2-LKO animals on HFD is not based on transcriptional alterations. Interestingly, comparison of the expression of genes found to be differentially expressed between loxP and TP53INP2-LKO animals on chow diet, with the results we obtained from animals on HFD shows, that these changes were abrogated by a HFD-treatment. This goes in line with the hypothesis, that there is a limited availability of endogenous ligands for PPARα (long-chain fatty acids and eicosanoids [253]) and LXRα (oxysterols [254]) in TP53INP2-depleted livers, as the dietary supply of ligands (or their precursors), by a diet rich in lipids, blunted the differential expression of genes.

We also evaluated the influence of hepatic TP53INP2 levels on cholesterol metabolism under HFD conditions.

Plasma and hepatic cholesterol levels of chow-fed animals were determined and compared with the levels of animals subjected to either 8 or 16 weeks of HFD. The HFD treatment elevated plasma cholesterol levels in all animals, and after 16 weeks of HFD we found a tendency for higher plasma cholesterol levels in TP53INP2-LKO animals compared to loxP mice. Liver cholesterol content was also enhanced by the HFD treatment. Precisely, TP53INP2-LKO animals showed higher cholesterol accumulation after 8 weeks of HFD, compared to loxP animals. However, a prolongation of the HFD treatment resulted in reduced levels of hepatic cholesterol in TP53INP2-LKOs compared to the 8 week timepoint, while hepatic cholesterol content of loxP animals further increased. This suggests that TP53INP2-depleted livers initially accumulate cholesterol faster, which possibly causes an adaptation.

The cholesterol distribution in plasma was measured by precipitating ApoB containing lipoproteins, while high-density lipoproteins (HDL) remain in the supernatant. We observed a tendency for an increase in the HDL-fraction in plasma of HFD-fed TP53INP2-LKO animals compared to loxP controls. Additionally, we measured the mRNA expression of ApoA1, the major apolipoprotein of HDLs [199, 200]. ApoA1 mRNA expression was similar on chow diet and increased upon HFD treatment and was significantly increased in TP53INP2-depleted livers after 8 weeks of HFD. While levels further increased upon prolongation of the HFD treatment, ApoA1 mRNA levels showed a high standard deviation between individual animals. Protein expression of ApoA1 was significantly increased in TP53INP2-depleted livers after 16 weeks of HFD. Moreover, plasma of loxP and TP53INP2-LKO animals on chow or subjected to 16 weeks of HFD were analyzed by 2D diffusion-ordered Nuclear Magnetic Resonance (NMR) spectroscopy. We observed that HFD treatment of animals caused an increase in HDL particle number and reduced the HDL particle diameter compared control animals on chow. However, these effects were more pronounced in loxP animals, resulting in lower HDL particle numbers and smaller HDL particle diameters in HFD-fed TP53INP2-LKO animals. We did not observe statistical differences in low-density lipoprotein (LDL) particle number or particle diameter between the genotypes. Together, these results suggest that TP53INP2-depletion in livers modifies HDL metabolism.

To enhance the cholesterol induced stress on livers, we decided to treat animals with a western diet (WD), rich in fat (40 %kcal) and cholesterol (0.02 % w / w), for a period of 16 weeks. WD treatment caused an increase in body weight, regardless of the genotype of the animals, without affecting the liver weight. However, we observed a mild reduction of TP53INP2 mRNA in livers of loxP animals subjected to a WD, implying that high expression of TP53INP2 might not be beneficial under these conditions. WD treatment did not alter plasma TG levels, but severely increased plasma cholesterol, as well as liver TG and cholesterol content, without statistical difference between the genotypes.

Liver morphology was severely impaired by the WD treatment, with drastic lipid accumulation in pericentral and periportal regions of the livers, but in the absence of accumulation of collagen and glycogen deposition. We did not observe an obvious difference in liver morphology between the genotypes. WD treatment increased the F4/80-positive area in TP53INP2-LKO livers but did not in loxP mice. This resulted in a tendency for increased F4/80-stained area in livers of WD-fed TP53INP2-LKO compared to loxP animals. Plasma concentration of the liver damage marker alanine aminotransferase (ALT) was increased by a WD treatment equally in both genotypes. Plasma aspartate aminotransferase (AST) levels were enhanced by a WD treatment only in the case of loxP animals, yet the difference in the F4/80-postive area did not reach statistical significance between the genotypes after WD-consumption.

A major part of cholesterol catabolism is the synthesis of bile acids (BAs) and their enterohepatic circulation, consisting of the secretion of BAs from the site of production (liver) into the intestinal tract, followed by the reabsorption into the blood stream and the re-uptake by liver. These processes are regulated by the transcription factor farnesoid X receptor α (FXRα), with BAs acting as its endogenous ligands [205-208]. We observed that loxP mice showed significantly higher total bile acid levels in plasma, as well as enhanced daily fecal bile acid secretion compared to TP53INP2-LKO mice, when animals were subjected to 16 weeks of WD.

Given the differences in the concentration of bile acids, in loxP and TP53INP2-LKO animals that were subjected to the WD, we analyzed the expression of FXRα target genes in liver and the terminal ileum, where the majority of BAs is reabsorbed [206].

In the liver, FXRα reduces for instance the expression of the rate-limiting enzyme of the neutral pathway for BA synthesis, cholesterol 7α-hydroxylase (Cyp7a1) and of the NA$^+$-dependent taurocholate cotransport peptide (Ntcp), reducing the uptake of BAs into hepatocytes [206]. The bile salt export pump (Bsep) is an FXRα target in the liver, that promotes bile salt export from hepatocytes. Although we detected an increase of FXRα-mRNA itself, the mRNA expression of its target genes Cyp7a1, Ntcp and Bsep was similar in both genotypes.

FXRα signaling in the ileum reduces the expression of the apical-sodium-dependent BA transporter (Asbt), also referred to as Ntcp2, impairing BA absorption [212]. The differences in Fxrα and Ntcp2 mRNA levels between loxP and TP53INP2-LKO animals in the ileum were not statistically significant.

Together, this data suggests that hepatic TP53INP2-depletion did not contribute to impaired steatosis in response to the high cholesterol content of the WD. Nonetheless, TP53INP2-depletion in livers resulted in altered total bile acid content in plasma and feces. It would be of interest, to further investigate gall bladder function and the bile acid composition in addition to the evaluation of the total amount, as both can influence liver function [255]. Another modulator of bile acid metabolism are bile acid-transforming gut microbiota [256, 257]. However, this factor might be a minor contributor to the observed effects of hepatic TP53INP2-depletion, as littermates of different genotypes were kept under co-housing conditions, allowing normalization of the gut-microbiome between animals through coprophagy [258].

5.4. Hepatocyte-specific TP53INP2-depletion impacts intracellular cholesterol trafficking

Given the accelerated accumulation of cholesterol in TP53INP2-depleted livers during a HFD treatment, followed by a decrease of cholesterol content upon prolongation of the treatment, we hypothesized TP53INP2 could contribute to intracellular cholesterol trafficking.

There are several mechanisms for intracellular cholesterol transport and distribution. First, the uptake of different cholesterol containing plasma lipoproteins is mediated by distinct receptors. Examples are the low-density lipoprotein (LDL) receptor (LDL-R) for LDLs [221], the scavenger receptor CD36 for oxidized LDLs (oxLDLs) [259], the Low-density lipoprotein (LDL) receptor-related protein 1 (LRP1) in case of aggregated LDLs (agLDLs) [225, 226] or the Scavenger receptor class B member 1 facilitating the uptake of high-density lipoproteins (HDLs) [260]. The exogenous cholesterol is taken up by endocytosis involving the different receptors, and cholesterol is transported into late endosomes and lysosomes [221]. Free cholesterol (FC) is sequestered from lysosomes in a process involving the coordinated action of Niemann-Pick C1 (Npc1) and Npc2 proteins [222]. Recently, it was reported that the lysosome-associated membrane protein 1 (LAMP-1) contributes to lysosomal FC egress, even upon inhibition of Npc1 by U18666A treatment [228]. Finally, free cholesterol is redistributed to other organelles and the plasma membrane, facilitated by intracellular proteins such as members of the steroidogenic acute regulatory protein (StAR)-related lipid transfer (START) domain family [218] or members of the Oxysterol-binding proteins (OSBPs) [219]. De novo synthesized cholesterol is transported from the site of synthesis (endoplasmic reticulum) to the plasma membrane, in an ATP-dependent vesicular manner involving the Golgi apparatus [220]. Taken together, intracellular is complex and depends on the interaction of different cellular mechanisms.

To determine the impact of TP53INP2-depletion on intracellular cholesterol trafficking, we treated primary hepatocytes isolated from loxP and TP53INP2-LKO livers with the inhibitor of Npc1 protein U18666A. Vehicle treated cells showed a similar content of free cholesterol (FC), determined by FC staining using Filipin III. However, we observed an enhanced accumulation of

FC in the lysosomal compartments in TP53INP2-depleted hepatocytes upon Npc1 inhibition, compared to loxP control cells. This result was reproduced in mouse embryonic fibroblasts (MEFs). Precisely, TP53INP2-KO MEFs accumulated higher levels of FC upon U18666A treatment than WT-MEFs, even though basal FC levels were moderately lower in vehicle treated KO-cells. Additionally, we incubated MEFs with U18666A, in addition to human native LDLs (nLDLs) or aggregated (agLDLs), two distinct cholesterol containing lipoproteins that are taken up by cells using different receptors, namely LDL-R and LRP1. Analysis of Filipin III stained cells showed an enhanced FC accumulation in TP53INP2-KO MEFs in either condition, suggesting the enhanced lysosomal accumulation is independent of the origin of exogenous cholesterol.

Interestingly, we found an increased protein expression of LDL-R in TP53INP2-KO MEFs, compared to WT-MEFs, while mRNA levels were similar. Since LDL-R protein expression depends on the cholesterol content in the membrane of the endoplasmic reticulum [261], we evaluated the levels of LDL-R in WT- and KO-MEFs after loading cells with cholesterol using LDLs. Additionally, intracellular cholesterol trafficking was blocked by U18666A treatment. The expression of LDL-R protein was significantly reduced by LDL-treatment in both WT- and KO-cells to similar levels, suggesting that TP53INP2-depleted cells are capable of LDL-R degradation. Upon blockage of intracellular cholesterol trafficking, LDL-R protein levels significantly increased in LDL-treated cells, likely due to the lower concentration of FC in the endoplasmic reticulum membrane, facilitating LDL-R expression. Additionally, we observed an increase in TP53INP2-protein levels in WT-MEFs upon U18666A treatment, likely due to the inhibition of autophagy caused by U18666A [262] and therefore reduced protein turnover.

Given the differences in LDL-R protein levels in WT- and TP53INP2-KO MEFs under basal conditions, we analyzed the expression of LDL-R in chow fed animals but did not detect differences in LDL-R protein levels between the genotypes.

We studied the role of autophagy in hepatocytes that were loaded with cholesterol, by an overnight LDL treatment. The autophagic flux was assessed and compared to PBS treated hepatocytes. We observed that TP53INP2-LKO hepatocytes show an impaired autophagic flux under basal conditions, in form of less LC3-II accumulation upon Bafilomycin A1 (BafA1) treatment. However, LDL-incubation of loxP hepatocytes impaired the autophagic flux and reduced it TP53INP2-LKO levels.

Given the enhanced FC accumulation in TP53INP2-depleted cells upon Npc1 blockage, even under conditions where autophagy is reduced to similar levels, there might be other factors contributing to the FC accumulation.

Since LAMP1 protein was reported to lower FC accumulation in lysosomes, even in conditions with blocked Npc1 protein, we analyzed the expression of LAMP1 protein in WT- and KO-MEFs. Indeed, we found enhanced basal levels of LAMP1 protein in KO-MEFs under basal conditions. When MEF cells were treated with U18666A to inhibit Npc1, WT-MEFs significantly increased the expression of LAMP1, while this upregulation did not occur in KO-MEFs. These results reveal the possible involvement of LAMP1 protein in enhanced FC accumulation in TP53INP2-depleted cells.

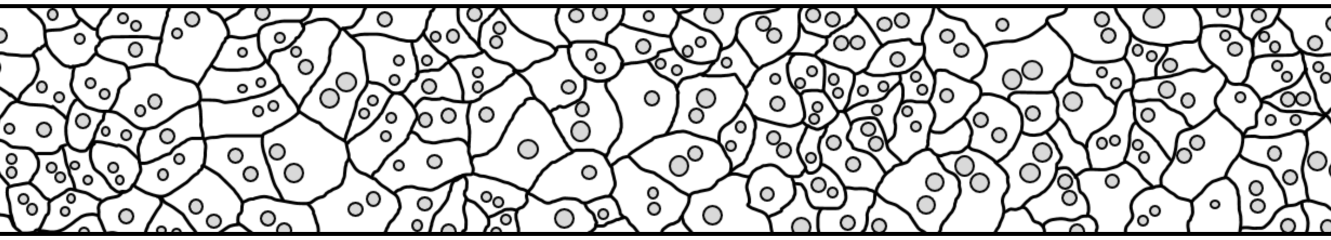

CONCLUSIONS

6. CONCLUSIONS

The data obtained in course of this doctoral thesis allow us to propose the following conclusions:

1. Hepatic expression of TP53INP2 is modulated by fasting or a high-fat diet (HFD) and is downregulated in a mouse model of non-alcoholic steatohepatitis.

2. Liver-specific depletion of TP53INP2 impairs hepatic autophagy, exacerbates fasting-induced accumulation of triglycerides and cholesterol, and attenuates hepatic fatty acid oxidation and ketogenesis.

3. Hepatocyte-specific TP53INP2 depletion impairs PPARα and LXRα transcriptional activity in liver, probably by reduced availability of endogenous ligands. In contrast to our observations *in vivo*, TP53INP2 expression in *in vitro* experiments inversely correlates with the transcriptional activity of PPARα and LXRα, possibly due to the enhanced availability of ligands.

4. Liver-specific TP53INP2 depletion enhances insulin resistance and triglyceride accumulation in a response to a HFD treatment. Under an HFD, TP53INP2 ablation increases ApoA1 expression, reduces hepatic cholesterol content, and most likely enhances HDL synthesis. Furthermore, it prevents bile acid accumulation in plasma and feces upon treatment with a western diet.

5. TP53INP2 deficiency enhances the accumulation of free cholesterol in lysosomes. This process may be dependent on the acceleration of endocytic uptake of extracellular cholesterol.

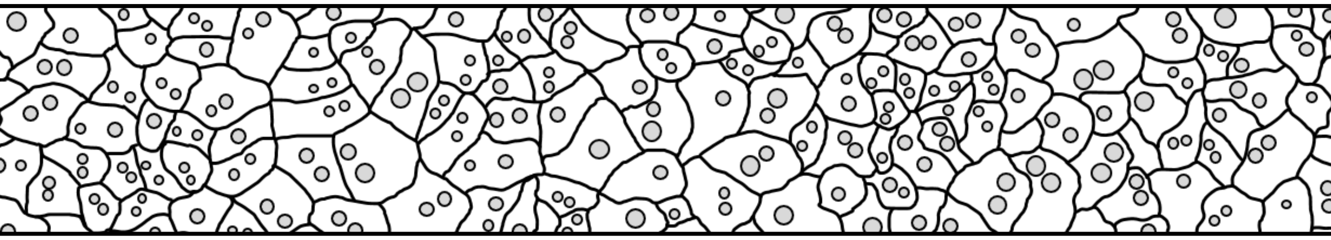

MATERIAL AND METHODS

7. MATERIAL AND METHODS

7.1. Material

The following tables specify the material used in experiments conducted in course of this PhD thesis.

7.1.1. Buffers, solutions and gels

Table 1. Composition of tail tip lysis buffer

Component	Final [c]	Source
EDTA	5 mM	Merck Millipore, 324503
NaCl	200 mM	Sigma-Aldrich, 71376
Proteinase K	2 % (v / v)	Sigma-Aldrich, RPROTK-RO
SDS	0.2 % (w / v)	Sigma-Aldrich, 11667289001
TRIS-HCl	100 mM	Sigma-Aldrich, 10812846001

The pH of the buffer was adjusted to 8.5.

Table 2. Composition of RIPA buffer

Component	Final [c]	Source
EDTA	5 mM	Merck Millipore, 324503
NaCl	100 mM	Sigma-Aldrich, 71376
NP40	1 % (v / v)	Sigma-Aldrich, I3021
SDS	0.1 % (w / v)	Sigma-Aldrich, 11667289001
Sodium deoxycholate	0.5 % (w / v)	Sigma-Aldrich, D6750
TRIS-HCl	50 mM	Sigma-Aldrich, 10812846001

RIPA buffer was stored at 4 °C. Protease inhibitors in form of one tablet cOmplete™, Mini, EDTA-free Protease Inhibitor Cocktail (Roche, 11836170001) per 10 mL RIPA buffer and 2 % (v / v) Phosphatase Inhibitor Cocktail Set IV (Merck Millipore, 524628), were added just before use.

Table 3. Composition of Hanks Balanced Salt Solution (HBSS)

Component	Final [c]	Source
D-Glucose	5.56 mM	Sigma-Aldrich, G7021
Hepes	50 mM	Sigma-Aldrich, H4034
$Na_2HPO_4.2H_2O$	0.338 mM	Sigma-Aldrich, 71643
NaCl	138 mM	Sigma-Aldrich, 71376
$NaHCO_3$	4.17 mM	Sigma-Aldrich, 71627
KCl	5.4 mM	Sigma-Aldrich, 60130
KH_2PO_4	0.44 mM	Sigma-Aldrich, 5655

The pH of the buffer was adjusted to 7.4, subsequently the buffer was sterile filtered using a pore size of 0.22 µm.

Table 4. Hepatocyte washing solution

Component	Final [c]	Source
EGTA	0.5 mM	Sigma-Aldrich, E4378

A 500 mM EGTA stock solution was prepared. The pH was brought to 8 in order to dissolve EGTA and adjusted to 7.4 afterwards. Subsequently, the solution was sterile filtered using a pore size of 0.22 µm. The EGTA stock solution was diluted in pre-warmed HBSS (37 °C) that was pre-gassed (humidified $O_2 : CO_2$) for at least 20 min. The washing solution was prepared on the day of hepatocyte isolation.

Table 5. Hepatocyte digestion solution

Component	Final [c]	Source
$CaCl_2$	5 mM	Sigma-Aldrich, C1016
Collagenase IV	0.025 % (w / v)	Sigma-Aldrich, C5138

A 60 mM $CaCl_2$ stock solution was prepared, and the pH was adjusted to 7.4. The solution was sterile filtered using a pore size of 0.22 µm. Collagenase IV was stored at -20 °C and was dissolved in HBSS that was pre-warmed (37 °C) and pre-gassed (humidified $O_2 : CO_2$) for at least 20 min. The buffer was prepared on the day of hepatocyte isolation.

Table 6. Protein loading dye (4X)

Component	Final [c]	Source
Bromophenol blue	0.04 % (w / v)	Sigma-Aldrich, 114391
DL-Dithiothreitol (DTT)	1 M	Sigma-Aldrich, D0632
DMF(N,N-dimethyl formamide)	4 % (v / v)	Sigma-Aldrich, D4551
Glycerol	40 % (v / v)	Sigma-Aldrich, G5516
SDS	8 % (w / v)	Sigma-Aldrich, 11667289001
TRIS-HCl	240 mM	Sigma-Aldrich, 10812846001

Table 7. Phosphate-buffered saline

Component	Final [c]	Source
$Na_2HPO_4 \cdot 2H_2O$	9 mM	Sigma-Aldrich, 71643
NaCl	136.9 mM	Sigma-Aldrich, 71376
KCl	2.7 mM	Sigma-Aldrich, 60130
KH_2PO_4	1.5 mM	Sigma-Aldrich, 5655

The pH of the buffer was adjusted to 7.4 and the solution was autoclaved.

Table 8. Separation buffer used for SDS-Page

Component	Final [c]	Source
TRIS-HCl	18.15 % (w / v)	Sigma-Aldrich, 10812846001

The pH of the buffer was adjusted to 8.8.

Table 9. Stacking buffer used for SDS-Page

Component	Final [c]	Source
TRIS-HCl	6.05 % (w / v)	Sigma-Aldrich, 10812846001

The pH of the buffer was adjusted to 6.8.

Table 10. Composition of separation gels used for SDS-Page

Component	Final [c]	Source
Acrylamide	20.0–44.7 % (v / v)	Sigma-Aldrich, A3699
APS	0.7 % (v / v)	Bio-Rad, 1610700
dH_2O	28.5–53.2 % (v / v)	Milli-Q® Direct
SDS	0.1 % (w / v)	Sigma-Aldrich, 11667289001
Separation buffer	25 % (v / v)	See Table 8
Temed	0.07 % (v / v)	Bio-Rad, 1610800

Table 11. Composition of stacking gels used for SDS-Page

Component	Final [c]	Source
Acrylamide	12.7 % (v / v)	Sigma-Aldrich, A3699
APS	1.2 % (v / v)	Bio-Rad, 1610700
dH_2O	59.4 % (v / v)	Milli-Q® Direct
SDS	0.1 % (w / v)	Sigma-Aldrich, 11667289001
Stacking buffer	24.3 % (v / v)	See Table 9
Temed	0.1 % (v / v)	Bio-Rad, 1610800

Table 12. Electrophoresis buffer used for SDS-PAGE

Component	Final [c]	Source
Glycine	900 mM	Sigma-Aldrich, 104169
SDS	1 % (w / v)	Sigma-Aldrich, 11667289001
Tris-HCl	400 mM	Sigma-Aldrich, 10812846001

Table 13. Transfer buffer used for Western blotting

Component	Final [c]	Source
Glycine	900 mM	Sigma-Aldrich, 104169
Tris-HCl	400 mM	Sigma-Aldrich, 10812846001

Table 14. Coomassie Staining / Coomassie destaining solution

Component	Final [c]	Source
Acetic acid	5 % (v / v)	Cayman, 10009200
Coomassie Brilliant Blue*	0.1 % (w / v)	SERVA, 17524
Methanol	25 % (v / v)	Panreac Quimica, 1410910716

*Coomassie destaining solution does not contain Coomassie Brilliant Blue.

7.1.2. Reagents, equipment and kits

The following tables enlist reagents and kits that were used for different experiments in course of this PhD thesis.

Table 15. Reagents used for various experiments

Name	Source
Benzonase® Nuclease	Millipore, E1014
Chameleon® Duo Pre-stained Protein Ladder	LI-COR Biosciences, 928-60000
Chloroform	Sigma-Aldrich, 8.22265
D-Glucose	Sigma-Aldrich, G7021
DNaseI, Bovine Pancreas	Millipore, 260913
ECL™ Western Blotting Reagents	Sigma-Aldrich, GERPN2106
Ethanol	Panreac Quimica, 2128000716
Fluoromount™ Aqueous Mounting Medium	Sigma-Aldrich, F4680
GeneRuler 100bp Plus DNA Ladder	Thermo Scientific™, SM0321
Isopentane	Sigma-Aldrich, M32631
Isopropanol	Fisher Chemical, 10477070
$MgCl_2$	Biotools, B&M Labs, 20.036
Milk-Powder (Desnatada)	Asturiana
NP-40 (IGEPAL®)	Sigma-Aldrich, CA-630, I3021
OCT	Sakura® Finetek, 4583
Paraformaldehyde solution 4 % in PBS	Santa Cruz Biotechnology, sc-281692
qScript™ cDNA SuperMix	Quanta Biosciences, 733-1177
Restore™ Western Blot Stripping Buffer	Thermo Scientific™, 21059
Revert™ 700 Total Protein Stain	LI-COR Biosciences, 926-11021
Spectra™ Protein Ladder	Thermo Scientific™, 26623
Poloxamer 407	Sigma-Aldrich, Pluronic® F-127, 2443
Power SYBR™ Green PCR Master Mix	Applied Biosystems, 4368702
tert-butanol	Sigma-Aldrich, 471712
Triton™ X-100	Sigma-Aldrich, T8787
TRIzol™ Reagent	Invitrogen™, 15596026
Tween® 20	Sigma-Aldrich, P1379
UltraPure™ Distilled Water	Invitrogen™, 10977035

Table 16. Equipment used in experiments

Name	Source
6 Tube Magnetic Stand	Ambion, AM10055
Amersham Hyperfilm™ ECL	GE Healthcare
Blood Chemistry Analyzer	MNCHIP Technologies, Pointcare® cM4
Butterfly needles	BD, 367288; Vacutainer® Safety-Lok™
Centrifuge for 1,5- and 2-mL vials	Eppendorf®, 5427 R
Centrifuge for 15 and 50mL falcons	Sigma Laborzentrifugen, 3-16KL
Contour next blood glucose test strips	Bayer
Contour XT Glucometer	Bayer
Countess™ II Automated Cell Counter	Thermo Scientific™, AMQAX1000
Countess™ Cell Counting Chamber Slides	Thermo Scientific™, C10312
Cover glasses, round, Ø 12 mm	Marienfeld, VWR®, 631-0666
Dounce Tissue Grinder, 1 mL	Wheaton®, 357538
FACSAria™ Fusion Flow Cytometer	BD Biosciences
Fuji Super RX-N film	Fujifilm
Hyper Processor Model AM4	Amersham Pharmacia Biotech
Inverted microscope	Nikon Eclipse TS100
Inverted microscope	Olympus ScanR
Luminometer tube	Ultra clear polypropylene tubes, Deltalab, 400800.1
Microfluidic disc for Blood Chemistry Analyzer	MNCHIP Technologies, Liver Function Panel Lyophilized Kit
Microplate Reader	BioTek®, Sunrise®
Mini-Beadbeater-24	Bio Spec Products, 112011
Mini-Protean system	Bio-Rad
Nano-Drop	Thermo Scientific™, NANODROP 2000
Odyssey Infrared Imaging System	LI-COR Biosciences, Model 9120
Peristaltic pump	Gilson Minipuls 3
Pierce™ Tissue Strainers, 250 µm	Thermo Scientific™, 87791
PVDF membrane	Merck Millipore, IPVH00010
PVDF membrane, Immobilon®-FL	Merck Millipore, IPFL85R
Sample preparation filter, CellTrics® 150 µm	Sysmex España, 04-004-2329
Single Tube Luminometer	Berthold Technologies, Lumat LB 9507
Thermocycler	GeneAMP®, PCR System 2700
Whatman® cellulose chromatography papers	Aldrich, WHA3030917
Zirconium oxide beads, Ø 2.8mm	VWR International

Table 17. Kits used for experiments

Name	Source
ß-Hydroxybutyrate	BioSystems, 12525
Cholesterol	BioSystems, 11505
Dual-Luciferase® Reporter Assay System	Promega Biotech, E1910
Mouse Total Bile Acids Kit	Crystal Chem, 80470
NEFA-HR(2) Assay	Fujifilm Wako Diagnostics, 270-77000, 434-91795 and 436-91995
Pierce™ BCA Protein Assay Kit	Thermo Scientific™, 23225
Purelink™ RNA Mini Kit	Invitrogen™, 12183018A
Triglycerides	Biosystems, 11528
Ultra Sensitive Mouse Insulin ELISA Kit	Crystal Chem, 90080

7.1.3. Research diets

Mice were subjected to the following diets for *in vivo* studies in course of this thesis.

Table 18. Research diets used for in vivo studies

Name	Source
Chow diet	Special Diets Services, RM1, 801151
Rodent diet with 60 %kcal fat (HFD)	Research Diets, D12492i
Western diet (WD) 40 %kcal fat, 0.02% cholesterol [w / w]	Research Diets, D12079Bi

7.1.4. Reagents, media, plasmids and vectors

The following reagents, media, plasmids and lentiviral vectors were used for *in vitro* experiments in course of this thesis.

Table 19. Reagents used in cell culture

Name	Source
Bafilomycin A1	Santa Cruz Biotechnology, sc-201550
BSA	Sigma-Aldrich, A6003
Cell scraper	Cell Lifter, Corning incorporated, 3008
DMSO	Fisher Chemical, 10080110
EBSS	Gibco™, 24010043
Gelatin	Dr. Oetker
GW3965 hydrochloride	Sigma-Aldrich, G6295
LG 100268 (LG268)	Cayman Chemical, 21606
Opti-MEM™ I	Gibco™, 31985047
Polyethylenimine hydrochloride	Polysciences, PEI MAX®, 24765-100
Polyethylenimine	Polysciences, PEI 25000, 23966-2
Puromycin dihydrochloride	Santa Cruz Biotechnology, sc-108071B
Sterile filter 22 µm	Whatman® Puradisc Syringe Filters, 10462200
Sterile filter 45 µm	Whatman® Puradisc Syringe Filters, 10462100
Trypan Blue	Thermo Scientific™, C10312
Trypsin-EDTA	Invitrogen™, 25300062
WY-14643	Sigma-Aldrich, C7081

Table 20. Details of hepatocyte isolation media

Component	Final [c]	Source
DMEM	500 mL	Gibco™, 11966
D-glucose	10 mM	Sigma-Aldrich, G7021
FBS	10 % (v / v)	Sigma-Aldrich, F7524
Penicillin-Streptavidin	1 % (v / v)	Gibco™, 15140122
Insulin	100 nM	Sigma-Aldrich, I0516
Dexamethasone	100 nM	Sigma-Aldrich, D2915

Table 21. Details of hepatocyte culture media

Component	Final [c]	Source
DMEM	500 mL	Gibco, 31885
FBS	10 % (v / v)	Sigma-Aldrich, F7524
Penicillin-Streptavidin	1 % (v / v)	Gibco™, 15140122
HEPES	25 mM	Sigma-Aldrich, H4034

Table 22. Details of culture media used for MEFs and Huh7 cell culture*

Component	Final [c]	Source
DMEM	500 mL	Gibco, 41966
FBS	10 % (v/v)	Sigma-Aldrich, F7524
Penicillin-Streptavidin	1 % (v/v)	Gibco™, 15140122
HEPES	25 mM	Sigma-Aldrich, H4034

*Huh7 culture media was supplemented with 1.5µg / mL puromycin to maintain selection pressure after lentiviral transduction.

Table 23. Plasmids used to transfect cells in cell culture

Plasmid	Source
pCDNA3.1-PPARα	Addgene, 169019
pCDNA3-3xFlag-hLXRα	Generated by Dr. Ghisletti, provided by Dr. Valledor
pCDNA3-RXRα	Generated and provided by Dr. Valledor
pRL-CMV (Renilla)	Promega Biotech, E2261
PPRE X3-TK-luc	Addgene, 1015
pTK-3xLXRE-luciferase	Generated and provided by Dr. Valledor

Table 24. Plasmids used for generation of stable overexpressing Huh7 cells

Plasmid	Source
pLenti::GFP	Generated and provided by Dr. Ivanova
pLenti::TP53INP2-GFP	Generated and provided by Dr. Ivanova
pCMV-VSV-G	Addgene, 8454
pMDLg/pRRE	Addgene, 12251
pRSV-Rev	Addgene, 12253

7.1.5. Primers for genotyping and Real-time quantitative PCR

The following tables contain the sequences of Forward- and Reverse Primers used for genotyping by PCR and for Real-time quantitative PCR (RT-qPCR). All primers were purchased from Sigma-Aldrich.

Table 25. Sequences of PCR-primer pairs utilized for genotyping

Target gene	Forward	Reverse
Cre	CGGTCGATGCAACGAGTGATGAGG	CCAGAGACGGAAATCCATCGCTCG
loxP	CTGTGAGACTTTAGGTAGTTATCTTATTTC	CCTGTCAAAGGGACTGAAAAGGAGTGG

Table 26. Sequences of primer pairs for Real-time quantitative PCR

Target gene	Forward	Reverse
Abca1	GGTTTGGAGATGGTTATACAATAGTTGT	TTCCCGGAAACGCAAGTC
Abcg5	TTGCGATACACAGCGATGCT	TGACTGCCTCTACCTTCTTGTTGT
Abcg8	GCTGCCCGGGATGATAGAG	CCGGAAGTCATTGGAAATCTG
Acly	AGGAAGTGCCACCTCCAACAGT	CGCTCATCACAGATGCTGGTCA
Acox1	TTACGTCACGTTTACCCCGG	ACCAGCTTCCCCGACTGAA
Albumin	AAACCTTGTCACTAGATGCAAAGACG	GGGTAGCCTGAGAAGGTTGTGG
Apoa1	TCCTCCTTGGGCCAACA	GAACCCAGAGTGTCCCAGTTT
β-actin	GGTCATCACTATTGGCAACGA	GTCAGCAATGCCTGG
Chrebp	CAGCCCAGCCTAGATGACTT	CAAAGCTGGGGGACTCTATG
Cyp2c55	ACACACACAAGCACTTTGTCA	GCTTCTGCTGGTAATCTGCG
Cyp7a1	GGGATTGCTGTGGTAGTGAGC	GGTATGGAATCAACCCGTTGTC
Fxrα	GGCAGAATCTGGATTTGGAATCG	GCTGAACTTGAGGAAACGGG
G6pc	CGACTCGCTATCTCCAAGTGA	GTTGAACCAGTCTCCGACCA
Ldlr	TGGCTGTTCCCACATCTG	CTCGTCAATATCTTCACACCTG
Srebp1c	GCGCTACCGGTCTTCTATCA	TGCGCAAGACAGCAGATTTA
Tp53inp2	AACCACAGCCTGCTTCTAATACCTT	TCAGCCAGTCTCAACACAAAACAC

7.1.6. Primary and secondary antibodies

The following tables include the primary and secondary antibodies that were used for western blots and / or immunofluorescence and the working conditions.

Table 27. Primary antibodies used for western blots and immunofluorescence.

Antibody	Host	Dilution	Source
Abca1	Rabbit	1:1,000	Novus Biologicals, NB400-105
α-tubulin	Mouse	1:2,500	Sigma-Aldrich, T5168
ApoA-I	Goat	1:2,000	Novus Biologicals, NB600-609
ß-actin	Mouse	1:2,500	Sigma-Aldrich, A1978
GFP	Rabbit	1:1,000	Abcam, ab290
LAMP1	Rat	1:1,000	Santa Cruz Biotechnology, sc-19992
LC3	Rabbit	1:1,000	MBL® International, PM036
Mouse LDL-R	Goat	1:1,000	Bio-Techne R&D Systems, AF2255
LXRα/β	Mouse	1:1,000	Santa Cruz Biotechnology, sc-377260
p62	Rabbit	1:1,000	MBL® International, PM045
TP53INP2	Mouse	1:500	Purified TP53INP2 3.652, produced in hybridoma cells in our group
Vinculin	Mouse	1:1,000	Abcam, ab18058

Table 28. Secondary antibodies used for western blots and immunofluorescence.

Antibody	Host	Dilution	Source
Anti-goat	Donkey	1:5,000	Invitrogen™, DyLight™ 680, SA5-10090
Anti-goat	Donkey	1:10,000	Jackson ImmunoResearch©, 705-035-147
Anti-mouse	Goat	1:5,000	Invitrogen™, DyLight™ 800 4X PEG, SA5-35521
Anti-mouse	Donkey	1:10,000	Jackson ImmunoResearch©,715-035-150
Anti-rabbit	Donkey	1:10,000	Jackson ImmunoResearch©, 711-035-152
Anti-rabbit	Goat	1:5,000	Invitrogen™, DyLight™ 800 4X PEG, SA5-35571
Anti-rat	Donkey	1:10,000	Jackson ImmunoResearch©, 712-005-150

7.2. *In vivo* Methods

All animal experiments I performed in course of this PhD thesis were in compliance with the guidelines established by the Committee on Animal Care of the University of Barcelona. Mice were housed in a 12 h dark / light cycle and fed with a standard chow diet (RM1, Special Diet Services) after weaning. Food and water were provided *ad libitum*.

7.2.1. Generation of a liver-specific TP53INP2 knockout model

The TP53INP2 liver-specific knockout model (TP53INP2-LKO) was initially generated in our group by Dr. Saška Ivanova [148]. This was performed utilizing the Cre/Lox recombination technology to delete a specific region within the TP53INP2 gene. TP53INP2$^{loxP/loxP}$ mice were previously used in our group by Dr. David Sala and Dr. Montserrat Romero [155, 159]. Those mice were transgenically modified to contain two loxP recombination sites within the TP53INP2 gene, which were placed before exon 3 and after exon 4 of the sequence, as shown in Figure 65. The activity of the Cre recombinase causes the excision of Exon 3 (containing the start codon ATG) and Exon 4, resulting in TP53INP2 protein ablation, specifically within hepatocytes.

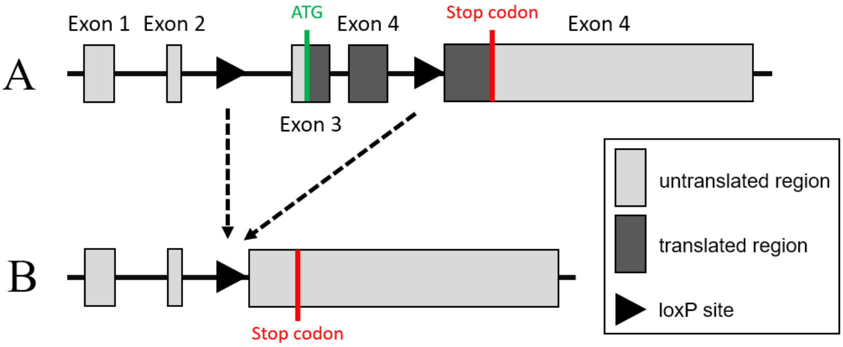

Figure 65. TP53INP2 gene structure of TP53INP2$^{loxP/loxP}$ control mice and TP53INP2-LKO mice. (A) The TP53INP2 gene in TP53INP2$^{loxP/loxP}$ mice contains all five exons. Cre recombinase target sites are inserted before exon 3 and after exon 4. (B) The TP53INP2 gene structure of TP53INP2-LKO mice after recombination is lacking exon 3 and exon 4, including the ATG start codon, preventing TP53INP2 protein translation.

The TP53INP2 liver-specific knockout model was generated by crossing homozygous TP53INP2$^{loxP/loxP}$ mice with a strain expressing the Cre recombinase under the hepatocyte-specific albumin promoter. Both mouse strains had a pure C57BL/6J genetic background. This crossing resulted in a first generation of heterozygous mice (Alb-Cre$^{-/+}$, TP53INP2$^{loxP-/loxP+}$). These mice were further crossed to obtain littermates of the two desired genotypes:

1. Alb-Cre$^{-/-}$, TP53INP2$^{loxP+/loxP+}$: Mice with normal TP53INP2 expression due to the absence of Cre recombinase. These mice are further referred to as loxP or control mice.
2. Alb-Cre$^{-/+}$, TP53INP2$^{loxP+/loxP+}$: Mice with hepatocyte-specific ablation of TP53INP2. These mice are further referred to as TP53INP2-LKO or LKO mice.

All mice assigned to experiments have been shown to be homozygous for carrying the loxP sequence by genotyping. Furthermore, mice were genotyped for Cre recombinase. Mice containing the sequence coding for Cre recombinase were considered TP53INP2-LKO mice, and littermates lacking this sequence were used as controls. The genotypes were confirmed at the end of experiments on RNA and protein level after necropsy.

7.2.2. Validation of the model by genotyping

Genotyping of liver-specific TP53INP2 knockout was performed by extraction of genomic DNA out of tail tips obtained at weaning. Extracted DNA was subsequently amplified by PCR. Finally, PCR-products are separated based on size through electrophoresis in agarose and are visualized using SYBR™ Safe DNA Gel Stain.

7.2.2.1. Isolation of genomic DNA

Extraction of genomic DNA from mouse tail tips was performed as follows:

1. Tail tips are digested in 500 µL tail tip lysis buffer containing Proteinase K (Material and Methods, Table 1) overnight at 55 °C and shaking at 450 rpm.

2. Proteinase K is deactivated at 80 °C for 2 min.
3. Samples are cooled down on ice and centrifuged at 18,000 g for 15 min at RT.
4. Supernatant is transferred to new vials containing 500 µL isopropanol and is mixed by inverting.
5. Vials are centrifuged at 14,000 g for 10 min at RT and supernatant is discarded.
6. The pellet is washed with 500 µL 70 % ethanol.
7. Samples are centrifuged at 14,000 g for 5 min at RT and supernatant is discarded.
8. Pellets are dried for 1 h.
9. Isolated DNA is resuspended in 500 µL of water and heated for 2 min at 65 °C.

7.2.2.2. Genotyping by polymerase chain reaction

In order to determine the genotype of mice, sequences of DNA were amplified by polymerase chain reaction (PCR) using two different primer sets for Cre and loxP. (Material and Methods, Table 25). Using this technique, selected sequences can be amplified exponentially to a concentration that allows visual detection in an agarose gel upon DNA staining with SYBR™ Safe DNA Gel Stain.

The Cre-primer pair targets a sequence of about 640 bp within the Cre recombinase gene and will only be amplified and detected in Cre-positive animals, as seen in Figure 66. Animals expressing Cre recombinase under the hepatocyte-specific albumin promoter, as well as TP53INP2-LKO mice (Alb-Cre$^{-/+}$, TP53INP2$^{loxP+/loxP+}$), show bands of 640 bp when genotyping. Cre-negative animals can be identified by the absence of the 640 bp band in the agarose gel.

The second primer pair is directed against the TP53INP2 sequence, resulting in an about 300 bp band in wildtype animals and an about 400 bp band in animals where loxP sequences are inserted in the genomic DNA. As seen in Figure 66, genotyping of Albumin-Cre mice and C57BL/6J wildtype mice results in a band detected at around 300 bp, while all experimental animals were transgenic for loxP sites inserted within the TP53INP2 gene sequence.

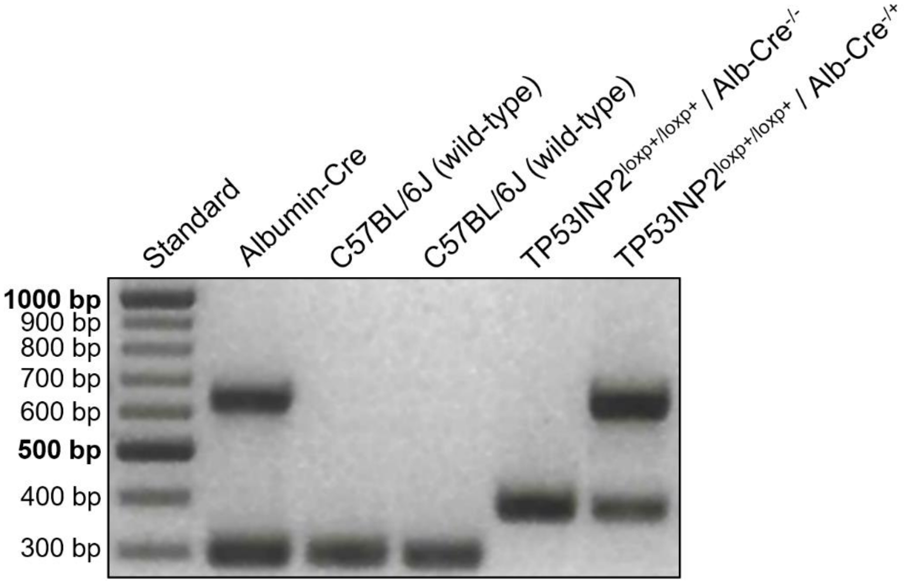
Standard
Albumin-Cre
C57BL/6J (wild-type)
C57BL/6J (wild-type)
TP53INP2loxp+/loxp+ / Alb-Cre-/-
TP53INP2loxp+/loxp+ / Alb-Cre-/+
1000 bp
900 bp
800 bp
700 bp
600 bp
500 bp
400 bp
300 bp

Figure 66. Genotyping of experimental animals by PCR. PCR-products visualized in an agarose gel after electrophoresis. Bands of 300 bp size are indicative for the wildtype TP53INP2 genomic sequence of animals. 400 bp bands are generated by PCR of genomic DNA isolated from TP53INP2 transgenic animals with inserted loxP sites. Bands of the size of 640 bp appear in the agarose gel, after PCR of Cre-positive animals, while this band is absent in Cre-negative animals.

7.2.3. High-fat diet, Methionine and choline deficient diet, and Western diet treatment

Male mice at 8 weeks of age were subjected to dietary manipulation. High-fat diet (HFD; D12492i, Research Diets) was performed for 8 or 16 weeks. Mice were fed *ad libitum* and weighed biweekly. Methionine and choline deficient diet was supplemented with 45% high fat diet (MCD; A06071305, Research diets). Male mice were subjected to this diet for a period of three weeks, while drinking water was supplemented with 0.1% L-methionine as previously described before [162]. High-fat and high-cholesterol containing western diet (WD; D12079Bi, Research Diets) was provided *ad libitum* for a period of 16 weeks.

7.2.4. Body composition measurement using Echo-MRI™

The EchoMRI™ equipment allows body composition analysis of live animals, providing information on fat, lean, total water and free water mass. The system utilizes quantitative nuclear magnetic resonance for analysis. Animals are placed inside a plastic holder and inserted into the system without the need for sedation or anesthesia. The determined fat mass is the total of all fat molecules within the animal expressed as equivalent weight of canola oil. The lean mass includes all body parts that contain water excluding fat, bone minerals, hair and claws. Free water consists mostly of urine within the bladder, while total water includes free water as well as water contained in lean mass.

7.2.5. Measurement of food intake and obtaining feces samples

In order to measure the food intake of animals on different diets, animals were single housed in individual cages. A weighed amount of diet of about 70 g was supplied to each cage, and food intake was measured by monitoring the amount of diet that is left after a period of 24 h. The weight difference between supplied and remaining diet was considered the daily food intake. Simultaneously, feces present in each cage was collected and weighed after a period of 24 h.

Animals were allowed to acclimatize to the single housing environment for two days. Afterwards, food intake and amount of feces was measured for two consecutive days before reuniting the animals with their littermates. Food intake and collection of feces samples was performed four weeks after initiation of high-fat diet or western diet treatment and in age-matched animals on control chow diet. Feces was dried at RT and considered fully dry when the weight no longer decreased and remained constant.

7.2.5.1. Evaluation of total bile acid content in murine feces

Total bile acids were extracted from dried murine feces as follows:

1. About 25 mg of dried feces is weighed and transferred to 2 mL tubes.
2. A volume of 20 µL 75 % ethanol / mg feces and three zirconium oxide beads are added to each tube.
3. Feces is homogenized for 30 s at 3,400 oscillations per minute using the Mini-Beadbeater disruptor (Bio Spec Products).
4. Samples are incubated at 50 °C for 2 h.
5. After incubation, samples are centrifuged at 1,050 g for 10 min at RT.
6. The supernatant is collected.
7. Aliquots of the supernatants are diluted 1:5 in PBS and measured using the Mouse Total Bile Acids Assay Kit (Crystal Chem) as described in 7.2.9.2.

7.2.6. Glucose tolerance test

The glucose tolerance test (GTT) is used to evaluate the capability to lower blood glucose to an euglycemic level after administration of a glucose bolus. The procedure was performed as follows:

1. Mice were fasted for 16 h overnight utilizing grids to prevent coprophagy.
2. Mice were distributed to individual boxes that were covered to diminish stress. Baseline blood glucose levels were measured by making a small incision on the tail. A small drop of blood was measured using blood test

strips inserted into a glucometer (Bayer Contour XT).

3. Baseline blood samples (timepoint 0) were collected in fasting state by using EDTA coated microvettes (Sarstedt).
4. A glucose bolus (2 g / kg bodyweight glucose) was administered intraperitoneally. A predetermined volume of a sterile filtered 20 % w / v glucose solution in 0.9 % NaCl was injected using a 29G needle.
5. Blood glucose levels were measured, and blood samples were collected 5, 15, 30, 60, 90 and 120 min after glucose bolus administration.
6. Collected blood samples were centrifuged at 2,000 g for 20 min at 4℃.
7. Supernatant (plasma) was collected and stored at -80 ℃ until analysis.
8. Plasma insulin concentration of samples was determined using the Ultra Sensitive Mouse Insulin ELISA Kit (Crystal Chem) following the manufacturer’s instructions.

7.2.7. Oral Lipid tolerance test

An oral lipid tolerance test (OLTT) is performed in order to evaluate the rate of intestinal secretion of dietary fat into circulation and consecutive clearance of postprandial lipids from blood. The test was performed as follows:

1. Mice are fasted for 16 h overnight utilizing grids to prevent coprophagy.
2. Mice are distributed to individual boxes that are covered to diminish stress.
3. Baseline blood samples (timepoint 0) in fasting state are collected by tail bleeding using EDTA coated microvettes (Sarstedt).
4. Mice are given an oral gavage of Intralipid (Sigma, I141) at a dose of 10 µL / g body weight.
5. Blood samples are collected 1, 2, 3 and 4 h after Intralipid administration.
6. Collected blood samples are centrifuged at 2,000 g for 20 min at 4 ℃.
7. Supernatant (plasma) is collected and stored at -80 ℃ until analysis.

8. Plasma triglycerides and non-esterified free fatty acids (NEFAs) are measured using colorimetric assays from BioSystems and FUJIFILM Wako Diagnostics (Material and Methods, 7.2.9.2).

7.2.8. Very-Low Density Lipoprotein Secretion Assay

The secretion of hepatic triglycerides, in form of very-low-density lipoproteins (VLDLs), can be evaluated by preventing lipid uptake into peripheral tissues using the lipase inhibitor Poloxamer 407 (P-407) [195]. The assay was performed as follows:

1. Mice are fasted for 4 h, beginning 2 h into the light cycle utilizing grids to prevent coprophagy.
2. Baseline blood samples (timepoint 0) are collected by tail bleeding using EDTA coated microvettes (Sarstedt).
3. A dose of 1 g / kg bodyweight P-407 (Sigma) solution is administered intraperitoneally. A predetermined volume of a sterile filtered 10 % w / v P-407 solution in 0.9 % NaCl is injected using a 29G needle.
4. Blood samples are collected 1, 2 and 4 h after P-407 administration.
5. Collected blood samples are centrifuged at 2,000 g for 20 min at 4 °C.
6. Supernatant (plasma) is collected and stored at -80 °C until analysis.
7. Plasma triglycerides and cholesterol are measured using colorimetric assays from BioSystems (Material and Methods, 7.2.9.2).

7.2.9. Blood sampling and plasma measurements

Blood collection during experiments was performed either by tail or facial vein extraction or by cardiac puncture during necropsy. Samples were centrifuged at 2,000 g for 20 min at 4 °C and the supernatant (plasma) was collected and stored at -80 °C until analysis.

7.2.9.1. Enzyme-linked Immunosorbent Assay

Enzyme-linked immunosorbent assays (ELISAs) are routinely used to detect proteins in plasma. Plasma concentrations of insulin was measured using Ultra Sensitive Mouse Insulin ELISA Kit (Crystal Chem) following the manufacturer’s instructions.

Briefly, 5 µL of plasma as well as a standard of known concentration are diluted and incubated in microtiter plates. The wells of the plate are coated with a specific immobilized antibody that is capturing the protein of interest. After incubation, the wells are emptied and washed to remove unbound material and nonspecifically bound proteins. A conjugate solution (containing an enzyme-linked antibody) is added, followed by another incubation. The wells are emptied and washed again before a substrate solution is added. After incubation, the reaction is stopped by adding a stop solution. Absorbance is measured at 450/630 nm using a spectrophotometer. The concentration of the protein of interest can be calculated by interpolating the unknown value from the standard curve that was simultaneously generated.

7.2.9.2. Colorimetric biochemical measurements

In course of this thesis, colorimetric assays were used to measure the concentrations of various metabolites, such as cholesterol, triglycerides, non-esterified fatty acids (NEFAs), total bile acids and ß-hydroxybutyrate (Material and Methods, Table 17) according to the manufacturer’s instruction. These assays contain reagents that undergo a detectable change of color in the presence of the metabolite. Color changes are dependent on the concentration of the metabolite and are measured using a spectrophotometer. Samples were measured in duplicates. Concentrations of metabolites were determined by interpolating the unknown values from a standard curve of a known concentration or by calculating the concentration using a calibrator in case of β-hydroxybutyrate.

7.2.9.3. Blood chemistry parameters related to liver function

Several parameters associated with liver function (Plasma total protein, albumin, globulin, alanine aminotransferase and aspartate aminotransferase) were measured in plasma obtained from 24-week-old animals on chow diet, age matched mice subjected to 16 weeks of high fat diet (HFD) or Western diet (WD), as well as one year old animals on chow diet. 100 µL of sample was added to microfluidic discs (MNCHIP Technologies) and inserted into the Blood Chemistry Analyzer Pointcare® cM4 (MNCHIP Technologies). Samples were processed by the Histopathology Facility of the IRB.

7.2.9.4. Determination of high-density lipoprotein cholesterol

The amount of total plasma cholesterol and cholesterol in the high-density lipoprotein (HDL) fraction were determined by the team of our collaborator Dr. Joan Carles Escolà-Gil at the Institut de Recerca de l’Hospital de la Santa Creu i Sant Pau. Plasma was depleted of apoB-containing lipoproteins by precipitation with phosphotungstic acid and magnesium ions (Roche Diagnostics). Cholesterol was determined enzymatically in untreated and apoB-depleted plasma using a commercial kit adapted to a COBAS c501 autoanalyzer (Roche Diagnostics) [263].

7.2.9.5. Lipoprotein analysis based on 2D Nuclear Magnetic Resonance Spectroscopy

Plasma lipoproteins were analyzed by the team of our collaborator Dr. Núria Amigó at the Biosfer Teslab. Plasma was analyzed with the Liposcale® test based on 2D diffusion-ordered Nuclear Magnetic Resonance (NMR) spectroscopy. This test allows the evaluation of size and number of the main lipoprotein particles (VLDLs and chylomicrons, LDLs and HDLs). Obtained spectra were analyzed using the Liposcale® medical software algorithm [264].

7.3. *Ex vivo* Methods

7.3.1. Histological analysis of liver samples

The morphology of mouse livers was analyzed microscopically using various standard staining techniques. Mice were sacrificed by cervical dislocation and liver tissue was collected immediately after. The liver was washed in PBS to remove residual blood and the right median lobe was cut in half using a scalpel. One part was immersed in 4 % paraformaldehyde and incubated overnight, while the other part was embedded in OCT solution and frozen in liquid nitrogen-cooled isopentane. Paraformaldehyde fixed livers were washed in PBS and stored at 4 °C before being transferred to the Histopathology Facility of the IRB. OCT embedded samples were stored at -80 °C.

Samples were processed by the Histopathology Facility of the IRB. They performed tissue embedding in paraffin, cutting of sections, mounting onto slides and staining. Livers were stained using hematoxylin and eosin (H/E), Periodic acid–Schiff stain (PAS), Masson’s trichrome stain and Sirius red stain. Furthermore, immunohistochemistry was performed for the macrophage marker F4/80. OCT embedded samples were cut, mounted and stained using Oil-Red-O. Slides were scanned using the NanoZoomer 2.0-HT (Hamamatsu).

Quantification of F4/80 stained livers was performed by analyzing three different regions per sample. The F4/80 stained area per image was determined using the ImageJ software

7.3.2. Extraction and analysis of hepatic lipids

The accumulation of lipids within the liver was determined by extraction of lipids using the classical Folch approach. The extraction was performed as follows:

1. Pieces of about 40 mg tissue are weighed and added to tubes containing 700 µL chloroform / methanol (2:1 v / v) and 50 µL of 0.1 N KOH and three zirconium oxide beads.
2. Tubes are inserted in the Mini-Beadbeater disruptor (Bio Spec Products) and homogenized for 30 s at 3,400 oscillations per minute.
3. Samples are rotated for 1 h at RT.
4. The samples are centrifuged for 5 min at 2,000 g at RT.
5. The upper aqueous phase and liver remnants are removed.
6. The organic phase is washed using 200 µL of a mixture of methanol / dH_2O / chloroform (48:47:3 v / v) and thorough mixing.
7. Samples are centrifuged for 5 min at 2,000 g at RT
8. The upper aqueous phase is removed.
9. The organic solvent is evaporated using a stream of nitrogen.
10. Once fully dried, lipids are resuspended in a mixture of tert-Butanol / Methanol / Triton X-100 (5:3:2 v/v).
11. Triglyceride and cholesterol content of samples are measured using calorimetric kits as described in Material and Methods, 7.2.9.2.

7.4. *In vitro* Methods

In this PhD thesis, mouse embryonic fibroblasts (MEFs), the hepatocellular carcinoma cell line Huh7 and isolated primary hepatocytes were used as cellular models. Wild-type (WT) and knockout (KO) mouse embryonic fibroblasts were generated and kindly provided by Dr. Saška Ivanova. Huh7 cells were a kind gift from Dr. Sonia Veiga. Primary hepatocytes were isolated as described in Material and Methods, section 7.4.2. Furthermore, HEK293T cells, obtained from ATCC, were used for lentivirus generation.

7.4.1. Culture of MEFs, Huh7 and HEK293T cells

MEF, Huh7 and HEK293T cells were cultured in the same manner. Cells were frozen in fetal bovine serum (FBS) with 10 % dimethylsulfoxide (DMSO) as a cryoprotective agent and vials of frozen cells were stored at -80 °C. Frozen cells were thawed in a water bath set to 37 °C and quickly mixed with pre-warmed culture media (Material and Methods, Table 22). The solution was centrifuged for 3 min at 300 g in order to resolve the cell pellet in media free of DMSO. Cells were cultured at 37 °C in incubators with a humidified atmosphere of 5 % CO_2 and 95 % air. Before reaching confluency, cells were passaged using trypsin every 2 - 3 days. In order to seed cells for experiments, cells were counted as described in Material and Methods, 7.4.3.

7.4.2. Isolation of primary hepatocytes

This protocol of primary hepatocyte isolation is based on the perfusion of the liver in order to cleave collagen using collagenase type IV from *Clostridium histolyticum* to release cells from tissue [265]. Primary hepatocytes were isolated according to following protocol:

1. Animals are anesthetized using 200 mg / kg bodyweight pentobarbital at a concentration of 20 mg / mL. Anesthesia starts to be fully effective after roughly 10 min, determined by the loss of the pedal withdrawal reflex upon firmly pinching the pad of a hindlimb.
2. Once anesthetized, the animal is put on a perfusion tray and limbs are immobilized.
3. The animal is rinsed with 70 % ethanol, the abdomen is opened, and intestines are moved to the right carefully to reveal the liver, vena portae and vena cava inferior.
4. After inserting the 23G butterfly needle into the vena cava inferior (Figure 67), the portal vein is cut to prevent high pressure.

5. After switching on the peristaltic pump (Gilson Minipuls 3), instant homogeneous loss of color of the liver is a sign of correct perfusion.

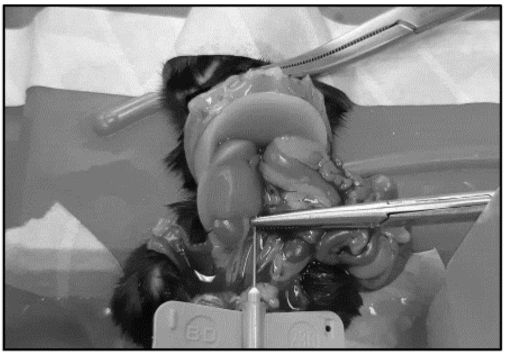

Figure 67. Isolation of primary hepatocytes. The anesthetized animal is immobilized on the perfusion tray, the abdomen is opened and the 23G butterfly needle is carefully inserted into the *vena cava inferior* and held in place by a metal clamp.

6. First, the liver is perfused with hepatocyte washing solution (Material and Methods, Table 4) for 10 min with a flow rate of 5 mL per min.
7. Subsequently, the liver is digested for about 12 min using hepatocyte digestion solution (Material and Methods, Table 5). In course of perfusion, the liver should change appearance due to the breakdown of its internal framework.
8. The liver is harvested and dissected in a culture dish containing hepatocyte washing solution.
9. Hepatocytes are filtered using a 250 µm filter and centrifuged at 500 rpm for 2 min at RT.
10. Supernatant is removed, and the cell pellet (typically 0.5 - 1 mL of volume) is resuspended in 10 mL of a HBSS, PBS (5X) and Percoll solution with a ratio of (3:2:5).
11. The cells are centrifuged at 500 rpm for 2 min at RT.
12. Cells are washed once with prewarmed isolation medium, followed by another centrifugation step.

13. The supernatant is removed, and cells are resuspended in isolation medium (Material and Methods, Table 20).
14. Viability and number of cells is determined as described in Material and Methods, 7.4.3. Only cells with a viability > 90 % are used for experiments.
15. Finally, the cell suspension is diluted with isolation medium to the desired seeding density and added to culture dishes pre-coated with 0.1 % gelatin. Culture dishes are then put into an incubator at 37 °C with a humidified atmosphere of 5 % CO_2 / 95 % air.
16. Four hours after seeding, cells are washed with PBS and media is changed to hepatocyte culture media (Material and Methods, Table 21). In vitro experiments were performed starting on the day after isolation.

7.4.3. Counting cells using the Countess™ II cell counter

The number and viability of cells were determined using the Countess™ II Automated Cell Counter (Thermo Scientific™). Homogeneous cell suspensions were diluted 1:1 with 0.4 % trypan blue stain. Adding trypan blue to cell suspensions before counting allows distinguishing dead and living cells. Trypan Blue is not absorbed by healthy viable cells but is able to stain cells with a damaged membrane. 10 µL of the sample mixture were pipetted into the sample loading area of disposable Countess™ Cell Counting Chamber Slide (Thermo Scientific™). The slide was then inserted into the cell counter.

Depending on the cell types, different count parameters (exposure, brightness, object size, circularity) can be adjusted to achieve optimal results. These settings were established for each cell line and these profiles were saved for future cell counting.

By pressing the capture button, the instrument captures an image and shows the total concentration of cells, as well as concentration and percentage of live and dead cells, already considering the 1:1 dilution with trypan blue.

7.4.4. EBSS treatment of isolated primary hepatocytes

Primary hepatocytes were treated one day after isolation. Cells were seeded into 100 mm culture dishes at a density of 6 x 10^6 cells per dish (for western blot analysis) or at a density of 1 x 10^6 cell per well into 6-well plates (for RT-qPCR analysis).

1. Media is removed, and cells are washed with PBS.
2. Fresh culture media (Material and Methods, Table 21) is added to control cells, EBSS buffer (Gibco™, 24010043) is added to cells for nutrient deprivation. Incubation is performed for the indicated times.
3. Cells are harvested for RNA or protein extraction (as described in Material and Methods, 7.5.1.1 and 7.5.3.1).

7.4.5. Treatment of primary hepatocytes with LXRα and RXRα agonists

Primary hepatocytes were treated one day after isolation. Cells were seeded at a density of 1 x 10^6 cell per well into 6-well plates (for RT-qPCR analysis).

1. Media is removed, and cells are washed with PBS.
2. Culture media (Material and Methods, Table 21) supplemented with a DMSO vehicle, LXRα and RXRα agonists is added to cells. The volume of DMSO is adjusted to the same level in all conditions. Cells are incubated for 24 h.

Vehicle:	2 µL DMSO
LXRα agonist:	1 µL DMSO + 1 µM GW3965 (1 µL)
LXRα and RXRα agonists:	1 µM GW3965 + 1 µM LG268 (1 µL each)

3. Cells are harvested for RNA or protein extraction (as described in Material and Methods, 7.5.1.1 and 7.5.3.1).

7.4.6. Lentivirus production using HEK293T cells

HEK293T cells were seeded into 10 cm dishes. At 60 % confluence, cells were co-transfected with vectors for lentiviral packaging (pRRE, pVSVG and pRSV) and a GFP- or a TP53INP2-GFP vector. Vector-DNA was kindly provided by Dr. Saška Ivanova, 5 µg DNA of each vector was used. Transfection of HEK293T cells was performed as follows:

1. DNA is diluted with 1,560 µL of a 150 mM NaCl solution before 78 µL of a 1 mg / mL PEI (PEI 25000, Polysciences) solution is added.
2. The DNA / PEI transfection solution is vortexed and incubated for 20 min at RT.
3. HEK293T cells are supplied with 8 mL of fresh culture media. Transfection solution is added to cells and incubated overnight.
4. The following day (24 h later) media is discarded, cells are supplied with 8 mL of fresh culture media and transferred to an incubator at 33 °C.
5. After 24 hours, the supernatant containing lentivirus is collected and sterile filtered using a filter with a 45 µm pore size and stored at 4 °C.
6. Cells are supplied once more with 8 mL of fresh culture media and incubated at 33 °C.
7. The next day (24 h later), supernatant is collected, sterile filtered and combined with the aliquot stored at 4 °C.
8. Aliquots (4 mL) of lentivirus containing supernatant can be used to transduce cells of interest or stored at -80 °C.

7.4.7. Lentiviral transduction of Huh7 cells to generate stable GFP- / TP53INP2-GFP overexpressing cells

Huh7 cells were seeded into 10 cm dishes. At 60 % confluence, cells were supplied with fresh media and 4 mL of lentivirus containing media (Material and Methods, 7.4.6) was added to cells. 48 h after lentiviral transduction, cells were washed once with PBS. At this point, positive cells have acquired a puromycin resistance conveyed by the lentivirus. Media, supplemented with 1.5 µg / mL puromycin, was added to start selection for GFP / TP53INP2-GFP overexpressing cells. After one week of selection, cells were subjected to Fluorescence-activated cell sorting (FACS) using the FACSAria™ Fusion Flow Cytometer (BD Biosciences). Autofluorescence was determined using Huh7 wildtype cells. GFP- and TP53INP2-GFP positive cells were sorted, and 100,000 cells were collected and expanded. FACS-sorted cells were cultured in media containing 1.5 µg / mL puromycin and were used for *in vitro* experiments.

7.4.8. Luciferase assays performed in Huh7 cells

LXRE and PPRE luciferase assays were performed in GFP- or TP53INP2-GFP overexpressing Huh7 cells. 6-well plates were used to seed cells at a density of 100,000 cells per well. On the next day, cells were transfected for 24 h using following protocol:

1. Two aliquots of 150 µL Opti-MEM are mixed well with either 5 uL of 1 mg / mL PEI MAX® or DNA (amount as follows) and incubated for 5 min at RT.

   DNA-amount per reaction for LXRE-luciferase assay:

   1 µg pTK-3xLXRE-luciferase
   0.1 µg pRL-CMV (Renilla luciferase)
   0.5 µg pCDNA3-3xFlag-hLXRα (only if mentioned)

DNA-amount per reaction for PPRE-luciferase assay:

1 µg PPRE X3-TK-luc
0.1 µg pRL-CMV (Renilla luciferase)
0.25 µg pCDNA3.1-PPARα (only if mentioned)

2. Diluted DNA is added to diluted PEI MAX®, mixed by pipetting and incubated for additional 30 min at RT.
3. Cells are washed once with PBS and supplied with fresh medium before the transfection reaction is finally added.

After 24 h, cells were washed once with PBS and treated with LXRα- or PPARα-agonists. Media containing either 1 µM GW3965 (in case of LXRE-luciferase assay), 100 µM WY-14643 (in case of PPRE-luciferase assays) or an equal volume of DMSO as a vehicle was used to treat cells for 24 h. After the treatment, cells were harvested and analyzed using the Dual-Luciferase® Reporter Assay System (Promega Biotech) according to the manufacturer's instructions using following protocol:

1. Culture dishes (6-well plates) containing cells are placed on ice, washed once with PBS and lysed using 100 µL Passive Lysis Buffer.
2. Each well is scraped using a cell scraper and 6-well dishes are incubated at RT for 15 min on a shaker set to 100 rpm.
3. Lysates are transferred to 1.5 mL tubes and centrifuged for 1 min at 30 g.
4. Aliquots of lysates (20 µL) are transferred to the bottom of a luminometer tube.
5. Lyophilized Luciferase Assay Substrate is resuspended in Luciferase Assay Buffer II and aliquots are stored at -80 °C.
6. Required amount of 50X Stop & Glo® Substrate is diluted with Stop & Glo® Buffer.

7. Luciferase Substrate (10 µL) is mixed with cell lysates and firefly luciferase activity is measured 10 s after adding the substrate using a Single Tube Luminometer (Berthold Technologies) for a period of 5 s. Results are recorded by the built-in printer.
8. After measuring the firefly luciferase activity of all samples, 10 µL of Stop & Glo® Substrate is mixed with each sample and Renilla luciferase activity is measured 20 s after adding the substrate for a period of 1 s.

Three biological replicates were measured for each experimental condition. Renilla luciferase activity was used as an internal control of transfection efficiency to normalize the firefly luciferase activity of the experimental reporter.

7.4.9. Luciferase assays performed in mouse embryonic fibroblasts

LXRE and PPRE luciferase assays were performed in wild-type and TP53INP2-KO MEF cells as described previously in Material and Methods 7.4.8, with slight adaptations to the protocol:

MEF cells were seeded at a density of 50,000 cells per well into 6-well plates. On the next day, cells were transfected for 24 h using following protocol:

1. Two aliquots of 150 µL Opti-MEM are mixed well with either 5 uL of 1 mg / mL PEI MAX® or DNA (amount as follows) and incubated for 5 min at RT.

   DNA-amount per reaction for LXRE-luciferase assay:
   1 µg pTK-3xLXRE-luciferase
   0.1 µg pRL-CMV (Renilla luciferase)
   0.5 µg pCDNA3-3xFlag-hLXRα

DNA-amount per reaction for PPRE-luciferase assay:

1 µg PPRE X3-TK-luc
0.1 µg pRL-CMV (Renilla luciferase)
0.25 µg pCDNA3.1-PPARα

2. Diluted DNA is added to diluted PEI MAX®, mixed by pipetting and incubated for additional 30 min at RT.
3. Cells are washed once with PBS and supplied with fresh medium before the transfection reaction is finally added.

The following day (after 24 h) cells were treated with LXRα- or PPARα-agonists for 24 h and the Dual-Luciferase® Reporter Assay System (Promega Biotech) was performed as described in Material and Methods, 7.4.8.

7.4.10. Assessment of autophagic flux in primary hepatocytes

Autophagic flux describes the complete process of degradation of cellular components into its breakdown products by autophagy, including phagophore and autophagosome formation, fusion with the lysosome and subsequent degradation and release of its contents back into the cytosol [266].

The macrolide Bafilomycin A1 (BafA1) is able to interrupt the autophagic flux via two distinct ways. First, BafA1 impedes lysosomal acidification and enzyme activation by inhibiting the proton pump V-ATPase. Furthermore, it also prevents autophagosome-lysosome fusion by inhibiting the endoplasmic reticulum calcium pump Ca-P60A/SERCA [166].

Assessment of the autophagic flux was performed in primary hepatocytes and was performed as follows:

1. 6 x 10^6 cells are seeded into 10 cm dishes.
2. One day after isolation, media is removed, and cells are washed with PBS.

3. Culture media containing 200 nM Bafilomycin A1 or an equal volume of a DMSO vehicle was added to cells.
4. After four hours of incubation, cells were harvested for protein extraction (as described in Material and Methods, section 7.5.3.1).

7.4.11. Isolation of human low-density lipoproteins and aggregation

Human low-density lipoproteins (LDL) were isolated and provided by the team of our collaborator Dr. Vicenta Llorente as previously described [267].

Briefly, human LDL (d1.019–d1.063 g/mL) was isolated from plasma of normocholesterolemic volunteers by sequential ultracentrifugation using a potassium bromide (KBr) density gradient. First, plasma is centrifuged at 36,000 rpm for 18 h and VLDLs are discarded. A layer of 1.063 g / mL KBr solution is added to adjust the density of VLDL-free plasma, followed by another centrifugation step at 36.000 rpm for 18 h. Subsequently, LDLs are dialyzed for 18 h against 0.02 M TRIS base, 0.15 M NaCl, 1 mM EDTA at pH 7.5, followed by dialysis against 0.9 % NaCl solution for 2 h. Finally, isolated human LDLs are sterile filtered using a pore size of 0.22 µm. Cholesterol and protein concentration are determined using commercially available kits (BCA protein assay and IL test Cholesterol, respectively).

Aggregated LDLs were prepared as previously described [225]. In brief, LDLs were aggregated at RT by vortexing in PBS. Aggregation was monitored by measuring turbidity (absorbance at 680nm). Aggregated LDLs were centrifuged at 10,000 g for 10 min, resuspended and diluted with PBS and used for experiments.

7.4.12. Evaluation of intracellular cholesterol localization in primary hepatocytes and mouse embryonic fibroblasts

Intracellular cholesterol localization in primary hepatocytes was analyzed using the Cholesterol Cell-Based Detection Assay Kit (Cayman, 1009779) according to the manufacturer's instruction. The assay is based on staining free cholesterol using Filipin III, an isomeric polyene macrolide isolated from *S. filipinensis*. The absorption and fluorescence spectra of Filipin III are altered upon interaction with cholesterol, allowing visualization using a microscope with excitation at 340 - 380 nm and emission at 385 - 470 nm. The Kit includes fixative and wash buffer in a ready to use format. A cholesterol trafficking inhibitor, U18666A is provided as a positive control. U18666A blocks cholesterol transport from late endosomes and lysosomes to the endoplasmic reticulum. Filipin III is solubilized in 200 µL 100 % ethanol and aliquots are stored at -80 °C. The assay was performed as follows:

In case of primary hepatocytes:

1. Isolated primary hepatocytes are seeded onto 12 mm cover glasses in 12 well dishes pre-coated with 0.1 % gelatin at a density of 200,000 cells / mL.
2. The following day, cells are treated with a DMSO vehicle or 1 µM U-18666A (an inhibitor of intracellular cholesterol trafficking).
3. After incubation, culture medium is removed from wells.
4. Cells are fixed with Cell-Based Assay Fixative Solution for 10 min.
5. Cells are washed with Cell-Based Assay Wash Buffer three times for 5 min each.
6. Filipin III stock solution is diluted 1:100 with Cholesterol Detection Assay Buffer and cells are incubated for 1 h avoiding light exposure.
7. Cells are washed twice for 5 min each using Cell-Based Assay Wash Buffer.

8. Cover glasses are mounted on microscope slides using Fluoromount® Mounting Medium and dried for 24 h at RT.
9. Samples are analyzed using the ScanR inverted microscope (Olympus) with an UV filter cube for excitation.

In case of mouse embryonic fibroblasts (MEFs):

1. MEFs were seeded onto 12 mm cover glasses in 12 well dishes at a density of 20,000 cells / mL.
2. The following day, cells are treated with isolated human low-density-lipoproteins (LDLs) or aggregated LDLs at a concentration of 100 µg / mL or a PBS vehicle for 24 h in FBS free media. Simultaneously, cells are treated with a DMSO vehicle or 1 µM U18666A (an inhibitor of intracellular cholesterol trafficking).
3. From this step on, the protocol is identical to the protocol used for evaluation of intracellular cholesterol localization in primary hepatocytes beginning at step 3.

7.4.13. Treatment of mouse embryonic fibroblasts with LXRα agonist

Wild-type and TP53INP2-KO mouse embryonic fibroblasts (MEFs) were seeded into 10 cm culture dishes at a density of 500,000 cells per dish and treatment was performed once cells reached confluency as follows:

1. Media is removed and cells are washed with PBS.
2. Culture media is supplemented with a DMSO vehicle or 1 µM GW3965 and is added to cells.
3. Cells are incubated for 24 h.
4. Cells are harvested for protein extraction (as described in Material and Methods, 7.5.3.1).

7.5. Molecular biology methodology

In the following paragraphs, standard molecular biology methods used to analyze cells and tissues will be described.

7.5.1. Determination of relative gene expression by quantitative polymerase chain reaction

Due to its sensitivity and dynamic range, the quantitative real time polymerase chain reaction (RT-qPCR) is considered the golden standard of methods to measure and compare the abundance of individual mRNAs within a sample.

Briefly, RNA is isolated, quantified and transcribed into complementary single-stranded DNA (Material and Methods, 7.5.1.1, 7.5.1.2 and 7.5.1.3). Finally, the resulting complementary single-stranded DNA (cDNA) is used as a template for a process called polymerase chain reaction (Material and Methods, 7.5.1.4).

During PCR, several cycles of denaturation and synthesis cause an exponential increase of double-stranded PCR products. Denaturation at high temperatures generates single-stranded DNA-templates. Lowering the temperatures allows the annealing of primers to the template. Primers are a set of two oligomers, designed to specifically match the desired target sequence. Once the primers attached to their target, the polymerase synthesizes the complementary DNA strand using free nucleotides.

SYBR®Green I dye is intercalating into double-stranded DNA, causing an increase in its fluorescence. By measuring fluorescence during every cycle of the RT-qPCR reaction, the increase of fluorescence within the process allows to calculate the initial copy number of the template. Housekeeping genes, that are constitutively active and expressed at relatively constant levels within most cells, serve as internal standards. It is important to run RT-qPCRs of genes of interest and housekeeping genes (such as gapdh or β-actin) simultaneously, to put the resulting initial copy numbers into perspective. Furthermore, negative control reactions containing all reagents except template cDNA are needed to rule out DNA contaminations of primers and reagents.

7.5.1.1. Isolation and purification of RNA

RNA was extracted using TRIzol™ and purified using Purelink™ RNA Mini High Yield columns by following the manufacturer's instructions. RNA extraction from cells was performed by removing media, adding 500 µL cold TRIzol™ to 6-well plates and scraping of cells. In case of tissues, pieces of about 30 mg were put into pre-chilled tubes containing three zirconium oxide beads and 500 µL cold TRIzol™. Tissue was homogenized using the Mini-Beadbeater disrupter (Bio Spec Products) for 30s at 3,400 oscillations per minute. The extracted RNA of cells and tissues was purified as follows:

1. 100 µL of chloroform is added to every 500 µL of TRIzol™, mixed thoroughly and incubated at RT for 2 min.
2. Samples are centrifuged for 15 min at 12,000 g and 4 °C to achieve phase separation.
3. The upper aqueous phase is carefully removed and added to 300 µL of pre-chilled 70 % ethanol.
4. The sample is transferred to a spin cartridge and centrifuged for 30 s at RT. The flow-through is discarded.
5. 350 µL Wash Buffer I is added to the spin cartridge followed by another centrifugation. Flow through is again discarded.
6. 80 µL PureLink™ DNase mixture is added directly to the surface of the spin cartridge membrane and incubated for 15 min at RT.
7. Step 5 is repeated.

8. 500 µL Wash Buffer II is added to the spin cartridge followed by another centrifugation. Flow through is again discarded.
9. Step 8 is repeated.
10. The empty spin cartridge is centrifuged for 1 min at 12,000 g and RT to dry the membrane with bound RNA.
11. 30 µL of pre-warmed RNase-free water (70 °C) is added and incubated for 1 min.
12. The spin cartridge is inserted into a recovery tube and centrifuged for 1 min at 12,000 g and RT.
13. Eluted RNA is stored at -80 °C.

7.5.1.2. RNA quantification

The quantity and purity of RNA was determined by spectrophotometry using the NanoDrop 2000 UV-Vis Spectrophotometer. The concentration of RNA is given in ng / µL and is typically about 300 ng / µL for RNA isolated from one well of a 6-well plate, or around 1000 ng / µL in case of a tissue sample. The purity of the RNA is specified by two different absorbance ratios. While nucleotides, RNA and DNA absorb light at 260 nm, proteins, phenol and other contaminants have a strong absorbance at 280 nm. A 260 / 280 ratio that is considerably lower than 2.0 indicates a contamination of a given sample. Contaminants such as carbohydrates, EDTA and phenol have absorbance near 230 nm. Thus, a 260 / 230 ratio that lies within the expected range of 2.0 - 2.2 is used as a secondary measure of nucleic acid purity.

7.5.1.3. Complementary single-stranded DNA preparation

Complementary single-stranded DNA (cDNA) is synthetized from an RNA template in a process called reverse transcription using the enzyme Reverse transcriptase (RT). In course of this thesis, cDNA was synthesized using qScript® cDNA SuperMix following the manufacturer’s instructions:

1. An amount of 1 µg RNA is brought to a final volume of 16 µL using UltraPure™ Distilled Water and 4 µL qScript® cDNA SuperMix is added to the reaction.
2. After thoroughly mixing the reactions, cDNA is synthesized using the GeneAmp® thermocycler by incubating the samples with the following conditions:
    - 5 min at 25 °C
    - 30 min at 42 °C
    - 5 min at 85 °C
    - 4 °C on hold
3. Once the samples cooled down to 4 °C, they are diluted 1:50 using UltraPure™ Distilled Water. Subsequently, 6 µL of this cDNA dilution is used for every reaction during quantitative polymerase chain reaction.

7.5.1.4. Real time quantitative polymerase chain reaction

Real time quantitative polymerase chain reaction (RT-qPCR) was performed in 384-well plates using the thermocycler QuantStudio™ 6 Flex Real-Time PCR System. Each sample was measured in triplicates and all measurements were normalized to β-actin. Reactions contained 6 ng of cDNA, 625 nM of forward and reverse primers, 6 µL of SYBR Green PCR Master Mix in a final volume of 16 µL.

The RT-qPCR is performed in three distinct steps. First, there is an initial denaturation step at 95 °C for 10 min. This is followed by 40 cycles of 15 s of 95 °C and 1 min at 60 °C. The last step is recording a melting curve, which serves as a positive control that only one specific PCR-product was amplified. The melting curve is generated by constantly detecting fluorescence while the temperature is increasing 0.05 °C / s. Rising temperatures cause dissociation of double-stranded DNA molecules, resulting in a decrease of SYBR®Green fluorescence. Melting temperatures are specific for each DNA molecule. Thus, RT-qPCRs that amplified a specific target will show a melting curve with one single peak, while RT-qPCRs that were unspecific will generate curves with multiple peaks.

7.5.2. Transcriptomics

In order to perform RNASeq, RNA was isolated from liver tissues of 24-week-old liver-specific TP53INP2 mice and their control littermates (Material and Methods, 7.5.1.1).

Isolated RNA was processed by the Functional Genomics Core Facility of the IRB Barcelona, which included initial quality control of the samples, library preparation and quality control of prepared libraries. Sequencing was performed at the CNAG sequencing unit of the Centre for Genomic Regulation using 50 nt single read length and 30 million reads per sample. Data was processed and analyzed by the Biostatistics and Bioinformatic Core Facility of the IRB Barcelona.

7.5.3. Protein analysis by Western Blot

Western blotting is a commonly used technique to detect proteins of interest within a protein extract. First, protein homogenates are prepared from cells or tissues. The concentration of protein is quantified, and samples are prepared for gel electrophoresis, a procedure that separates proteins based on their size. An electrical current is used to transfer the proteins from the gel onto a membrane. The membrane is then incubated in solutions containing specific antibodies to detect selected proteins. The primary antibody is designed to bind the protein of interest, while the secondary antibody is directed against the primary antibody. Secondary antibodies are often conjugated to a fluorophore or enzymes like horseradish peroxidase (HRP). These conjugates allow detection of desired proteins by imaging systems (such as the Odyssey® Fc Imaging System) or by incubating the membrane with a substrate solution (ECL). HRP, which is conjugated to the secondary antibody, catalyzes the conversion of chemiluminescent substrates, which emits low intensity light that can be detected using X-ray films. Finally, detected signals can be quantified by densitometric analysis.

7.5.3.1. Protein extraction from cells

1. Culture dishes (6 or 10 cm dishes) are placed on ice and cells were harvested in culture media using a cell scraper.
2. Cell suspension is transferred to pre-chilled 2 mL microcentrifuge tubes and centrifuged at 300 g at 4 °C for 5 min (5427 R, Eppendorf™).
3. The supernatant is removed, and the pellet is washed once with ice-cold PBS.
4. Centrifugation at 1,600 rpm at 4 °C for 5 min.
5. Supernatant is removed and the cell-pellet is frozen at -80 °C.
6. The cell-pellet is resolved in RIPA buffer and incubated on ice for 15 min.
7. Samples are centrifuged at 18,200 g for 10 min at 4 °C.
8. Supernatant is collected and protein content is quantified (Material and Methods, 7.5.3.3) and adjusted to 5 µg / µL.

7.5.3.2. Protein extraction from tissues

Animals were sacrificed by CO_2 inhalation. The animal was rinsed with 70 % ethanol and the abdomen was opened. Tissues were harvested, weighed and snap-frozen in liquid nitrogen and stored at -80 °C until further processing.

1. Pieces of about 20-30 mg tissue are added to tubes containing 600 µL RIPA buffer and three zirconium oxide beads.
2. Tubes are inserted to the Mini-Beadbeater disruptor (Bio Spec Products) and homogenized for 30 s at 3,400 oscillations per minute.

3. Samples are rotated for 30 min at 4 °C.
4. Homogenates are centrifuged at 18,200 g for 10 min at 4 °C.
5. Supernatant is collected and quantified (Material and Methods, 7.5.3.3) and adjusted to 5 µg / µL.

7.5.3.3. Protein quantification

Protein homogenates were quantified using Pierce™ BCA Protein Assay Kit following the manufacturer's instructions. This procedure is based on the generation of a violet compound in amounts proportional to the protein concentration of the sample. In an alkaline environment, proteins within the sample reduce Cu^{2+} to Cu^{1+}, which is also known as the Biuret reaction. Bicinchoninic acid (BCA) is highly sensitive to Cu^{1+} cations and is converted into purple reaction products that can be quantified by measuring the absorbance at 562 nm using a spectrophotometer. Samples are measured in duplicates. The kit contains an albumin standard solution with a concentration of 2 mg / mL that was used to prepare a standard curve. Water was used as a blank.

1. An albumin standard curve ranging from 1 to 20 mg is pipetted into wells of a microtiter plate.
2. Samples (1.5 µL) are added to microtiter wells.
3. BCA reagent B is diluted 1:50 with BCA reagent A and 200 µL of the solution are added to each well.
4. The plate is incubated at 37 °C for 30 min.
5. Finally, the absorbance at 562 nm is detected using a microplate reader (BioTek®, Sunrise®).
6. Protein concentration of samples is calculated by interpolating the unknown value from the standard curve.

7.5.3.4. Sample preparation

Protein homogenates are brought to a desired concentration with ultrapure water. Three volumes of sample are mixed with one volume of 4X loading dye (Material and Methods, Table 6), and samples are boiled at 95 °C for 5 min to denature proteins. Protein homogenates destined for detection of high molecular weight proteins by Western blot were not boiled.

7.5.3.5. Sodium dodecyl sulfate–polyacrylamide gel electrophoresis

Sodium dodecyl sulfate–polyacrylamide gel electrophoresis (SDS-PAGE) was performed using the Mini-Protean system (Bio-Rad). Gels of 1.5 mm depth were poured between two clean glass plates (sandwich of spacer and short glass). Depending on the molecular weight of the proteins of interest, a 6 % - 13 % acrylamide separation gel is prepared (Material and Methods, Table 10), poured between the glasses and topped with isopropanol to straighten the gels surface. The gel is allowed to polymerize. The stacking gel is prepared (Material and Methods, Table 11) and added on top of the polymerized separation gel after elimination of the isopropanol. Depending on the volume of samples, 1.5 mm thick 10- or 15-well combs were inserted into the stacking gel to create wells of 66 µL or 40 µL, respectively. The gel was allowed to polymerize before the comb was removed. Gels were used immediately or stored up to 4 days at 4 °C.

Glass sandwiches containing polymerized gels were placed into the electrophoresis system. The buffer tank was filled with electrophoresis buffer (Material and Methods, Table 12). The gel was allowed to equilibrate for 15 min before the protein standard (Material and Methods, Table 15) and samples were loaded into the wells. The electrophoresis chamber was closed using a lid that is connected to the power supply. The gel was run using a constant electrical potential difference of 90 V until the migration front reached the bottom of the gel.

7.5.3.6. Transfer of proteins to PVDF membranes

After SDS-PAGE, proteins need to be transferred from the gel to a membrane in order to be detected. In course of this thesis PVDF membranes (Material and Methods, Table 16) that require activation in 100 % methanol prior to transfer, were used. In order to transfer the proteins, a sandwich out of filter papers (Whatman®), sponges, gel and membrane was prepared in color-coded cassettes in a box filled with transfer buffer (Material and Methods, Table 13). Care was taken to avoid bubbles between the layers, which prevent the transfer of proteins. The sandwich was assembled in the following order:

1. A sponge soaked in transfer buffer is placed on the black part of the cassette.
2. A transfer buffer-soaked filter paper is placed on top of the sponge.
3. The gel containing separated proteins is equilibrated in transfer buffer and placed onto the filter paper.
4. A piece of PVDF membrane, activated for 1 min in methanol, is placed onto the gel.
5. Another filter paper soaked in transfer buffer, is placed on top of the membrane.
6. A transfer buffer-soaked sponge is placed on top of the filter paper.
7. The transparent part of the cassette is pressed onto the layers and the cassette is closed.

The cassette was inserted into the transfer tank. The color-coded cassettes and electrodes of the tank ensure the correct orientation of the gel and membrane during transfer. A cooling unit was inserted into the transfer tank before it was filled with transfer buffer. The transfer chamber was closed using a lid that is connected to the power supply. The power was turned on, and the gel was run for 999 min using an electrical current of 90 mA. After the transfer, the membrane is removed from the cassette and is used for immunodetection of proteins (Material and Methods, 7.5.3.7.).

7.5.3.7. Immunodetection of proteins of interest

Proteins transferred onto a membrane can be immunodetected using primary antibodies that specifically bind to proteins of interest, and secondary antibodies directed against primary antibodies. Immunodetection consist of four main steps including blocking, incubation with primary and secondary antibody and finally detection.

First, the membrane is placed into a blocking solution of PBS containing 0.1 % (v / v) Tween-20 (PBST), supplemented with 5 % (w / v) skimmed milk powder. The membrane is incubated for one hour on a shaker with agitation (100 rpm). This step reduces background signals by blocking non-specific binding sites for antibodies using a solution rich in proteins.

The blocked membrane is then immersed in the primary antibody solution. Specific conditions depend on the antibody that is used and are described in detail in Material and Methods, Table 27. Membranes are incubated overnight inside 50 mL tubes placed on a TubeRoller™ at 4 °C. After incubation, the membranes are washed three times using PBST for 10 min each. The washing steps are performed with agitation on a shaker at RT.

The membrane that is now free of unbound primary antibody is immersed in a secondary antibody solution that is prepared in PBST containing 5 % (w / v) skimmed milk powder. Specific conditions are detailed in Material and Methods, Table 28. Secondary antibodies target primary antibodies and are conjugated to fluorophores or enzymes that allow their detection. Membranes are incubated for 1 h at RT and with agitation. After incubation, the membranes are washed three times using PBST for 10 min each. In case of fluorescently labelled secondary antibodies, membranes were washed one more time using PBS without Tween-20.

Lastly, the protein of interest is detected. This was done in two different ways, depending on the secondary antibodies that were used. Membranes incubated with HRP-conjugated secondary antibodies were incubated with a substrate solution (ECL™, GE Healthcare) according to the manufacturer’s instructions. Briefly, solution A (luminol solution) and solution B (peroxidase solution) are mixed (1:1) and the surface of the membrane is covered. After 1 min of incubation, excess solution is removed, and the membranes were placed between plastic sheets into an X-ray film cassette. Depending on the intensity of the signal, standard or high-sensitive films were exposed to the membranes for different times inside a dark room. The exposed films were subsequently developed using the Hyper Processor Model AM4 (Amersham Pharmacia Biotech).

In the case of membranes incubated with fluorescently labelled secondary antibodies, the membranes were scanned using the Odyssey® Fc Imaging System and the Images were acquired using the Image Studio™ Software, according to the manufacturer’s instruction.

7.5.3.8. Densitometric analysis using Image J (Fiji)

In order to determine the relative amount of the proteins of interest and housekeeping proteins, developed X-ray films were scanned using the HP Officejet Pro X576dw printer. The software Image J (Fiji) was used to quantify the density (intensity) of bands on the X-ray scans.

7.5.3.9. Image Studio™ Lite Quantification Software

Images of membranes acquired with the Odyssey® Fc Imaging System were analyzed using the Image Studio™ Lite Quantification Software.

7.5.3.10. Stripping of membranes

Restore™ Western Blot Stripping Buffer was used to remove primary and secondary antibodies from PVDF membranes in order to incubate the same membrane using different antibodies. Membranes were incubated in Stripping Buffer for 15 min, followed by blocking and incubation with another set of primary and secondary antibodies.

7.5.3.11. Coomassie Brilliant Blue staining of membranes

To proof the homogeneous transfer of proteins from gels onto PVDF membranes, proteins were stained using Coomassie Brilliant Blue. Since this staining is irreversible, membranes were only stained at the end of an experiment. The membrane was immersed in Coomassie staining solution (Material and Methods, Table 14) for 15 s. Afterwards, the membrane was washed 4 times in Coomassie destaining solution (Material and Methods, Table 14) for 5 min each.

7.6. Statistics

Unless stated otherwise, data within this PhD thesis are presented as mean ± SEM. An unpaired two-tailed Student’s t-test was used to compare differences between groups. Significance was established at $p < 0.05$. Statistical analysis was only applied to data from $n \geq 3$ independent experiments.

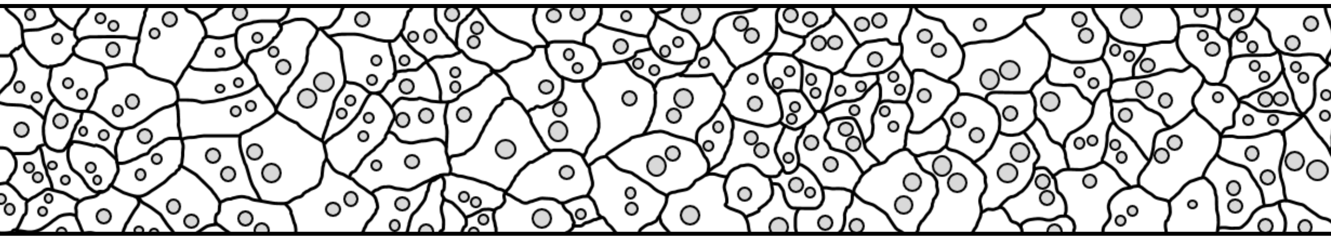

References

8. REFERENCES

1. Saklayen, M.G., *The Global Epidemic of the Metabolic Syndrome.* Curr Hypertens Rep, 2018. **20**(2): p. 12.
2. Reaven, G.M., *Banting lecture 1988. Role of insulin resistance in human disease.* Diabetes, 1988. **37**(12): p. 1595-607.
3. Aguilar, M., et al., *Prevalence of the metabolic syndrome in the United States, 2003-2012.* JAMA, 2015. **313**(19): p. 1973-4.
4. Locke, A.E., et al., *Genetic studies of body mass index yield new insights for obesity biology.* Nature, 2015. **518**(7538): p. 197-206.
5. Pollex, R.L. and R.A. Hegele, *Genetic determinants of the metabolic syndrome.* Nat Clin Pract Cardiovasc Med, 2006. **3**(9): p. 482-9.
6. Lanningham-Foster, L., L.J. Nysse, and J.A. Levine, *Labor saved, calories lost: the energetic impact of domestic labor-saving devices.* Obes Res, 2003. **11**(10): p. 1178-81.
7. Dunstan, D.W., et al., *Too much sitting--a health hazard.* Diabetes Res Clin Pract, 2012. **97**(3): p. 368-76.
8. Gross, L.S., et al., *Increased consumption of refined carbohydrates and the epidemic of type 2 diabetes in the United States: an ecologic assessment.* Am J Clin Nutr, 2004. **79**(5): p. 774-9.
9. Jenkins, D.J., et al., *Too much sugar, too much carbohydrate, or just too much?* Am J Clin Nutr, 2004. **79**(5): p. 711-2.
10. Berg, C.M., et al., *Food patterns and cardiovascular disease risk factors: the Swedish INTERGENE research program.* Am J Clin Nutr, 2008. **88**(2): p. 289-97.
11. Williams, K.J. and X. Wu, *Imbalanced insulin action in chronic over nutrition: Clinical harm, molecular mechanisms, and a way forward.* Atherosclerosis, 2016. **247**: p. 225-82.
12. Gigante, A., et al., *Metabolic syndrome and adipokine levels in systemic lupus erythematosus and systemic sclerosis.* Clin Rheumatol, 2021. **40**(10): p. 4253-4258.
13. Medina, G., et al., *Metabolic syndrome, autoimmunity and rheumatic diseases.* Pharmacol Res, 2018. **133**: p. 277-288.
14. Luo, Y., et al., *The influence of metabolic syndrome on gastric cancer: A meta-analysis.* Asian J Surg, 2021. **44**(12): p. 1596-1597.
15. Bjørge, T., et al., *Metabolic syndrome and breast cancer in the me-can (metabolic syndrome and cancer) project.* Cancer Epidemiol Biomarkers Prev, 2010. **19**(7): p. 1737-45.
16. Berrino, F., et al., *Metabolic syndrome and breast cancer prognosis.* Breast Cancer Res Treat, 2014. **147**(1): p. 159-65.
17. Gacci, M., et al., *Meta-analysis of metabolic syndrome and prostate cancer.* Prostate Cancer Prostatic Dis, 2017. **20**(2): p. 146-155.
18. Marhl, M., et al., *Diabetes and metabolic syndrome as risk factors for COVID-19.* Diabetes Metab Syndr, 2020. **14**(4): p. 671-677.

19. Costa, F.F., et al., *Metabolic syndrome and COVID-19: An update on the associated comorbidities and proposed therapies.* Diabetes Metab Syndr, 2020. **14**(5): p. 809-814.
20. Cardozo, E., M.E. Pavone, and J.E. Hirshfeld-Cytron, *Metabolic syndrome and oocyte quality.* Trends Endocrinol Metab, 2011. **22**(3): p. 103-9.
21. Gonzalez, M.B., R.L. Robker, and R.D. Rose, *Obesity and oocyte quality: significant implications for ART and emerging mechanistic insights.* Biol Reprod, 2022. **106**(2): p. 338-350.
22. Kort, H.I., et al., *Impact of body mass index values on sperm quantity and quality.* J Androl, 2006. **27**(3): p. 450-2.
23. Hammoud, A.O., et al., *Male obesity and alteration in sperm parameters.* Fertil Steril, 2008. **90**(6): p. 2222-5.
24. Robeva, R., et al., *[Sperm disorder in males with obesity and metabolic syndrome--pilot study].* Akush Ginekol (Sofiia), 2008. **47**(3): p. 11-4.
25. Kim, C.H. and Z.M. Younossi, *Nonalcoholic fatty liver disease: a manifestation of the metabolic syndrome.* Cleve Clin J Med, 2008. **75**(10): p. 721-8.
26. Katsiki, N., et al., *Is Nonalcoholic Fatty Liver Disease Indeed the Hepatic Manifestation of Metabolic Syndrome?* Curr Vasc Pharmacol, 2018. **16**(3): p. 219-227.
27. Estes, C., et al., *Modeling the epidemic of nonalcoholic fatty liver disease demonstrates an exponential increase in burden of disease.* Hepatology, 2018. **67**(1): p. 123-133.
28. Min, H.K., et al., *Increased hepatic synthesis and dysregulation of cholesterol metabolism is associated with the severity of nonalcoholic fatty liver disease.* Cell Metab, 2012. **15**(5): p. 665-74.
29. Ioannou, G.N., *The Role of Cholesterol in the Pathogenesis of NASH.* Trends Endocrinol Metab, 2016. **27**(2): p. 84-95.
30. Tilg, H. and A.R. Moschen, *Insulin resistance, inflammation, and non-alcoholic fatty liver disease.* Trends Endocrinol Metab, 2008. **19**(10): p. 371-9.
31. Williams, C.D., et al., *Prevalence of nonalcoholic fatty liver disease and nonalcoholic steatohepatitis among a largely middle-aged population utilizing ultrasound and liver biopsy: a prospective study.* Gastroenterology, 2011. **140**(1): p. 124-31.
32. Musso, G., M. Cassader, and R. Gambino, *Non-alcoholic steatohepatitis: emerging molecular targets and therapeutic strategies.* Nat Rev Drug Discov, 2016. **15**(4): p. 249-74.
33. Adams, L.A., et al., *The histological course of nonalcoholic fatty liver disease: a longitudinal study of 103 patients with sequential liver biopsies.* J Hepatol, 2005. **42**(1): p. 132-8.
34. Ekstedt, M., et al., *Long-term follow-up of patients with NAFLD and elevated liver enzymes.* Hepatology, 2006. **44**(4): p. 865-73.
35. Singh, S., et al., *Fibrosis progression in nonalcoholic fatty liver vs nonalcoholic steatohepatitis: a systematic review and meta-analysis of paired-biopsy studies.* Clin Gastroenterol Hepatol, 2015. **13**(4): p. 643-54.e1-9; quiz e39-40.
36. Loomba, R., et al., *AGA Clinical Practice Update on Screening and Surveillance for Hepatocellular Carcinoma in Patients With Nonalcoholic Fatty Liver Disease: Expert Review.* Gastroenterology, 2020. **158**(6): p. 1822-1830.

37. Loomba, R., S.L. Friedman, and G.I. Shulman, *Mechanisms and disease consequences of nonalcoholic fatty liver disease.* Cell, 2021. **184**(10): p. 2537-2564.
38. Desai, A., et al., *Hepatocellular carcinoma in non-cirrhotic liver: A comprehensive review.* World J Hepatol, 2019. **11**(1): p. 1-18.
39. Michelotti, A., et al., *NAFLD-Related Hepatocarcinoma: The Malignant Side of Metabolic Syndrome.* Cells, 2021. **10**(8).
40. Sung, H., et al., *Global Cancer Statistics 2020: GLOBOCAN Estimates of Incidence and Mortality Worldwide for 36 Cancers in 185 Countries.* CA Cancer J Clin, 2021. **71**(3): p. 209-249.
41. (EASL), E.A.f.t.S.o.t.L., E.A.f.t.S.o.D. (EASD), and E.A.f.t.S.o.O. (EASO), *EASL-EASD-EASO Clinical Practice Guidelines for the management of non-alcoholic fatty liver disease.* J Hepatol, 2016. **64**(6): p. 1388-402.
42. Becares, N., et al., *Impaired LXRα Phosphorylation Attenuates Progression of Fatty Liver Disease.* Cell Rep, 2019. **26**(4): p. 984-995.e6.
43. González-Rodríguez, A., et al., *Impaired autophagic flux is associated with increased endoplasmic reticulum stress during the development of NAFLD.* Cell Death Dis, 2014. **5**: p. e1179.
44. Wu, W.K.K., L. Zhang, and M.T.V. Chan, *Autophagy, NAFLD and NAFLD-Related HCC.* Adv Exp Med Biol, 2018. **1061**: p. 127-138.
45. Targher, G., C.P. Day, and E. Bonora, *Risk of cardiovascular disease in patients with nonalcoholic fatty liver disease.* N Engl J Med, 2010. **363**(14): p. 1341-50.
46. Targher, G. and C.D. Byrne, *Clinical Review: Nonalcoholic fatty liver disease: a novel cardiometabolic risk factor for type 2 diabetes and its complications.* J Clin Endocrinol Metab, 2013. **98**(2): p. 483-95.
47. Masuoka, H.C. and N. Chalasani, *Nonalcoholic fatty liver disease: an emerging threat to obese and diabetic individuals.* Ann N Y Acad Sci, 2013. **1281**: p. 106-22.
48. Angulo, P., *NAFLD, obesity, and bariatric surgery.* Gastroenterology, 2006. **130**(6): p. 1848-52.
49. Ertunc, M.E. and G.S. Hotamisligil, *Lipid signaling and lipotoxicity in metaflammation: indications for metabolic disease pathogenesis and treatment.* J Lipid Res, 2016. **57**(12): p. 2099-2114.
50. Yamauchi, T., et al., *Targeted disruption of AdipoR1 and AdipoR2 causes abrogation of adiponectin binding and metabolic actions.* Nat Med, 2007. **13**(3): p. 332-9.
51. Hui, J.M., et al., *Beyond insulin resistance in NASH: TNF-alpha or adiponectin?* Hepatology, 2004. **40**(1): p. 46-54.
52. Musso, G., et al., *Hypoadiponectinemia predicts the severity of hepatic fibrosis and pancreatic Beta-cell dysfunction in nondiabetic nonobese patients with nonalcoholic steatohepatitis.* Am J Gastroenterol, 2005. **100**(11): p. 2438-46.
53. Crespo, J., et al., *Gene expression of tumor necrosis factor alpha and TNF-receptors, p55 and p75, in nonalcoholic steatohepatitis patients.* Hepatology, 2001. **34**(6): p. 1158-63.
54. Hotamisligil, G.S., N.S. Shargill, and B.M. Spiegelman, *Adipose expression of tumor necrosis factor-alpha: direct role in obesity-linked insulin resistance.* Science, 1993. **259**(5091): p. 87-91.

55. Kern, P.A., et al., *Adipose tissue tumor necrosis factor and interleukin-6 expression in human obesity and insulin resistance.* Am J Physiol Endocrinol Metab, 2001. **280**(5): p. E745-51.
56. Wieckowska, A., et al., *Increased hepatic and circulating interleukin-6 levels in human nonalcoholic steatohepatitis.* Am J Gastroenterol, 2008. **103**(6): p. 1372-9.
57. Marchesini, G. and G. Forlani, *NASH: from liver diseases to metabolic disorders and back to clinical hepatology.* Hepatology, 2002. **35**(2): p. 497-9.
58. Semova, I. and S.B. Biddinger, *Triglycerides in Nonalcoholic Fatty Liver Disease: Guilty Until Proven Innocent.* Trends Pharmacol Sci, 2021. **42**(3): p. 183-190.
59. Lacy, P.E., et al., *New hypothesis of insulin secretion.* Nature, 1968. **219**(5159): p. 1177-9.
60. Malaisse, W.J., *Insulin secretion and food intake.* Proc Nutr Soc, 1972. **31**(2): p. 213-7.
61. Tokarz, V.L., P.E. MacDonald, and A. Klip, *The cell biology of systemic insulin function.* J Cell Biol, 2018. **217**(7): p. 2273-2289.
62. Haas, M.E., A.D. Attie, and S.B. Biddinger, *The regulation of ApoB metabolism by insulin.* Trends Endocrinol Metab, 2013. **24**(8): p. 391-7.
63. Dimitriadis, G., et al., *Insulin effects in muscle and adipose tissue.* Diabetes Res Clin Pract, 2011. **93 Suppl 1**: p. S52-9.
64. Newsholme, E.A. and G. Dimitriadis, *Integration of biochemical and physiologic effects of insulin on glucose metabolism.* Exp Clin Endocrinol Diabetes, 2001. **109 Suppl 2**: p. S122-34.
65. Stols-Gonçalves, D., et al., *NAFLD and Atherosclerosis: Two Sides of the Same Dysmetabolic Coin?* Trends Endocrinol Metab, 2019. **30**(12): p. 891-902.
66. Fuchs, C.D., T. Claudel, and M. Trauner, *Role of metabolic lipases and lipolytic metabolites in the pathogenesis of NAFLD.* Trends Endocrinol Metab, 2014. **25**(11): p. 576-85.
67. Videla, L.A., et al., *Insulin resistance and oxidative stress interdependency in non-alcoholic fatty liver disease.* Trends Mol Med, 2006. **12**(12): p. 555-8.
68. Chen, Z., et al., *Emerging Molecular Targets for Treatment of Nonalcoholic Fatty Liver Disease.* Trends Endocrinol Metab, 2019. **30**(12): p. 903-914.
69. Pagadala, M., et al., *Role of ceramides in nonalcoholic fatty liver disease.* Trends Endocrinol Metab, 2012. **23**(8): p. 365-71.
70. Vilar-Gomez, E., et al., *Weight Loss Through Lifestyle Modification Significantly Reduces Features of Nonalcoholic Steatohepatitis.* Gastroenterology, 2015. **149**(2): p. 367-78.e5; quiz e14-5.
71. Klein, S., et al., *Gastric bypass surgery improves metabolic and hepatic abnormalities associated with nonalcoholic fatty liver disease.* Gastroenterology, 2006. **130**(6): p. 1564-72.
72. Billeter, A.T., et al., *Combined Non-alcoholic Fatty Liver Disease and Type 2 Diabetes Mellitus: Sleeve Gastrectomy or Gastric Bypass?-a Controlled Matched Pair Study of 34 Patients.* Obes Surg, 2016. **26**(8): p. 1867-74.
73. Marihart, C.L., A.R. Brunt, and A.A. Geraci, *Older adults fighting obesity with bariatric surgery: Benefits, side effects, and outcomes.* SAGE Open Med, 2014. **2**: p. 2050312114530917.

74. DiMasi, J.A., H.G. Grabowski, and R.W. Hansen, *Innovation in the pharmaceutical industry: New estimates of R&D costs.* J Health Econ, 2016. **47**: p. 20-33.
75. Munos, B., *Lessons from 60 years of pharmaceutical innovation.* Nat Rev Drug Discov, 2009. **8**(12): p. 959-68.
76. Eslam, M. and J. George, *Genetic Insights for Drug Development in NAFLD.* Trends Pharmacol Sci, 2019. **40**(7): p. 506-516.
77. Steensels, S., J. Qiao, and B.A. Ersoy, *Transcriptional Regulation in Non-Alcoholic Fatty Liver Disease.* Metabolites, 2020. **10**(7).
78. Martinez-Lopez, N., et al., *Autophagy in the CNS and Periphery Coordinate Lipophagy and Lipolysis in the Brown Adipose Tissue and Liver.* Cell Metab, 2016. **23**(1): p. 113-27.
79. Berthier, A., et al., *PPARs in liver physiology.* Biochim Biophys Acta Mol Basis Dis, 2021. **1867**(5): p. 166097.
80. Eberlé, D., et al., *SREBP transcription factors: master regulators of lipid homeostasis.* Biochimie, 2004. **86**(11): p. 839-48.
81. Oosterveer, M.H., et al., *The liver X receptor: control of cellular lipid homeostasis and beyond Implications for drug design.* Prog Lipid Res, 2010. **49**(4): p. 343-52.
82. Clifford, B.L., et al., *FXR activation protects against NAFLD via bile-acid-dependent reductions in lipid absorption.* Cell Metab, 2021. **33**(8): p. 1671-1684.e4.
83. Lu, J., et al., *Effect of heterodimer partner RXRalpha on PPARgamma activation function-2 helix in solution.* Biochem Biophys Res Commun, 2008. **365**(1): p. 42-6.
84. Nakamura, M.T., et al., *Mechanisms of regulation of gene expression by fatty acids.* Lipids, 2004. **39**(11): p. 1077-83.
85. Montagner, A., et al., *Liver PPARα is crucial for whole-body fatty acid homeostasis and is protective against NAFLD.* Gut, 2016. **65**(7): p. 1202-14.
86. Skat-Rørdam, J., et al., *A role of peroxisome proliferator-activated receptor γ in non-alcoholic fatty liver disease.* Basic Clin Pharmacol Toxicol, 2019. **124**(5): p. 528-537.
87. DeBose-Boyd, R.A. and J. Ye, *SREBPs in Lipid Metabolism, Insulin Signaling, and Beyond.* Trends Biochem Sci, 2018. **43**(5): p. 358-368.
88. Tall, A.R. and L. Yvan-Charvet, *Cholesterol, inflammation and innate immunity.* Nat Rev Immunol, 2015. **15**(2): p. 104-16.
89. Patel, M.B., et al., *Liver x receptor: a novel therapeutic target.* Indian J Pharm Sci, 2008. **70**(2): p. 135-44.
90. Wang, B. and P. Tontonoz, *Liver X receptors in lipid signalling and membrane homeostasis.* Nat Rev Endocrinol, 2018. **14**(8): p. 452-463.
91. Zelcer, N. and P. Tontonoz, *Liver X receptors as integrators of metabolic and inflammatory signaling.* J Clin Invest, 2006. **116**(3): p. 607-14.
92. Klionsky, D.J., et al., *Autophagy in major human diseases.* EMBO J, 2021. **40**(19): p. e108863.
93. Orenstein, S.J. and A.M. Cuervo, *Chaperone-mediated autophagy: molecular mechanisms and physiological relevance.* Semin Cell Dev Biol, 2010. **21**(7): p. 719-26.

94. Sun, Q., et al., *Identification of Barkor as a mammalian autophagy-specific factor for Beclin 1 and class III phosphatidylinositol 3-kinase.* Proc Natl Acad Sci U S A, 2008. **105**(49): p. 19211-6.
95. Qian, H., et al., *Autophagy in liver diseases: A review.* Mol Aspects Med, 2021. **82**: p. 100973.
96. Lu, J., et al., *NRBF2 regulates autophagy and prevents liver injury by modulating Atg14L-linked phosphatidylinositol-3 kinase III activity.* Nat Commun, 2014. **5**: p. 3920.
97. Takahashi, Y., et al., *Bif-1 interacts with Beclin 1 through UVRAG and regulates autophagy and tumorigenesis.* Nat Cell Biol, 2007. **9**(10): p. 1142-51.
98. Pattingre, S., et al., *Bcl-2 antiapoptotic proteins inhibit Beclin 1-dependent autophagy.* Cell, 2005. **122**(6): p. 927-39.
99. Zhong, Y., et al., *Distinct regulation of autophagic activity by Atg14L and Rubicon associated with Beclin 1-phosphatidylinositol-3-kinase complex.* Nat Cell Biol, 2009. **11**(4): p. 468-76.
100. Zhang, L., et al., *Unraveling the roles of Atg4 proteases from autophagy modulation to targeted cancer therapy.* Cancer Lett, 2016. **373**(1): p. 19-26.
101. Wild, P., D.G. McEwan, and I. Dikic, *The LC3 interactome at a glance.* J Cell Sci, 2014. **127**(Pt 1): p. 3-9.
102. Komatsu, M. and Y. Ichimura, *Physiological significance of selective degradation of p62 by autophagy.* FEBS Lett, 2010. **584**(7): p. 1374-8.
103. Lamark, T., et al., *NBR1 and p62 as cargo receptors for selective autophagy of ubiquitinated targets.* Cell Cycle, 2009. **8**(13): p. 1986-90.
104. Xu, Y. and W. Wan, *TP53INP2 mediates autophagic degradation of ubiquitinated proteins through its ubiquitin-interacting motif.* FEBS Lett, 2019. **593**(15): p. 1974-1982.
105. Li, X., S. He, and B. Ma, *Autophagy and autophagy-related proteins in cancer.* Mol Cancer, 2020. **19**(1): p. 12.
106. Noda, N.N., *Atg2 and Atg9: Intermembrane and interleaflet lipid transporters driving autophagy.* Biochim Biophys Acta Mol Cell Biol Lipids, 2021. **1866**(8): p. 158956.
107. Takahashi, Y., et al., *VPS37A directs ESCRT recruitment for phagophore closure.* J Cell Biol, 2019. **218**(10): p. 3336-3354.
108. Takahashi, Y., et al., *An autophagy assay reveals the ESCRT-III component CHMP2A as a regulator of phagophore closure.* Nat Commun, 2018. **9**(1): p. 2855.
109. Shoemaker, C.J., et al., *CRISPR screening using an expanded toolkit of autophagy reporters identifies TMEM41B as a novel autophagy factor.* PLoS Biol, 2019. **17**(4): p. e2007044.
110. Morita, K., Y. Hama, and N. Mizushima, *TMEM41B functions with VMP1 in autophagosome formation.* Autophagy, 2019. **15**(5): p. 922-923.
111. Ropolo, A., et al., *The pancreatitis-induced vacuole membrane protein 1 triggers autophagy in mammalian cells.* J Biol Chem, 2007. **282**(51): p. 37124-33.
112. Nowak, J., et al., *The TP53INP2 protein is required for autophagy in mammalian cells.* Mol Biol Cell, 2009. **20**(3): p. 870-81.
113. Itakura, E., C. Kishi-Itakura, and N. Mizushima, *The hairpin-type tail-anchored SNARE syntaxin 17 targets to autophagosomes for fusion with endosomes/lysosomes.* Cell, 2012. **151**(6): p. 1256-69.

114. Furuta, N., et al., *Combinational soluble N-ethylmaleimide-sensitive factor attachment protein receptor proteins VAMP8 and Vti1b mediate fusion of antimicrobial and canonical autophagosomes with lysosomes.* Mol Biol Cell, 2010. **21**(6): p. 1001-10.
115. Jäger, S., et al., *Role for Rab7 in maturation of late autophagic vacuoles.* J Cell Sci, 2004. **117**(Pt 20): p. 4837-48.
116. Eskelinen, E.L., *Roles of LAMP-1 and LAMP-2 in lysosome biogenesis and autophagy.* Mol Aspects Med, 2006. **27**(5-6): p. 495-502.
117. Hubert, V., et al., *LAMP-2 is required for incorporating syntaxin-17 into autophagosomes and for their fusion with lysosomes.* Biol Open, 2016. **5**(10): p. 1516-1529.
118. Singh, R., et al., *Autophagy regulates lipid metabolism.* Nature, 2009. **458**(7242): p. 1131-5.
119. Fukuo, Y., et al., *Abnormality of autophagic function and cathepsin expression in the liver from patients with non-alcoholic fatty liver disease.* Hepatol Res, 2014. **44**(9): p. 1026-36.
120. Schulze, R.J., A. Sathyanarayan, and D.G. Mashek, *Breaking fat: The regulation and mechanisms of lipophagy.* Biochim Biophys Acta Mol Cell Biol Lipids, 2017. **1862**(10 Pt B): p. 1178-1187.
121. Kaushik, S. and A.M. Cuervo, *Degradation of lipid droplet-associated proteins by chaperone-mediated autophagy facilitates lipolysis.* Nat Cell Biol, 2015. **17**(6): p. 759-70.
122. Schulze, R.J., et al., *Direct lysosome-based autophagy of lipid droplets in hepatocytes.* Proc Natl Acad Sci U S A, 2020. **117**(51): p. 32443-32452.
123. Sathyanarayan, A., M.T. Mashek, and D.G. Mashek, *ATGL Promotes Autophagy/Lipophagy via SIRT1 to Control Hepatic Lipid Droplet Catabolism.* Cell Rep, 2017. **19**(1): p. 1-9.
124. Zimmermann, R., et al., *Fat mobilization in adipose tissue is promoted by adipose triglyceride lipase.* Science, 2004. **306**(5700): p. 1383-6.
125. Schott, M.B., et al., *Lipid droplet size directs lipolysis and lipophagy catabolism in hepatocytes.* J Cell Biol, 2019. **218**(10): p. 3320-3335.
126. Du, H., et al., *Targeted disruption of the mouse lysosomal acid lipase gene: long-term survival with massive cholesteryl ester and triglyceride storage.* Hum Mol Genet, 1998. **7**(9): p. 1347-54.
127. Schroeder, B., et al., *The small GTPase Rab7 as a central regulator of hepatocellular lipophagy.* Hepatology, 2015. **61**(6): p. 1896-907.
128. Li, Z., et al., *A novel Rab10-EHBP1-EHD2 complex essential for the autophagic engulfment of lipid droplets.* Sci Adv, 2016. **2**(12): p. e1601470.
129. Gutierrez, M.G., et al., *Rab7 is required for the normal progression of the autophagic pathway in mammalian cells.* J Cell Sci, 2004. **117**(Pt 13): p. 2687-97.
130. Xu, D., et al., *Rab18 promotes lipid droplet (LD) growth by tethering the ER to LDs through SNARE and NRZ interactions.* J Cell Biol, 2018. **217**(3): p. 975-995.
131. Li, Q., et al., *Depletion of Rab32 decreases intracellular lipid accumulation and induces lipolysis through enhancing ATGL expression in hepatocytes.* Biochem Biophys Res Commun, 2016. **471**(4): p. 492-6.

132. O'Rourke, E.J. and G. Ruvkun, *MXL-3 and HLH-30 transcriptionally link lipolysis and autophagy to nutrient availability.* Nat Cell Biol, 2013. **15**(6): p. 668-76.

133. Settembre, C., et al., *TFEB controls cellular lipid metabolism through a starvation-induced autoregulatory loop.* Nat Cell Biol, 2013. **15**(6): p. 647-58.

134. Seok, S., et al., *Transcriptional regulation of autophagy by an FXR-CREB axis.* Nature, 2014. **516**(7529): p. 108-11.

135. Lee, J.M., et al., *Nutrient-sensing nuclear receptors coordinate autophagy.* Nature, 2014. **516**(7529): p. 112-5.

136. Xiong, J., et al., *TFE3 Alleviates Hepatic Steatosis through Autophagy-Induced Lipophagy and PGC1α-Mediated Fatty Acid β-Oxidation.* Int J Mol Sci, 2016. **17**(3): p. 387.

137. Lettieri Barbato, D., et al., *FoxO1 controls lysosomal acid lipase in adipocytes: implication of lipophagy during nutrient restriction and metformin treatment.* Cell Death Dis, 2013. **4**: p. e861.

138. Xiong, X., et al., *The autophagy-related gene 14 (Atg14) is regulated by forkhead box O transcription factors and circadian rhythms and plays a critical role in hepatic autophagy and lipid metabolism.* J Biol Chem, 2012. **287**(46): p. 39107-14.

139. Lohmann, D., et al., *Monoubiquitination of ancient ubiquitous protein 1 promotes lipid droplet clustering.* PLoS One, 2013. **8**(9): p. e72453.

140. Spandl, J., et al., *Ancient ubiquitous protein 1 (AUP1) localizes to lipid droplets and binds the E2 ubiquitin conjugase G2 (Ube2g2) via its G2 binding region.* J Biol Chem, 2011. **286**(7): p. 5599-606.

141. Tatsumi, T., et al., *Forced lipophagy reveals that lipid droplets are required for early embryonic development in mouse.* Development, 2018. **145**(4).

142. Schulze, R.J., et al., *Hepatic Lipophagy: New Insights into Autophagic Catabolism of Lipid Droplets in the Liver.* Hepatol Commun, 2017. **1**(5): p. 359-369.

143. Goodman, J.M., *The importance of microlipophagy in liver.* Proc Natl Acad Sci U S A, 2021. **118**(2).

144. Baumgartner, B.G., et al., *Identification of a novel modulator of thyroid hormone receptor-mediated action.* PLoS One, 2007. **2**(11): p. e1183.

145. Nowak, J., et al., *Assignment of the tumor protein p53 induced nuclear protein 2 (TP53INP2) gene to human chromosome band 20q11.2 by in situ hybridization.* Cytogenet Genome Res, 2005. **108**(4): p. 362.

146. Sancho, A., et al., *DOR/Tp53inp2 and Tp53inp1 constitute a metazoan gene family encoding dual regulators of autophagy and transcription.* PLoS One, 2012. **7**(3): p. e34034.

147. Mauvezin, C., et al., *DOR undergoes nucleo-cytoplasmic shuttling, which involves passage through the nucleolus.* FEBS Lett, 2012. **586**(19): p. 3179-86.

148. Ivanova, S., et al., *Regulation of death receptor signaling by the autophagy protein TP53INP2.* EMBO J, 2019. **38**(10).

149. Xu, Y., et al., *TP53INP2/DOR, a mediator of cell autophagy, promotes rDNA transcription via facilitating the assembly of the POLR1/RNA polymerase I preinitiation complex at rDNA promoters.* Autophagy, 2016. **12**(7): p. 1118-28.

150. Mauvezin, C., et al., *The nuclear cofactor DOR regulates autophagy in mammalian and Drosophila cells.* EMBO Rep, 2010. **11**(1): p. 37-44.

151. Huang, R. and W. Liu, *Identifying an essential role of nuclear LC3 for autophagy.* Autophagy, 2015. **11**(5): p. 852-3.

152. Kabeya, Y., et al., *LC3, GABARAP and GATE16 localize to autophagosomal membrane depending on form-II formation.* J Cell Sci, 2004. **117**(Pt 13): p. 2805-12.

153. Geng, J. and D.J. Klionsky, *The Atg8 and Atg12 ubiquitin-like conjugation systems in macroautophagy. 'Protein modifications: beyond the usual suspects' review series.* EMBO Rep, 2008. **9**(9): p. 859-64.

154. You, Z., et al., *TP53INP2 contributes to autophagosome formation by promoting LC3-ATG7 interaction.* Autophagy, 2019. **15**(8): p. 1309-1321.

155. Sala, D., et al., *Autophagy-regulating TP53INP2 mediates muscle wasting and is repressed in diabetes.* J Clin Invest, 2014. **124**(5): p. 1914-27.

156. Francis, V.A., A. Zorzano, and A.A. Teleman, *dDOR is an EcR coactivator that forms a feed-forward loop connecting insulin and ecdysone signaling.* Curr Biol, 2010. **20**(20): p. 1799-808.

157. Vaux, D.L. and S.J. Korsmeyer, *Cell death in development.* Cell, 1999. **96**(2): p. 245-54.

158. Fulda, S. and K.M. Debatin, *Extrinsic versus intrinsic apoptosis pathways in anticancer chemotherapy.* Oncogene, 2006. **25**(34): p. 4798-811.

159. Romero, M., et al., *TP53INP2 regulates adiposity by activating β-catenin through autophagy-dependent sequestration of GSK3β.* Nat Cell Biol, 2018. **20**(4): p. 443-454.

160. Ross, S.E., et al., *Inhibition of adipogenesis by Wnt signaling.* Science, 2000. **289**(5481): p. 950-3.

161. Bennett, C.N., et al., *Regulation of Wnt signaling during adipogenesis.* J Biol Chem, 2002. **277**(34): p. 30998-1004.

162. Hernández-Alvarez, M.I., et al., *Deficient Endoplasmic Reticulum-Mitochondrial Phosphatidylserine Transfer Causes Liver Disease.* Cell, 2019. **177**(4): p. 881-895.e17.

163. McGill, M.R., *The past and present of serum aminotransferases and the future of liver injury biomarkers.* EXCLI J, 2016. **15**: p. 817-828.

164. Komatsu, M., et al., *Impairment of starvation-induced and constitutive autophagy in Atg7-deficient mice.* J Cell Biol, 2005. **169**(3): p. 425-34.

165. Tanida, I., T. Ueno, and E. Kominami, *LC3 conjugation system in mammalian autophagy.* Int J Biochem Cell Biol, 2004. **36**(12): p. 2503-18.

166. Mauvezin, C. and T.P. Neufeld, *Bafilomycin A1 disrupts autophagic flux by inhibiting both V-ATPase-dependent acidification and Ca-P60A/SERCA-dependent autophagosome-lysosome fusion.* Autophagy, 2015. **11**(8): p. 1437-8.

167. Rui, L., *Energy metabolism in the liver.* Compr Physiol, 2014. **4**(1): p. 177-97.

168. Wang, H., et al., *Cloning, expression, and characterization of three new mouse cytochrome p450 enzymes and partial characterization of their fatty acid oxidation activities.* Mol Pharmacol, 2004. **65**(5): p. 1148-58.

169. Bernal-Mizrachi, C., et al., *Dexamethasone induction of hypertension and diabetes is PPAR-alpha dependent in LDL receptor-null mice.* Nat Med, 2003. **9**(8): p. 1069-75.

170. Morrow, M.R., et al., *Inhibition of ATP-citrate lyase improves NASH, liver fibrosis, and dyslipidemia.* Cell Metab, 2022. **34**(6): p. 919-936.e8.

171. Tugwood, J.D., et al., *The mouse peroxisome proliferator activated receptor recognizes a response element in the 5' flanking sequence of the rat acyl CoA oxidase gene.* EMBO J, 1992. **11**(2): p. 433-9.
172. Repa, J.J., et al., *Regulation of ATP-binding cassette sterol transporters ABCG5 and ABCG8 by the liver X receptors alpha and beta.* J Biol Chem, 2002. **277**(21): p. 18793-800.
173. Yu, X.H., et al., *ABCG5/ABCG8 in cholesterol excretion and atherosclerosis.* Clin Chim Acta, 2014. **428**: p. 82-8.
174. Chiang, J.Y., R. Kimmel, and D. Stroup, *Regulation of cholesterol 7alpha-hydroxylase gene (CYP7A1) transcription by the liver orphan receptor (LXRalpha).* Gene, 2001. **262**(1-2): p. 257-65.
175. Repa, J.J., et al., *Regulation of mouse sterol regulatory element-binding protein-1c gene (SREBP-1c) by oxysterol receptors, LXRalpha and LXRbeta.* Genes Dev, 2000. **14**(22): p. 2819-30.
176. Sallam, T., et al., *The macrophage LBP gene is an LXR target that promotes macrophage survival and atherosclerosis.* J Lipid Res, 2014. **55**(6): p. 1120-30.
177. Wagner, B.L., et al., *Promoter-specific roles for liver X receptor/corepressor complexes in the regulation of ABCA1 and SREBP1 gene expression.* Mol Cell Biol, 2003. **23**(16): p. 5780-9.
178. Barbier, O., et al., *Peroxisome proliferator-activated receptor alpha induces hepatic expression of the human bile acid glucuronidating UDP-glucuronosyltransferase 2B4 enzyme.* J Biol Chem, 2003. **278**(35): p. 32852-60.
179. Dong, B., et al., *Suppression of Idol expression is an additional mechanism underlying statin-induced up-regulation of hepatic LDL receptor expression.* Int J Mol Med, 2011. **27**(1): p. 103-10.
180. Giral, H., et al., *Cytotoxicity of peroxisome proliferator-activated receptor alpha and gamma agonists in renal proximal tubular cell lines.* Toxicol In Vitro, 2007. **21**(6): p. 1066-76.
181. Liu, Y. and C. Tang, *Regulation of ABCA1 functions by signaling pathways.* Biochim Biophys Acta, 2012. **1821**(3): p. 522-9.
182. Chow, A.M., et al., *Measurement of liver* T_1 *and* T_2 *relaxation times in an experimental mouse model of liver fibrosis.* J Magn Reson Imaging, 2012. **36**(1): p. 152-8.
183. Ozen, H., *Glycogen storage diseases: new perspectives.* World J Gastroenterol, 2007. **13**(18): p. 2541-53.
184. Jindal, A., et al., *Fat-laden macrophages modulate lobular inflammation in nonalcoholic steatohepatitis (NASH).* Exp Mol Pathol, 2015. **99**(1): p. 155-62.
185. Baratta, J.L., et al., *Cellular organization of normal mouse liver: a histological, quantitative immunocytochemical, and fine structural analysis.* Histochem Cell Biol, 2009. **131**(6): p. 713-26.
186. MILLER, L.L., et al., *The dominant role of the liver in plasma protein synthesis; a direct study of the isolated perfused rat liver with the aid of lysine-epsilon-C14.* J Exp Med, 1951. **94**(5): p. 431-53.
187. Bernardi, M., et al., *Albumin in decompensated cirrhosis: new concepts and perspectives.* Gut, 2020. **69**(6): p. 1127-1138.
188. Schreiber, G., et al., *The secretion of serum protein and the synthesis of albumin and total protein in regenerating rat liver.* J Biol Chem, 1971. **246**(14): p. 4531-8.

189. Chojkier, M., *Inhibition of albumin synthesis in chronic diseases: molecular mechanisms.* J Clin Gastroenterol, 2005. **39**(4 Suppl 2): p. S143-6.
190. Princen, J.M., G.P. Mol-Backx, and S.H. Yap, *Restoration effects of glucose refeeding on reduced synthesis of albumin and total protein and on disaggregated polyribosomes in liver of starved rats: evidence of a post-transcriptional control mechanism.* Ann Nutr Metab, 1983. **27**(3): p. 182-93.
191. Sevall, J.S., *The albumin gene: DNA-protein interaction.* Fed Proc, 1986. **45**(9): p. 2412-5.
192. Peavy, D.E., J.M. Taylor, and L.S. Jefferson, *Correlation of albumin production rates and albumin mRNA levels in livers of normal, diabetic, and insulin-treated diabetic rats.* Proc Natl Acad Sci U S A, 1978. **75**(12): p. 5879-83.
193. Lee, S., et al., *Comparison between surrogate indexes of insulin sensitivity and resistance and hyperinsulinemic euglycemic clamp estimates in mice.* Am J Physiol Endocrinol Metab, 2008. **294**(2): p. E261-70.
194. Mensenkamp, A.R., et al., *Hepatic steatosis and very low density lipoprotein secretion: the involvement of apolipoprotein E.* J Hepatol, 2001. **35**(6): p. 816-22.
195. Millar, J.S., et al., *Determining hepatic triglyceride production in mice: comparison of poloxamer 407 with Triton WR-1339.* J Lipid Res, 2005. **46**(9): p. 2023-8.
196. Tan, S.Y., et al., *Partial deficiency of CTRP12 alters hepatic lipid metabolism.* Physiol Genomics, 2016. **48**(12): p. 936-949.
197. Wang, Y., et al., *Transcriptional regulation of hepatic lipogenesis.* Nat Rev Mol Cell Biol, 2015. **16**(11): p. 678-89.
198. Kawano, Y. and D.E. Cohen, *Mechanisms of hepatic triglyceride accumulation in non-alcoholic fatty liver disease.* J Gastroenterol, 2013. **48**(4): p. 434-41.
199. Lee, J.Y. and J.S. Parks, *ATP-binding cassette transporter AI and its role in HDL formation.* Curr Opin Lipidol, 2005. **16**(1): p. 19-25.
200. Ossoli, A., C. Pavanello, and L. Calabresi, *High-Density Lipoprotein, Lecithin: Cholesterol Acyltransferase, and Atherosclerosis.* Endocrinol Metab (Seoul), 2016. **31**(2): p. 223-9.
201. Zannis, V.I., et al., *Intracellular and extracellular processing of human apolipoprotein A-I: secreted apolipoprotein A-I isoprotein 2 is a propeptide.* Proc Natl Acad Sci U S A, 1983. **80**(9): p. 2574-8.
202. Kathiresan, S., et al., *Increased small low-density lipoprotein particle number: a prominent feature of the metabolic syndrome in the Framingham Heart Study.* Circulation, 2006. **113**(1): p. 20-9.
203. Urbina, E.M., et al., *Lipoprotein particle number and size predict vascular structure and function better than traditional lipids in adolescents and young adults.* J Clin Lipidol, 2017. **11**(4): p. 1023-1031.
204. Nakashima, H., et al., *Activation of CD11b+ Kupffer cells/macrophages as a common cause for exacerbation of TNF/Fas-ligand-dependent hepatitis in hypercholesterolemic mice.* PLoS One, 2013. **8**(1): p. e49339.
205. Chiang, J.Y., *Regulation of bile acid synthesis: pathways, nuclear receptors, and mechanisms.* J Hepatol, 2004. **40**(3): p. 539-51.
206. Chiang, J.Y., *Bile acid metabolism and signaling.* Compr Physiol, 2013. **3**(3): p. 1191-212.
207. Hofmann, A.F., *Bile Acids: The Good, the Bad, and the Ugly.* News Physiol Sci, 1999. **14**: p. 24-29.

208. Shin, D.J. and L. Wang, *Bile Acid-Activated Receptors: A Review on FXR and Other Nuclear Receptors.* Handb Exp Pharmacol, 2019. **256**: p. 51-72.
209. Chiang, J.Y., et al., *Farnesoid X receptor responds to bile acids and represses cholesterol 7alpha-hydroxylase gene (CYP7A1) transcription.* J Biol Chem, 2000. **275**(15): p. 10918-24.
210. Denson, L.A., et al., *The orphan nuclear receptor, shp, mediates bile acid-induced inhibition of the rat bile acid transporter, ntcp.* Gastroenterology, 2001. **121**(1): p. 140-7.
211. Ananthanarayanan, M., et al., *Human bile salt export pump promoter is transactivated by the farnesoid X receptor/bile acid receptor.* J Biol Chem, 2001. **276**(31): p. 28857-65.
212. Chen, F., et al., *Liver receptor homologue-1 mediates species- and cell line-specific bile acid-dependent negative feedback regulation of the apical sodium-dependent bile acid transporter.* J Biol Chem, 2003. **278**(22): p. 19909-16.
213. Bittman, R. and S.A. Fischkoff, *Fluorescence studies of the binding of the polyene antibiotics filipin 3, amphotericin B, nystatin, and lagosin to cholesterol.* Proc Natl Acad Sci U S A, 1972. **69**(12): p. 3795-9.
214. Ishibashi, S., T. Yamazaki, and K. Okamoto, *Association of autophagy with cholesterol-accumulated compartments in Niemann-Pick disease type C cells.* J Clin Neurosci, 2009. **16**(7): p. 954-9.
215. Börnig, H. and G. Geyer, *Staining of cholesterol with the fluorescent antibiotic "filipin".* Acta Histochem, 1974. **50**(1): p. 110-5.
216. Wattenberg, B.W. and D.F. Silbert, *Sterol partitioning among intracellular membranes. Testing a model for cellular sterol distribution.* J Biol Chem, 1983. **258**(4): p. 2284-9.
217. Blanchette-Mackie, E.J., *Intracellular cholesterol trafficking: role of the NPC1 protein.* Biochim Biophys Acta, 2000. **1486**(1): p. 171-83.
218. Alpy, F. and C. Tomasetto, *Give lipids a START: the StAR-related lipid transfer (START) domain in mammals.* J Cell Sci, 2005. **118**(Pt 13): p. 2791-801.
219. Olkkonen, V.M., et al., *The OSBP-related proteins (ORPs): global sterol sensors for co-ordination of cellular lipid metabolism, membrane trafficking and signalling processes?* Biochem Soc Trans, 2006. **34**(Pt 3): p. 389-91.
220. DeGrella, R.F. and R.D. Simoni, *Intracellular transport of cholesterol to the plasma membrane.* J Biol Chem, 1982. **257**(23): p. 14256-62.
221. Brown, M.S. and J.L. Goldstein, *A receptor-mediated pathway for cholesterol homeostasis.* Science, 1986. **232**(4746): p. 34-47.
222. Sleat, D.E., et al., *Genetic evidence for nonredundant functional cooperativity between NPC1 and NPC2 in lipid transport.* Proc Natl Acad Sci U S A, 2004. **101**(16): p. 5886-91.
223. Lu, F., et al., *Identification of NPC1 as the target of U18666A, an inhibitor of lysosomal cholesterol export and Ebola infection.* Elife, 2015. **4**.
224. Brown, W.V., R.I. Levy, and D.S. Fredrickson, *Further characterization of apolipoproteins from the human plasma very low density lipoproteins.* J Biol Chem, 1970. **245**(24): p. 6588-94.
225. Llorente-Cortés, V., J. Martínez-González, and L. Badimon, *LDL receptor-related protein mediates uptake of aggregated LDL in human vascular smooth muscle cells.* Arterioscler Thromb Vasc Biol, 2000. **20**(6): p. 1572-9.

226. Llorente-Cortés, V., et al., *Human coronary smooth muscle cells internalize versican-modified LDL through LDL receptor-related protein and LDL receptors.* Arterioscler Thromb Vasc Biol, 2002. **22**(3): p. 387-93.
227. Granger, B.L., et al., *Characterization and cloning of lgp110, a lysosomal membrane glycoprotein from mouse and rat cells.* J Biol Chem, 1990. **265**(20): p. 12036-43.
228. Singhal, A., et al., *Hydroxypropyl-beta and -gamma cyclodextrins rescue cholesterol accumulation in Niemann-Pick C1 mutant cell via lysosome-associated membrane protein 1.* Cell Death Dis, 2018. **9**(10): p. 1019.
229. Li, J. and S.R. Pfeffer, *Lysosomal membrane glycoproteins bind cholesterol and contribute to lysosomal cholesterol export.* Elife, 2016. **5**.
230. Yang, Y., et al., *Oxidative stress induces downregulation of TP53INP2 and suppresses osteogenic differentiation of BMSCs during osteoporosis through the autophagy degradation pathway.* Free Radic Biol Med, 2021. **166**: p. 226-237.
231. Chen, R., et al., *Protective role of autophagy in methionine-choline deficient diet-induced advanced nonalcoholic steatohepatitis in mice.* Eur J Pharmacol, 2016. **770**: p. 126-33.
232. Ni, H.M., et al., *Liver-specific loss of Atg5 causes persistent activation of Nrf2 and protects against acetaminophen-induced liver injury.* Toxicol Sci, 2012. **127**(2): p. 438-50.
233. Takamura, A., et al., *Autophagy-deficient mice develop multiple liver tumors.* Genes Dev, 2011. **25**(8): p. 795-800.
234. Inami, Y., et al., *Persistent activation of Nrf2 through p62 in hepatocellular carcinoma cells.* J Cell Biol, 2011. **193**(2): p. 275-84.
235. Ma, D., et al., *Autophagy deficiency by hepatic FIP200 deletion uncouples steatosis from liver injury in NAFLD.* Mol Endocrinol, 2013. **27**(10): p. 1643-54.
236. Hara, T., et al., *FIP200, a ULK-interacting protein, is required for autophagosome formation in mammalian cells.* J Cell Biol, 2008. **181**(3): p. 497-510.
237. Jaber, N., et al., *Class III PI3K Vps34 plays an essential role in autophagy and in heart and liver function.* Proc Natl Acad Sci U S A, 2012. **109**(6): p. 2003-8.
238. Sun, Y., et al., *Liver-specific deficiency of unc-51 like kinase 1 and 2 protects mice from acetaminophen-induced liver injury.* Hepatology, 2018. **67**(6): p. 2397-2413.
239. McAlpine, F., et al., *Regulation of nutrient-sensitive autophagy by uncoordinated 51-like kinases 1 and 2.* Autophagy, 2013. **9**(3): p. 361-73.
240. Blackwell, B.N., et al., *Longevity, body weight, and neoplasia in ad libitum-fed and diet-restricted C57BL6 mice fed NIH-31 open formula diet.* Toxicol Pathol, 1995. **23**(5): p. 570-82.
241. Rusli, F., et al., *A weekly alternating diet between caloric restriction and medium fat protects the liver from fatty liver development in middle-aged C57BL/6J mice.* Mol Nutr Food Res, 2015. **59**(3): p. 533-43.
242. Mazzaccara, C., et al., *Age-Related Reference Intervals of the Main Biochemical and Hematological Parameters in C57BL/6J, 129SV/EV and C3H/HeJ Mouse Strains.* PLoS One, 2008. **3**(11): p. e3772.
243. Mizushima, N. and T. Yoshimori, *How to interpret LC3 immunoblotting.* Autophagy, 2007. **3**(6): p. 542-5.

244. Young, M.E., et al., *Impaired long-chain fatty acid oxidation and contractile dysfunction in the obese Zucker rat heart.* Diabetes, 2002. **51**(8): p. 2587-95.
245. Geisler, C.E., et al., *Hepatic adaptations to maintain metabolic homeostasis in response to fasting and refeeding in mice.* Nutr Metab (Lond), 2016. **13**: p. 62.
246. Polizzi, A., et al., *Hepatic Fasting-Induced PPARα Activity Does Not Depend on Essential Fatty Acids.* Int J Mol Sci, 2016. **17**(10).
247. Kim, K.H., et al., *Autophagy deficiency leads to protection from obesity and insulin resistance by inducing Fgf21 as a mitokine.* Nat Med, 2013. **19**(1): p. 83-92.
248. Shibata, M., et al., *The MAP1-LC3 conjugation system is involved in lipid droplet formation.* Biochem Biophys Res Commun, 2009. **382**(2): p. 419-23.
249. da Silva Lima, N., et al., *Inhibition of ATG3 ameliorates liver steatosis by increasing mitochondrial function.* J Hepatol, 2022. **76**(1): p. 11-24.
250. Levitt, D.G. and M.D. Levitt, *Human serum albumin homeostasis: a new look at the roles of synthesis, catabolism, renal and gastrointestinal excretion, and the clinical value of serum albumin measurements.* Int J Gen Med, 2016. **9**: p. 229-55.
251. Fulks, M., R.L. Stout, and V.F. Dolan, *Albumin and all-cause mortality risk in insurance applicants.* J Insur Med, 2010. **42**(1): p. 11-7.
252. Cuchel, M., et al., *Inhibition of microsomal triglyceride transfer protein in familial hypercholesterolemia.* N Engl J Med, 2007. **356**(2): p. 148-56.
253. Wang, Y., et al., *PPARs as Metabolic Regulators in the Liver: Lessons from Liver-Specific PPAR-Null Mice.* Int J Mol Sci, 2020. **21**(6).
254. Komati, R., et al., *Ligands of Therapeutic Utility for the Liver X Receptors.* Molecules, 2017. **22**(1).
255. Bidault-Jourdainne, V., et al., *TGR5 controls bile acid composition and gallbladder function to protect the liver from bile acid overload.* JHEP Rep, 2021. **3**(2): p. 100214.
256. Sayin, S.I., et al., *Gut microbiota regulates bile acid metabolism by reducing the levels of tauro-beta-muricholic acid, a naturally occurring FXR antagonist.* Cell Metab, 2013. **17**(2): p. 225-35.
257. Staley, C., et al., *Interaction of gut microbiota with bile acid metabolism and its influence on disease states.* Appl Microbiol Biotechnol, 2017. **101**(1): p. 47-64.
258. Robertson, S.J., et al., *Comparison of Co-housing and Littermate Methods for Microbiota Standardization in Mouse Models.* Cell Rep, 2019. **27**(6): p. 1910-1919.e2.
259. Jay, A.G., et al., *CD36 binds oxidized low density lipoprotein (LDL) in a mechanism dependent upon fatty acid binding.* J Biol Chem, 2015. **290**(8): p. 4590-4603.
260. van Bennekum, A., et al., *Class B scavenger receptor-mediated intestinal absorption of dietary beta-carotene and cholesterol.* Biochemistry, 2005. **44**(11): p. 4517-25.
261. Nohturfft, A., et al., *Sterols regulate cycling of SREBP cleavage-activating protein (SCAP) between endoplasmic reticulum and Golgi.* Proc Natl Acad Sci U S A, 1999. **96**(20): p. 11235-40.
262. Maharjan, Y., et al., *Autophagy alteration prevents primary cilium disassembly in RPE1 cells.* Biochem Biophys Res Commun, 2018. **500**(2): p. 242-248.

263. Errico, T.L., et al., *LXR-dependent regulation of macrophage-specific reverse cholesterol transport is impaired in a model of genetic diabesity.* Transl Res, 2017. **186**: p. 19-35.e5.

264. Mallol, R., et al., *Liposcale: a novel advanced lipoprotein test based on 2D diffusion-ordered 1H NMR spectroscopy.* J Lipid Res, 2015. **56**(3): p. 737-746.

265. Dentin, R., et al., *Hepatic glucokinase is required for the synergistic action of ChREBP and SREBP-1c on glycolytic and lipogenic gene expression.* J Biol Chem, 2004. **279**(19): p. 20314-26.

266. Klionsky, D.J., et al., *Guidelines for the use and interpretation of assays for monitoring autophagy.* Autophagy, 2012. **8**(4): p. 445-544.

267. Benitez-Amaro, A., et al., *Molecular basis for the protective effects of low-density lipoprotein receptor-related protein 1 (LRP1)-derived peptides against LDL aggregation.* Biochim Biophys Acta Biomembr, 2019. **1861**(7): p. 1302-1316.

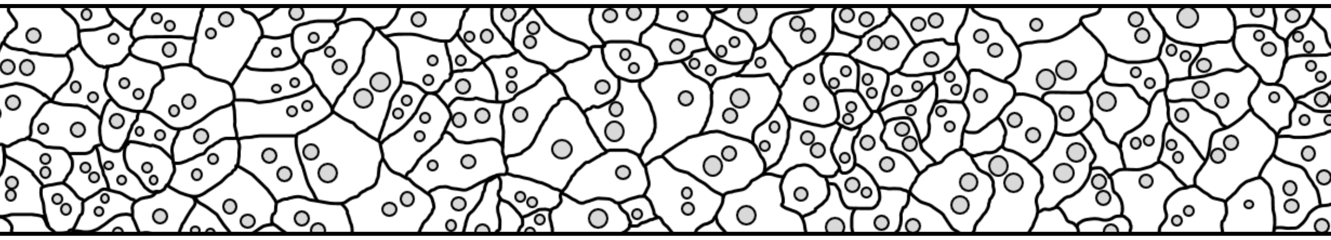

List of Figures

9. LIST OF FIGURES

Figure 1. Progression of non-alcoholic fatty liver disease. 7
Figure 2. Schematic models of the three major types of autophagy 13
Figure 3. Schematic models of protein complexes involved in the initiation and nucleation of autophagy. 15
Figure 4. Schematic model of the elongation of the phagophore. 16
Figure 5. Schematic model of processes involved in lipophagy. 20
Figure 6. Sequence of murine TP53INP2 protein including highlighted known motifs. 24
Figure 7. Relative mRNA expression of TP53INP2 in various mouse tissues. 27
Figure 8. Overnight fasting upregulates mRNA and depletes protein levels of TP53INP2 in livers and isolated primary hepatocytes. 38
Figure 9. High-fat diet treatment transiently alters hepatic TP53INP2 levels. 39
Figure 10. Hepatic TP53INP2 protein levels are depleted in a mouse model of non-alcoholic steatohepatitis. 40
Figure 11. Liver-specific knockout of TP53INP2 markedly reduced TP53INP2 levels in livers. 41
Figure 12. Body weight, body composition and weight of tissues are similar in control and TP53INP2-LKO mice in young adult mice. 42
Figure 13. Twelve-month-old TP53INP2-LKO mice show lower body weight compared to control mice due to less fat accumulation. 43
Figure 14. Aging causes a similar increase of hepatic triglyceride and cholesterol content in loxP and TP53INP2-LKO mice. 44
Figure 15. One-year-old TP53INP2-LKO mice show higher alanine aminotransferase levels than controls. 44
Figure 16. TP53INP2-depleted livers show impaired lipidation of LC3 protein when autophagy is activated by fasting. 46
Figure 17. Primary hepatocytes isolated from TP53INP2-LKO animals show an impaired autophagic flux. 46
Figure 18. Overnight fasting provokes a similar weight loss in control and TP53INP2-LKO animals. 47

Figure 19. TP53INP2-LKO animals show normal glucose handling. 48
Figure 20. A short fast reveals impaired lipid oxidation in TP53INP2-LKO animals....49
Figure 21. TP53INP2-depleted livers generate less ketone bodies upon overnight fasting. 50
Figure 22. Fasted TP53INP2-LKO animals accumulate more lipids upon overnight fasting. 51
Figure 23. TP53INP2-depleted livers show enhanced accumulation of triglycerides and cholesterol upon overnight fasting. 51
Figure 24. TP53INP2-depletion results in 235 differentially expressed genes in livers of loxP and TP53INP2-LKO animals. 52
Figure 25. PPAR signaling and fatty acid metabolism pathways are downregulated in TP53INP2-depleted livers...53
Figure 26. EnrichR Gene set enrichment analysis associated downregulated genes in TP53INP2-depleted livers with the transcription factors LXR, RXR and PPARα.54
Figure 27. TP53INP2-depleted livers show impaired transcription of PPARα and LXRα target genes. 55
Figure 28. LXRα and RXRα agonist treatment results in enhanced expression of Abca1 in TP53INP2-depleteted hepatocytes. 56
Figure 29. TP53INP2-KO MEF cells show enhanced transcriptional activity of PPARα and LXRα...58
Figure 30. TP53INP2-KO MEFs have enhanced Abca1 protein levels in basal and agonist treated conditions. 58
Figure 31. Validation of GFP or TP53INP2-GFP overexpression in the Huh7 hepatocellular carcinoma cell line...59
Figure 32. TP53INP2-GFP overexpressing Huh7 cells show impaired PPARα transcriptional activity. 60
Figure 33. Agonist treated TP53INP2-GFP overexpressing Huh7 cells show impaired LXRα transcriptional activity upon LXRα-overexpression. 61
Figure 34. Timeline of high-fat diet experiments. 62
Figure 35. High-fat diet treatment of 16 weeks causes increased liver weight in TP53INP2-depleted animals. 63
Figure 36. Morphological studies of livers of chow and 16-weeks high-fat diet fed animals. 65

Figure 37. High-fat diet treatment of 16 weeks increases F4/80-positive area in TP53INP2-depleted livers. 66
Figure 38. Plasma alanine aminotransferase and aspartate aminotransferase levels are similar in loxP and TP53INP2-LKO animals upon high-fat diet treatment. 67
Figure 39. TP53INP2-LKO animals show reduced plasma protein concentrations on standard diet, abrogated by high-fat diet treatment. 68
Figure 40. High-fat diet treatment of 7 weeks causes insulin resistance in TP53INP2-LKO animals. 70
Figure 41. TP53INP2-LKO animals subjected to high-fat diet show impaired glucose handling during a glucose tolerance test. 70
Figure 42. Overnight fasted TP53INP2-LKO animals subjected to 7 weeks of high-fat diet show decreased plasma ketone bodies and cholesterol levels. 71
Figure 43. High-fat diet treatment of 16 weeks causes reduced plasma but elevated liver triglyceride levels in TP53INP2-LKO animals. 72
Figure 44. Livers of TP53INP2-LKO subjected to 16 weeks of HFD show increased Oil-Red-O staining. 72
Figure 45. TP53INP2-LKO animals subjected to a HFD show normal lipid metabolism during an oral lipid tolerance test. 74
Figure 46. TP53INP2-LKO animals show normal very-low-density lipoprotein secretion compared to control animals. 75
Figure 47. Elevated liver triglyceride content in TP53INP2-depleted livers on high-fat diet is not caused by enhanced lipogenesis. 76
Figure 48. TP53INP2-LKO animals show enhanced hepatic cholesterol accumulation in course of a high-fat diet treatment, followed by decreased levels upon prolongation of the treatment. 78
Figure 49. TP53INP2-depletion in livers of high-fat diet treated animals impacts high-density lipoprotein metabolism. 79
Figure 50. TP53INP2-depletion causes alterations in high-density lipoprotein particle number and diameter after 8 weeks of a high-fat diet treatment. 80
Figure 51. Timeline of western diet experiments. 82
Figure 52. Western diet treatment causes no differences in body or liver weight between loxP and TP53INP2-LKO animals but results in a reduction of hepatic TP53INP2 expression. 82

Figure 53. Elevated liver triglycerides and increased plasma and liver cholesterol levels caused by a western-diet treatment are not affected by hepatic TP53INP2-depletion. 83

Figure 54. Morphological analysis of livers of chow and 16-weeks western diet fed animals. 84

Figure 55. Western diet treatment of 16 weeks increases F4/80-positive area in TP53INP2-depleted livers. 85

Figure 56. Western-diet elevates plasma alanine aminotransferase but not aspartate aminotransferase levels in TP53INP2-LKO animals. 86

Figure 57. TP53INP2-depletion prevents increased plasma and fecal bile acid levels caused by western diet treatment. 88

Figure 58. Niemann-Pick C1 protein inhibition by U18666A treatment causes increased free cholesterol accumulation in TP53INP2-depleted hepatocytes. 90

Figure 60. Niemann-Pick C1 protein inhibition by U18666A results in higher free cholesterol levels in TP53INP2-KO mouse embryonic fibroblasts in the presence of (aggregated) low-density lipoprotein. 92

Figure 61. TP53INP2-KO mouse embryonic fibroblasts show enhanced protein levels of LDL-Receptor under basal conditions. 93

Figure 62. LDL-Receptor protein levels are similar to controls in TP53INP2-depleted livers. 94

Figure 63. Cholesterol loading of primary hepatocytes by low-density lipoprotein treatment reduces autophagic flux in loxP cells to the level of TP53INP2-LKO hepatocytes. 95

Figure 64. TP53INP2-KO mouse embryonic fibroblasts have enhanced basal protein levels of LAMP1 compared to controls but don’t accumulate LAMP1 upon U18666A treatment. 96

Figure 65. TP53INP2 gene structure of TP53INP2$^{\mathrm{loxP/loxP}}$ control mice and TP53INP2-LKO mice. 138

Figure 66. Genotyping of experimental animals by PCR. 141

Figure 67. Isolation of primary hepatocytes. 151

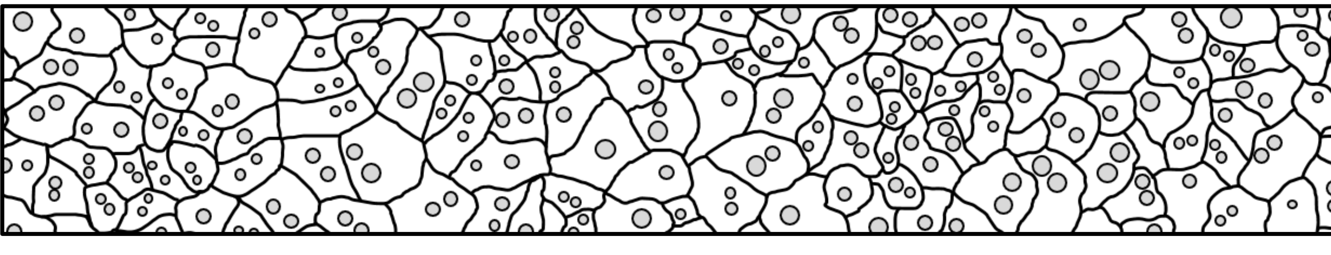

List of Tables

10. LIST OF TABLES

Table 1. Composition of tail tip lysis buffer 127

Table 2. Composition of RIPA buffer 127

Table 3. Composition of Hanks Balanced Salt Solution (HBSS) 128

Table 4. Hepatocyte washing solution 128

Table 5. Hepatocyte digestion solution 128

Table 6. Protein loading dye (4X) 129

Table 7. Phosphate-buffered saline 129

Table 8. Separation buffer used for SDS-Page 129

Table 9. Stacking buffer used for SDS-Page 129

Table 10. Composition of separation gels used for SDS-Page 129

Table 11. Composition of stacking gels used for SDS-Page 130

Table 12. Electrophoresis buffer used for SDS-PAGE 130

Table 13. Transfer buffer used for Western blotting 130

Table 14. Coomassie Staining / Coomassie destaining solution 130

Table 15. Reagents used for various experiments 131

Table 16. Equipment used in experiments 132

Table 17. Kits used for experiments 133

Table 18. Research diets used for in vivo studies 133

Table 19. Reagents used in cell culture 134

Table 20. Details of hepatocyte isolation media 134

Table 21. Details of hepatocyte culture media 134

Table 22. Details of culture media used for MEFs and Huh7* cell culture 135

Table 23. Plasmids used to transfect cells in cell culture 135

Table 24. Plasmids used for generation of stable overexpressing Huh7 cells 135

Table 25. Sequences of PCR-primer pairs utilized for genotyping 135

Table 26. Sequences of primer pairs for Real-time quantitative PCR 136

Table 27. Primary antibodies used for western blots and immunofluorescence. 137

Table 28. Secondary antibodies used for western blots and immunofluorescence. 137